Beam ripple modelling in wideband dual-reflector antenna systems

Jacques Wolmarans

Thesis presented in partial fulfilment of the requirements for the degree of Master of Engineering (Electronic) it the Faculty of Engineering at Stellenbosch University

Supervisor: Prof. D. I. L. de Villiers
Department of Electrical and Electronic Engineering

April 2022

Declaration

By submitting this thesis electronically, I declare that the entirety of the work contained therein is my own, original work, that I am the sole author thereof (save to the extent explicitly otherwise stated), that reproduction and publication thereof by Stellenbosch University will not infringe any third party rights and that I have not previously in its entirety or in part submitted it for obtaining any qualification.

Date: April 2022
. . . .

Abstract

English

Efficient modelling of the rapid far-field frequency variations found in the radiation of electrically small dual reflector antennas is of high interest due to their increasing use in array configurations for interferometry. These rapid variations, most discernible in broadside directivity across frequency, are a result of internal field interference between the radiation from the feed and reflector apertures causing chromatic aberration. Their quasi-sinusoidal nature presents a significant challenge from a modelling perspective, as computationally expensive samples at the Nyquist rate or above are required to capture the ripple during frequency interpolation.

This thesis presents the design of a physics based surrogate model able to reconstruct the ripple with a sparse set of samples independent of its frequency, and therefore, at a mere fraction of the Nyquist rate, significantly reducing the computational cost of wideband characterisation. The model is designed to assist during the evaluation of reflector geometry and feed suitability through interpolation of MoM or PO solutions with the characteristic basis function expansion method (CBFP). An adaptive sampling approach is adopted to minimise the number of direct antenna simulations needed for the generation of an accurate global model able to facilitate rapid design and analysis.

The surrogate model implementation shown here is able to capture the chromatic aberration ripple inherent to reflector surfaces of several tens of wavelengths with a sample density $\approx \frac{1}{10}^{th}$ of the Nyquist rate per octave bandwidth, for analytical Gaussian primary patterns. Prediction error is typically less than $10\,\%$ of the ripple amplitude, provided enough samples are used such that the CBFP expansion successfully isolates geometric beam features. A higher sampling density is required for primary patterns from practical antennas due to their effects on the macro behaviour of the secondary pattern across frequency, however, this is typically below $\frac{1}{4}$ of Nyquist density.

Overall, far-field radiation pattern prediction error is tied to the number of frequency samples available to train the CBFP expansion, therefore, any modelling limitation previously imposed by the chromatic aberration ripple is removed.

Afrikaans

Die effektiewe modellering van vinnige ver-veld variasies gevind in die radiasie patroon van elektriese klein dubbel reflektor antennas is van groot belang a.g.v. die toenemende gebruik van antenna samestellings vir interferometrie. Hierdie vinnige variasies, mees prominent in die breëkant gerigtheid oor frekwensie is a.g.v. die interne veld interferensie tussen die voer- en reflektor openinge se radiasie, veroorsaak deur chromatiese afwyking. Vanaf ‘n modellerings perspektief bied die kwasi-sinusvormigheid van die variasies ‘n groot uitdaging, omrede duur berekenings monsters nodig is, teen die Nyquist-koers of hoër, vir suksesvolle opvang van die rimpel tydens frekwensie interpolasie.

Hierdie tesis handel oor die ontwerp van ‘n fisika-gebaseerde surrogaat model, in staat daarvan om die rimpel vanaf ‘n stel yl monsters onafhanklik van die frekwensie te rekonstrueer, teen ‘n blote breukdeel van die Nyquist-koers, voor, wat gevolglik tot ‘n groot afname in die berekenings koste vir breëband karakterisering lei. Die model dien as ‘n hulpmiddel tydens die evaluering van reflektor geometrie en voer geskiktheid deur interpolasie van die moment metode en fisiese optika oplossings met die karakteristieke basis funksie uitbreidings (KBFU) metode te kombineer. ‘n Aanpasbare steekproef benadering word aangeneem om die aantal direkte antenna simulasies, nodig vir die generasie van akkurate globale modelle vir vinnige prototipering en kalibrasie, te minimeer.

Die surrogaatmodel implimentering wat hier voorgelê word, is daartoe instaat om die chromatiese aberrasie rimpel, inhirent tot reflektoroppervlakte van verskeie tientalle golflengtes met ’n monster digtheid $\approx \frac{1}{10}^{th}$ van die Nyquist koers per oktaaf bandwydte vir analitiese Gauss primêre patrone, op te vang. Die voorspellingsfout is tipies minder as 10% van die rimpelamplitude, mits genoeg monsters gebruik word sodat die KBFU die geometriese balk kenmerke suksesvol kan isoleer. ’n Hoër steekproefdigtheid word benodig vir primêre patrone van praktiese antennas a.g.v. hul effek op die makro gedrag van die sekondêre patroon oor frekwensie, alhoewel dit tipies onder $\frac{1}{4}$ van die Nyquist-digtheid is.

Algemene ver-veld radiasie patroon voorspellingsfout is gekoppel aan die aantal frekwensie monsters beskikbaar om die KBFU op te lei, daarom is enige modellerings beperkinge voorheen opgelê deur die chromatiese aberrasie verwyder.

Acknowledgements

First and foremost I would like to thank my supervisor prof. Dirk de Villiers, for sharing his extensive knowledge of antennas with me and creating this fulfilling project.

I would also like to several colleagues from the EMACS research group:
William Cerfonteyn for his help explaining the nuances of interfacing with GRASP and entertaining discussions regarding the art of modelling dual reflectors.

Rina-Mari Weidemann for her role in helping me understand and implement VEXPA.

Dr. Fahmi Mokhupuki for sharing his QRFH CST model and assistance with batch mode operation of CST.

I would also like to thank my girlfriend Stefana for her ongoing support and help in creating illustrations which convey concepts beautifully.

To my parents, Pierre and Lynne, and siblings, Claire and Carl, for their support of my bizarre life choices throughout this challenging period and general writing advice. To William Dommisse for his entertaining conversations in the RADAR lab and extensive Afrikaans grammar assistance.

Finally to the rest of my friends, for making my time in Stellenbosch memorable, whether in the lab, on the tennis court, on stage, in the mountains or in the Ocean.
Thank you for helping me become who I am today.

"Intelligence is the ability of a living creature to perform pointless or unnatural acts."
- Arkady Strugatsky

"Things are what they are, and whatever will be will be."
- Jonas Jonasson

Contents

List of Figures

List of Tables

Chapter 1

Introduction

1.1. Overview of dual reflector antennas

Antennas are conducting surfaces used to transmit and receive electromagnetic pulses in space. As passive, reciprocal components their identical electrical properties during instances of both transmission and reception facilitate the accurate detection and generation of transverse EM field variations through free-space [4]. This allows circuitry to extract signals from specific directions in space and process the information embedded within them. Hence, antennas form the interface between electrical circuits and surrounding physical space, allowing for the study of electromagnetic phenomena that would otherwise be impossible to interpret.

Single and Dual Reflector (DR) antennas utilise reflective structures in addition to a primary radiation source, often a horn or dipole, to focus EM fields into a narrow beam (≈0.1° to 3°) with larger reflectors increasing the extent to which focusing can occur. This focusing is a simple, passive method for effectively increasing the gain of the antenna, making reflectors particularly beneficial in low signal level environments [5]. The radiation pattern can also be accurately steered by changing the physical orientation of the entire antenna, provided the relative position of radiating elements remain constant, making reflector antenna arrays suitable for synthesis imaging [6].

These characteristics are particularly useful in satellite communication and radio interferometry settings, where spectral patterns several light years from the Earth's surface need to be detected at high resolution. An example of such use is the analysis of radiation spectra from neighbouring galaxies such as Andromeda M31, in order to approximate the elemental composition and layout through analysis of diffuse interstellar bands [7]. The 1420 MHz band associated with Hydrogen, also referred to as the 21 cm line attributed to its wavelength, is used to determine the size of constellations and galaxies, making it a primary target frequency for interferometers [8].

The physical structure of a dual reflector antenna is as follows:

1. The primary feed structure. Generally a single or hybrid mode wave-guide and antenna to illuminate the sub-reflector (SR).

2. The Sub or Secondary Reflector. A reflective aperture structure with a focal point at the radiating aperture of the primary feed antenna shaped to illuminate the main reflector.

3. The Main Reflector (MR). The largest reflective structure, which after illumination, will focus the radiation in the observation direction.

Figure 1.1: Photograph of a pair of Cassegrain dual reflector antennas used at the Stockert observatory in Eifel, Germany [1].

The dual reflector configuration is widely used in radio telescope interferometers, as it allows the feed to be positioned within the support structure of the primary reflector to create a physically compact and accessible design [9]. This is particularly useful in large diameter dishes of 20 m or more, as a small sub-reflector with a simple support structure is all that is needed illuminate the large reflector while minimising blockage. A large, highly focused feed can be positioned underneath the main reflector itself, sharing the main support, reducing the physical complexity of the antenna frame as in Figure 1.1.

Interstellar spectroscopy requires an extremely low noise figure in order to obtain the receiver sensitivity required for successful extraction of frequency information, typically below 18 K as in the *Meerkat* 64 element interferometer [10]. To meet these stringent specifications receivers often require bulky cryogenic cooling systems and wave-guiding structures to excite the feed antenna with minimal added noise.

The single reflector topology quickly becomes impractical in these situations, or similar lower S/UHF-band frequency systems, where both the reflector and LNA are several square meters or larger. This creates logistical complexities such as increased manufacturing costs due to separate support structures and excessive blockage in the main beam direction [11].

Noise considerations are always paramount in small signal systems, and a dual reflector configuration offers the possibility of orientating the feed radiation away from the ground towards the larger sub-reflector aperture, reducing unwanted illumination of noisy Earth surfaces, termed *spillover*, a primary contributing factor to antenna noise temperature [12]. Additionally, reflector surfaces can be shaped and extended to decrease spillover while maintaining directivity performance [13].

The combination of high gain with low noise figure make the dual reflector a robust tool in RF systems to boost signal to noise ratio levels through passive EM spacial filtering, as a narrower beam allows for improved rejection of incident signals from unwanted sources in communication and radio astronomy applications. This mitigates performance dependency on the LNA stage, which is often expensive and difficult to improve due to semiconductor inconsistencies and associated component costs [14]. Such improvement is highly beneficial in multi element antenna arrays where reducing the cost and complexity of each individual antenna significantly reduces the cost and difficulty of overall project implementation.

1.2. Dual Reflectors in modern interferometry

Interferometers utilise the interference between coherent signals to remove noise and improve the resolution of an observed image. Superimposing the EM fields received at separate antenna phase references observing a single point from known locations, causes destructive interference between unwanted spurious spectral components, and similarly, constructive interference between constant signals, thereby filtering out random Gaussian white noise. A simple high-level system layout of an interferometer utilising signals from a DR array is shown in Figure 1.2.

As with all RF component design there are always complex multi variable trade-offs that must be considered — interferometer arrays are no different. The trade-off in question involves receiver sensitivity and image resolution against computational and logistical cost [15].

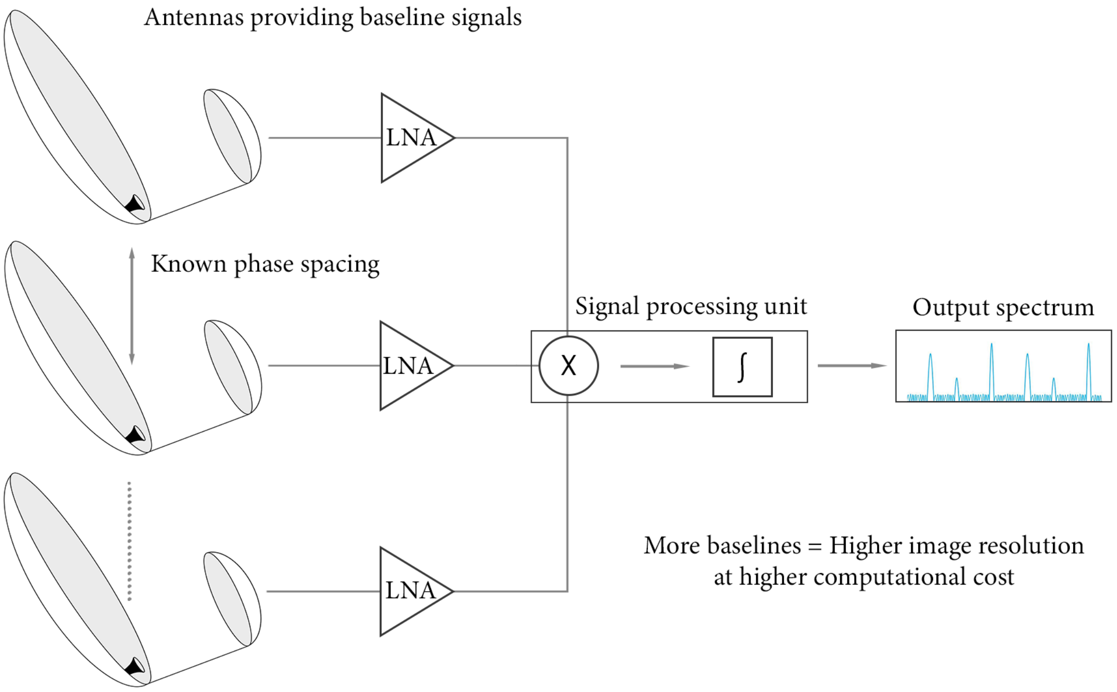

Figure 1.2: Overview of a DR interferometer system

Additional antennas provide more baseline signals for a single observation point, and therefore, higher image resolution with less noise after correlation and aperture synthesis. This contributes to the effective aperture and sensitivity of the receiver. The drawback of more antenna elements is the increased cost associated with many more LNA units, matching networks and cabling as well as the increased computational requirements for sufficient data processing and correlation of each element's data-stream.

The increase in the computational capacity and availability of high fidelity FPGA systems for rapid signal processing and accurate aperture synthesis have created a trend for radio telescopes to adopt a multi antenna approach instead of the extremely large reflector antennas prominent in the late 70's and 80's [12]. Larger reflectors are difficult to manufacture precisely and are encumbered with increased logistical costs and challenges from a construction, operation and maintenance perspective [16]. However, current computational abilities are not yet above the threshold to allow for many hundreds of tiny elements to be simultaneously processed in real time, upholding individual antenna performance as a critical part of system sensitivity [17].

At the present time, arrays consisting of several tens of high gain reflector antenna elements, with diameters of several meters (ranging from tens to thousands of wavelengths) presents the most effective trade-off between cost and performance. This is illustrated in the SKA (130 x 15 m & 64 x 13.5 m) and ALMA (54 x 12 m & 12 x 7 m) radio telescope arrays. Reflector surfaces of this size are cheaper to manufacture, transport and install, and eliminate the need for specialised cranes and machines or powerful actuator motors [18].

This antenna size is also convenient for fitting receiver units underneath the main reflector, inside its support structure. This provides EM shielding and easy access for maintenance or repairs of electrical components, increasing the effectiveness of these antenna geometries from a logistical perspective. Such logistical considerations are important due to the remote locations such arrays are typically placed in to reduce background noise [12]. This creates a strong case for the continued use of such reflector arrays into the foreseeable future of radio astronomy.

With active research into GPU optimisation to further improve the rapid data processing capability of FPGA units continuing [19], [20] and computer driven design methods able to obtain aperture efficiencies of above 65 % on dishes smaller than 50λ where analytical GO procedures are no longer suitable, the trend of sub 20 m MR diameters for use in the UHF band is set to continue. This means unwanted coupling between components and subsequent surface current scattering will have a significant effect on beam characteristics due to the smaller reflector surfaces, creating a new demand for accurate modelling of the non-ideal wideband far-field effects associated with electrically small reflectors, especially during the initial design phase.

1.3. Wide-band characterisations of dual reflector gain

Modern radio telescopes typically operate over bandwidths of several GHz, with antennas even using multiple feeds, such that a single reflector geometry can be used across multiple bands [10]. The focal point of a reflector aperture undergoes small rapid changes across frequency when its physical size is not much larger than the wavelengths of the EM waves in question ($D < 80\lambda$). This phenomenon is termed *chromatic aberration*, and results in equally rapidly varying phase errors in the surface current of the radiating reflectors. These phase errors cause internal field interference between the radiation from each aperture in the dual reflector, driving unwanted ray diffraction and mutual reflector coupling [21].

The extent of this non-ideal behaviour for a dual reflector geometry at a certain frequency is directly tied to the electrical size of the reflectors, worsening as their effective apertures become smaller. These effects are linked to residual spherical features in electromagnetic waves not accounted for with geometric optics (GO) based designs [22].

The rapid chromatic aberration ripple evident in the main beam of far-fields of dual reflectors with primary aperture blockage, due to the SR and/or supporting struts, is attributed to the formation of a harmonic standing wave between the reflectors. Clear aperture configurations, such as the offset Gregorian geometry, mitigate the effects caused by blockage of the radiation paths within the antenna, however, at lower frequencies where the MR and SR diameters fall below approximately 15λ and 40λ respectively, feed radiation with spherical wave-front characteristics will diffract around the sub-reflector upon incidence.

This diffraction is accentuated by broadening of the feed pattern at lower frequencies due to constant aperture size and increasing wavelength. The result is additional radiation behind the SR, which in turn, will interfere with the full antenna beam producing similar wideband variations and a slope pattern over the main beam and side-lobes. These chromatic aberration ripples are best described as small, quick pseudo-sinusoidal oscillations mostly visible near broadside across frequency [23] as illustrated in Figure 1.3.

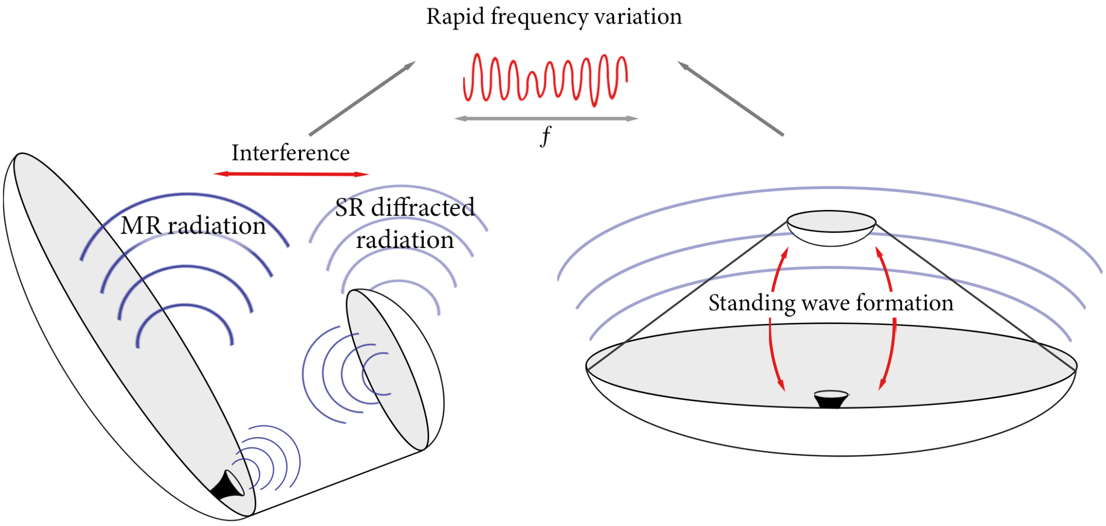

Figure 1.3: Physical geometric features of dual reflectors contributing to rapid far-field variations across frequency mostly visible in the main antenna beam.

While the frequency of the standing wave component can be analytically approximated by examining the plane wave path length between the reflective surfaces, the spherical wave phase differences of the diffracted radiation behind the sub-reflector [21], which determine the rate and amplitude of the dynamic ripple, make it impossible to predict analytically [23].

Furthermore, the Fourier components of the ripple, typically in the several tens of MHz range, inhibit the accuracy of interpolated computer simulation results without dense

Nyquist rate sampling. Accurate descriptions of this ripple are of great importance during the image calibration of interferometers to prevent ambiguity in observations [22]. Ultimately, the wideband frequency variations evident in dual reflector far-field patterns close to broadside can be attributed to two phenomena:

1. Coupling and diffraction interference between reflector fields due to chromatic aberration.
2. Variations in the radiation pattern of the feed due to propagation of different TE modes.

The $-12\,\mathrm{dB}$ beam-width of the feed antenna's radiation pattern, or primary pattern, has a major effect on reflector system gain as it determines the current density across the sub-reflector.The beam's taper typically changes according to a smooth, slow varying function across frequency, meaning the primary pattern affects the macro directivity behaviour of the secondary pattern across frequency. Frequencies where modal crossover is present in the aperture of the feed create regions of non-linearity as beam broadening increases spillover beyond the SR rim, often causing sharp declines in the aperture efficiency of the dual reflector.

1.4. Modern dual reflector design procedures

Modern RF systems continually place an emphasis on antenna stage performance, particularly from a signal level standpoint, to minimise information loss. Other notable specifications are $-12\,\mathrm{dB}$ beam-width, first side-lobe level (SLL), antenna noise temperature and co-cross polarisation isolation. These requirements are even more stringent in radio astronomy, where spectroscopy requires stable, highly directive, radiation patterns for bandwidths of an octave or more, with practical designs optimised to perform close to the theoretical maximum.

It is, therefore, pertinent to evaluate whether a dish geometry is suitable for an application early in the design stage, which typically depends on the main beam gain possible above the noise floor together with the available feed. This is best described using *aperture efficiency* when only the reflector geometry is under evaluation, and all other components are assumed lossless and ideal. For successful spectral analysis, the reflectors must be able to perform throughout the bandwidth(s) of interest, without geometry driven frequency variations which can create ambiguity in the received spectral information [15]. As such, it is common practice to first evaluate geometries using an analytically defined Gaussian feed pattern with a constant taper across frequency [24].

Powerful computational electromagnetic software built upon the boundary element method, method of moments (MoM), is able to perform full-wave simulations in order to deliver a near exact performance prediction for the antenna. Such software has reduced the need for expensive, and often tedious, physical measuring of large antennas for calibration, making software driven *third generation* calibration tractable [22].

Furthermore, the availability of accurate EM field data has lead to the development of multi-objective optimisation techniques which use high fidelity results to shape and extend reflector surfaces in order to compensate for beam distortion caused by the practical antenna structure [12].

The drawback of such a direct approach is the computational cost associated with a full-wave solution, often rendering such simulations far too time-consuming to be feasible early in the design. This is especially true if the surface area of the reflectors is electrically large, as the number of discrete mesh elements required to accurately model surface current density scales, linearly at best, according to the number of frequency samples. Computationally cheaper approximations are, therefore, imperative for large reflectors ($D > 25\lambda$).

The most common reflector current density approximations in literature are Geometric optics (GO) and Physical Optics (PO). These methods assume levels of uniformity in surface current density, reducing the cost of computer based analysis [25]. The accuracy of these approximations, particularly GO, is directly proportional to the electrical size of the radiating elements. This renders GO based field estimations obsolete for electrically small dual reflectors, where diffraction and coupling significantly affect far-field behaviour.

Physical Optics, including the physical theory of diffraction (PTD), can be setup to consider first reflection coupling (by re-evaluating SR currents using the MR field as incident) and diffraction to produce functional field estimations for much smaller reflectors [26], making it the most widely used method. However, if the radiation pattern of the antenna must be calculated at several hundred frequencies to sufficiently capture rapid deviations, PO estimations of the far-field become the most costly design activity [22].

Henceforth, the development of so called *surrogate models*, or *meta-models*, able to accurately estimate wideband aperture efficiency with all diffraction and coupling effects with less computational expense, by augmenting costly PO or MoM based simulations with computationally cheap alternatives, is an active research field.

de Villiers presents a method in [23] which combines geometric ray path analysis and simulation generated field data to characterise wideband offset dual reflector far-field behaviour. It can reproduce wideband chromatic aberration ripple at 0.5 % maximum error for multiple clear aperture configurations, at a sample density roughly one sixth of the Nyquist rate.

Such approaches are unfavourable as they are dependant on accurate user analysis, which is open to misinterpretation. Research surrounding universal low-cost, fully computer based modelling tools has lead to their application in the design and optimisation of microwave components [27]. Such models are well suited to electromagnetic problems, where the generation of a predictive model across the design space is cheaper than a single direct simulation sample, and analytical methods require extensive user understanding [28].

These approaches utilise algorithmic strategies to find the optimal trade-off between cost and accuracy for data driven design tasks, without prior system knowledge or user analysis. Interpolation is used to connect sparse, high-fidelity, computationally expensive results with continuous interpolants for the creation of a cheap, approximate, high density model. Kriging interpolation is effective and robust in this regard, as it supports model modification through adaptive sampling of the design space. Here, strategic, iterative sample placement, through the use of a *sampling function*, is done to reduce the number of samples required for an accurate model prediction anywhere in the design space [27]. The sampling function analyses the covariance matrix of the Kriging interpolant at each step in the process, in an effort to determine the location at which the addition of another high-cost data sample will maximise global model improvement.

Such methods have been successfully applied to the design and optimisation of horn antennas specifically for use in reflector systems [3], by utilising characteristic basis function expansions which split complex antenna behaviour into several orthogonal, slowly varying dimensions. These single dimensions are easy to accurately interpolate, resulting in a model which adequately captures antenna behaviour for accurate beam predictions. A similar interpolation approach has been used to capture the rapid far-field variations of dual reflectors in [22] and [29].

The sample density for both approaches is limited by the Nyquist criterion of the oscillatory chromatic aberration ripple, removing the benefit of an adaptive sampling approach. In addition, analytical procedures are required in both cases to ensure sufficient sampling density for model construction. They do, however, provide definitive proof of concept.

1.5. Surrogate interpolation model using the characteristic basis function patterns

This thesis builds upon the characteristic basis function pattern (CBFP) method for accurate antenna beam predictions presented by Young et. al in [30]. This method is able to capture both geometric and frequency variations in far-field patterns, including side-lobes, with fewer basis functions than other (for example Jacobi-Bessel) basis expansions [6]. The focus of this thesis is to apply the CBFP interpolation method to the wideband characterisation dual reflector far-fields as in [22], without Nyquist limitations.

The CBFP expansion splits far-field features through singular value decomposition (SVD) of available beam data to create a set of complex coefficients, weighted in order of significance, corresponding to orthogonal basis functions which together capture the qualities of the antenna beam for a given frequency domain. This allows for an approximation of the actual radiation pattern of the antenna in all known directions to be generated at any frequency for which the significant CBFP coefficient values are correct. Henceforth, this method is well suited to interpolation and adaptive design procedures, as typically less than 15 correct single dimension frequency coefficients are needed to produce an accurate spacial reconstruction of the antenna beam [22].

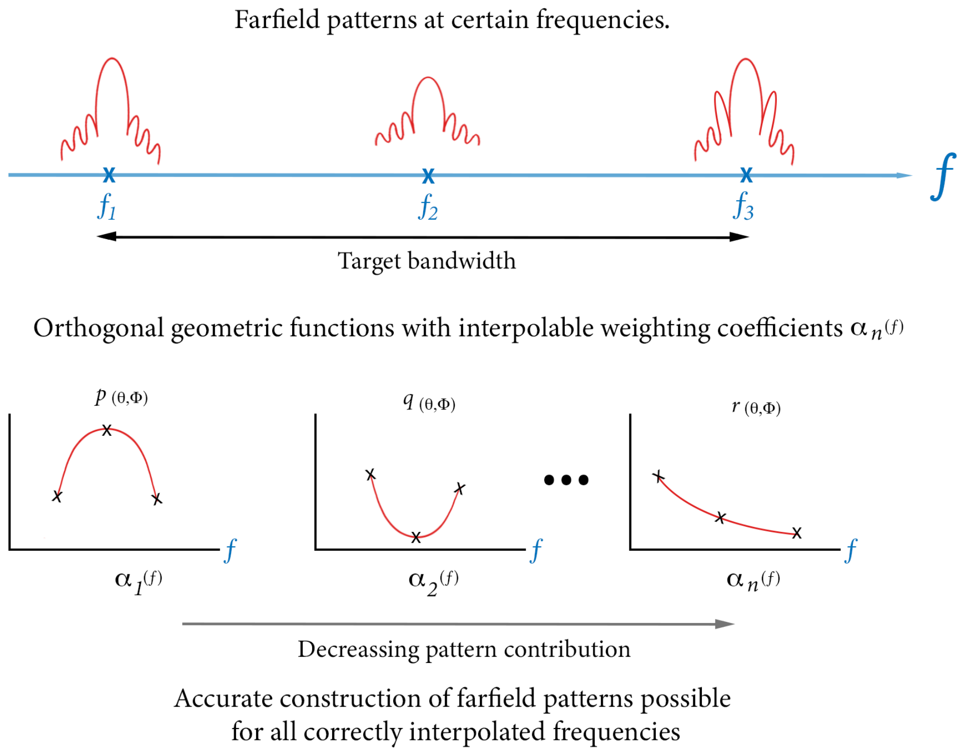

Figure 1.4: CBFP interpolation method to predict radiation patterns with orthogonal basis functions p, q and $r(\theta, \phi)$ created through beam SVD at f_{1-3} weighted by coefficients $\alpha_{1-3}(f)$.

Figure 1.4 summarises how beam predictions in the target bandwidth can be made from the interpolants of CBFP coefficients generated from known pattern data at certain frequencies, with n clarifying that the number of coefficients is limited by the number of source patterns.

The draw back of directly applying this method to wideband dual reflector characterisation is that care needs to be taken to ensure the frequency domain is sampled with sufficient resolution to satisfy the Nyquist criterion of any underlying chromatic aberration far-field ripple. Sample schemes too sparse across frequency will result in aliasing of the CBFP coefficients, and subsequently, inaccurate field estimation. This is the most severe shortcoming of the CBFP interpolation method from a computational efficiency standpoint. While there is extensive literature on the cause of such variations, as well as analytical geometry based methods to predict their periodicity, it requires a physical understanding of reflector antennas [22] inhibiting robust use of unsupervised software driven design procedures.

This creates a demand for modelling based solely on simulation data, able to produce accurate wideband characterisations of electrically small dual reflector antennas at a low computational cost, without any prior knowledge of the antenna geometry or Nyquist baseline sample resolution. An open space in literature exists for a robust simulation (PO/MoM) driven method which can deliver wideband results to the same accuracy as those presented in [22] but with a much cheaper, sparse sample density, as in [23].

1.6. Overview of the superposition method

The physically driven nature of the rapid frequency variations observed in the aperture efficiency of dual reflector systems is well established in modern literature. There is a clear consensus that interference of diffracted rays behind the SR with the radiated field from the main reflector [21] and standing wave formation between the MR and SR [31] cause the chromatic aberration ripples visible in far-field radiation patterns across frequency.

This is the principle on which the method presented in this thesis is built. It is postulated that removing coupling and interference effects, by regarding the far-field radiation contributions of the feed and sub reflector as a single radiating entity, and the contributions of the main reflector as another, will produce two independent far-field patterns which exhibit slow variations across frequency.

These single entity far-field patterns are, therefore, well suited for interpolation, and should allow for the superposition of two sparsely sampled CBFP expansions to reconstruct the full dual reflector pattern with any embedded interference or coupling. The sequential manner in which PO based simulations estimate the induced reflector surface current density allows for the convenient formulation of a mathematical abstraction for the radiation from the main reflector aperture. If the far-field radiation of the feed and sub-reflector is projected onto the global elevation and azimuth reference for the antenna, it can be subtracted from the the full dual reflector far-field pattern to create an accurate representation of the main reflector far-field when illuminated with the feed and sub-reflector combination in question which is free from chromatic aberration ripple. An illustration of how the ripple near broadside is removed with this approach to give to two slowly varying directivity distributions is illustrated in Figure 1.5 below.

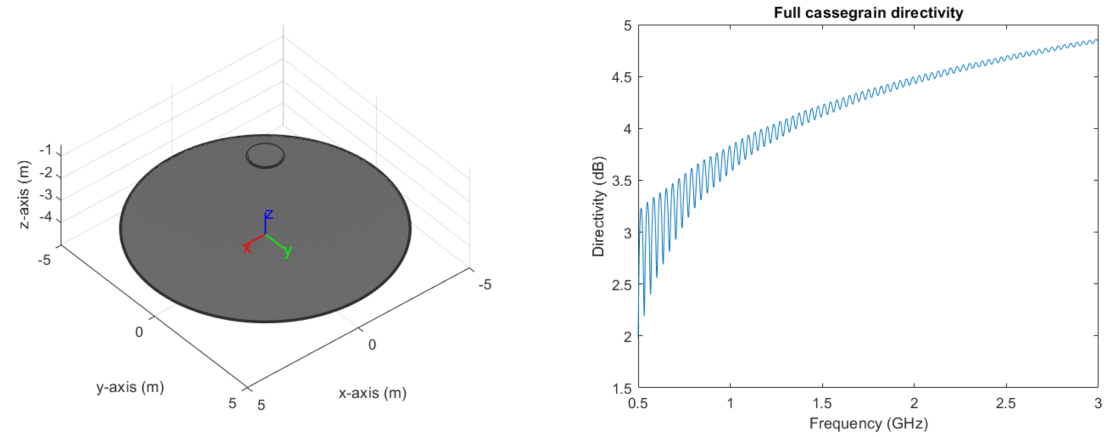

(a) Electrically small Cassegrain geometry exhibiting significant chromatic aberration ripple

(b) Significant chromatic aberrations visible in broadside directivity

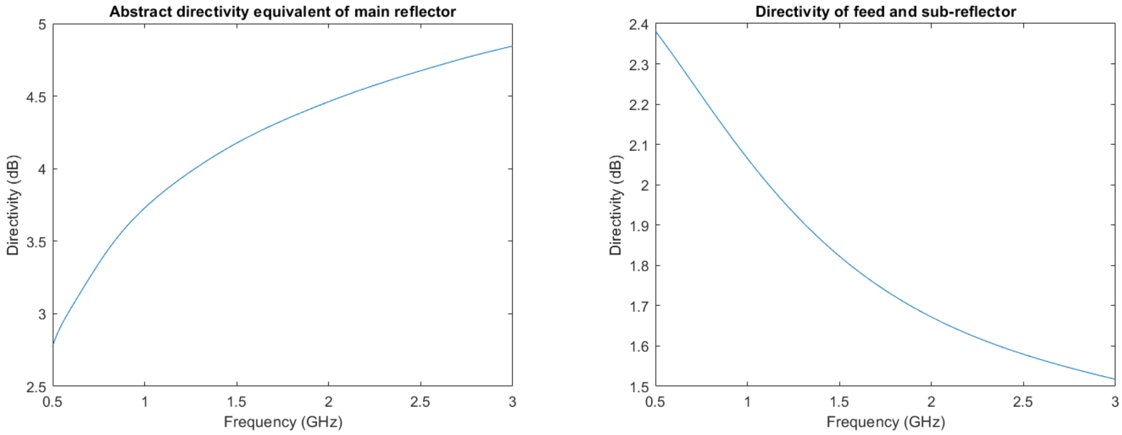

(c) Smooth directivity equivalent of main reflector after subtraction $(\mathbf{E}_{DR} - \mathbf{E}_{FSR})$

(d) Smooth directivity contribution of feed and sub-reflector

Figure 1.5: Illustration of effective rapid ripple removal with field subtraction

This subtraction should allow for rapid frequency variations present in the fields to be accurately reconstructed with sparse frequency samples, by taking the sum of the two separated CBFP expansion coefficients after interpolation. Here the only requirement is that a sufficient number of samples, which facilitates successful isolation of the major radiation factors into individual coefficients, is used to build the interpolant. This will ensure that physical features are correctly ranked according to their pattern influence, allowing for the accurate capture of all small frequency dependant variations.

1.7. Aims and objectives of study

A robust software tool facilitating the rapid wideband characterisation of dual reflector antennas, regardless of electrical size, is the primary development aim of this study. Interpolation is separately applied to the feed and sub-reflector far-field and equivalent main reflector far-field patterns, by generating a characteristic basis function expansion for each specific data-set, free from rapid variations. All diffraction interference is, therefore, captured with a sample density well below the Nyquist rate of any rapid variation in the full dual reflector antenna patterns using the process outlined in Figure 1.6.

Practically, the goal is to reduce the number of expensive frequency samples needed to construct an interpolation based model able to predict wide-band far-field data, which includes rapid beam ripple, at an accuracy sufficient for antenna design and analysis such as the model presented in [22].

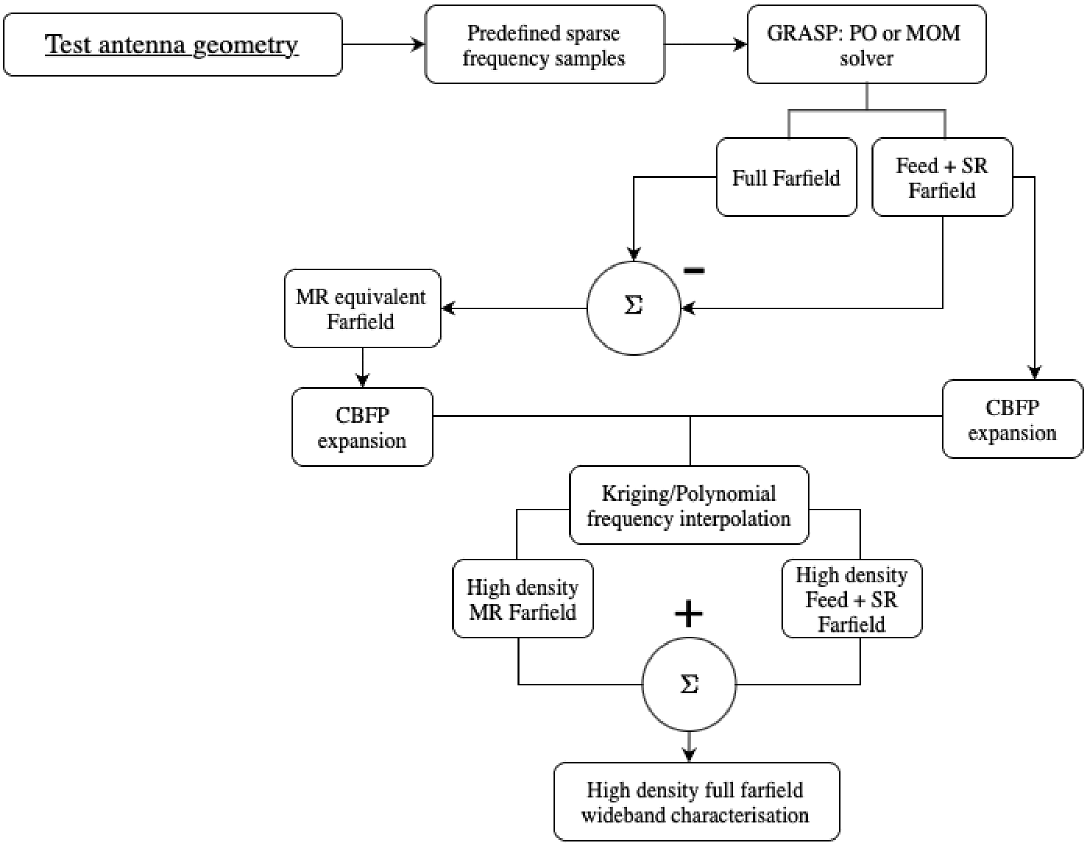

Figure 1.6: Overview of CBFP interpolation applying field superposition for known dual reflector systems

The significant improvement over present interpolation models in literature [23], [22], [29] is the ability to obtain a far-field prediction, with an accurate main beam and first side-lobe, without any prior knowledge of the dual reflector under test, or the frequency of the ripple it exhibits.

The primary limitation of these existing approaches is that they are dependent on either knowledge of the ripple frequency (obtained through costly dense sampling) or geometry based assumptions thereof, to ensure enough direct samples are used such that no field variations are lost to aliasing.

Subtraction of the feed and SR radiation to manufacture a definition of the far-field radiation from the MR removes the physical cause of the ripple entirely, tying the necessary sample density to capturing the macro-behaviour of these slow varying fields only. Adaptive sampling schemes can be applied to reduce the uncertainty of the interpolant on an iterative basis, by tracking the convergence of significant CBFP coefficients according to the number of samples. The model can then make an informed decision regarding the total amount needed for an acceptable model prediction, eliminating the risk of an insufficient sample density being specified by the user. Figure 1.7 gives a possible algorithm which tracks convergence of CBFP coefficients on a per sample basis to independently determine if the direct data available is sufficient.

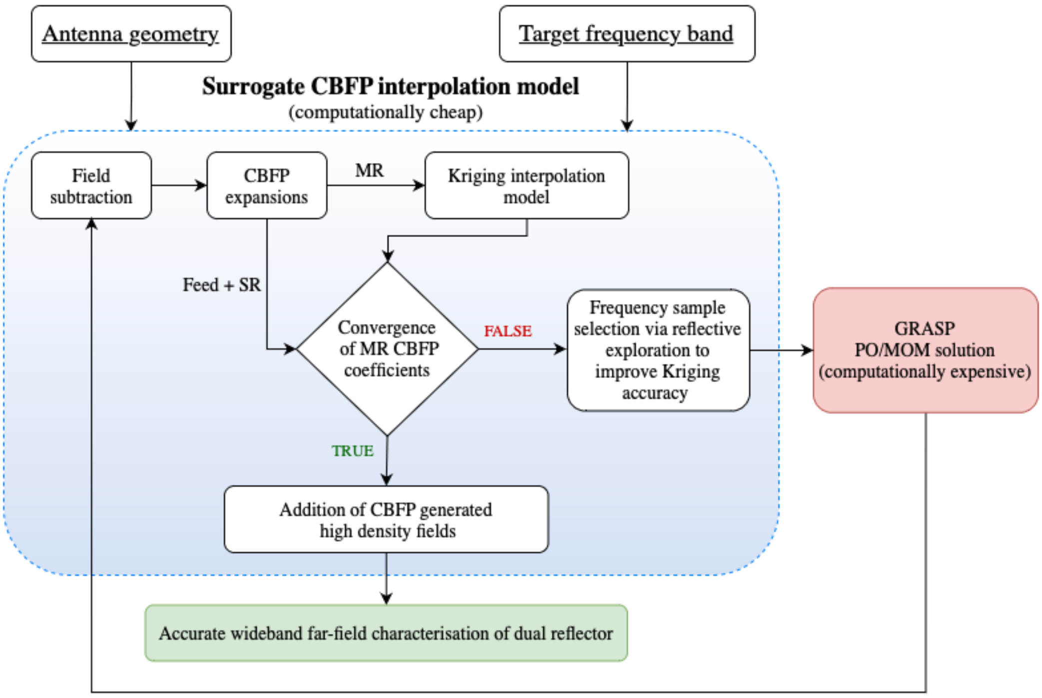

Figure 1.7: Overview of the CBFP superposition simple Kriging based surrogate model applying adaptive sampling in the MR space which tracks CBFP coefficient convergence to determine the number of required samples

The model allows for the illumination of the reflectors using either a physical antenna or an analytically defined Gaussian pattern, and interfaces directly with commercial computational electromagnetic (CEM) solvers to characterise the aperture efficiency ripples inherent to the geometry. A robust algorithm places frequency samples on an exploratory basis, covering the domain of the slowly varying basis coefficients with as few support samples as possible, such that once the early coefficient expansion patterns settle, a far-field prediction can be obtained, including frequency information that would previously be unattainable with such low resolution.

These features are presented under a single user interface, to create a software tool which facilitates fully software driven calibration and design testing of dual reflector systems.

1.8. Thesis Overview

1.8.1. Chapter 2

Firstly this chapter presents the mathematical notation and physical geometry of dual reflector systems utilised throughout future chapters. This is followed with an overview of pertinent electromagnetic principles associated with dual reflector systems, most notably spherical incidence and surface current density approximations. A discussion of the figures of merit concerning antenna performance is then conducted with a clear exposition of aperture efficiency. Background regarding horn antennas in dual reflector feed structures and their modelling is presented before the chapter concludes with a high level description of the relevant computational processes and methods required for the synthesis of a CBFP interpolation based surrogate model.

1.8.2. Chapter 3

Due to the phase adjustments and far-field phase reference positioning in GRASP (and other PO/CEM solvers), electric field solutions contain a fast varying periodic phase variation across frequency which is not related to physical antenna behaviour [22]. This presents a major problem for interpolation schemes due to the high density samples required if the carrier frequency of the variation is unknown, or cannot be removed. This chapter shows that validated complex exponential analysis (VEXPA), which utilises the aliasing pattern of co-prime sub-sampling, can be used to calculate a far-field phase shift factor r_{norm}, which in turn can be applied to the electric field patterns to remove the periodic phase variation using samples which add value to the interpolation process.

1.8.3. Chapter 4

This chapter gives a specific breakdown of the physics based superposition strategy used to capture the rapid small frequency variations in the directivity of dual reflector systems, caused by internal field interference as a result of chromatic aberration of the reflector foci. It then presents a surrogate model implementation generated with fixed sample distribution, analysis type data sets, where prior knowledge of the antenna system and its associated basis function patterns is known. Kriging and Polynomial interpolation of CBFP coefficients as well as the required number of associated support points are discussed for symmetrical and offset dual reflector systems.

1.8.4. Chapter 5

The design of an adaptive sampling based surrogate model, where the support samples used to interpolate CBFP coefficients are obtained through adaptive sampling of the design space, and not specified by the user, is presented in this chapter. Iterative single dimension simple Kriging interpolation of the real and imaginary part of the highest order converging CBFP coefficient is used to place samples at frequencies which maximise the information gained by the global surrogate model. A robust framework applying relative thresholds to evaluate the convergence of basis function coefficients, without any pre-defined sample limits or system information, is presented and shown to be effective in capturing the far-field frequency variations associated with electrically small geometry.

1.8.5. Chapter 6

In this chapter the effects of using a practical antenna radiation pattern to illuminate a dual reflector system on its CBFP expansion is investigated. A surrogate model using the CBFP superposition approach is then shown to be effective for characterisation of a fully practical dual reflector system.

1.8.6. Chapter 7

A final conclusion is drawn regarding the effectiveness and relevance of such an interpolation tool in modern software driven dual reflector design and calibration. The shortcomings and limitations of the surrogate model are also discussed. Finally, the thesis is concluded by mentioning relevant spaces for further work such as the development of a full Pareto multi-objective framework driven by similar surrogate models for all relevant dual reflector performance metrics, and possible improvements to the adaptive sampling approach for the CBFP superposition method.

Chapter 2

Theoretical Background

This chapter will present a high level discussion of relevant antenna and physics theory applicable to the modelling of dual reflectors, as well as discuss the literature surrounding the CBFP expansion method and its application to practical DR far-field patterns estimated using computational solvers. This thesis follows the *IEEE Standard for Definitions of Terms for Antennas* [32], with reflector specific metrics included for clarity.

2.1. Overview of antenna theory

In technical terms, an antenna is a transducer converting electromagnetic radiation guided through transmission lines and circuitry to directed radiation, propagating through free-space [33]. From a circuit perspective an antenna converts a potential difference or voltage (V) defined between two conductors, to a radiating EM wave with an electric field strength (E_v) defined relative to the force required to displace a positive point charge by one meter in free-space ($\frac{\mathrm{V}}{\mathrm{m}}$). Through the theorem of reciprocity, almost all antennas exhibit identical electrical behaviour during transmission and reception. This allows antennas to be designed as if operating *transmit mode* which is often favourable from a visualisation and understanding perspective.

2.1.1. Field Regions

The antenna is a radiating device, meaning the path between the antenna itself and the point at which it is observed or measured has an influence on the shape of the EM field it receives or creates as evident in Figure 2.1. The boundaries for which different mathematical models can be used, to an acceptable degree of accuracy, are frequency dependant and are, therefore, defined using electrical length described in wavelengths, λ.

All fields in future discussions of this paper are assumed to be in the *far-field* region of the antenna unless stated otherwise. The impact is that a plane wave model is most suitable to capture the natural state of the radiated wave-front, as the distance from the antenna, r, is so electrically large that all spherical features of the radiation pattern are invisible at the observation point, therefore, the observed pattern is independent of distance [34].

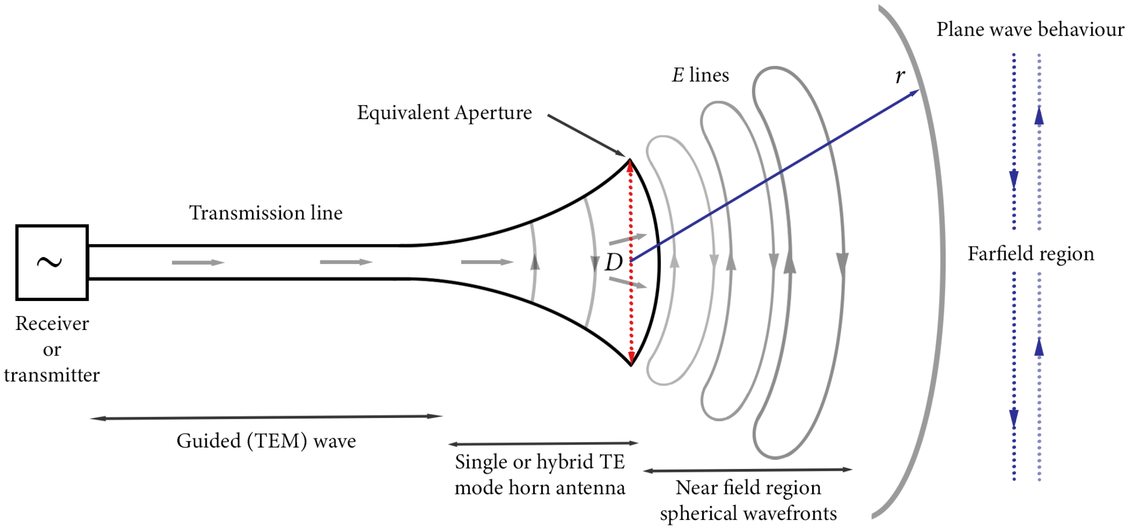

Figure 2.1: Field regions around an antenna aperture

Here r represents a radial distance between the antenna's phase centre and the observation point, with the boundary for the far-field approximation valid for $r > \frac{2D^2}{\lambda}$, where D is the effective diameter of the radiating aperture at its phase centre [12]. The phase centre of an antenna is the point where the spherical wave begins to radiate.

Ideally the phase reference and phase centre of the antenna is identical, however, in wideband systems the phase centre will gradually shift with frequency, this shift is fairly negligible if the antenna is well designed, and practically, a position minimising deviation for all frequencies is chosen to be the new phase reference [6]. Electric fields, $\mathbf{E}$, at an arbitrary point relative to the phase reference of the antenna are used to characterise far-field radiation patterns. Mathematically this is expressed in the spherical co-ordinate system of the antenna at some point r in the far-field region of a medium with propagation constant k:

$$\mathbf{E}(r, \theta, \phi) = \frac{1}{r}\exp(-jkr)\mathbf{G}(\theta, \phi). \tag{2.1}$$

The radiation pattern, $\mathbf{G}$, is defined along an axis of propagation, chosen as the Z axis of the global antenna co-ordinate system in free-space for simplicity, using an angle of elevation, θ, and an azimuth angle, ϕ, as shown in Figure 2.2 below. The radiation is best described as a plane wave with the electric field contained in the plane orthogonal to the direction of propagation once in the far-field region of the antenna. Changes in the observation point along the axis of propagation, therefore, simply correlates to a phase difference in the time harmonic electric field. This phase difference is denoted using the divergence and phase factor of the *free-space far-field Green's function*:

$$\frac{1}{r}\exp\left(-j\frac{2\pi}{\lambda}r\right) \tag{2.2}$$

this models the antenna radiation such that the point of observation is so far from the antenna itself, its physical structure is indistinguishable from a single point, with the amplitude reduction accounting for the enlargement of the sphere around the antenna as the wave propagates. This Green's function is derived from the spherical wave equation in an unbounded lossless homogeneous medium, a full description can be found in Harrington [35] pg. 121.

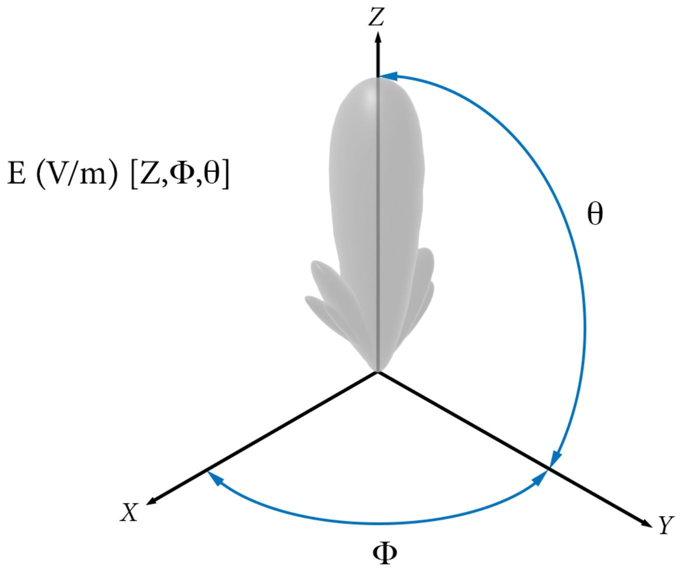

Figure 2.2: Spherical representation of the far-field radiation pattern of an antenna

As long as the geometric regions of θ and ϕ in which antenna radiation patterns are defined remain constant, they may be added and subtracted as vector fields, using typical vector notation and procedures [12].

2.1.2. Directivity, gain & radiation intensity

The Poynting vector, $\mathbf{W}$, represents the instantaneous power of a radiating planar EM wave, analytically evaluated as the cross product of the $\mathbf{E}$ and $\mathbf{H}$ field, with $\eta_0 = 377\Omega$, the free-space intrinsic impedance:

$$\mathbf{W} = \frac{1}{2}\operatorname{Re}\left(\mathbf{E}\times\mathbf{H}^*\right) = \frac{\hat{\mathbf{k}}}{2\eta_0}|\mathbf{E}(r,\theta,\phi)|^2\bigg|_{r\to\infty} \tag{2.3}$$

with the far-field defined infinitely far away from the source antenna, the radiation intensity, $\mathbf{U}$, is given with the limit as $r \to \infty$:

$$\mathbf{U}(\theta, \phi) = \lim_{r\to\infty} r^2|\mathbf{W}| = \frac{1}{2\eta_0}\left|\mathbf{G}(\theta, \phi)\right|^2. \tag{2.4}$$

Henceforth, $\mathbf{U}(\theta, \phi)$, represents the radiation intensity of the antenna in all directions. The total radiated power from an antenna, P_{rad} , can be expressed, regardless of distance, by taking the spherical integral of the square of the complex far-field function:

$$P_{\text{rad}} = \int_0^{2\pi}\int_0^{2\pi} \mathbf{U}(\theta, \phi)\sin\theta d\theta d\phi = \frac{1}{2\eta_0}\int_0^{2\pi}\int_0^{2\pi} \left|\mathbf{G}(\theta, \phi)\right|^2 \sin\theta d\theta d\phi \tag{2.5}$$

the average radiation intensity of the antenna in all directions, U_{ave}, is related to P_{rad} by:

$$U_{ave} = \frac{P_{\text{rad}}}{4\pi}. \tag{2.6}$$

In practice, during the design stages of antennas, where receivers or other circuitry has not yet been concluded, P_{rad} is set to 4π in order to normalise the average radiation intensity such that directivity, $\mathbf{D}$, can be directly extracted from $\mathbf{U}(\theta, \phi)$. Directivity in a single direction is expressed as:

$$\mathbf{D}(\theta, \phi) = \frac{4\pi[\mathbf{U}(\theta, \phi)]}{P_{rad}} = \frac{4\pi\left|\mathbf{G}(\theta, \phi)\right|^2}{\int_0^{2\pi}\int_0^{2\pi}\left|\mathbf{G}(\theta, \phi)\right|^2 \sin\theta d\theta d\phi} \tag{2.7}$$

here directivity is a ratio between the isotropic radiation intensity and the radiation intensity in the specified direction of (θ, ϕ). Of interest in reflector antennas, and other pencil beam sources, is the broadside directivity at $(\theta, \phi) = (0°, 0°)$ as it is ideally the direction of maximum radiation intensity, an important performance metric. Antenna gain, G, defined as the ratio between the power accepted, $P_{Accepted}$, and radiated, P_{rad}, by the antenna, is a crucial part of RF systems, and is a focus during the design of dual reflectors. It is related to directivity by *radiation efficiency*, e_{rad}:

$$P_{rad} = e_{rad}P_{Accepted} \tag{2.8}$$

however, if the antenna is assumed to be perfectly ideal with no sub-efficiency losses, $e_{rad} = 1$, gain and directivity become interchangeable. This rule is applied throughout this text, as only the radiated characteristics of the antenna are under evaluation, and the circuit behaviour of the antenna is assumed to be ideal and, therefore, lossless.

2.1.3. Beam patterns / Practical Beam patterns

Dual reflectors fall under a class of antennas termed *pencil-beam antennas*, geometrically characterised by a narrow half-power beamwidth as well as relatively low sidelobe levels in their principle plane, or plane which captures the highest radiation intensity with the E-field polarisation in question. The fields presented in this text are defined with full spherical description, meaning the results should be applicable to circular or linear polarisation use cases. A typical reflector beam is annotated in Figure 2.3 below:

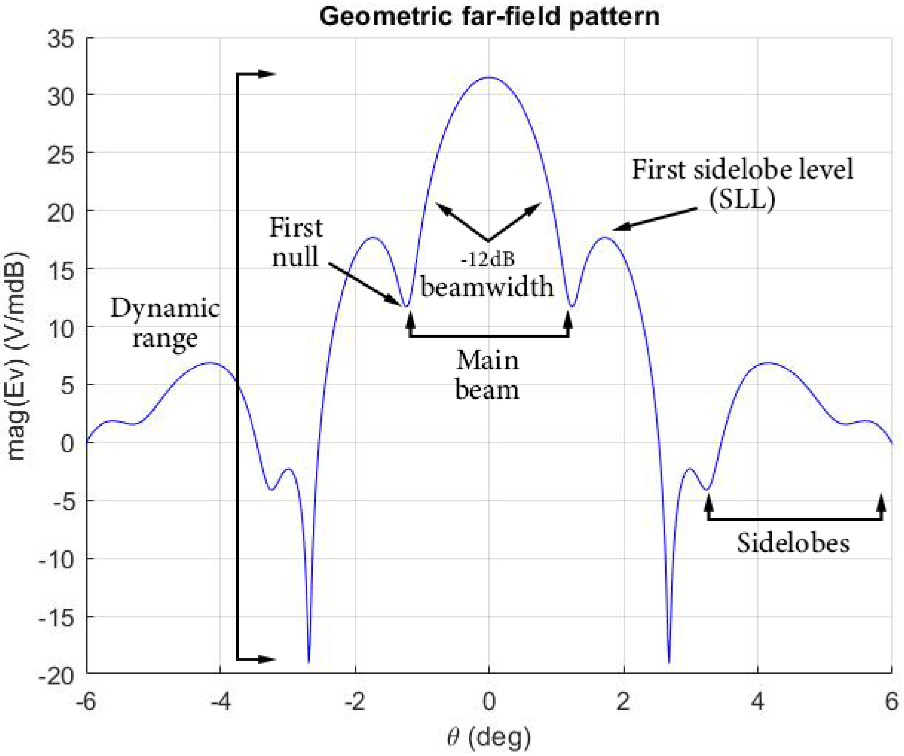

Figure 2.3: Pencil beam far-field features

2.2. Reflector antenna terminology

All reflector antennas are discussed using a primary and secondary radiation pattern in literature. Here *primary pattern* refers to the spherical waves emanating from the feed structure of the reflector system, and *secondary pattern* refers to the radiation from the all radiating apertures (feed + reflectors), best modelled as a collimated plane wave propagating in the focus direction of the entire reflector antenna system.

Antennas utilising parboloidal dishes have an intrinsic symmetry in their secondary pattern in the azimuth plane, meaning that the radiation is constant across ϕ under ideal conditions. Practically, however, it is very difficult to obtain a perfectly symmetrical pattern due to blockages and other non-ideal elements inside the near-field region of the antenna. These blockages, caused by required support or other structures, can also cause beam squint and phase disruptions in the secondary pattern. Beam squint refers to a pattern with an asymmetrical beamwidth about $\theta = 0°$, common in offset geometry.

2.2.1. Aperture efficiency

The system characterisation which best captures the gain of a reflector configuration is *aperture efficiency*. For a paraboloidal reflector, the field aperture in question is well defined as a disc with the same diameter of the reflector itself located at the shallowest side of the dish's taper. A uniform electric field distribution across an aperture with a field intensity of $0\,\mathrm{V\,m^{-1}}$ at its rim maximises its directivity [5].

Such a distribution is impossible to obtain practically, but serves as a useful benchmark from which to evaluate reflector systems. Realistically, the main beam of the illuminating radiation attempts to create a gradually tapered distribution across the diameter of the dish before falling to a sufficiently low null, typically several dB lower, at the rim. A comparison is made between the absolute maximum directivity, D_{max}, obtainable with perfect illumination of a reflector, and the directivity obtained with the tapered illumination from the feed and sub-reflector under test, D_{test}. The maximum gain, $G_{\max}$, from an ideally matched PEC aperture of a certain size (A_{phys}) at a frequency with wavelength equal to λ is:

$$G_{\max} = D_{\max} = \frac{4\pi}{\lambda^2} A_{phys} \tag{2.9}$$

with *aperture efficiency*, η_{ap}, simply the ratio between the maximum gain obtained with the test geometry against its fundamental maximum:

$$\eta_{ap} = \frac{D_{test}}{D_{max}}. \tag{2.10}$$

Finally we define *effective aperture*, A_e, which is a ratio of the instantaneous power at an antenna's port and the power density of a radiated plane wave in the direction of maximum intensity. (designed to be broadside for reflector antennas)

$$A_e = \frac{P_{accepted}}{U(\theta, \phi)|_{max}}. \tag{2.11}$$

It represents the size of an ideally illuminated aperture that the system was able to achieve, and relates the performance back to the physical dimensions of the main reflector:

$$A_e = A_{phys} e_{rad} e_{pol} \eta_{ap} \tag{2.12}$$

often a good starting point for the design of a dual reflector is to use the feed and sub-reflector structure to illuminate the main reflector for maximum directivity. This is why *aperture efficiency* (η_{ap}) is used as the primary performance metric for the test geometry discussed in this thesis.

2.2.2. Other performance characterisations

The overall goal for reflector systems is to facilitate spectral analysis with a high signal to noise ratio (SNR), for ideal antennas this is related to receiver sensitivity, S:

$$S = \frac{\eta_{ap}}{T_{sys}} \tag{2.13}$$

where T_{sys} is the equivalent system noise temperature. A dual reflector geometry allows for useful signals to be contained to *colder*, less noisy, electrical surfaces, making them more impervious to noise scattered and radiated by the Earth's surface. This is achieved both through orientation and reflector extension, such that spillover from the widest propagating feed beam or its reflections can be directed towards the sky, and the main reflector itself can be integrated to assist with shielding of RF amplifiers. The antenna is the first link in the receiver signal chain and consequently, any noise leakage will be amplified by the following stages. The system noise power contribution as a result of noise penetrating the antenna signal is quantified using equivalent antenna noise temperature, T_{ant}:

$$T_{ant} = T_{sys} - T_{rec} \tag{2.14}$$

where T_{rec} is the noise temperature of the receiver LNA and other components. Reflector antenna noise is very difficult to calculate due to many, orientation specific, contributing factors. The main contributors are spillover noise scattered from the ground, Ohmic losses in the reflector surface and incoming noise from sources in the sky, represented with an equivalent noise temperature T_{sky}. A very basic high level approximation is:

$$T_{ant} = T_{sky} + (1 - \eta_{spill})T_n \tag{2.15}$$

where η_{spill} is the spillover efficiency of the full antenna applied to T_n, the ground temperature, typically approximated as 293 K. The noise temperature of an antenna is also subject to frequency variations, modelling of these variations is considerably more complex than the aperture efficiency ripple and is an active research field [36], [37]. From a receiver standpoint, wideband variations are typically dominated by those from aperture efficiency in electrically small geometries. Noise temperature is not regarded in the model presented in this thesis due to its complexity, but is mentioned for context.

2.3. Dual Reflector antenna Geometry

Reflector antennas are derived from geometric optics (GO), where a lens is used to guide electromagnetic *rays* to its focal point. Reflector surfaces are typically analytically defined conic-sections with the paraboloidal reflector being the most widely used due to its rotational symmetry. Dual reflector configurations can be divided into two types, axial (on-axis) symmetrical, where the sub-reflector and main reflector have foci along a common axis, or offset asymmetrical, where the main reflector has a single focal point at the secondary focus of the sub-reflector, which has a pair of foci on different axes. Dual reflectors are then further divided according to the concavity of the sub-reflector, with Cassegrain antennas using a convex surface and Gregorian antennas using a concave surface [6].

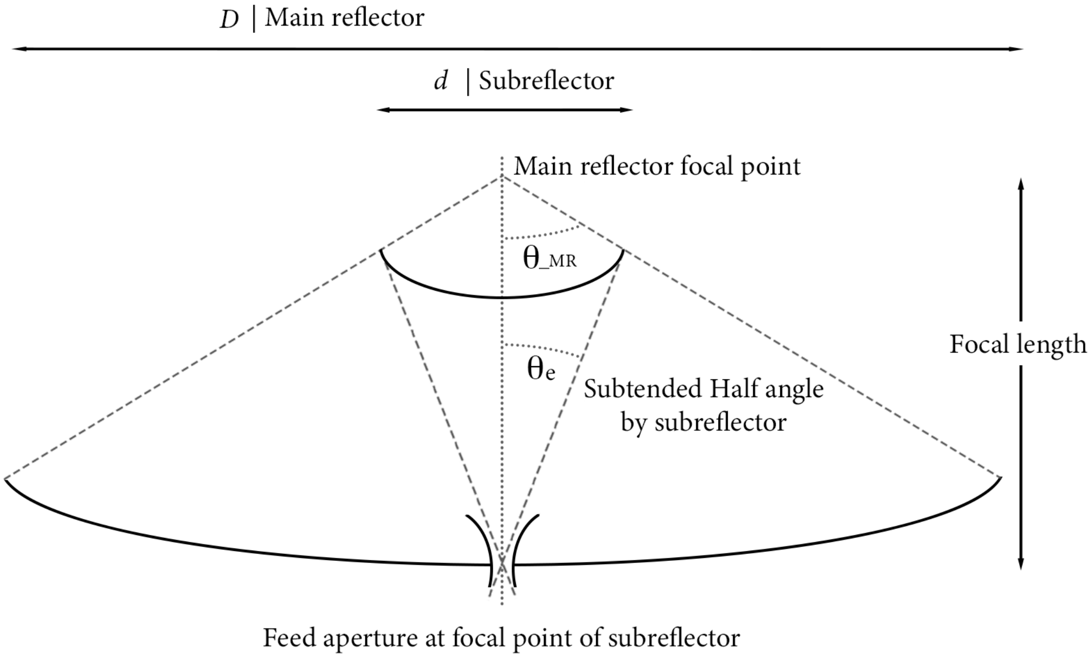

Figure 2.4: Symmetrical Cassegrain DR with related subtended half angle and axial foci

The main characteristics of a dual reflector geometry are the half-angles subtended by the sub-reflector on the feed located at its focal point and the diameters, or major chord for the offset case, of each reflector. While both geometries can be used in both symmetrical or offset configurations, the cassegrain topology lends itself towards symmetrical setups due to the reduction in sub-reflector blockage, as a smaller convex lens is able to effectively illuminate the main reflector when compared to a concave counterpart. The focal length, F_{length}, of a symmetric paraboloidal main reflector with diameter D_{MR}, which subtends angle θ_{MR} between its focus and rim, can be calculated as:

$$F_{length} = \frac{D_{MR}}{4} \cot\left(\frac{\theta_{MR}}{2}\right). \tag{2.16}$$

The drawback of this is that a feed with a narrower illuminating beam taper is required, however, it is generally possible to position a larger feed underneath the MR, which is effective as long as the diameter of its aperture is smaller or equal to the diameter of the sub-reflector.

Analytical descriptions of the subtended angles and focal lengths of other more complex conic sections such as hyperboloids and ellipsoids can be found in the appendix.

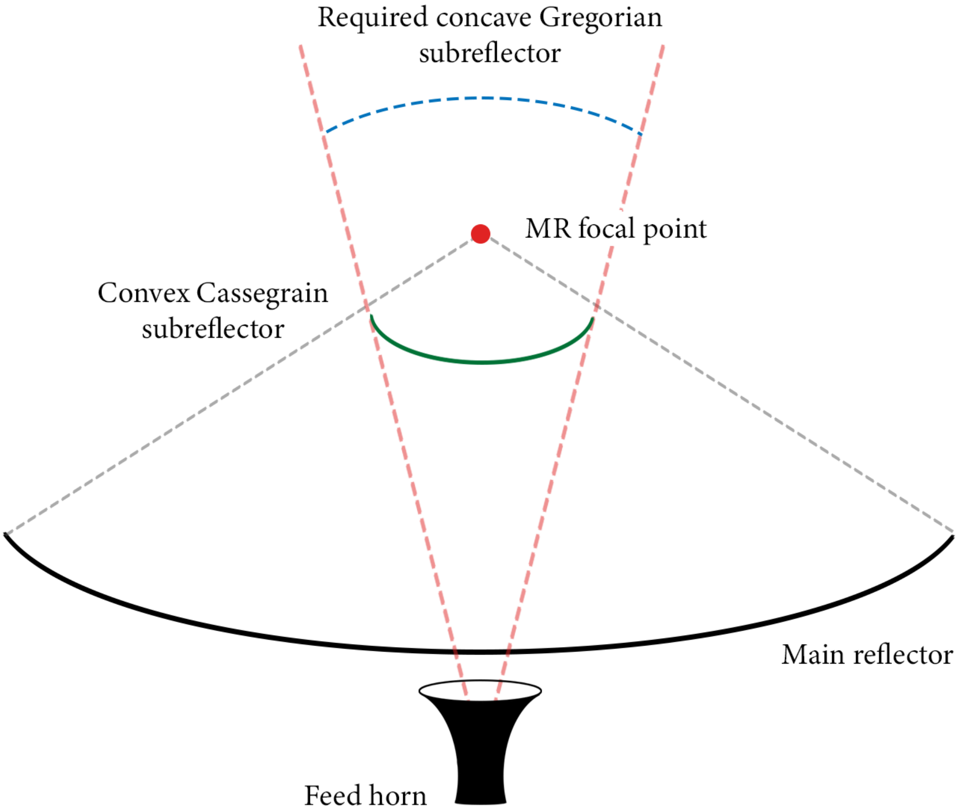

Figure 2.5: Symmetrical Cassegrain geometry with a candidate Gregorian SR increasing blockage and subtending larger half angle at the feed

A Gregorian sub-reflector is typically more suited to an offset configuration, as the concave shape allows for increased focal distance to the feed and a larger surface, such that a smaller feed antenna with a wider illuminating beam can be effective. In general, offset geometries are designed to be *clear aperture*, with no blockage of the main beam caused by the SR or its support structure, this also allows for multiple feeds to be incorporated in the design, a fairly common practice to improve bandwidth without any detriment to aperture efficiency [38], [24]. The equivalent electrical aperture is typically circular when projected onto the axis of observation.

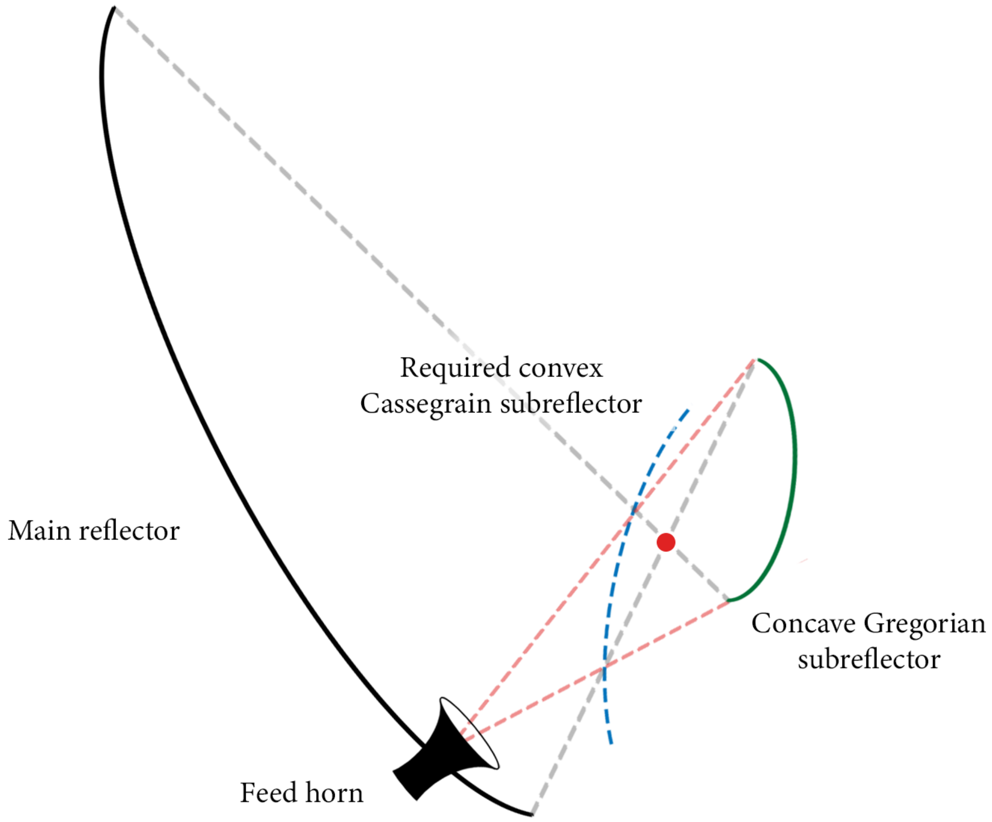

Figure 2.6: Offset Gregorian geometry with a candidate Cassegrain SR subtending a smaller half-angle at the feed

2.3.1. Symmetrical Cassegrain and offset Gregorian antennas in practice

These are the two main topologies with well established practical design procedures and performance predictions. Granet presents a method of obtaining full analytical descriptions of symmetrical dual reflector geometry, which minimise blockage and ensure correct feed placement, with only three input parameters in [39], a strong starting point for the synthesis of an effective symmetrical DR geometry.

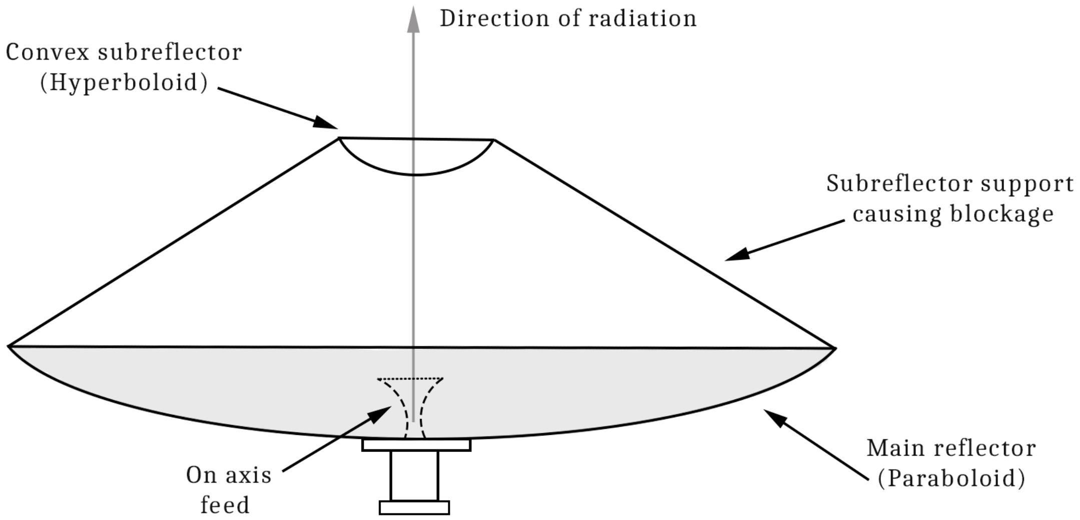

Figure 2.7: Practical example of a symmetrical Cassegrain support structure

The blockage caused by the sub-reflector and its supports in symmetrical topologies does negatively effect the aperture efficiency of the antenna, they are also known to couple with the main reflector if constructed from conducting surfaces causing beam squint, increased SLL and additional aperture efficiency variation across frequency.

The simple design process for such antennas and overall good performance with simple analytical geometry for manufacture has, however, made them a common feature in microwave systems for satellite communication and radio astronomy [5].

Granet also presents a similar parameter driven design for offset configurations in [40], where now 7 input parameters are needed to calculate a further 14, to create a 21 parameter full analytical description of the offset geometry. These designs all satisfy the Mizuguchi-Dragone condition [41] for reduced cross polarised radiation in antennas with an electrically large main reflector ($D_{MR} > 80\lambda$).

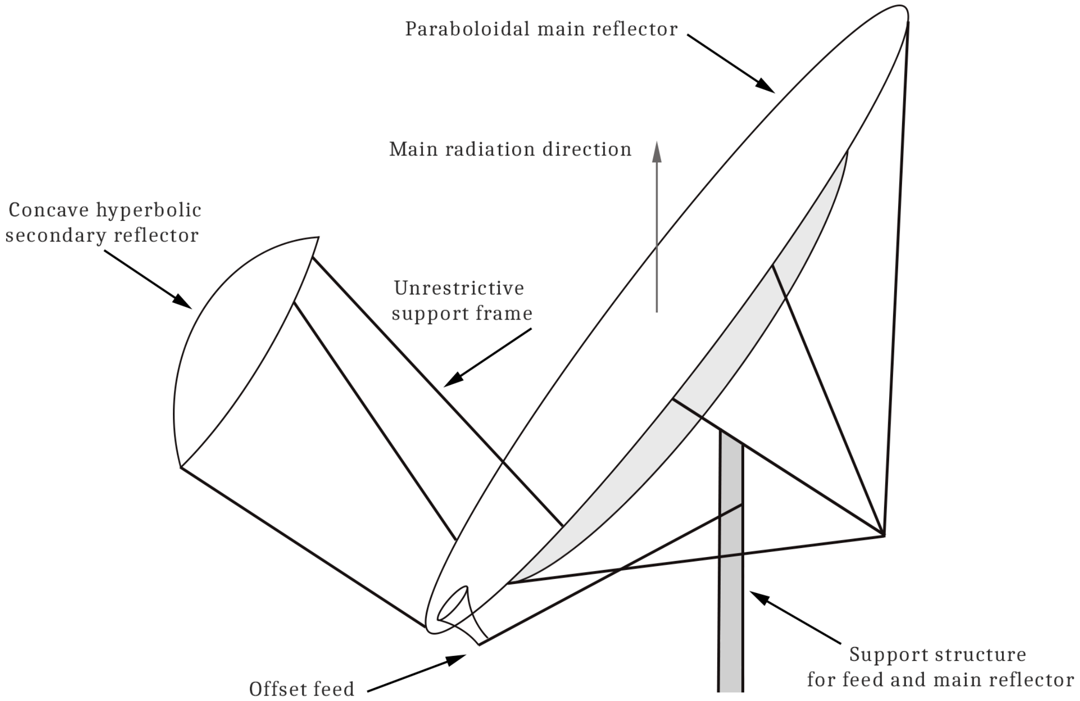

Figure 2.8: Typical practical clear aperture offset Gregorian structure

Offset, clear aperture, configurations have recently become more prominent due to the availability of computational electromagnetic methods (CEM) which can accurately estimate far-field behaviour, allowing for simulation driven reflector shaping to optimise the illuminating fields for increased gain and sensitivity [42], particularly as the dishes become electrically small [43]. This, coupled with the possibility of extending offset sub-reflectors to reduce the spillover and noise from compact cheaper feed structures (see 2.5.2) improves their per antenna element cost to performance ratio [44].

2.4. Reflector shaping

Reflector surfaces can be modified from their standard GO form to improve the radiated beam characteristics [45] or sensitivity of the antenna [43]. At frequencies where the geometry is electrically small, GO surface current density approximations have limited accuracy and do not consider coupling or diffraction. Full wave methods, such as the method of moments (MoM), account for all coupling and surface current distortion such that it can be considered when refining a reflector design.

2.4.1. Co-ordinate systems

Due to the complex geometry associated with reflector surfaces, either analytically defined or shaped through beam analysis, it is of great convenience, and is common practice during modelling, to define these surfaces in separate local co-ordinate systems with known relative positions to the global co-ordinate system of the antenna, rather than define the entire antenna geometry from a single reference.

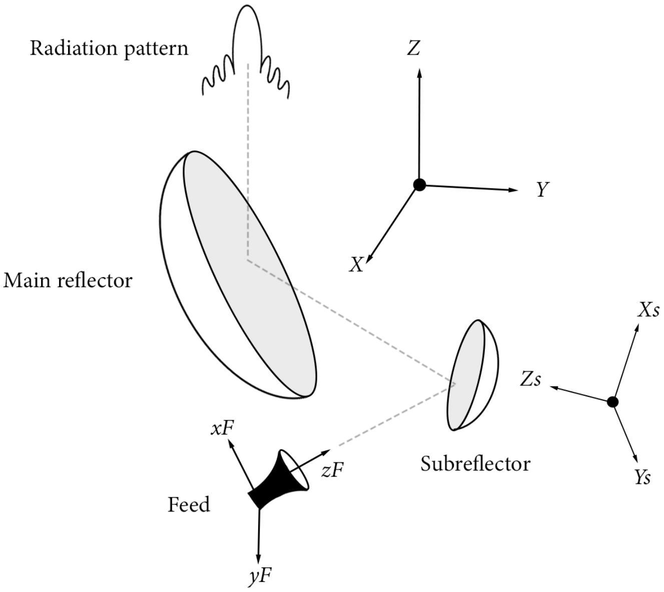

Figure 2.9: Local co-ordinate systems typically used to define dual reflector geometry

The feed co-ordinate system is defined with its origin at a focal point of the sub-reflector, such that its axis Z_F bisects the subtended angle. The sub-reflector origin is then defined at the focal point of the main reflector such that its axis, Z_s is directed towards the MR. The main reflector surface is then defined using the global co-ordinate system, with its focal point at the origin, to easily relate the reflective surface and its radiated field orientation. The global $\hat{\mathbf{z}}$ direction is defined to travel through the centre of the secondary radiation pattern in the direction of propagation.

A rotationally symmetric paraboloidal reflector, $\mathbf{MR}_s$, such as in Figure 2.4 can be defined using a cylindrical co-ordinates as:

$$\mathbf{MR}_s(\rho,\varphi) = \rho\hat{\boldsymbol{\rho}} + z(\rho)\hat{\mathbf{z}}; \quad \hat{\boldsymbol{\rho}} = \cos\varphi\hat{\mathbf{x}} + \sin\varphi\hat{\mathbf{y}} \tag{2.17}$$

$$\text{with} \quad z(\rho) = -F_{length} + \rho^2/(4F_{length}) \quad \text{for } 0 \leq \rho \leq D_{MR}/2, \tag{2.18}$$

This analytical description serves as the most common starting point for the design of a main reflector surface, as its symmetry allows for a simple Fourier series based prediction of the reflected radiation, if the illuminating pattern is ideal [25].

2.5. Dual reflector feed antennas

Characteristics of the incident electromagnetic field intensity significantly influence the radiation behaviour of any reflector, therefore, primary pattern plays a crucial role in the aperture efficiency of dual reflector systems. Generally the sub-reflector is located in the radiating near-field of the feed, therefore, its radiation pattern controls the quantity of energy which escapes beyond its rim or is lost in non-radiating surface current [40]. Modelling is typically performed using a spherical wave expansion on the far-field pattern, as the expansion allows for the accurate reconstruction of the near-field pattern equivalent in its radiating region, down to a minimum sphere with radius r_{SWE} defined as

$$r_{SWE} = \frac{N_{Modes}\lambda}{2\pi} \tag{2.19}$$

where N_{modes} is the maximum number of polar modes describing the spherical fields [26].

For this reason, the design and optimisation of antennas with stable radiation patterns across bandwidths of an octave or more, specifically for reflector systems, is an active research field. The influence of the primary pattern variation is reduced by diffraction effects as geometry becomes electrically small [24], however, it remains a significant performance contributor.

It is possible to feed reflector systems with ground plane supported dipoles or log-periodic array configurations of dipoles and microstrip antennas, circular, corrugated or ridged horn antennas are primarily used in high performance systems, as they provide simplified coaxial receiver matching (eliminating the need for a balun) and a physically malleable radiation pattern with wideband stability and focus [46].

(a) Axially corrugated horn [47]

(b) CST model of a quad ridged flared horn [3]

Figure 2.10: Circular aperture horn antennas suitable for dual reflector primary patterns

Ridges and corrugations are included in the horn taper in order to improve the wideband stability of the reflection coefficient and radiation pattern by delaying the propagation of higher order, *circular*, modes as wavelength decreases [47]. The role of the feed is to symmetrically illuminate the sub-reflector as uniformly as possible while minimising spillover. Henceforth, two radiation characteristics become pertinent:

1. −12 dB half beamwidth / beam taper
2. BOR_1 efficiency (η_{BOR_1})

In general the half angle, θ_e, subtended by the sub-reflector at the feed should coincide with the −12 dB half beamwidth of the feed's far-field pattern. Side-lobes and back-lobes should remain below −15 dB to reduce spillover and noise leakage. Of interest also, is the phase centre stability and backward radiation properties of the horn, which may contribute to aperture efficiency and noise temperature variations across frequency [38], [21].

BOR refers to *bodies of revolution*, with BOR_1 referring to a $\hat{\mathbf{z}}$ directed antenna excited such that it can be represented with a Huygens equivalent incremental current source in the $\hat{\mathbf{y}}$ direction, yielding a far-field radiation pattern, $\mathbf{G}_{BOR_1}$, of the form:

$$\mathbf{G}_{BOR_1}(\theta, \varphi) = G_E(\theta)\sin\varphi\hat{\boldsymbol{\theta}} + G_H(\theta)\cos\varphi\hat{\boldsymbol{\varphi}} \tag{2.20}$$

where G_E and G_H are the complex far-field functions in the electric and magnetic planes respectively. This symmetrical variation across φ is valuable as it allows for analytical integration and ensures that only surface currents which contribute to desirable radiation are induced in a target paraboloid. This is the ideal case from which η_{BOR_1} is defined, and is the reference with which feed pattern variations across φ measured. Spillover efficiency, η_{spill}, is a similar efficiency measuring the energy lost outside the angle subtended by the rim, $2\theta_e$, against the ideal zero loss case. Feed performance is not a target of the modelling presented in this thesis, therefore, these sub-efficiencies are not evaluated.

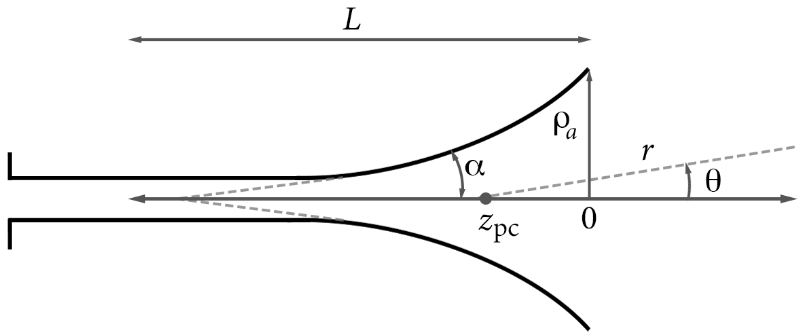

Figure 2.11: Cross section of horn antenna in symmetry plane with far-field phase centre Z_{pc}, aperture radius ρ_a, half flare-angle α and taper length L

2.5.1. Flare-angle controlled horns

In situations where the wavelength of radiated fields is small compared to the aperture area of the horn, defined using aperture radius ρ_a, the far-field pattern beamwidth is proportional to the half flare-angle, α, of the horn. For an ideal flare-angle controlled horn with far-field phase centre,Z_{pc} and taper length, L, the $-3\,\mathrm{dB}$ beamwidth, θ_0, can be calculated (in radians) as:

$$\theta_0 = \frac{\rho_a}{L} \quad \text{with} \quad z_{pc} = -L. \tag{2.21}$$

Such horn feeds are physically long, because, the flare-taper needs to be gradual to create an aperture size which is sufficient for radiation with a narrow beam taper comparable to the subtended half angle of the sub-reflector [25]. For this reason, these feeds are more suited to symmetrical dual reflectors and are typically used in electrically large systems ($D_{MR} > 100\lambda$), where the taper length, L, of the horn can be easily accounted for above, or below, the MR surface. A flare-angle controlled horn requires a large phase variation, Φ, over the aperture such that:

$$\Phi_{\max} \gg \pi \tag{2.22}$$

2.5.2. Aperture controlled horns

In these horns the beamwidth is primarily influenced by diffraction in the aperture plane. This occurs when the wavelength of the radiation is significantly larger that the horn aperture area. The beamwidth is now, subsequently, frequency dependant. The phase centre, Z_{pc}, also shifts along its axis with frequency. The phase variation across the aperture field is assumed to be small, with a zero phase variation aperture controlled beamwidth expressed analytically in free-space (propagation constant k) as:

$$\theta_0 = 2/\left(k\rho_a\right) = 0.54\lambda/\rho_a \quad \textit{with} \quad Z_{pc} = 0. \tag{2.23}$$

In the context of this thesis, all feeds are expected to be aperture controlled based on the electrical size of the reflector systems. Minimal phase variation in the horn aperture field is of particular significance in electrically small reflector cases ($D_{MR} < 20\lambda$), to reduce destructive surface current interference as a result of phase error (from different ray paths). Shifting of the primary pattern phase centre out of the sub-reflector's focal point also inhibits aperture efficiency, therefore, wide-band stability of Z_{pc} is an equally important feature.

This presents a trade-off between the size of the sub-reflector and horn aperture, with a smaller horn cheaper to manufacture and more conducive to minimal aperture phase variation at the price of a wider beam taper, and subsequently larger sub-reflector to accommodate the larger subtended angle. This trade-off has lead to the offset Gregorian geometry becoming more prevalent in electrically small dual reflector arrays for interferometry, as the decrease in feed system manufacturing cost is not coupled with a loss in directivity in a clear aperture topology. Some offset designs, such as the SKA [44], incorporate extensions shaped through computational analysis on the sub-reflector to help reduce noise contributions from ground scattered feed rays for small horn apertures, by purposely directing the radiation upwards past the main reflector [43] to increase sensitivity.

2.5.3. Analytical feed descriptions for reflector geometry design

As the design of Horn antennas is extremely complex it is convenient to use analytical feed approximations during the initial synthesis of DR geometry. This is done by using an analytical tapered Gaussian beam which satisfies Maxwell's equations in the near and far-field. Such a beam can be generated using a Huygens point source, an infinitely small magnetic and electric dipole, at the origin of the feed co-ordinate system. This Huygen's source has a BOR_1 far-field of the form:

$$\mathbf{E}(r,\theta,\phi) = E_0\frac{\exp(-jkr)}{r}(1+\cos\theta)(\cos\phi\hat{\boldsymbol{\theta}} - \sin\phi\hat{\boldsymbol{\phi}}). \tag{2.24}$$

The taper can be controlled by shifting the point source by a complex number, $-jb$, along its axis (Z_f) [26]. This allows for manipulation of the feed pattern such that the taper level A_{taper} relative to broadside can be described in dB for a specific theta value θ_{taper} (taper angle in GRASP). A $-12\,$dB taper across θ_e is routinely chosen for geometry evaluation. The far-field can be expressed after the shift of $-jb$ as:

$$\mathbf{E}(r,\theta,\phi) = N_f\frac{\exp(-jkr)}{kr}\exp(kb\cos\theta)(1+\cos\theta)(\cos\phi\hat{\boldsymbol{\theta}} - \sin\phi\hat{\boldsymbol{\phi}}) \tag{2.25}$$

where N_f is the constant normalising the field to dBi. The complex shift b for a taper level in dB $A, \quad A<0$, at θ_{taper} is then calculated as:

$$b = \frac{20\log_{10}((1+\cos\theta_{taper})/2) - A_{taper}}{20k(1-\cos\theta_{taper})\log_{10}\mathrm{e}}. \tag{2.26}$$

This is a fair approximation of the typical radiation from a well designed horn with its aperture phase centre placed exactly at the focal point of the SR, however, the radiation pattern deviations present in practical antenna beams over frequency are neglected. This approximation also excludes backward radiation from the pattern, which can contribute to the aperture efficiency variations of an offset DR [21], such considerations must be kept in mind during wideband evaluations. Nevertheless, this approximation serves as a sufficient baseline for the maximum obtainable aperture efficiency with a particular geometry given a feed which meets the desired taper specifications with a perfect BOR_1 pattern.

2.6. Computational methods for the calculation of reflector antenna far-fields

With advances in modelling software available in industry, reflector antennas are almost always evaluated with computational simulation prior to the construction of a prototype. Several methods are well established in literature to approximate the far-field patterns of a dual reflector configuration. These methods will be summarised from a perspective of accuracy based on the electrical size of reflector surfaces.

2.6.1. Aperture field integration

A rapid far-field solution for a reflector can be obtained by approximating its EM scattering with a disc shaped uniform field aperture and computing a two dimensional Fourier transform. This method is not suitable for electrically small reflectors and, therefore, is not discussed further [25].

2.6.2. Surface current integration

It is known that the electric and magnetic far-fields radiated by a conducting surface can be calculated by applying the magnetic **F** and electric **A** vector potentials to satisfy the boundary conditions of Maxwell's equation, [6] with:

$$\mathbf{A} = \frac{\mu}{4\pi} \iint_B \mathbf{J}_\mathrm{s}\left(\mathbf{r}'\right) \frac{\exp(-jkR)}{R} ds' \tag{2.27}$$

$$\mathbf{F} = \frac{\varepsilon}{4\pi} \iint_B \mathbf{M}_\mathrm{s}\left(\mathbf{r}'\right) \frac{\exp(-jkR)}{R} ds'. \tag{2.28}$$

Where $\mathbf{J}_\mathrm{s}$ and $\mathbf{M}_\mathrm{s}$ are the impressed surface electric and magnetic current density and R, the distance between the observation point $\mathbf{r}$ and integration variable $\mathbf{r}'$:

$$R = |\mathbf{r} - \mathbf{r}'| \tag{2.29}$$

B denotes the integration region on the reflector surface. This allows for the fields to be expressed in general time harmonic differential form as [6]:

$$\mathbf{E} = -j\omega \left(\mathbf{A} + \frac{1}{k^2} \nabla \left(\nabla \cdot \mathbf{A} \right) \right) - \frac{1}{\varepsilon} \nabla \times \mathbf{A} \tag{2.30}$$

$$\mathbf{H} = \frac{1}{\mu} \nabla \times \mathbf{F} - j\omega \left(\mathbf{F} + \frac{1}{k^2} \nabla \left(\nabla \cdot \mathbf{F} \right) \right) \tag{2.31}$$

During reflector analysis the fields are required in a global co-ordinate system. This is illustrated in the figure below with a global co-ordinate system described at the phase centre of the Horn antenna:

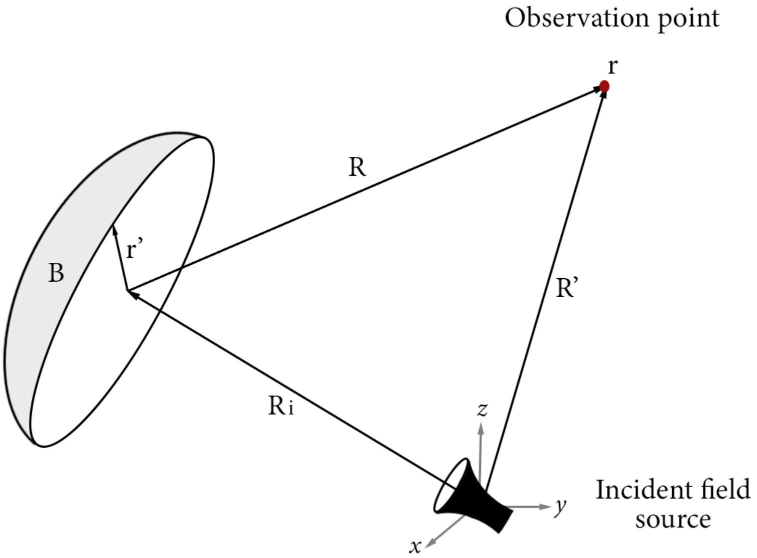

Figure 2.12: Radiating fields from a surface current in global co-ordinates

Here R remains the same with R_i the distance between the origin and the integration point and R' is the distance between the origin and observation point. Application of differential operators and the introduction of η the free-space intrinsic impedance $(\eta = \sqrt{\frac{\mu_0}{\varepsilon_0}} = 377\Omega)$ yields [6]:

$$\begin{aligned}\mathbf{E}_{scattered}(\mathbf{r}) = \frac{\eta}{4\pi}\iint_B \Bigg(\mathbf{J}_\text{s}\left(-\frac{j}{kR} - \frac{1}{k^2R^2} + \frac{j}{k^3R^3}\right) \\ + \left(\mathbf{J}_\text{s}\cdot\hat{\mathbf{R}}\right)\hat{\mathbf{R}}\left(\frac{j}{kR} + \frac{3}{k^2R^2} - \frac{3j}{k^3R^3}\right)\Bigg)\exp(-jkR)k^2ds' \\ - \frac{1}{4\pi}\iint_B \mathbf{M}_\text{s}\times\hat{\mathbf{R}}\frac{1}{k^2R^2}(1+jkR)\exp(-jkR)k^2ds'\end{aligned} \tag{2.32}$$

$$\begin{aligned}\mathbf{H}_{scattered}(\mathbf{r}) = \frac{1}{4\pi}\iint_B \mathbf{J}_\text{s}\times\hat{\mathbf{R}}\frac{1}{k^2R^2}(1+jkR)\exp(-jkR)k^2ds' \\ + \frac{1}{4\pi\eta}\iint_B \Bigg(\mathbf{M}_\text{s}\left(-\frac{j}{kR} - \frac{1}{k^2R^2} + \frac{j}{k^3R^3}\right) \\ + \left(\mathbf{M}_\text{s}\cdot\hat{\mathbf{R}}\right)\hat{\mathbf{R}}\left(\frac{j}{kR} + \frac{3}{k^2R^2} - \frac{3j}{k^3R^3}\right)\Bigg)\exp(-jkR)k^2ds'\end{aligned} \tag{2.33}$$

where:

$$\hat{\mathbf{R}} = \frac{\mathbf{r}-\mathbf{r}'}{|\mathbf{r}-\mathbf{r}'|} = \frac{\mathbf{r}-\mathbf{r}'}{R'}. \tag{2.34}$$

In the far-field region the contributions of terms including $\frac{1}{R^2}$ and $\frac{1}{R^3}$ are negligible, with the reflector scattered far-fields expressed after applying the principle of duality as in [26]:

$$\begin{aligned}\mathbf{E}_{Far} &= -\frac{j\eta}{4\pi}\iint_B \left(\mathbf{J}_\mathrm{s} - (\mathbf{J}_\mathrm{s}\cdot\hat{\mathbf{r}})\,\hat{\mathbf{r}}\right)\exp(jk\mathbf{r}'\cdot\hat{\mathbf{r}})k^2 ds' \\ &+ \frac{j}{4\pi}\hat{\mathbf{r}}\times\iint_B \mathbf{M}_\mathrm{s}\exp(jk\mathbf{r}'\cdot\hat{\mathbf{r}})k^2 ds'\end{aligned} \tag{2.35}$$

$$\begin{aligned}\mathbf{H}_{Far} &= -\frac{j}{4\pi}\hat{\mathbf{r}}\times\iint_B \mathbf{J}_\mathrm{s}\exp(jk\mathbf{r}'\cdot\hat{\mathbf{r}})k^2 ds' \\ &- \frac{j}{4\pi\eta}\iint_B \left(\mathbf{M}_\mathrm{s} - (\mathbf{M}_\mathrm{s}\cdot\hat{\mathbf{r}})\,\hat{\mathbf{r}}\right)\exp(jk\mathbf{r}'\cdot\hat{\mathbf{r}})k^2 ds'\end{aligned} \tag{2.36}$$

with the far-field direction $\hat{\mathbf{r}}$ as:

$$\hat{\mathbf{r}} = \frac{\mathbf{r}}{|\mathbf{r}|} \tag{2.37}$$

This is the fundamental principle on which CEM solvers are built upon. They numerically compute the integrals in Equation 2.32 and 2.33 in order to obtain the unknown current density $\mathbf{J_s}$, and then further integrate this current density (2.35,2.36) to obtain the far-fields as a discrete set of complex data capturing both phase and magnitude.

2.6.3. Geometrical optics (GO)

GO is built upon the classical law of reflection, where the angles of incidence and reflection are equal. Here radiation is considered solely as set of straight line stationary ray paths, with constant power and uniform, path dependant phase, which can be traced back to single points on the origin antenna aperture. This is known as *ray tracing* [42] and is the method on which dual reflector antenna geometries can be analytically derived using lens focal points [40], [39]. This is best illustrated in Figure 2.13 below:

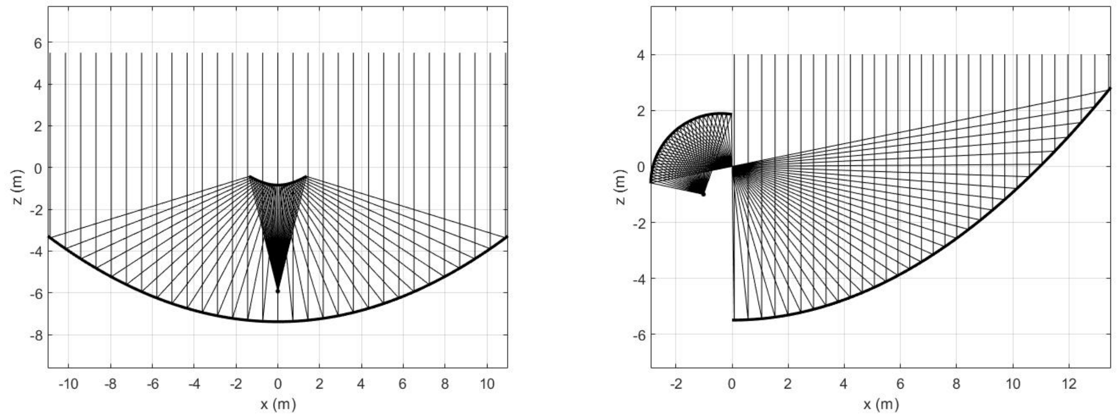

(a) Symmetrical Cassegrain geometry **(b)** Offset Gregorian geometry

Figure 2.13: Ray Tracing DR synthesis visualisation

It is evident here that the GO approximation does not account for diffraction effects at the rim or along the surface of the reflectors, as the rays are projected in straight lines, meaning the reflector focal point is absolute. The GO approximation offers great improvements to computational efficiency with acceptable accuracy for electrically large main reflectors above 150λ and sub-reflectors above 60λ in respective diameter [48]. In reflectors of this size, or larger, the diffraction and coupling effects contributing to rapid far-field variations are often negligible, and therefore, are not suitable targets for the modelling presented here. [49] presents a detailed discussion on the relationship between electrical radius of a reflecting surface and the accuracy of GO synthesised far-fields.

2.6.4. Physical Optics (PO)

The PO method is a highly useful approximation in the analysis of dual reflector antennas with reflectors shaped with electrical radii of below 30λ, $(D < 60\lambda)$. On reflector surfaces of above this size, the enhanced accuracy does not warrant the increase in computational expense. The PO approximation assumes the the induced surface current density $\mathbf{J}_s$, from an EM wave incident on a PEC reflector is uniform in a single direction, and is solely controlled by the incident magnetic field $\mathbf{H_i}$ and surface normal $\hat{\mathbf{n}}$:

$$\mathbf{J}_s = \mathbf{J}_{\text{PO}} = 2\hat{\mathbf{n}} \times \mathbf{H}_i. \tag{2.38}$$

The approximation neglects current density induced by tangential components of the incident field and assumes $\mathbf{J_s} = 0$ for all regions which are not directly illuminated [12]. Of particular interest here, is that the PO approximation captures the effects of diffraction along reflector surfaces, allowing for an approximation of radiation effects caused by interference between diffracted component as a result of chromatic aberration, whereby the focal point of the reflector becomes frequency dependant due to field interactions beneath the aperture rim. The PO equivalent surface current density, $\mathbf{J}_{\text{PO}}$, is only inaccurate near the rim of the reflectors and produces fields of a suitable accuracy for reflective surfaces with an electrical radius of above $\approx 8\lambda$. Neither PO or GO account for diffraction around the rim of reflectors. This presents a problem in wideband characterisations of electrically small offset DR systems, where frequency dependant diffraction past the SR is significant [21], and as such computational methods which account for edge diffraction must be included.

2.6.5. Geometrical & physical theory of diffraction (GTD & PTD)

GTD and PTD are a set of procedures used to apply the theory of diffraction for radiation incident on the rim of a reflector, to compensate for the fact that GO & PO approximations assume that the field at the rim falls to zero, such that the fields in the regions *shadowed* by reflectors can be approximated. An EM wave incident on a reflector edge is subject to edge and creeping wave diffraction, the latter primarily contributing to the surface current density behind the reflector [34]. The fields surrounding the reflector edge are too complex to accurately model due to the random interference between diffracted field components.

GTD is an extension of a GO calculated field including a diffracted and reflected component for rays incident on the rim. The approximation developed by Keller in [50] gives an asymptotic field solution including a diffracted field based on Fermat's principle. It is suitable for modelling the diffraction effects of electrically large reflectors with a marginal increase in computational expense. GTD is not suitable for modelling the target, diffraction driven, characterisation figures of this paper due to the electrically small sub-reflectors in question [51].

The physical theory of diffraction (PTD) is therefore required to accurately model diffracted field components, particularly for offset geometries. PTD extends GTD and PO to accurately model edge diffraction, correcting GTD by removing singularities near shadow boundaries through the inclusion of a non-uniform *fringe* current density, J_{fringe} in regions directly inside (directly illuminated) the reflector boundary curve [51]:

$$\mathbf{J}_s = \mathbf{J}_{PO} + \mathbf{J}_{fringe} \tag{2.39}$$

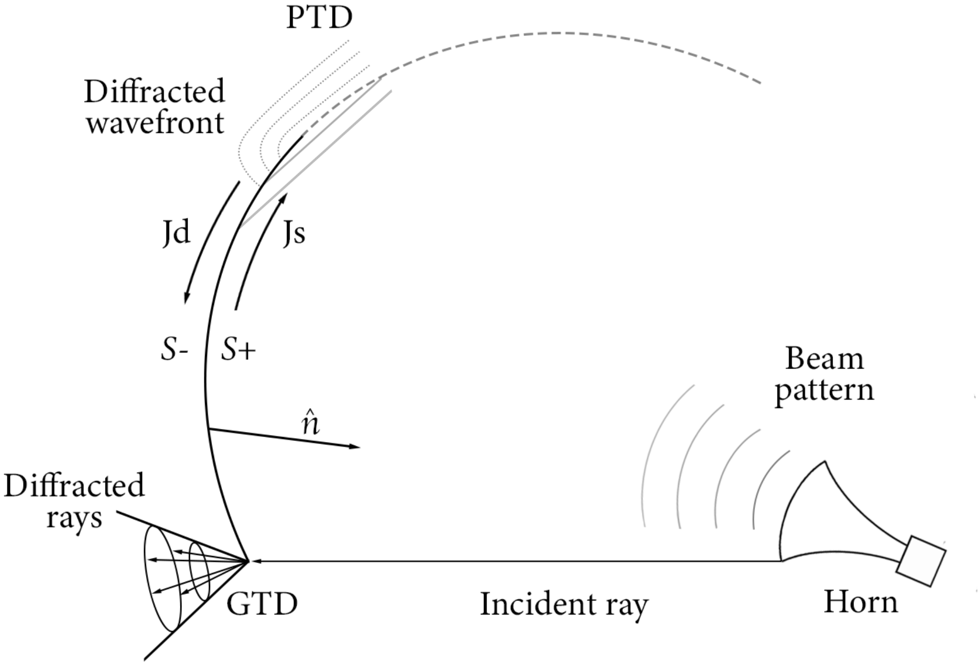

Figure 2.14: Illustration of basic edge diffraction and current on the shadowed side of an offset reflector

This method was developed by Ufimtsev in [52] which shows a detailed derivation for the *fringe* current localised around the conducting surface boundary. The PTD model does not include creeping wave diffraction, which is typically negligible for reflector sizes where the modelling presented here is applicable [53].

2.6.6. Dual reflector field synthesis

The resultant radiation of a dual reflector antenna, $\mathbf{E}_{DR}$, is best described in the far-field, $\mathbf{r}$, with complex farfield function $\mathbf{G}_{DR}$ as follows:

$$\mathbf{E}_{DR}(\mathbf{r}) = \mathbf{E}_F(\mathbf{r}) + \mathbf{E}_{SR}(\mathbf{r}) + \mathbf{E}_{MR}(\mathbf{r}) = \frac{1}{r}\exp(-jkr)\mathbf{G}_{DR}(\hat{\mathbf{r}}) \tag{2.40}$$

with E_{MR}, E_{SR} and E_F the electric fields radiated from the MR, SR and Feed apertures respectively. The far-field function of the dual reflector can be expressed in its global co-ordinate system as:

$$\mathbf{G}_{DR}(\hat{\mathbf{r}}) = \mathbf{G}_F(\hat{\mathbf{r}})\exp(jk\,(\mathbf{r}_F \cdot \hat{\mathbf{r}})) + \mathbf{G}_{\mathrm{SR}}(\hat{\mathbf{r}})\exp(jk\,(\mathbf{r}_{SR} \cdot \hat{\mathbf{r}})) + \mathbf{G}_{\mathrm{MR}}(\hat{\mathbf{r}}) \tag{2.41}$$

with phase referenced to the global co-ordinate system, $\hat{\mathbf{r}}$, with $\mathbf{r}_f$ & $\mathbf{r}_{SR}$ describing the position of the phase centre of the feed and SR apertures respectively. It is clear here that the full field is simply the sum of all three sources projected in a single co-ordinate system. The sequential procedure for efficient computations is common for all surface current approximations but is shown explicitly for PO with PTD with radiation integral operator $\mathbf{I}$, which is the primary modelling approach for electrically small reflector systems:

1. The illuminating radiation of the feed $\mathbf{E}_F$ is generated by applying spherical wave expansion to the calculated far-field pattern of the feed to synthesise an equivalent radiating near-field pattern.

2. This field is then set as incident on the SR and the approximate surface currents are derived as $\mathbf{J}_{SR} = \mathbf{J}_{PO:SR} + \mathbf{J}_{fringe:SR}$

3. The scattered field from the SR, $\mathbf{E}_{SR}$ is calculated as: $\mathbf{I}(\mathbf{J}_{PO:SR} + \mathbf{J}_{fringe:SR})$

4. This field is then used as incident illumination on the MR, and its current density is approximated as $\mathbf{J}_{MR} = \mathbf{J}_{PO:MR} + \mathbf{J}_{fringe:MR}$

5. The scattered fields from the MR, $\mathbf{E}_{MR}$ are calculated as: $\mathbf{I}(\mathbf{J}_{PO:MR} + \mathbf{J}_{fringe:MR})$

6. The fields scattered by both the SR and the feed aperture are added and transformed to the Global (MR) co-ordinate system. $\mathbf{E}_{FSR} = \mathbf{E}_F + \mathbf{E}_{SR}$

7. The feed and sub-reflector field is then added to the MR field to obtain a final far-field approximation: $\mathbf{E}_{DR} = \mathbf{E}_{FSR} + \mathbf{E}_{MR}$

It is possible to incorporate additional surface current procedures, such as the currents induced on the SR from the MR field, to increase the amount of coupling and other non-ideal field interactions, however, for the purposes of wideband characterisation, geometries where these interactions dominate field behaviour would be so electrically small that samples produced with full wave solutions are preferred, and obtainable without adverse effects on computational performance [26], [22].

2.6.7. Full wave solutions using MoM

In a dual reflector with reflecting surfaces that are extremely small in terms of wavelengths ($> 8\lambda$), a full wave solution is required to accurately compute the scattered field because mutual coupling between the radiating surfaces dominates the surface current densities, J_{MR} and J_{SR}, to a similar extent as the direct illumination. The PO approximation only considers a *first incidence* of radiation upon a surface, and therefore, becomes obsolete if multiple reflections (coupling) between the reflectors distort their surface current densities to a comparable degree [26]. Full wave solutions are extremely computationally expensive, and suffer severe performance degradation as electrical size increases. Research into frameworks for accelerating full wave schemes, particularly for *BOR* structures common in DR systems [54], is ongoing.

The most widely used full wave approach is the method of moments (MoM). A mesh of polygons, typically triangular or quadrilateral with sides smaller than $\frac{\lambda}{8}$, containing known boundary conditions are placed at discrete points along the antenna to define conducting surfaces and their boundaries [26]. The surface current in each element, due to incidence and coupling with neighbouring elements, is sequentially calculated before the overall current approximation is numerically integrated to accurately estimate the radiated electric field. All mutual coupling between mesh elements is included at great computational cost, rapidly increasing with mesh size [55] (N^3 solver complexity).

MoM optimisation is typically achieved through mesh simplification. The Multi-level fast multipole method (MLFMM) is the most common augmentation of MoM found in CEM solvers for full wave solutions of larger radiating surfaces. MLFMM groups differential elements into hierarchical clusters determined by the expected significance of mesh calculations based on inter-element spacing. Operations on clusters far apart from one another are simplified through mid-point approximation before the overall accuracy of the solution is tested on an iterative basis. Clusters in close proximity to one another are handled identically to standard MoM offering a significant cost reduction with negligible change in estimation accuracy, provided the clusters are properly selected [26].

Another augmentation is the inclusion of *patch regions* for areas with predictable surface currents. On *BOR* surfaces a patch region at the centre can be represented with fewer, larger mesh elements exhibiting a residual field error which can be reduced through the application of macro basis test functions (MBF) [55] or in some cases a PO region.

The most common MoM procedure for reflector system analysis is the mixed-potential Electric Field Integral Equation formulation (EFIE) [26] for an arbitrary PEC reflector surface, S, the boundary conditions for Maxwell's equations can be expressed as:

$$\hat{\mathbf{n}} \times \mathbf{E}^{\mathrm{i}} = \hat{\mathbf{n}} \times L_0 \mathbf{J}_s, \quad \mathbf{r} \in S \tag{2.42}$$

where $\hat{\mathbf{n}}$ is the surface normal vector, $\mathbf{J}_s$ is the surface current density and L_0 is the integral operator defined as

$$L_0 \mathbf{J}_s = j\omega\mu_0 \left(\int_S \mathbf{J}_s(\mathbf{r}') \, G_0(\mathbf{r}, \mathbf{r}') \, dS' \quad + \frac{1}{k_0^2} \int_S \nabla_s' \cdot \mathbf{J}_s(\mathbf{r}') \, \nabla G_0(\mathbf{r}, \mathbf{r}') \, dS' \right). \tag{2.43}$$

Where ∇_s' is the surface divergence with respect to the primed coordinates, and $G_0(\mathbf{r}, \mathbf{r}')$ is the free space Green's function:

$$G_0(\mathbf{r}, \mathbf{r}') = \frac{\exp(-jk_0 |\mathbf{r} - \mathbf{r}'|)}{4\pi |\mathbf{r} - \mathbf{r}'|}. \tag{2.44}$$

This is the integral equation used to estimate the radiated field with the discrete matrix approximation of the surface current density $\mathbf{J}_s$, constructed with the mesh.

2.6.8. Comparative analysis of suitability for electrically small reflectors

It is possible to combine MoM solutions with PO solutions, whereby a MoM description is obtained for the SR surface current density before the PO/PO+PTD approximation is applied to the MR surface current density. Such a hybrid approach is common in antennas with very small sub reflectors (D<8λ), where the PO approximation of $\mathbf{J}_{SR}$ is inaccurate [26], such that the incident field on the MR is correctly modelled.

The selection of the appropriate computational approach for a DR system is a complex problem, as the subtended angles of the geometry, as well as the path lengths between elements can have a major influence on method accuracy [51]. Table 2.1 is an approximate guideline for balancing accuracy of diffraction and coupling effects with computational efficiency. For offset geometries, where the sub-reflector is in such close proximity to the feed it sits inside, or on the edge of the non-radiating near-field region, a full wave solution is recommended for the calculation of $\mathbf{J}_{SR}$ [26].

Table 2.1: Appropriate surface current computational methods for electrical size

Recommended HF Method	Main reflector	Sub-reflector
PO with PTD	D_{MR}>40λ	D_{SR} >10λ
PO / MOM Hybrid	D_{MR}>20λ	D_{SR}<10λ
Full wave: MOM / MLFMM / BOR-MOM	D_{MR}<20λ	D_{SR} <10λ

2.7. The Characteristic Basis Function Pattern (CBFP) expansion method

The CBFP method is a parametric modelling method which incorporates a weighted set of physics-based orthogonal basis functions to capture the radiation pattern variations of an antenna [30]. The method can be used to capture both frequency and geometric variations, however, in this paper it is presented solely from a frequency variation perspective, where the geometric information is constant and far-fields are generated via CEM simulations. Consider a single antenna far-field pattern at frequency f_0:

$$\mathbf{E}(r,\theta,\phi,f)_{f=f_0} = \frac{1}{r}\exp(-jkr)\mathbf{G}(\theta,\phi,f)_{f=f_0} \tag{2.45}$$

The basis function expansion allows it to be represented as:

$$\frac{1}{r}\exp(-jkr)\mathbf{G}(\theta,\phi,f_0) = \sum_{n=1}^{N}\alpha_n \boldsymbol{f}_n(\theta,\phi) \tag{2.46}$$

where, N, is the number of basis functions, $\boldsymbol{f}_n(\theta,\phi)$, is a single geometric, frequency independent, basis function and α_n is the frequency weighting coefficient for the basis function with common subscript n. For the physics-based CBFP, N, the total number of characteristic basis functions, is limited by the number of frequencies for which the beam pattern of the antenna is known, such that they can accurately trace the beam pattern with constant arguments once multiplied by the corresponding set of complex coefficients α which correctly orders their influence on the beam at that frequency [30].

Now consider multiple beam patterns generated from a single antenna, with known geometric variations across θ and ϕ, at multiple frequencies $F = [f_0, f_1 ... f_n]$. A singular value decomposition (SVD) is performed on the patterns at all known frequencies, breaking them down according to common geometric features (θ,ϕ), such that the beam at each frequency can be generated by adjusting the amplitude weighting coefficients α of a discrete set of characteristic basis functions:

$$CBF = [\boldsymbol{f}_1(\theta,\phi), \boldsymbol{f}_2(\theta,\phi)..\boldsymbol{f}_N(\theta,\phi)] \tag{2.47}$$

which are refined by the SVD as more antenna pattern information becomes available for their generation. The field representation at each frequency in F can, therefore, be expressed as:

$$\mathbf{E}(r,\theta,\phi,f)_{f\in F} = \sum_{n=1}^{N} \alpha_n(f) CBF[n] = \sum_{n=1}^{N} \alpha_n(f) \boldsymbol{f}_n(\theta,\phi), f \in F \tag{2.48}$$

note how the complex weighting coefficients α are now frequency dependant while the basis functions remain frequency independent. As more frequencies are added to the beam information, the set of basis functions, CBF, begins to converge such that the first coefficient α_1 weighting the fundamental basis function $\boldsymbol{f}_1$ represents the dominant common geometric feature at all known frequencies (generally the main beam amplitude and width) with the subsequent weighting coefficients and basis functions representing the less dominant beam information such as the sidelobe distributions and other fine geometric contours [22].

Now the robust utility of this method reveals itself, if we consider the fully general form for continuous frequency f:

$$\mathbf{E}(r,\theta,\phi,f) = \sum_{n=1}^{N} \alpha_n(f) \boldsymbol{f}_n(\theta,\phi) \tag{2.49}$$

If enough frequency samples are used to generate a converged set of N basis functions able to order the geometric features to a very small amplitude, a perfect far-field pattern can be generated at any frequency where the N values of α_n are known. Now the highly complex multivariate problem of predicting antenna beams between known frequencies has been reduced to predicting N complex numbers, each of which is controlled by independent functions of frequency. Young et. al. show in [30] that using these complex exponential basis functions, only 9 coefficients are required to accurately predict far-fields of an electrically small offset Gregorian ($D_{SR} = 8\lambda \quad \& \quad D_{MR} = 25\lambda$) with average normalised geometric error of below $10^{-3}\%$ over a 30 dB dynamic range. This is far fewer than would be required with other established basis function sets (Bessel, Fourier etc.)

The CBFP method, therefore, facilitates efficient and accurate beam prediction with simple, single dimension interpolation, where the real and imaginary part of N complex coefficients, α, are individually interpolated, to predict the antenna's far-field at unknown frequencies. This reduces the information requirement to predict dual reflector radiation patterns, driven by non-linear physics based interference and coupling, to accurate single dimension interpolation.

2.8. Techniques for CBFP interpolation

Many interpolation schemes are suitable for the simple interpolation of the real and imaginary α_n components. The two explored in this thesis are that of the polynomial method of least squares fit and simple Kriging with Matèrn covariance weighting functions.

2.8.1. Polynomial method of least squares

A polynomial fit, $poly(x)$, of degree n, approximating an underlying function, $y(x)$, with an error of ϵ produced with a set of samples P along x can be denoted as the following:

$$y(x) \approx poly(x) = C_n x^n + C_{n-1}x^{n-1} + ... + C_1 x + \epsilon \tag{2.50}$$

While polynomial fitting is extremely computationally efficient, divergence at the boundaries of the domain inhibits accuracy in non-radially sampled data sets. Furthermore, while the divergence can be fixed using samples radially spaced across the domain, over-fitting, whereby oscillatory behaviour is incorrectly assumed due to an excessive polynomial degree, is a problem when modelling the slowly varying basis coefficients, particularly if the zero error at known points approach of $N_{poly} = N_{samples} - 1$ is adopted for large sample sets. A severe over-fitted interpolant is shown in Figure 2.15.

The best polynomial fit for a smooth function occurs when the degree of the polynomial is one higher than the number of inflections in the underlying function:

$$N_{poly} = N_{inflections} + 1. \tag{2.51}$$

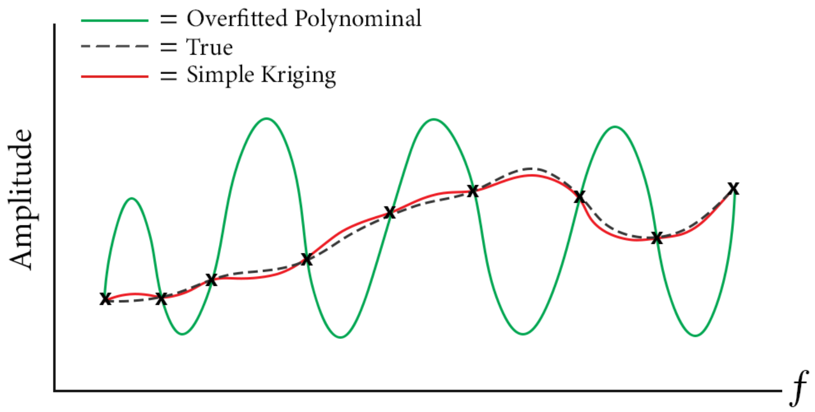

Figure 2.15: Illustration of over-fitting during interpolation with excessive polynomial degree and simple Kriging error balancing

This presents a problem for polynomial based interpolation if the basis function pattern shapes are unknown at the beginning of a multi-sample problem, as an excessive polynomial degree can lead to severe over-fitting (oscillations).

The method of least squares seeks to reduce global error by solving the following set of linear equations to find the best set of predicted coefficients, C, for N samples:

$$\begin{bmatrix} N & \sum_{i=1}^{N} x_i & \cdots & \sum_{i=1}^{N} x_i^n \\ \sum_{i=1}^{N} x_i & \sum_{i=1}^{N} x_i^2 & \cdots & \sum_{i=1}^{N} x_i^{n+1} \\ \vdots & \vdots & \vdots & \vdots \\ \sum_{i=1}^{N} x_i^n & \sum_{i=1}^{N} x_i^{n+1} & \cdots & \sum_{i=1}^{N} x_i^{2n} \end{bmatrix} \begin{bmatrix} C_0 \\ C_1 \\ \vdots \\ C_n \end{bmatrix} = \begin{bmatrix} \sum_{i=1}^{N} y_i \\ \sum_{i=1}^{N} x_i y_i \\ \vdots \\ \sum_{i=1}^{N} x_i^n y_i \end{bmatrix} \tag{2.52}$$

However, the maximum possible degree must be specified by the user, therefore, a polynomial fit is suitable for a CBFP coefficient set if the points of inflection in each pattern are known, allowing the user to detect regions where over-fitting is present. This does, of course, require existing knowledge of the system's behaviour.

2.8.2. Simple Kriging with a Matérn covariance function

Simple Kriging interpolation is a Gaussian process based interpolation orientated towards generating a smooth fit across the domain by assuming the mean and covariance of the data-set is known. Kriging is more attractive as it is not encumbered with any divergence and poses less over-fitting issues than polynomials for a scattered data-set. Kriging interpolation balances local and global probability according to its co-variance matrix to determine the path of least error between known points, while also considering the sensibility of the chosen path across the entire domain [56].

A prediction for some single dimensional function, $y(x)$ using simple Kriging can be denoted as:

$$y(x) \approx \mu + Z(x). \tag{2.53}$$

Where μ is the regression function, the mean of the available samples, assumed to be constant and correct, and $Z(x)$ is the residual Gaussian process based function with zero mean and variance equal to the square of one standard deviation, σ^2. The covariance is assumed to be perfectly described by a given function for simple Kriging interpolation, and for the case of CBFP coefficients the Matérn set of covariance functions offer a flexible local and global smoothness response. In general the Matérn covariance function is:

$$\mathcal{M}\left(h; v, \rho, \sigma^2\right) = \sigma^2 \frac{2^{1-v}}{\Gamma(v)} \left(\frac{\sqrt{2v}}{\rho} h\right)^{v} \mathcal{K}_v \left(\frac{\sqrt{2v}}{\rho} h\right) \tag{2.54}$$

with ρ and v as the non-negative range and smoothness factors respectively, which balance the local precision and global smoothness of the interpolant through mean-square differentiability. $\mathcal{K}_v$ is the modified Bessel function of the second kind, Γ is the gamma function and h is the distance between samples [57]. A robust trade-off between local correlation decay and global smoothness, slightly biased towards the latter, is obtained with a smoothness factor of $v = \frac{3}{2}$ referred to as the Matérn $(\frac{3}{2})$ covariance function:

$$\mathcal{M}\left(h; v, \rho, \sigma^2\right) = \sigma^2 \left(1 + \frac{\sqrt{3}h}{\rho}\right) \exp\left(-\frac{\sqrt{3}h}{\rho}\right). \tag{2.55}$$

Half integers allow for an accurate representation of the Matérn function using the Taylor series expansions of a natural exponential and a polynomial to obtain the form above. The smoothness factor reduces the likelihood of over-fitting for a particular problem with clusters of dense samples, as the interpolant is shaped using the covariance matrix and is, therefore, independent of the sample distribution. This is useful if a highly non-linear region, requiring dense samples, exists in the dual reflector field patterns for a small band, while remaining slowly varying for the rest of the frequencies.

Another feature which contributes to the effectiveness of simple Kriging modelling, is the ability of the covariance matrix to determine the regions where the error of the predicted path between samples is highest. This allows for the implementation of sequential design processes, where no system information is available prior to the start of sample computation, by considering the location coupled to the highest probability of improvement for the iterative placement of samples [30].

2.9. Surrogate modelling using CBFP

Surrogate modelling, in microwave circuits, refers to an interfacing piece of computational software focused on optimising the trade-off between accuracy and computational effort during CEM solver design. The onus is to reduce the number of computationally expensive simulations required for a new *surrogate* model, generated via fitting of sparse samples across a design space, to predict a result data-set at the same or comparable accuracy as a data-set generated from a finely sampled direct simulation analysis approach [58]. Interpolation based models have shown to be effective for passive microwave circuits, and have been successfully applied to dual reflector antennas [28].

For dual reflector systems wideband field data is typically in the order of several mega or gigabytes, interpolation models are also valuable from a data storage perspective, as only the interpolant coefficient values and and the basis function definitions, typically less than

15 for adequate CBFP reconstruction [22], are required to generate specific field results. This is valuable during parameter variation or optimisation which require a large number of iterations for parameter convergence, and the user wishes to store the iterative results.

This thesis uses the CBFP expansion to create a simple Kriging interpolation based surrogate model able to generate accurate wideband far-field data which captures any variations due to non-ideal coupling and diffraction by creating separate CBFP expansions for the equivalent radiation from the main reflector as well as for the radiation from the feed and sub-reflector pair.

Approaching the problem in this manner simplifies the interpolation process considerably by removing the physical cause of rapid variations in order to generate two smooth sets of complex CBFP coefficients. The full dual reflector pattern is then regarded as the sum of the radiation predicted using both CBFP models, restoring any rapid variation.

The computationally expensive direct antenna simulations used to build both CBFP interpolants, termed *support points*, are added to the design space until the set of coefficients (α) converge below a specified maximum deviation per additional support point. Most importantly, this surrogate modelling allows for the optimisation of a fully computationally driven design process with no prior analysis of the dual reflector geometry required.

This is achieved through a process termed *reflective exploration*, a sequential design approach whereby for each sample the current state of the model is used to predict the location of an additional support point which will reduce model uncertainty the most. The model uncertainty is evaluated via adaptive sampling algorithms.

2.10. Adaptive sampling algorithms

Adaptive sampling algorithms are comprised of two types, exploratory and exploitative. The former focuses on exploration of the design space, and determines which point in the sample space is furthest from known samples, based on statistical analysis of the underlying fitted data. It then uses these results to minimise the number of samples needed to adequately explore the antenna bandwidth. An illustration of how this approach is used to improve an interpolant is shown in Figure 2.16.

Exploitative methods scan the underlying data fit for specified regions of interest containing valuable information about the underlying problem, typically maxima, minima or regions of high non-linearity, and determines a suitable next support point accordingly.

Such methods are typically not suitable for antenna characterisation, where the entire bandwidth is of equal interest. Secondary patterns of dual reflectors also typically have slowly varying macro far-field features across frequency and, therefore, an exploratory approach is more suitable [29].

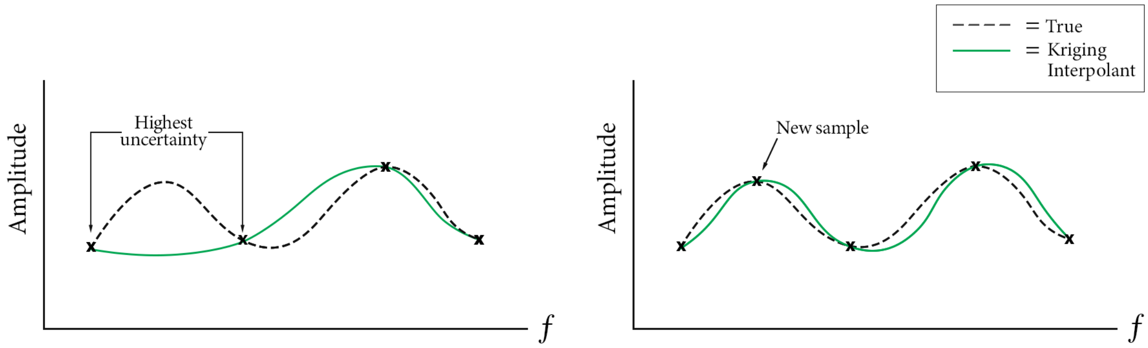

Figure 2.16: Basic illustration of exploratory *adaptive sampling*: a single iterative sample placement based on model uncertainty to maximise global model improvement

2.11. Conclusion

An overview of the theoretical knowledge needed for CEM driven wideband characterisation of electrically small dual reflector systems has been provided. The exposition includes the fundamental antenna theory needed to develop an understanding of performance metrics and terminology associated with the secondary far-field pattern such as aperture efficiency and receiver sensitivity, as well as the underlying electromagnetic principles driving dual reflector geometry and feed antenna synthesis.

Electrical size has a strong influence on the validity of common approximations made to optimise direct full wave methods. Selection of a suitable direct simulation method is paramount to ensuring an accurate CBFP surrogate model capturing all significant diffraction and coupling effects can be synthesised.

Chapter 3

Far-field pre-processing using VEXPA

3.1. Chapter Overview

Accurate computationally efficient interpolation of far-fields across frequency is valuable during the design of dual reflector antenna systems. Due to the phase reference adjustments and field positioning in GRASP [26](CEM solvers), far-field data contains an artificial fast varying periodic phase variation across frequency [22]. This inhibits computationally effective interpolation due to the large amount of field samples required if the carrier frequency of the variation is unknown, or cannot be removed. This chapter presents a method able to remove these variations without expensive Nyquist rate sampling by applying validated complex exponential analysis (VEXPA) [59].

3.2. Far-field solutions from GRASP

Interpolation of CBFP coefficients across frequency is an effective method for modelling the wideband behaviour of antenna far-field radiation patterns. The spatial qualities of the antenna far-field are captured using frequency in-dependant, orthogonal, basis functions which are weighted using frequency dependant complex coefficients. This allows for the directional fields of the antenna to be accurately reconstructed provided the correct coefficients of the relevant basis set is known at that frequency [30].

When applying a CBFP approach to the interpolation of dual reflector antenna far-fields across frequency, the performance is hindered by two rapid variations. The first of which is a quasi-periodic variation caused by physical diffraction of internal fields in the geometry, prompting either interference between radiation from the reflector and feed apertures or the formation of standing waves between them [21]. The second is perfectly sinusoidal across frequency and is caused by periodic phase variation of the free space far-field Green's function $\exp(-jkr)$ (see 2.1), given the point of observation r [22].

It is stressed to the reader that this second periodic phase frequency variation is artificial, and linked solely to the loss of inter-frequency phase information during software modelling of the antenna. Far-field solutions generated with GRASP of the MeerKAT shaped offset Gregorian dual reflector at an extremely fine linear sample density of 2 MHz, from 0.5 GHz to 2.0 GHz, when illuminated with a −12 dB analytical Gaussian beam primary pattern taper across the sub-reflector ($\theta_e = 49°$) are used for demonstration below and throughout this chapter.

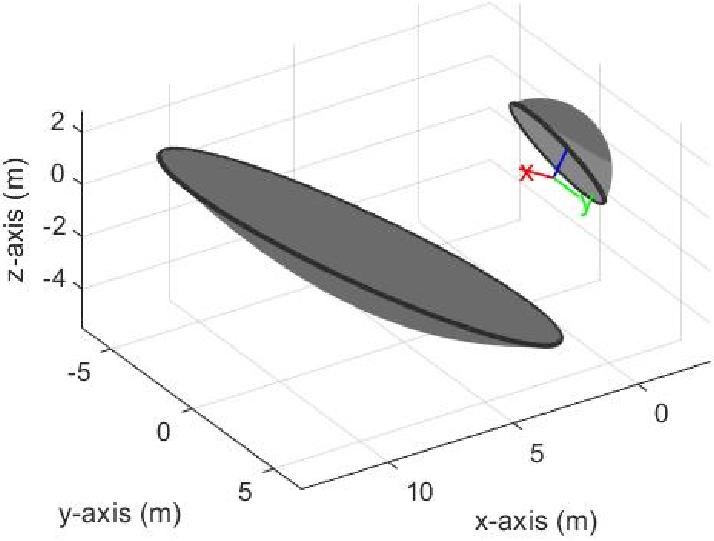

Figure 3.1: 3D plot of MEERKAT antenna reflector geometry

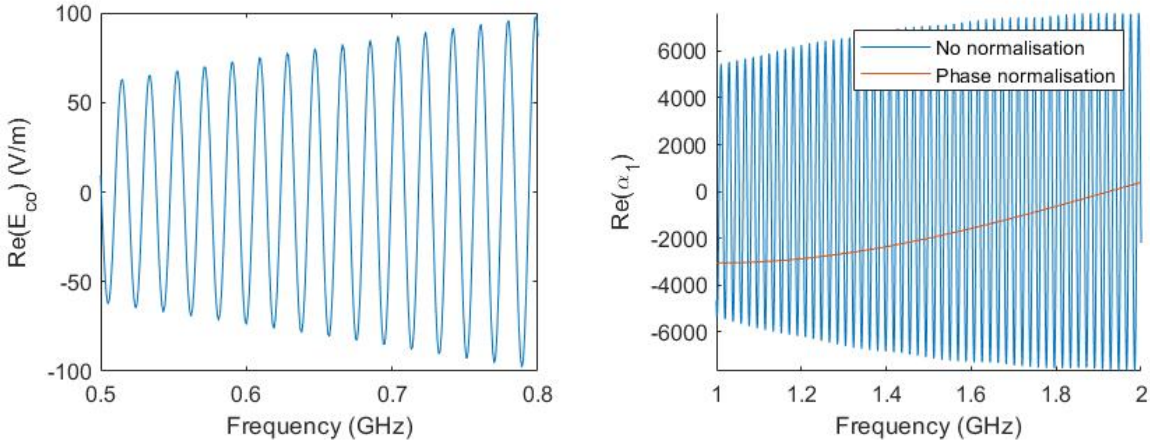

(a) Real component of broadside far-field result with no normalisation

(b) Real part of CBFP coefficient 1 before and after phase normalisation

Figure 3.2: Fast non-physical periodic variation across frequency in field solutions and associated CBFP coefficients.

Figure 3.2 illustrates the value of a method that does not require Nyquist resolution sampling, as it is impossible to predict the periodicity of the underlying artificial phase variation prior to computational analysis of field data due to its dependency on the phase of the SR incident fields. This makes it difficult to choose an effective sample density safely above the Nyquist rate beforehand.

3.3. Factors Causing Field Variation

A study of the far-field generation process in GRASP lead to the discovery of two modelling factors influencing the periodic phase variation and, subsequently, insight as to how it can be removed.

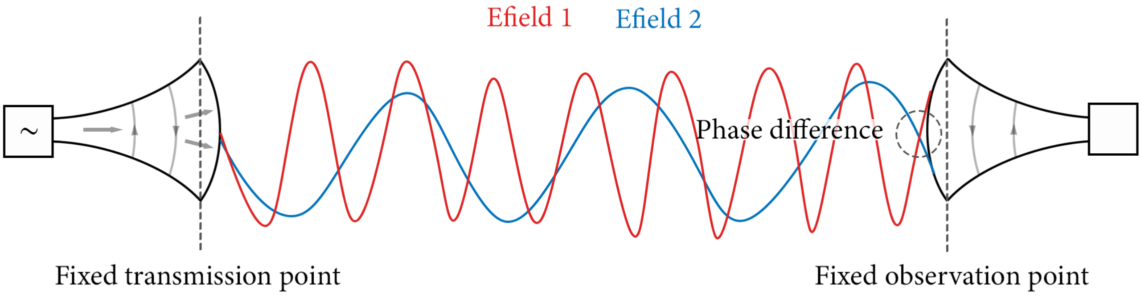

Figure 3.3: Illustration of phase difference caused by fixed 0° phase reference and change in electrical path length

If two time harmonic EM fields of different frequency are radiated from an ideal antenna and observed at a point a fixed physical distance away from the antenna in free-space, the wave-fronts will exhibit different phase in their field components upon arrival, except for the improbable case where an exact harmonic distance of the two frequencies is chosen.

An ideal antenna will have a fixed phase centre for all frequencies, and therefore, the phase difference for a far-field plane wave will be a linear function of frequency due to the constant propagation velocity of electromagnetic plane waves in space:

$$c = f\lambda \tag{3.1}$$

where f is frequency, λ is wavelength and $c \approx 3 \times 10^8 \mathrm{m\,s^{-1}}$ in free-space. This connects with the free-space far-field function where

$$\mathbf{E}(r,\theta,\phi) = \frac{1}{r}\exp\left(-j\frac{2\pi r}{\lambda}\right)\mathbf{G}(\theta,\phi) \tag{3.2}$$

at an observation point, r, in the far-field region.

GRASP compensates for the phase difference across frequency in the feed field, regardless of whether it is a spherical wave expansion generated from a physical antenna far-field pattern or an analytical Gaussian pattern (GRASP default), such that the field exhibits 0° phase upon incidence on the sub-reflector at any frequency.

Consequently the field illuminating the SR, as well as its reflection which illuminates the MR (similarly for any additional reflectors), has an artificial, frequency dependant, phase difference upon incidence on the scattering surface in question. Hence, the surface current densities $\mathbf{J}_s : SR$ and $\mathbf{J}_s : MR$ have a frequency dependant phase shift. Furthermore, the fields are diffracted differently for each frequency (PO+PTD/MoM) when considering electrically small reflectors, such that application of analytical ray tracing to calculate the required phase shift is ineffective.

The phase information belonging to the surface current density of an antenna is lost during evaluation of the far-field radiation integral, which applies the Fraunhofer approximation to evaluate the integral at an infinite distance [6], where the physical antenna structure is negligible, and is indistinguishable from a single point. The phase shift, therefore, does not impact the far-field radiation pattern at each frequency under evaluation, however, it distorts the phase relationship between adjacent frequencies.

The combination of the aforementioned factors drives the rapid linear phase periodic variation across frequency in far-field data obtained from GRASP, as the phase variation of the feed field due to changing wavelength is lost when evaluating the far-field integral, and augmented by the phase compensation shift applied by GRASP. Ultimately this applies an artificial frequency dependant phase shift across frequency to the surface current density used to estimate the far-field, coupling it to the data across frequency.

Fortunately, the *shift* applied to the phase of the feed field is linearly dependant on frequency, and can, therefore, be removed by shifting the far-field observation point by a certain distance, r_{norm}, with a linear phase gradient according to the free-space far-field Green's function phase factor:

$$\frac{1}{r_{norm}} \exp(-jkr_{norm}) \tag{3.3}$$

which counteracts the artificial oscillation, such that only phase variation across frequency which has a physical cause is present in the far-field radiation data. The fundamental problem now is reliable calculation of the required phase normalisation shift, r_{norm}, for all antenna models in GRASP, as the factors influencing the artificial phase periodic variation are antenna specific, making it impossible to predict.

3.4. Far-field phase normalisation for CBFP interpolation

Now that the modelling factors causing the rapid linear phase variation are understood, it can be removed with an analytical physics approach.

For a dual reflector the far-fields can be modelled across frequency in the form

$$\mathbf{E}_{DR}(r,\theta,\phi,f) = \mathbf{G}(\theta,\phi,f)\frac{1}{r}\exp(jkr + jkx(f) + jkA(f)) \tag{3.4}$$

where $x(f)$ is the linear phase shift due to compensation of the feed field to counteract the changing wavelength in propagating radiation at each frequency and $A(f)$ is the true physical phase centre variation across frequency of the dual reflector geometry. The deviation of the phase centre due to physical dual reflector factors across frequency, $A(f)$, should remain negligible when compared to the other phase factors across narrow bandwidths (several 10's of MHz), provided there are no steep changes in the primary pattern or internal field diffraction. The same condition applies to the radiation pattern, $\mathbf{G}(\theta,\phi,f)$, which in a direction close to broadside should be equally slowly varying across frequency.

This allows us to extract the required observation point shift, r_{norm}, if the variation period can be extracted from a region of field data where only $x(f)$ influences far-field phase and amplitude.

This can be simply done by generating far-field data over a dense grid of frequency samples which satisfies the Nyquist criterion of the artificial linear phase periodic complex exponential, with argument equal to the constant derivative of $x(f)$:

$$\exp(-j(x')f) \quad \text{with} \quad \text{and} \quad x' = \frac{\partial}{\partial f}x(f) \tag{3.5}$$

such that Fourier analysis on the broadside directed ($\theta = 0°$) field variation across frequency will reveal a variation period P, in frequency, (in the range of 15 MHz to 30 MHz for the geometry tested in this thesis) which can be related back to a physical shift in meters (in free-space with wave velocity c) by

$$\frac{c}{(x')} = \frac{c}{P} = r_{norm} \tag{3.6}$$

which will remove the artificial periodic phase variation from the far-field data of a specific antenna geometry for all frequencies, provided the spectral analysis is performed across a domain with negligible changes in $A(f)$ and $\mathbf{G}(\theta,\phi,f)$.

The fundamental issue with this approach is that the variation period P is unknown to the user at the start of modelling, due to its dependency on the phase compensation in the feed source field during GRASP simulations at different frequencies, which is unique to each physical antenna model.

In addition to the risk of selecting an insufficient sample density, the phase periodic variation is so much faster than the antenna pattern variations that the expensive direct simulations needed to obtain the samples for its removal are wasted from a modelling standpoint. This is because the goal is to interpolate the slowly varying antenna patterns over a bandwidth of typically an octave, and inclusion of support points at Nyquist density will not reduce error in the wideband interpolant, and may, in fact, bias the SVD used to generate the CBFP expansion towards patterns at the frequencies used for phase normalisation in sample sets where the number of normalisation samples is comparable to the total. This reduces its overall effectiveness as a basis set orientated to capture far-field pattern features for a narrow bandwidth may reduce the rank of significant beam features in different frequency ranges, decreasing the smoothness of CBFP coefficients outside of the densely sampled region thereby increasing the difficulty of accurate interpolation.

A method which facilitates the use of samples which are sufficiently spaced such that they can add value to CBFP interpolants while still allowing for the calculation of a phase normalising far-field shift, r_{norm} is, therefore, of great computational value [22].

3.5. Validated Exponential Analysis - VEXPA

Validated EXPonential Analysis through regular sub-sampling (VEXPA) [59] is an algorithm which allows for the extraction of complex exponential base terms, and therefore, the frequency of underlying oscillations, by exploiting predictable patterns in the aliasing effect inherent to regularly spaced co-prime sample sets at sub-Nyquist intervals.

Implementation involves selecting a resolution for a *virtual grid* of samples which satisfies the Nyquist criterion. In dual reflector applications a 1 MHz grid resolution should be sufficient to capture variations associated with reflectors which occupy a spherical volume of several cubic meters.

Next two co-prime intervals: σ and ρ, defined using the resolution of the virtual sample grid, are chosen to construct the scaled and shifted sample sets used to identify base terms via cluster analysis in the complex plane [59]. The values of σ and ρ must be co-prime in order for VEXPA to successfully validate the embedded complex exponential base terms, else the aliasing effects will remain unrecoverable as for the standard Fourier analysis case. Smaller values for σ and ρ are desirable as it increases the separation between each complex exponential term as they rotate around the complex plane unit circle [2].

Consider a signal comprised of a sum of complex exponential components of different frequencies:

$$\Phi(t) = \sum_{n=1}^{m} \gamma_n \exp(-j2\pi f_n t) \tag{3.7}$$

here $\gamma_n \exp(-j2\pi nt)$ represents a single complex exponential base term with amplitude γ and frequency f, in a set of m base terms up to a highest frequency f_m whose sum describes a zero average time varying function $\Phi(t)$. Fourier analysis of such a signal requires a sample interval smaller than half the period of the highest harmonic base term in order to successfully extract the base terms of all the harmonics present in the signal, without ambiguity caused by aliasing.

This becomes increasingly inefficient in situations where only a single high frequency harmonic is present, and the desired information is embedded in harmonics which vary at $\frac{1}{10}^{th}$ of its rate, as a set of samples at Nyquist density for the highest frequency are needed to calculate the outlying base term. The information in these samples is effectively wasted, as most of it is used to verify which in-between base terms are indeed zero.

VEXPA allows for extraction of n base terms from $2n$ σ and n ρ samples regardless of their interval, provided the underlying function is constant or has negligible variation. A single high frequency harmonic can, therefore, be extracted with a set of three sub-Nyquist rate samples. Hence, VEXPA is congruent for antenna field normalisation, as it is able to isolate the fast varying base term without the wasted verification of intermediate zero-base harmonics with a sample density sparse enough to assist during wide-band field interpolation.

For analysis of the MeerKAT far-field data the chosen values for σ and ρ are 47 and 23 respectively, chosen here simply to show the normalisation process. Wider co-prime intervals are suitable for normalisation, the extent of which is discussed in later chapters.

Figure 3.4 illustrates the co-prime spacing of the shifted and scaled sample sets as well as how they relate to the underlying virtual sample grid.

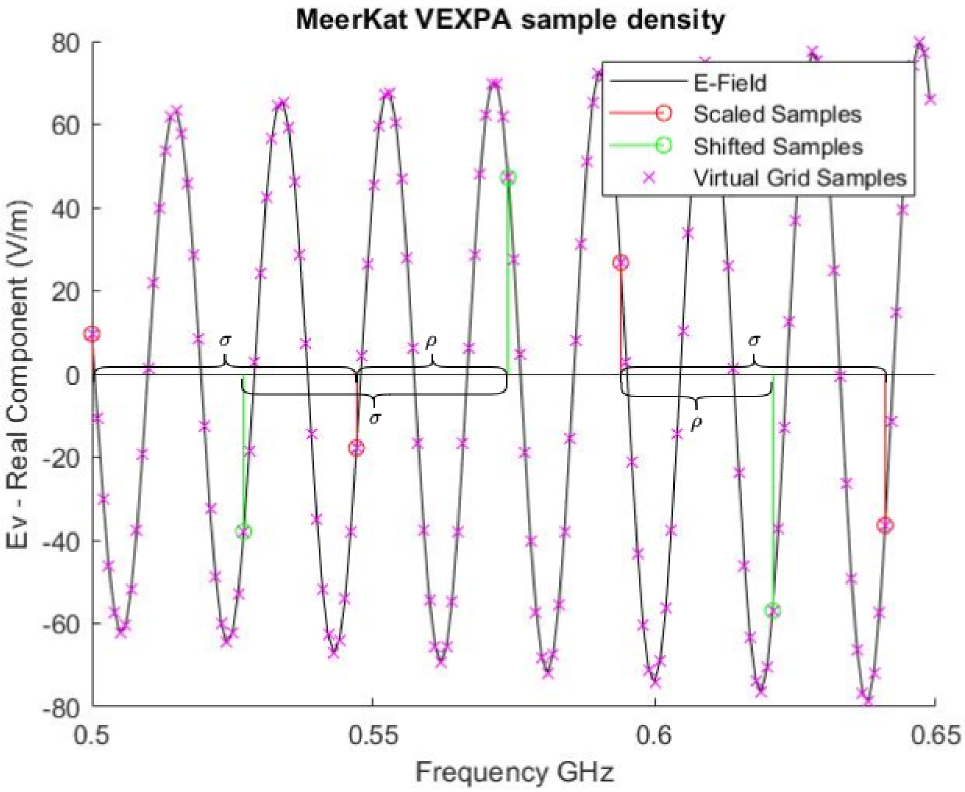

Figure 3.4: General VEXPA regular co-prime sub-Nyquist sampling layout as well as the maximum obtainable sample density represented by the virtual sample grid.

As shown above a regular interval of σ Hz exists between each sample in both sets. The *scaled* set refers to a sample set starting at the first sample, with every subsequent sample located σ away in frequency. The *shifted* set is a set of samples also located at regular intervals of σ, however, each sample in this set is ρ samples away from the matching sample in the scaled set and, henceforth, is termed the *shifted* set. The exponential analysis of the these two sets allows for the signals to be reconstructed as if they were sampled at a rate of the virtual underlying grid, provided the σ and ρ shifts are co-prime to generate a unique set of common base terms between the two sets allowing for recovery after aliasing.

Recovery after aliasing is performed by analysis of the possible base terms on the complex plane which correspond to the σ and ρ sample set. The complex exponential base terms will sit on the unit circle if generated in a noise free environment. For the phase normalisation implementation presented here, noise is virtually non existent in the target far-field data due to the analytical nature of the far-field Green's function. If noisy measurement data is used, more co-prime samples or *snapshots* across frequency must be included such that a clustering method can filter through the added noise to detect the correct base terms [2].

A function for which the virtual Grid is below the Nyquist rate cannot be successfully decomposed using VEXPA, as such aliasing will push complex roots beyond 2π radians on the complex plane, making them indistinguishable from lower harmonic roots.

A candidate base term is generated for each underlying virtual grid interval between the regular co-prime sets. The co-prime nature of the spacing between the sets will make it such that any base terms which are common for both sets (located at the same position on the complex plane unit circle) are true components of the sampled signal [2]. This is true regardless of where the common term is located on the complex plane unit circle, whereas for Fourier analysis, any leakage of base terms outside of the first quadrant will create ambiguity between true underlying frequency components and components which posses *negative frequency*.

A visualisation of possible base terms corresponding to each of the VEXPA sample sets when applied to an ideal function containing a single base term (phase normalisation case) [2] using a ρ value of 7 marked with circles and σ value of 11 marked with crosses is shown in Figure 3.5, the common complex root represents the argument of the true base term.

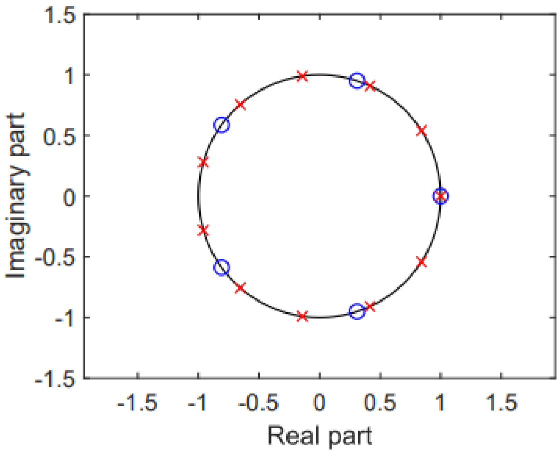

Figure 3.5: Co-prime sample spacing allowing for verification of the single true common base term despite aliasing. Circles indicate possible base terms for ρ samples and crosses indicate possible base terms for σ samples [2].

This makes the use of extremely high values for σ and ρ risky, as many possible solutions may result in ambiguity between which base term is indeed common, due to the decreasing distance between candidate complex roots as shown in Figure 3.6, especially if the underlying function is not exactly constant across the analysis domain as is the case with antenna patterns [59].

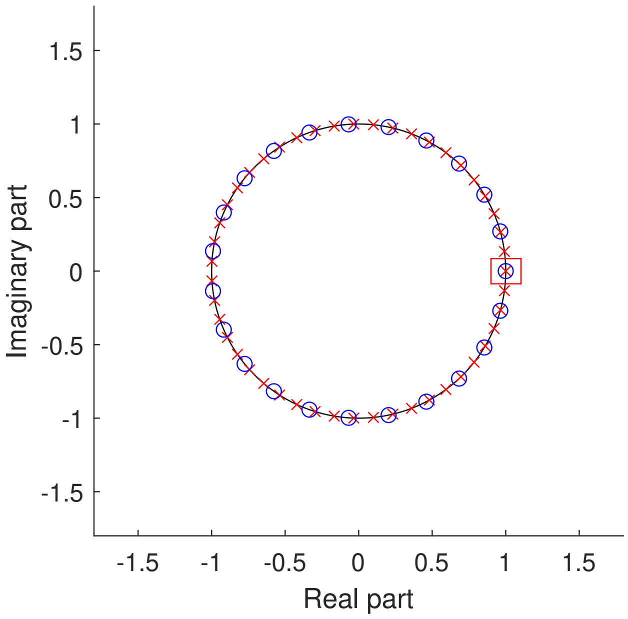

Figure 3.6: Illustration of increased difficulty to isolate base terms when using larger σ and ρ values. Circles indicate possible base terms for $\rho = 23$ samples and crosses indicate possible base terms for $\sigma = 47$ samples, the true common term is located in the red rectangle.

Again the other limitation of VEXPA is that the underlying sample grid must satisfy the Nyquist criterion of the variations in the function being analysed, however, the virtual grid density can be overestimated, while still allowing for co-prime spaced samples to add value to both phase normalisation and CBFP interpolation illustrated in Figure 3.7 with $\sigma = 47$ and $\rho = 23$ on a 1 MHz virtual grid for MeerKAT field data.

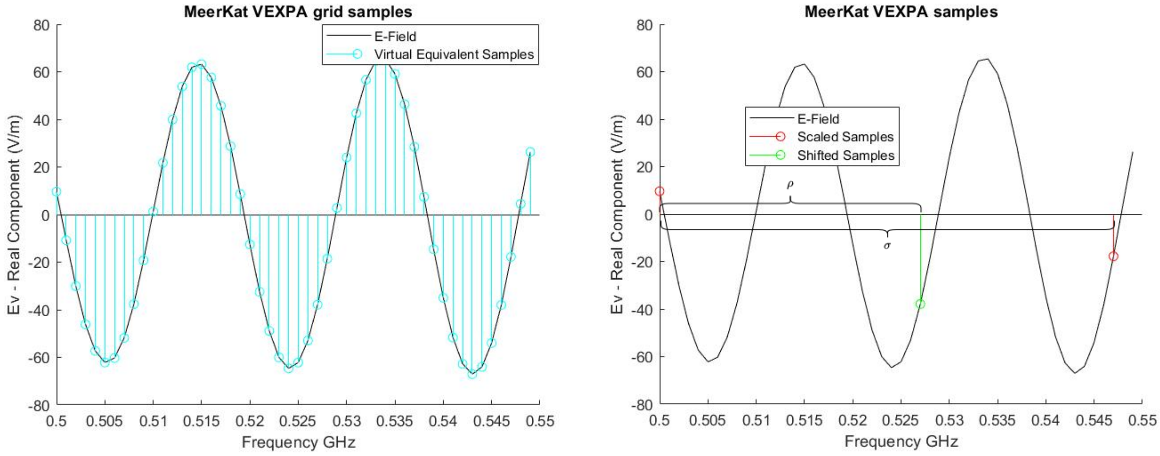

(a) Illustration of the maximum Fourier sample density possible with a 1 MHz VEXPA virtual grid.

(b) possible VEXPA sample spacing on a grid much finer than the Nyquist rate

Figure 3.7: Illustration of a practical VEXPA grid applied for phase normalisation with an extremely fine virtual sample grid to eliminate risk of aliasing.

3.5.1. Single common base term VEXPA implementation

The change in phase centre of dual reflector primary patterns (typically in the order of several mm) generally has a negligible impact on the path length between the feed and sub-reflector apertures. In addition primary and secondary patterns are effectively constant when compared to the rate of the modulating periodic variation, such that a single common high frequency complex exponential base term in both co-prime sample sets best represents the modulation.

A basic implementation of the VEXPA algorithm for extraction of this single complex exponential is created by approximating the underlying far-field magnitude and phase centre as constant, placing the periodic field phase variation in approximate Prony form as a function of frequency [2], where $\mathbf{E}_{DR:\theta=0^\circ}(f)$ can be denoted in VEXPA form with a single amplitude modulating complex exponential, which is a function of frequency:

$$\mathbf{E}_{DR:\theta=0^\circ}(f) = \gamma \exp(jPf + j\phi) \tag{3.8}$$

where γ is an assumed constant electric field strength setting the amplitude of the linear phase variation with argument, P, the variation period, with an arbitrary phase offset ϕ. Two regularly spaced σ samples can be defined with a linear phase offset as a result of their regular spacing where m is the frequency sample identifier:

$$f_{m\sigma}(f) = \mathbf{E}_{DR:\theta=0^\circ}(f) \exp(jm\sigma P) \quad m \in N \quad \{0, 2\} \tag{3.9}$$

P is the linear phase gradient of the periodic variation we wish to extract. one additional ρ sample, a co-prime distance away from the first σ sample, to place the three samples in VEXPA form [59], has phase related to the σ samples:

$$f_{m\rho}(f) = \mathbf{E}_{DR:\theta=0^\circ}(f) \exp(j(m\sigma + \rho)x) = f_{m\sigma}(f) \exp(j\rho x) \quad [m = 0] \tag{3.10}$$

where the full notation applicable for additional samples has been included for generality, but here $m = 0$ as only one ρ sample is used.

Now the base terms of $\exp(jm\sigma x)$, which are estimations of the possible underlying harmonics in the function we are evaluating, are calculated using the matrix pencil method, as we have only a single frequency *snapshot* value of the samples [59].
For three samples:

$$\sigma(mf) = \begin{Bmatrix} \sigma_{f1} \\ \sigma_{f2} \end{Bmatrix} \tag{3.11}$$

$$\rho(mf) = \rho_{f3} \tag{3.12}$$

where $f3 - f1$ is co-prime and less than $f2 - f1$. Typically sigma samples are used to construct a pair of Hankel matrices, however, because of the small matrix dimensions, the pencil parameter falls to zero, meaning $\sigma(mf)$ can be directly converted into a set of linear equations, U, through a singular value decomposition:

$$U = SVD(\sigma(mf)) = \begin{Bmatrix} U_0 \\ U_1 \end{Bmatrix} \tag{3.13}$$

the candidate base terms of the σ samples are then generally found as:

$$\Psi_\sigma = [eig(U^{-1})]^T \tag{3.14}$$

where T represents the transpose of the matrix and eig represents the eigenvalues. For the single common base term case this is equal to:

$$\Psi_\sigma = \frac{U_0}{U_1}. \tag{3.15}$$

Now that the base term of $\sigma(mf)$ is known, a Vandermode linear set of equations, matrix V, is used to solve for the candidate base terms of the ρ sample:

$$V = \begin{Bmatrix} 1 + 0j \\ \Psi_\sigma \end{Bmatrix}. \tag{3.16}$$

The base term amplitude γ_σ simply becomes the value of the first sigma sample as it is the solution of the first Vandermode equation:

$$\sigma(mf)V = \begin{Bmatrix} \gamma_\sigma \\ \gamma_\rho \end{Bmatrix} \tag{3.17}$$

$$\gamma_\sigma = \sigma_{f1}. \tag{3.18}$$

The complex coefficient Ψ_ρ of ρ_{mf} can now be found as:

$$\Psi_\sigma = \frac{\rho_{f3}}{\gamma_\sigma} \tag{3.19}$$

as the system only has one common base term, belonging to the single complex exponential modulating the field data. The 2x1 Vandermode matrix will return σ possible base terms (harmonics) from the σ_{mf} sample set:

$$\begin{aligned} \Psi_i &= \left(\Psi_i^{\sigma}\right)^{\frac{1}{\sigma}} \\ &= \exp\left(\psi_i d\sigma\right)^{\frac{1}{\sigma}} \\ &= \left\{ \exp\left(\psi_i d + \frac{2\pi j}{\sigma}\ell\right) : \ell = 0, \ldots, \sigma - 1 \right\} \end{aligned} . \tag{3.20}$$

Once the possible base terms belonging to the pair of σ frequency samples have been calculated, the ρ candidate values will be obtained from the ρ_{mf} sample set as:

$$\begin{aligned} \Psi_i &= \left(\Psi_i^{\rho}\right)^{\frac{1}{\rho}} \\ &= \exp\left(\psi_i d\rho\right)^{\frac{1}{\rho}} \\ &= \left\{ \exp\left(\psi_i d + \frac{2\pi j}{\rho}k\right) : k = 0, \ldots, \rho - 1 \right\} \end{aligned} . \tag{3.21}$$

The candidate base terms produced from the ρ sample set will all have a phase shift of $\exp(-j\rho)$ from the σ candidates. Common base terms in both sets correspond to harmonics which actually exist in the source signal, because the co-prime relationship between σ and ρ eliminates the possibility of accidental overlap. In this case, the single common root for both sets on the complex plane corresponds to the linear phase harmonic $\exp(jPf)$ we wish to extract and will appear at a single location on the scatter plot as in Figure 3.5.

3.5.2. Relating VEXPA output base term to far-field shift

VEXPA returns the common base term present in both sample sets which is the complex exponential with argument equal to P the period of periodic phase variation in frequency. It is related to an equivalent free-space distance using the free-space wave propagation velocity, c as before. Where b_t is the base term returned by VEXPA:

$$b_t = \exp(-jPf) \tag{3.22}$$

its linear argument P can be calculated as

$$Arg = \frac{2\pi}{|\Im(\log(b_t))|} \tag{3.23}$$

where *log* is the natural logarithm and $||$ represents magnitude. This argument represents the phase change between two elements on the virtual frequency Grid. This can then be converted to the required normalisation shift in meters (r_{norm}) by relating it to the frequency resolution of the virtual grid F_{Grid}:

$$r_{norm} = \frac{C}{\arg(F_{Grid})} \tag{3.24}$$

moving the far-field to a new observation point r_{norm} will remove the amplitude modulation effect from the far-field data. It is imperative to shift the field components of the MR and FSR back to their original observation point during superposition to restore any removed relative phase differences. $\mathbf{E}_{MR}$ and $\mathbf{E}_{FSR}$ have different normalisation shifts as they are separate physical antenna models during field calculation in GRASP.

3.6. MeerKAT far-field test results

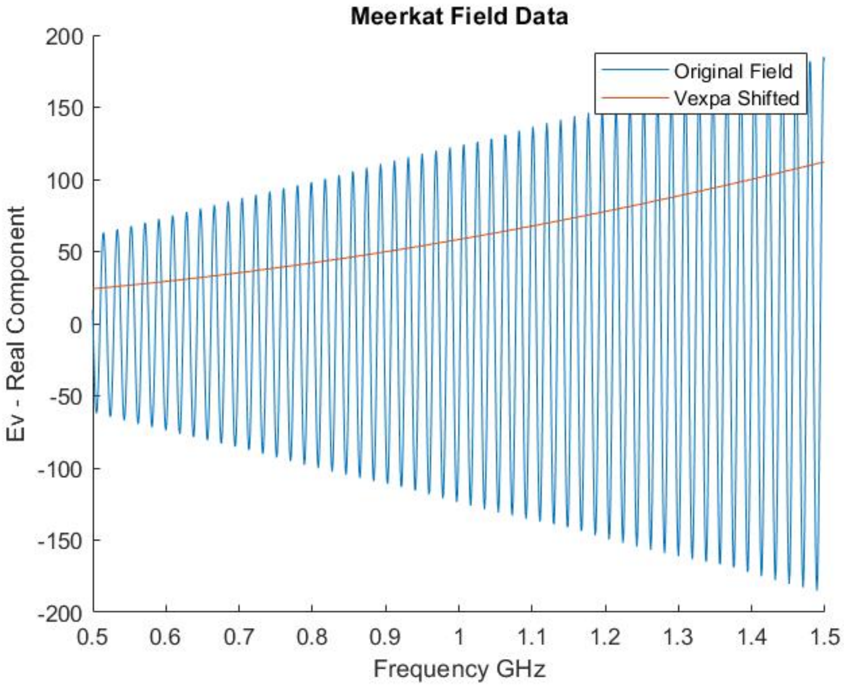

Figure 3.8: Real part of Complex far-field data before and after the VEXPA calculated shift r_{norm} of 15.82 m is applied for phase normalisation.

Figure 3.8 shows how VEXPA accurately removes the modulating complex exponential present in the field solutions, such that the field data in a single direction is a smooth slow-varying function of frequency as expected. This is crucial for the generation of CBFP complex coefficients which also vary slowly with frequency such that they can be accurately interpolated to represent the physical behaviour of the antenna beams across frequency, without the influence of any artificial phase variation.

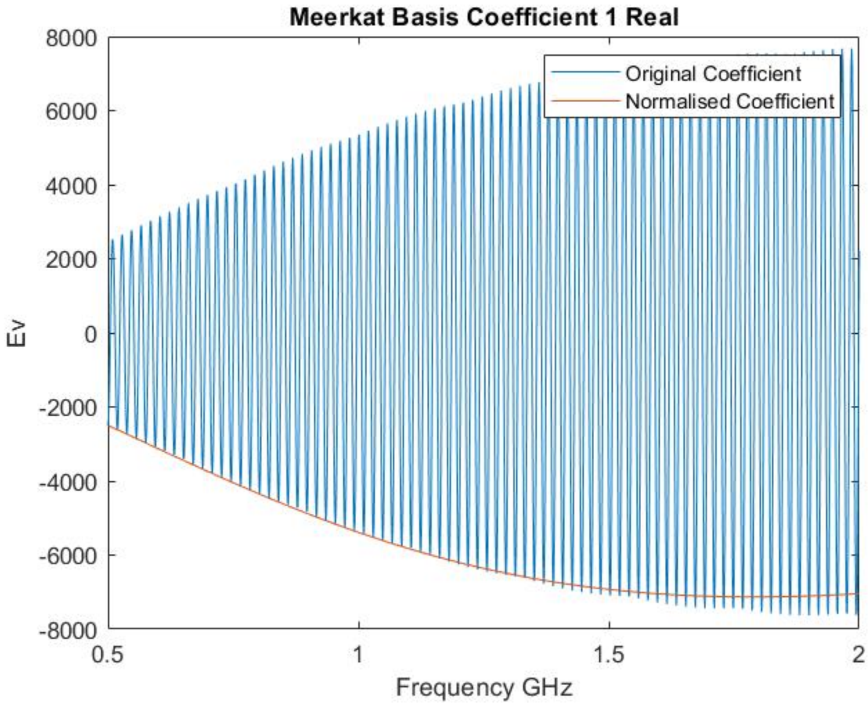

(a) α_1: Real

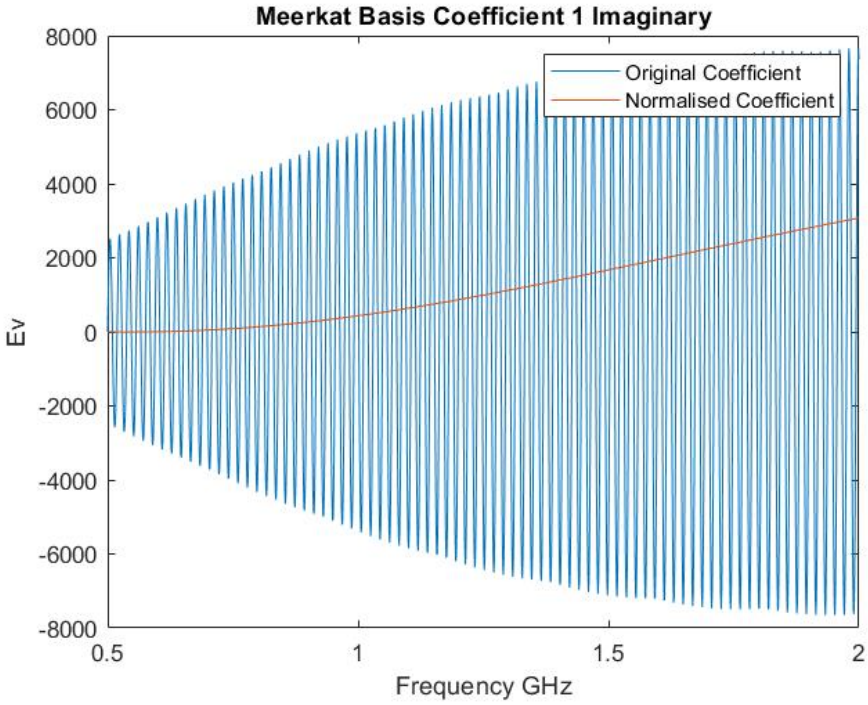

(b) α_1: Imaginary

Figure 3.9: Comparison of complex CBFP frequency coefficient α_1 before and after phase normalisation through far-field shift $\frac{1}{r_{norm}} \exp(-jkr_{norm})$

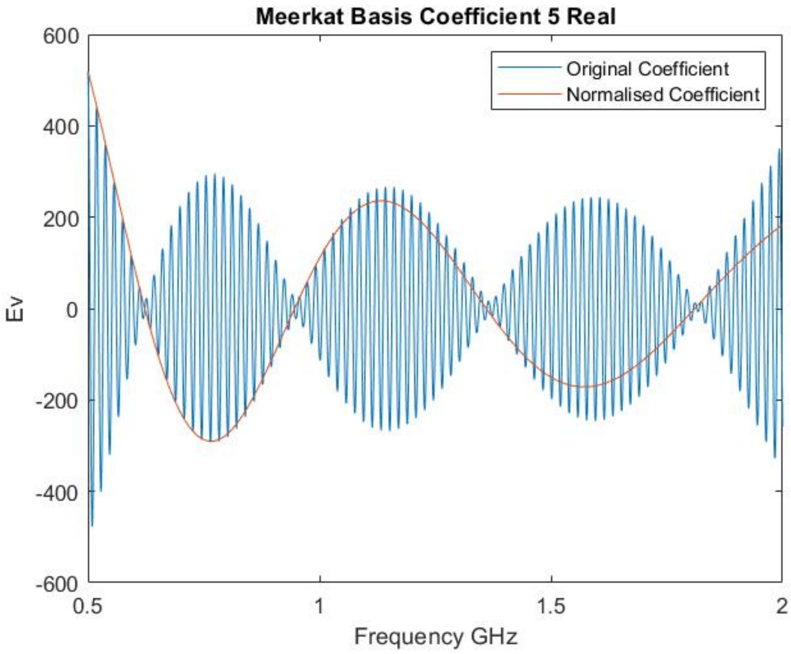

(a) α_5: Real

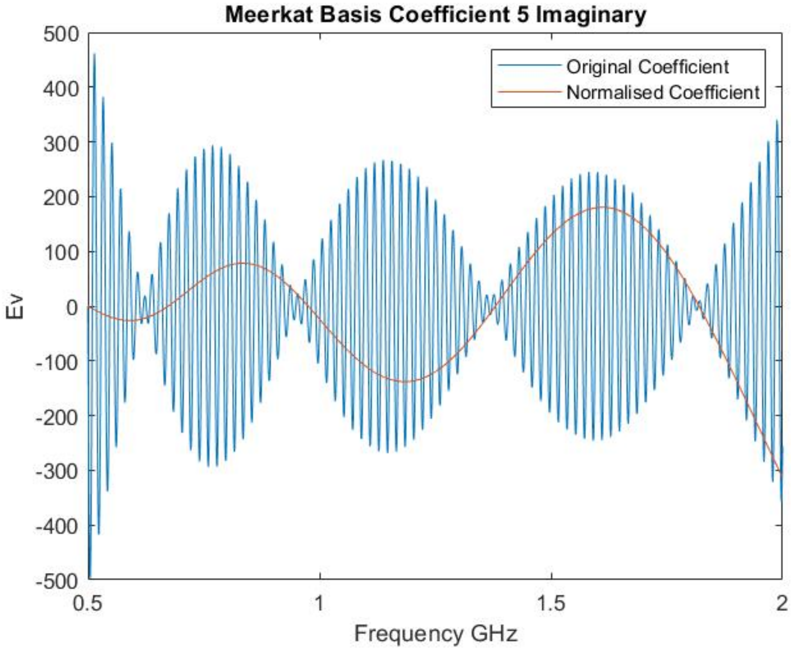

(b) α_5: Imaginary

Figure 3.10: Comparison of normalised and un-normalised complex CBFP frequency coefficient α_5 before and after phase normalisation through far-field shift $\frac{1}{r_{norm}}\exp(-jkr_{norm})$

Figures 3.9 and 3.10 show the importance of accurate phase normalisation to obtain CBFP coefficients suitable for frequency interpolation. Most importantly, they provide conclusive evidence that VEXPA is able to remove the modulating harmonic using 3 samples which can be spaced sparser than Nyquist density such that the exact oscillation period does to need to be known and the samples can add value to an interpolant.

3.7. Summary and conclusions

Far-field data of dual reflector antennas is subject to rapid periodic phase variation due to phase compensation at the feed aperture to obtain a constant fixed 0° $\mathbf{J}_s$ phase across frequency. For a constant physical model, the path length between feed aperture and SR surface and from the SR to MR surface varies linearly according to the constant propagation velocity of EM waves in free-space $\frac{c}{f}$. Changes in electrical path length with frequency is, therefore, absent on the surface current densities used to estimate the far-field radiation, such that field-data is amplitude modulated across frequency by a single complex exponential harmonic $\exp(-jPf)$ with argument P corresponding to the frequency period of the phase variation.

The linear phase variation across frequency can be removed by shifting all far-fields belonging to a physical antenna model by a radial distance of r_{norm} which removes this artificial phase variation according to the free-space far-field Green's function phase factor $\frac{1}{r_{norm}}\exp(-jkr_{norm})$ [22].

It is impossible to predict the rate of phase variation prior to field data-analysis as it is linked to the diffraction qualities of the physical antenna geometry and software modelling factors influencing surface current phase, therefore, the selection of an appropriate sample rate is difficult without prior knowledge of the variation. VEXPA allows for calculation of the modulating complex exponential using only 3 samples with a density well below the Nyquist threshold, the result of VEXPA is related to r_{norm} by $r_{norm} = \frac{C}{\arg(F_{Grid})}$ where F_{Grid} is the virtual sample grid interval.

VEXPA requires that the two regularly spaced sample sets are located at co-prime relative positions, such that common base terms are only found for harmonics present in the source signal. The virtual sample grid on which VEXPA is performed must be at a rate above Nyquist for correct phase normalisation, grid resolution of 1 MHz is suitable for dual reflector antennas in this thesis, but this may need to be refined when applied to much physically smaller or larger antennas.

VEXPA is dependant on the physics based assumptions of constant secondary pattern field intensity and feed aperture phase centre for the analysis bandwidth. This limits the bandwidth which can be used for practical primary patterns.

Ultimately correct use of VEXPA allows for the analytical removal of periodic phase variation from CEM far-field result data with three sub-Nyquist rate samples, such that accurate frequency interpolation of CBFP coefficients is possible.

Chapter 4

Simple interpolation models with CBFP superposition

4.1. Chapter overview

This chapter will cover the implementation procedure for synthesis of an interpolation model accurate enough for wideband calibration of an electrically small dual reflector with the field superposition approach. The procedure is specified using PO+PTD field results, as they are the most relevant for reflector surfaces of several meters ($\approx$10 to 100λ) in the UHF band of 300 MHz to 3000 MHz, it is, however, applicable to fields generated by any CEM method.

4.2. Far-field superposition approach

Due to the fact that the rapid chromatic aberration ripple present in far-field radiation of electrically small dual reflector systems is primarily driven by the interaction of diffracted field components and coupling between the reflectors, it can be inferred that grouping the feed and sub-reflector as a single radiating entity and the main reflector as another during modelling will result in much slower variations across frequency, and thus, a substantially less challenging interpolation problem.

This approach is highly conducive to the framework followed by PO solvers for reflector analysis, whereby surface currents on each reflector in the system are sequentially calculated based on the fields incident upon them (mutual coupling not considered). For a PO+PTD simulation approach the surface currents on the sub-reflector are always required to obtain a full solution for the DR far-field, and projecting the field it radiates to the global co-ordinate system is a computationally inexpensive endeavour.
The CEM instructions for this approach are as follows:

1. The surface current density, $\mathbf{J}_{SR}$, is calculated from a spherical wave expansion of the feed's far-field pattern to approximate the radiating near-field where applicable [26].

2. The field radiated by the feed and SR (FSR) is calculated with respect to the global co-ordinate system, before continuing with a standard PO implementation as in Section 2.6.6.
3. The main reflector surface current density, $\mathbf{J}_{MR}$, is calculated with the SR field as incident as in Section 2.6.6.
4. The field radiated from MR surface currents are calculated in the Global Co-ordinate system.
5. The FSR field is added to the MR field to complete the DR far-field solution.

Note that failure to add the FSR field to the MR radiated field will result in a non-physical result, as the SR diffraction components are absent [26]. Now there are two physically accurate field results expressed with complex data, containing both magnitude and phase, projected in the global co-ordinate system: $\mathbf{E}_{DR}$ the far-field of the full DR system, containing the chromatic aberration ripple, and $\mathbf{E}_{FSR}$ the far-field of the feed and sub-reflector, which exhibits slow variations across frequency. A physically accurate representation of the total far-field components radiating from the main reflector can, therefore, be formulated as:

$$\mathbf{E}_{MR}(\mathbf{r}) = \mathbf{E}_{DR}(\mathbf{r}) - \mathbf{E}_{SR}(\mathbf{r}) - \mathbf{E}_{F}(\mathbf{r}) \tag{4.1}$$

Which is equivalent to (with all three vectors defined using global co-ordinates):

$$\mathbf{E}_{MR}(\mathbf{r}) = \mathbf{E}_{DR}(\mathbf{r}) - \mathbf{E}_{FSR}(\mathbf{r}) \tag{4.2}$$

Now we can generate CBFP representations for both $\mathbf{E}_{MR}$ and $\mathbf{E}_{FSR}$, which should both exhibit gradual variations across frequency while possessing all the phase information contributing to diffraction as well as standing wave effects if full wave MoM is applied. This is illustrated below:

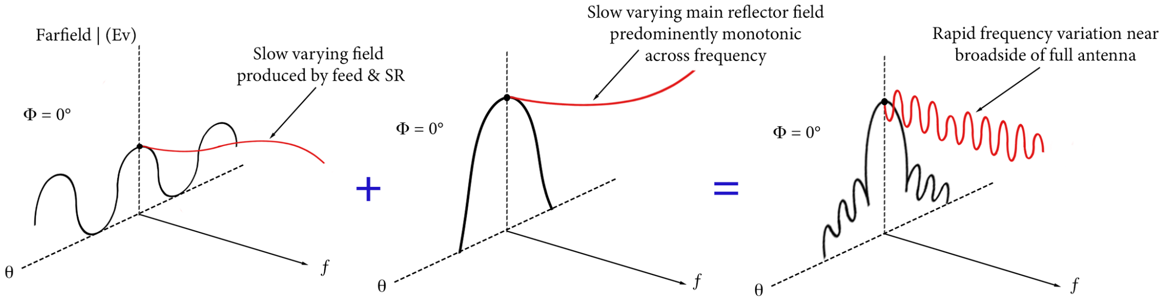

Figure 4.1: Graphical Representation of Field Superposition

This facilitates the accurate reconstruction of any rapid chromatic aberration ripple, with a sample density well below the Nyquist-Shannon threshold, by generating accurate field predictions across unknown frequency bands with the interpolated CBFP coefficients of basis sets generated from $\mathbf{E}_{MR}(\mathbf{r})$ and $\mathbf{E}_{FSR}(\mathbf{r})$ respectively. A successful implementation on the MeerKAT and ngVLA offset Gregorian antennas [22], [60], as well as a symmetrical Cassegrain antenna presented by Granet in [39] is outlined below.

4.3. Characterisation of the MeerKAT offset Gregorian

In order to illustrate a basic implementation of the CBFP field superposition approach, an interpolation model was generated from 0.5 GHz to 6 GHz using the above commands for PO+PTD analysis in GRASP. This varies D_{SR} from 6λ to 80λ and D_{MR} from 22.5λ to 270λ to make it clear that the method captures the ripple even when its amplitude is extremely small at higher frequencies.

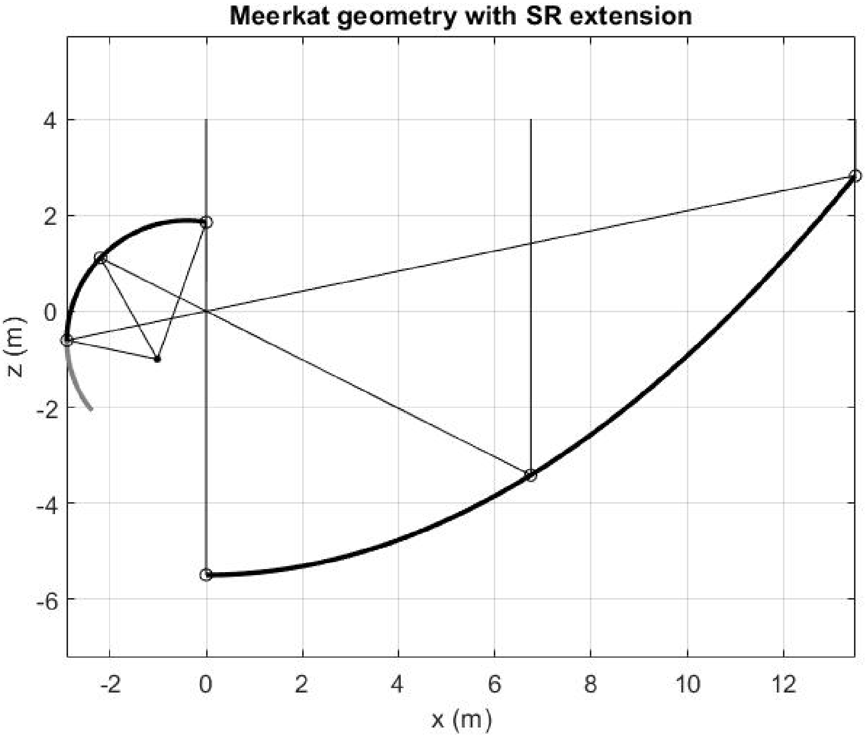

Figure 4.2: Symmetry plane cut of the MeerKAT offset Gregorian geometry

The MeerKAT offset Gregorian features a classical offset paraboloid main reflector and an extended ellipsoid sub-reflector. The extension is added to decrease noise temperature. This is a prime example of a modern DR with a subtended half angle of $\theta_e = 49°$, obtainable with a compact aperture controlled feed horn, for radio astronomy purposes. This antenna geometry is in active use on the MeerKAT interferometer in South Africa [30].

4.3.1. Polynomial model

A sample scheme of 14 radially spaced samples was used to interpolate a far-field geometric pattern with θ range from 0° to 4° using 301 linearly spaced samples at intervals of 0.02°, and 37 ϕ cuts every 5° covering variation from 0° to 180°. All 14 generated basis coefficients were used for the MR field with 7 used for FSR beam generation. VEXPA pre-processing was performed using a 1 MHz equivalent grid density with σ & ρ values of 21 and 86 respectively. A 13^{th} order polynomial was used according to the robust zero support sample error approach of the method of least squares.

The lowest frequencies in the radial sample set of 500 MHz, 521 MHz and 586 MHz were used for normalisation, with the calculated $\mathbf{a}_z$ shift for $\mathbf{E}_{MR}(\mathbf{r})$ equal to 15.82 m and 1.21 m for $\mathbf{E}_{FSR}(\mathbf{r})$.

Care must be taken not to use excessively high values for σ and ρ, as this can result in an incorrect shift calculated by VEXPA, due to the assumption of a constant underlying function [2]. Intervals less than 300 grid samples are recommended, shift estimation error for the meerkat against values of σ with ρ equal to the closet co-prime value to $\frac{\sigma}{2}$ is shown in Figure 4.3.

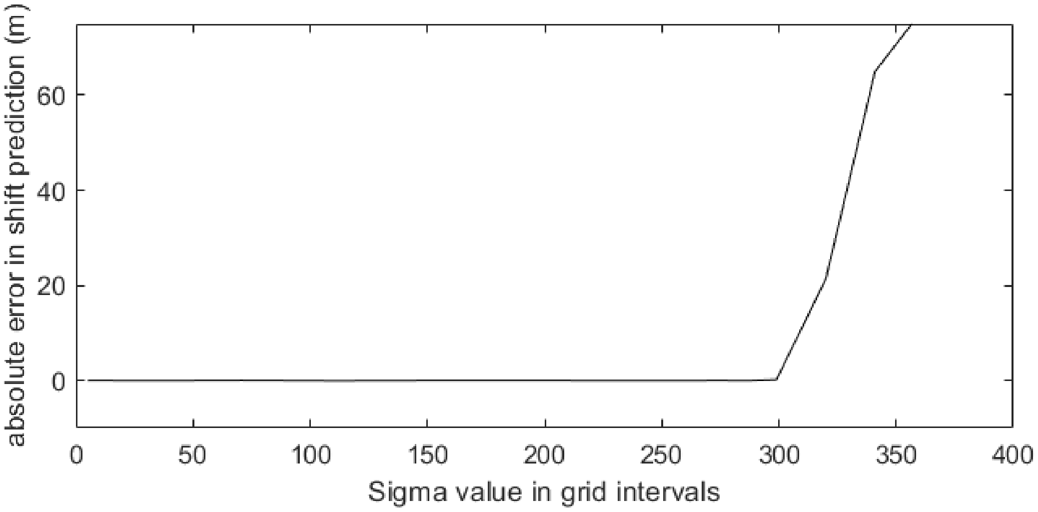

Figure 4.3: Shift prediction error for E_{MR} of the MeerKAT as the values of σ and ρ increase on an equivalent grid density of 1 MHz

The shift results remain within a tolerable noise limit until σ surpasses 300 virtual 1 MHz grid intervals, after which the VEXPA algorithm is unable to isolate the correct base term in the increasing number of candidates, resulting in inaccurate shift calculations. Similar results were obtained for $\mathbf{E}_{FSR}$. Figure 4.4 presents field estimations using normalised CBFP interpolants.

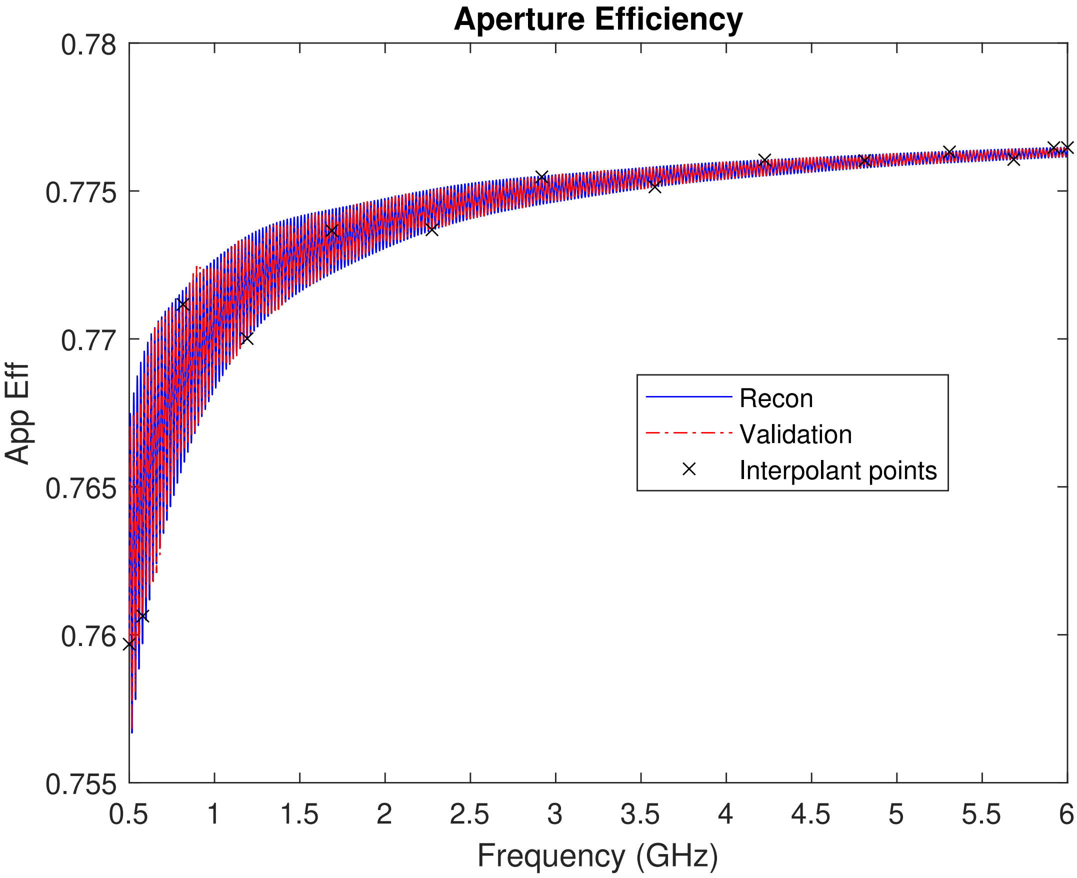

Figure 4.4: MeerKAT aperture efficiency prediction across a bandwidth of 5.5 GHz with rapid chromatic aberration ripple period of approximately 20 MHz, where *Recon* refers to the predicted aperture efficiency based on the CBFP superposition interpolants generated from 14 support points marked with crosses.

This result accentuates the vast bandwidth obtainable with a sparse sample density when seperate modelling is performed in the $\mathbf{E}_{FSR}$ and equivalent $\mathbf{E}_{MR}$ design space. The sample density in Figure 4.4 is linearly equivalent to approximately 390 MHz per sample (including VEXPA samples). A direct interpolation at the Nyquist rate would require a density of below 10 MHz as in [22].

This shows a factor of 10 improvement in baseline computational cost for aperture efficiency characterisation at a suitable analysis accuracy of below 10 % error on the ripple amplitude. A clearer illustration of the ripple prediction accuracy for this antenna is shown in Figure 4.5:

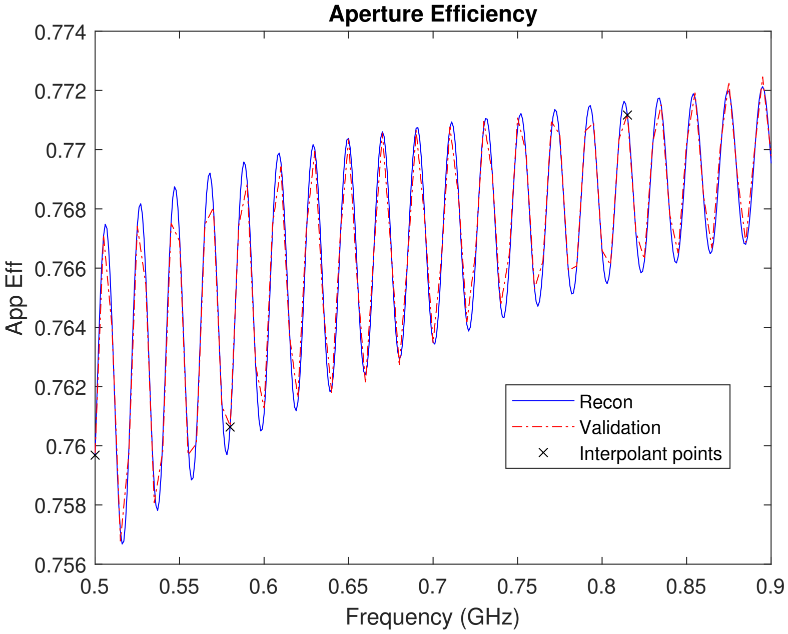

(a) CBFP interpolant reconstructed aperture efficiency vs. validation aperture efficiency from 0.5 GHz to 0.9 GHz

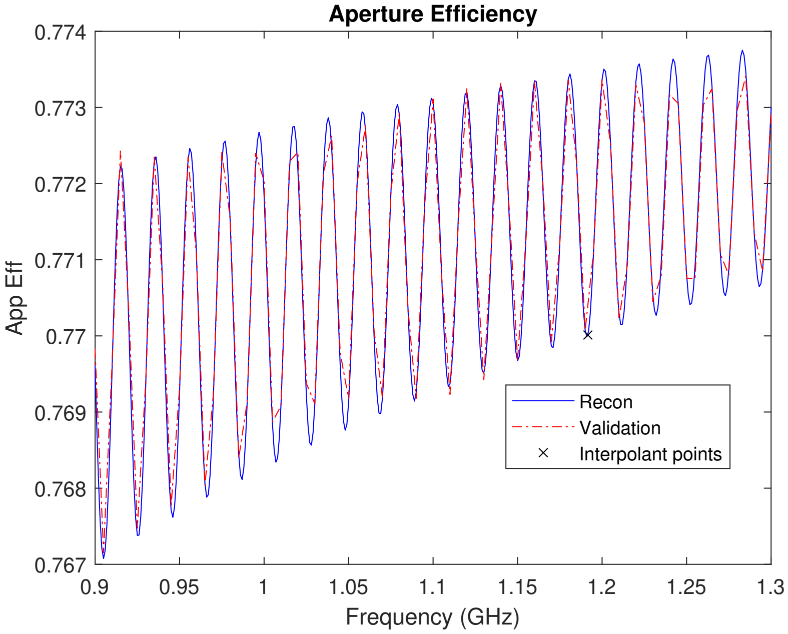

(b) CBFP interpolant reconstructed aperture efficiency vs. validation aperture efficiency from 0.9 GHz to 1.3 GHz

Figure 4.5: Accuracy of MeerKAT aperture efficiency prediction at electrically small band where chromatic aberration ripple is more pronounced.

The accuracy is similar across the band, with the validation set visibly indistinguishable from the reconstructed set, and therefore, more than adequate for ripple analysis. An order 13 method of least squares polynomial fit was fitted across the basis coefficients.

This result clearly indicates that 14 basis coefficients is sufficient to capture the aperture efficiency across frequency as expected from [22]. The CBFP coefficients weighted according to the SVD of the geometric far-field pattern, α_{1-n}, are illustrated in Figures 4.6 and 4.7 for the MR and FSR CBFP expansion respectively.

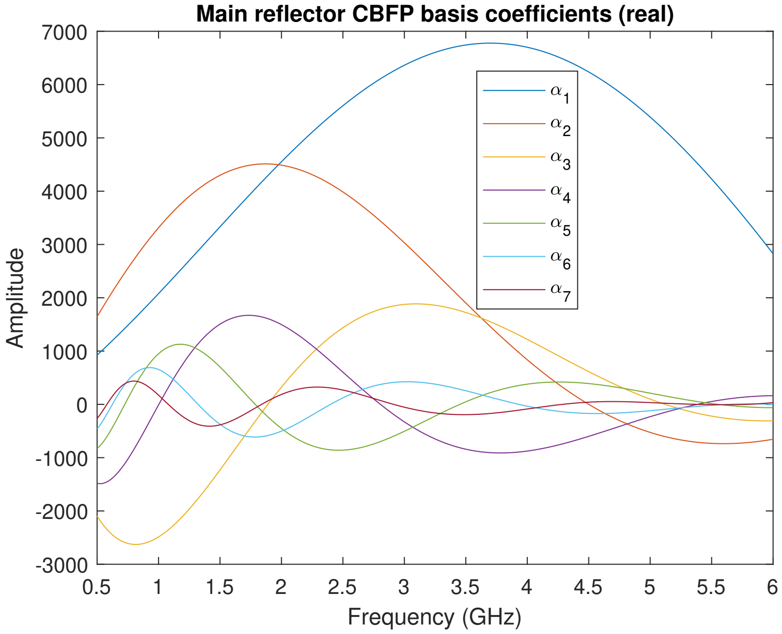

(a) Real coefficient components

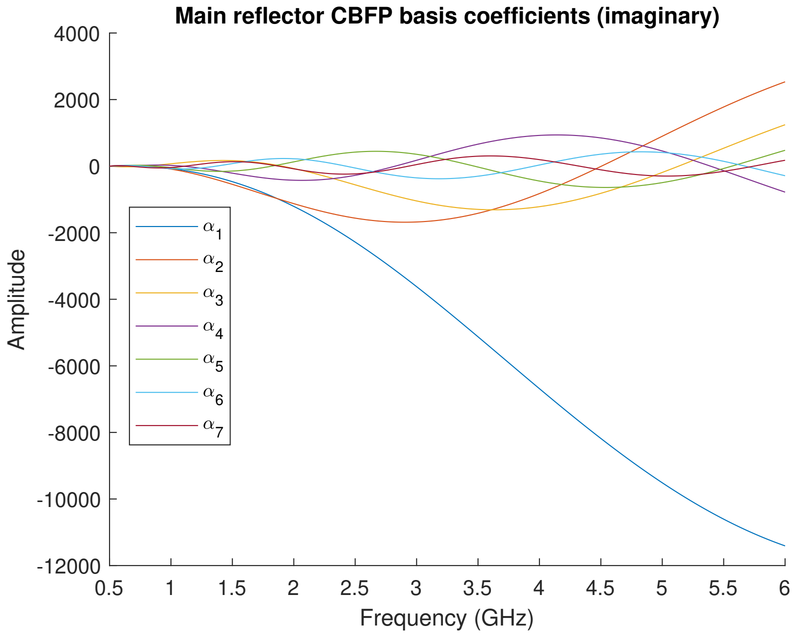

(b) Imaginary coefficient components

Figure 4.6: Method of least squares polynomial interpolants of coefficients of the first 7 $\mathbf{E}_{MR}$ in the 14 Basis Function set.(αMR_{1-7})

These results grant insight into the high efficiency of the SVD performed on geometric pattern data to generate the antenna physics based CBFP expansion, as the maximum amplitude of coefficient 7 in either the real or imaginary plane is less than $\frac{1}{50}^{th}$ of the first coefficient. Furthermore, it is evident that the first coefficients model the slowly varying main beam, and subsequent coefficients varying quicker to capture the sidelobes. This confirms the conclusion drawn in [30] and [22], that less than 15 basis coefficients are required to adequately model (−40 dB) the MeerKAT far-fields through SVD into numerical basis functions.

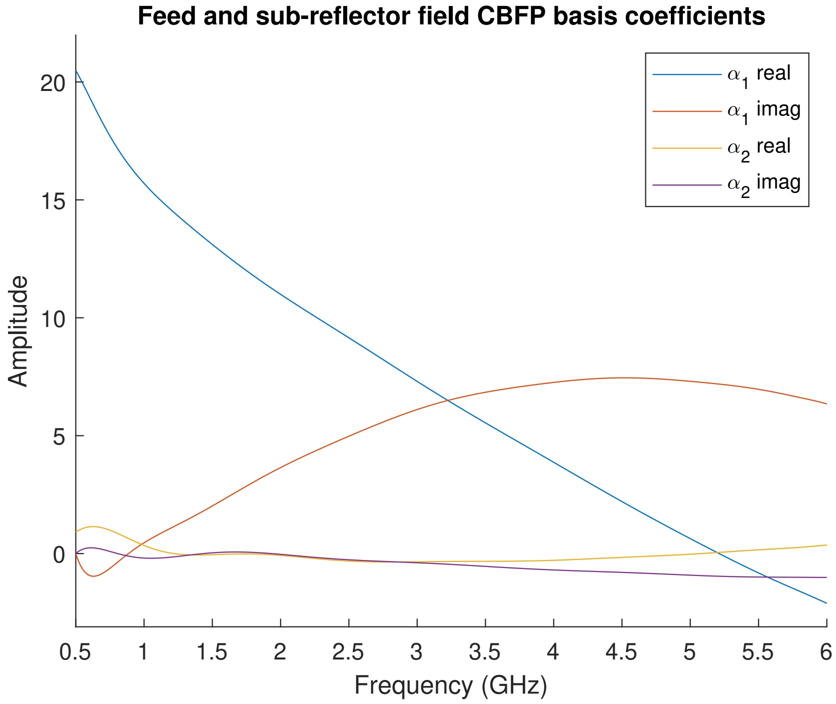

Figure 4.7: Method of least squares polynomial interpolants of complex coefficients 1 and 2 of the feed and sub-reflector field in the 7 Basis Function set. ($\mathbf{E}_{FSR:}\alpha_{1\&2}$)

Figure 4.7 illustrates the lower field intensity and increased pattern consistency across frequency of $\mathbf{E}_{FSR}$ in the global reference, resulting in a sharp attenuation of coefficient amplitudes, reducing the number of basis functions needed in order to generate an accurate field estimation.

The root mean square geometric far-field intensity error (RMSE) across the 0° to 4° θ range, chosen to capture the main lobe and first sidelobe at the lowest test frequency, for a single ϕ cut is used to evaluate the predicted far-field patterns. The error analysis procedure is constant throughout this thesis. First the equivalent error far-field is evaluated through subtraction of complex far-field data as:

$$\mathbf{E}_{error} = \mathbf{E}_{valid} - \mathbf{E}_{recon} \tag{4.3}$$

where $\mathbf{E}_{error}$ is the error field, $\mathbf{E}_{valid}$ is the validation field and $\mathbf{E}_{recon}$ is the reconstructed field from generated from the superposition of CBFP interpolants for E_{MR} and E_{FSR}.

RMSE is then calculated at each frequency as:

$$RMSE_{\phi=0^\circ}[f] = \sqrt{\frac{\sum_{\theta=\theta_{min}}^{\theta_{max}} |\mathbf{E}_{error}[\theta,\phi,f]|^2}{N_\theta[f]}} \tag{4.4}$$

where θ_{min} and θ_{max} are the respective upper and lower boundaries of θ for the beam under analysis at a single frequency, f, consisting of N_θ samples. Square brackets are used to indicate that they are discrete complex values obtained via CEM methods.

The absolute error between the aperture efficiency obtained for the test set, $\eta_{ap}[test]$, using E_{recon} and the validation set $\eta_{ap}[valid]$ is evaluated as

$$\eta_{ap}[error] = \eta_{ap}[valid] - \eta_{ap}[test] \tag{4.5}$$

in efficiency percentage points. The chromatic aberration ripple is qualitatively sinusoidal and is the primary goal of the modelling presented here, therefore, it is somewhat logical to present the absolute aperture efficiency error against the ripple amplitude. This approximate error boundary is synthesised by subtracting the average value of η_{ap}, $(mean(\eta_{ap}))$, from η_{ap} for every effective period of the chromatic aberration ripple:

$$10\,\%\text{ error envelope} = \frac{\eta_{ap}[valid] - mean(\eta_{ap}[valid])}{10}. \tag{4.6}$$

The error envelope is an approximate as it assumes constant mean aperture efficiency for a single chromatic aberration period, where there may be a small amplitude change. It also assumes a constant ripple period which is not always true, in actuality the ripple period may change slightly with frequency due to wavelength dependant diffraction behaviour [21].

Nevertheless, it serves as an understandable and appropriate error metric, especially for DR modelling with an ideal primary pattern. This is applied to all expositions of absolute aperture efficiency error where the ripple is acceptably sinusoidal.

A maximum aperture efficiency error of 7 % across the full bandwidth was recorded with the poorest accuracy for the CBFP model prediction around 4.7 GHz. A maximum RMSE of less than 4.24 $\mathrm{V\,m^{-1}}$ and a mean RMSE of 2 $\mathrm{V\,m^{-1}}$ was obtained with the polynomial interpolant prediction. The results are illustrated in Figure 4.8.

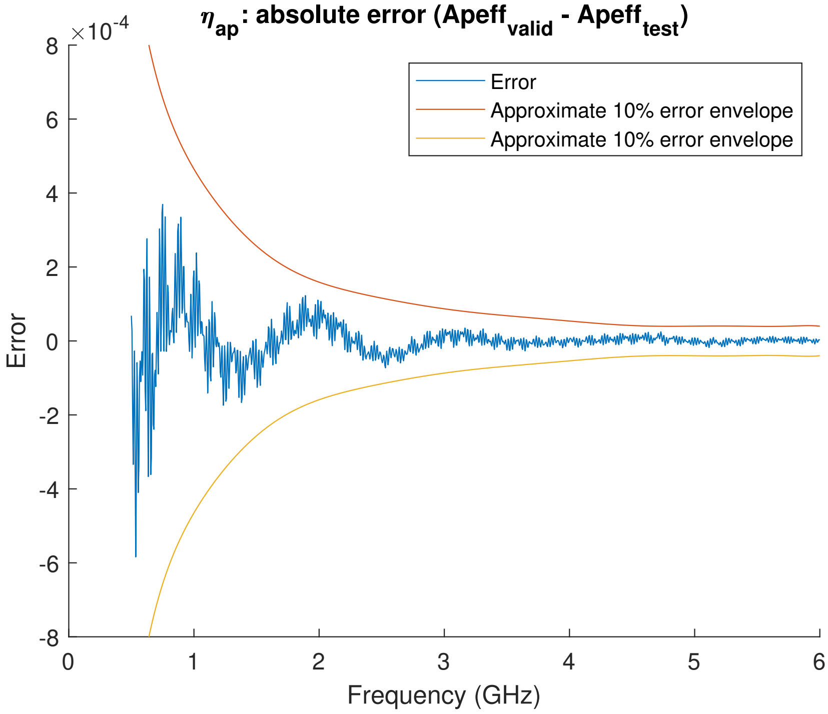

(a) Absolute aperture efficiency error $\eta_{ap}[error]$ vs. 10 % of chromatic aberration ripple amplitude in validation set.

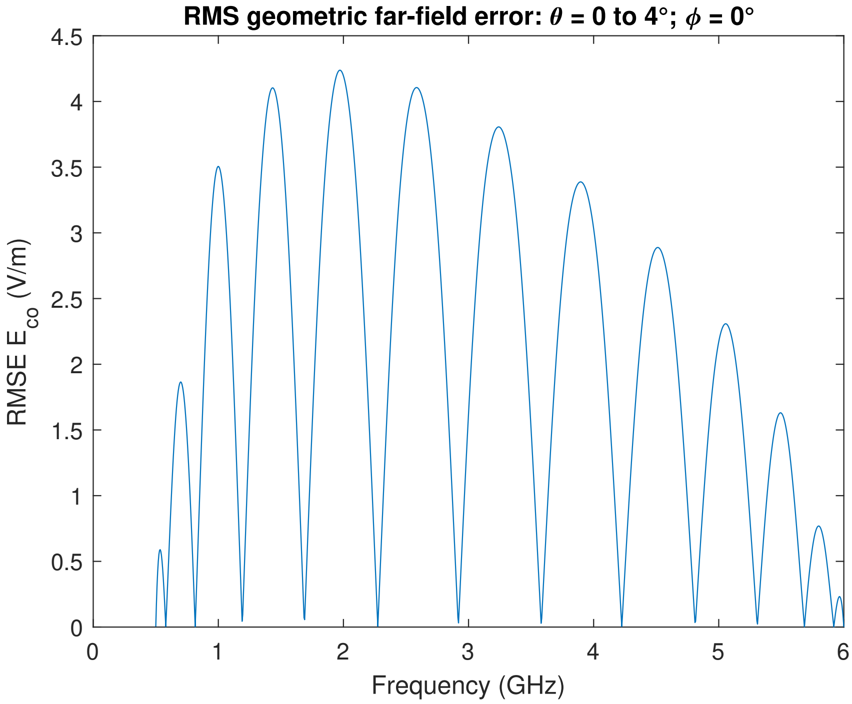

(b) Geometric far-field pattern error ($RMSE_{\phi=0°}[f]$)

Figure 4.8: Aperture efficiency error and RMSE of geometric far-field pattern magnitude for 14 sample polynomial CBFP model

The normalised far-field patterns for the worst case and mean RMSE are shown in Figure 4.9 to place the error in the context of the far-field pattern dynamic range.

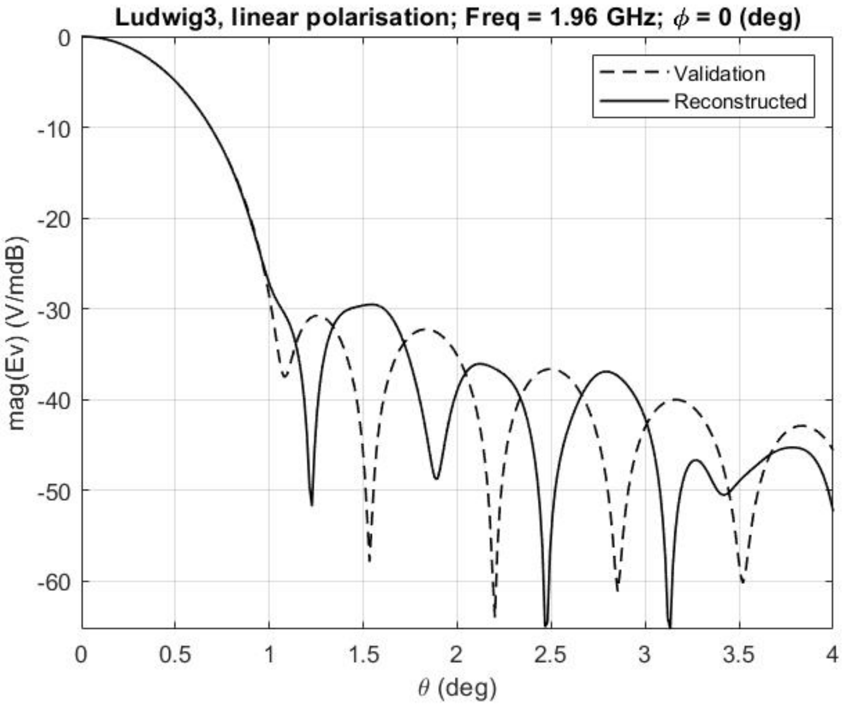

(a) Geometric error at 1.605 GHz (mean RMSE)

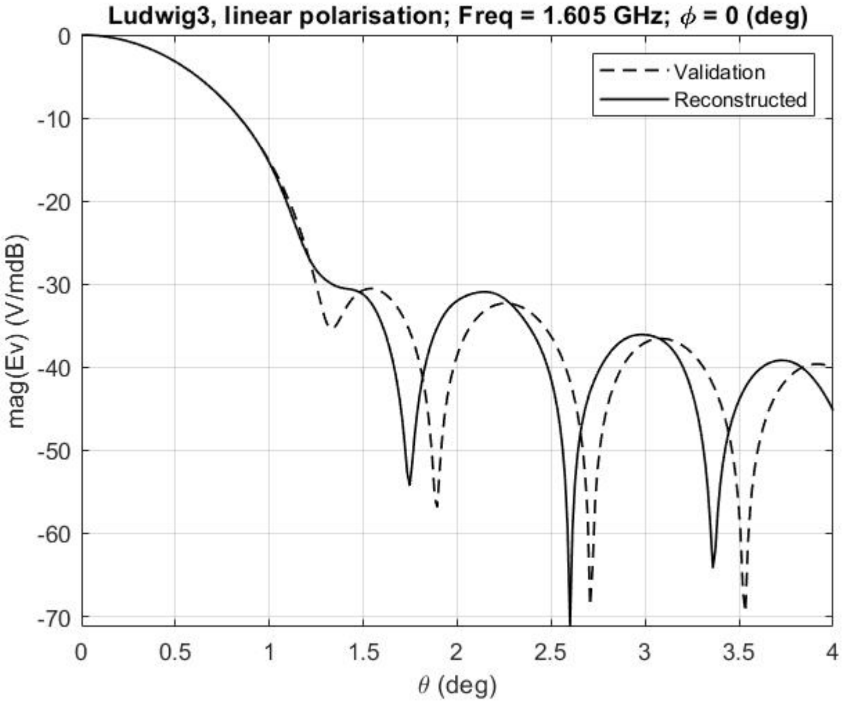

(b) Worst case geometric error at 1.96 GHz

Figure 4.9: Worst case and average RMSE of radiation pattern when interpolated using a polynomial least squares fit with 14 radial support samples

These magnitude patterns show that the CBFP superposition beam predictions for this example have a 27 dB dynamic range with error apparent in the first sidelobe. The weakness of a polynomial based interpolation model is that if the error is too high, it is difficult to add direct samples to the new model due its tendency to diverge at domain boundaries, therefore, the cost of underestimating sample density is high. For general DR systems a guideline of at least 14 radial samples in total is required such that the beam SVD performed to build the CBFP expansion is sufficient, with no less than 6 support samples per octave bandwidth. This is a robust buffer for polynomial based models to predict aperture efficiency when broader beam features are not of interest, however, as the number of samples increases, so too does the risk of over-fitting.

4.3.2. Simple Kriging model

An interpolation model utilising simple Kriging with a Matérn $(\frac{3}{2})$ covariance function [56] for interpolation required 26 radially spaced samples to converge to a comparable accuracy, 24 and 7 characteristic basis functions were used for $\mathbf{E}_{MR}$ & $\mathbf{E}_{FSR}$ respectively. VEXPA was performed on the first two radial samples in the set as before.

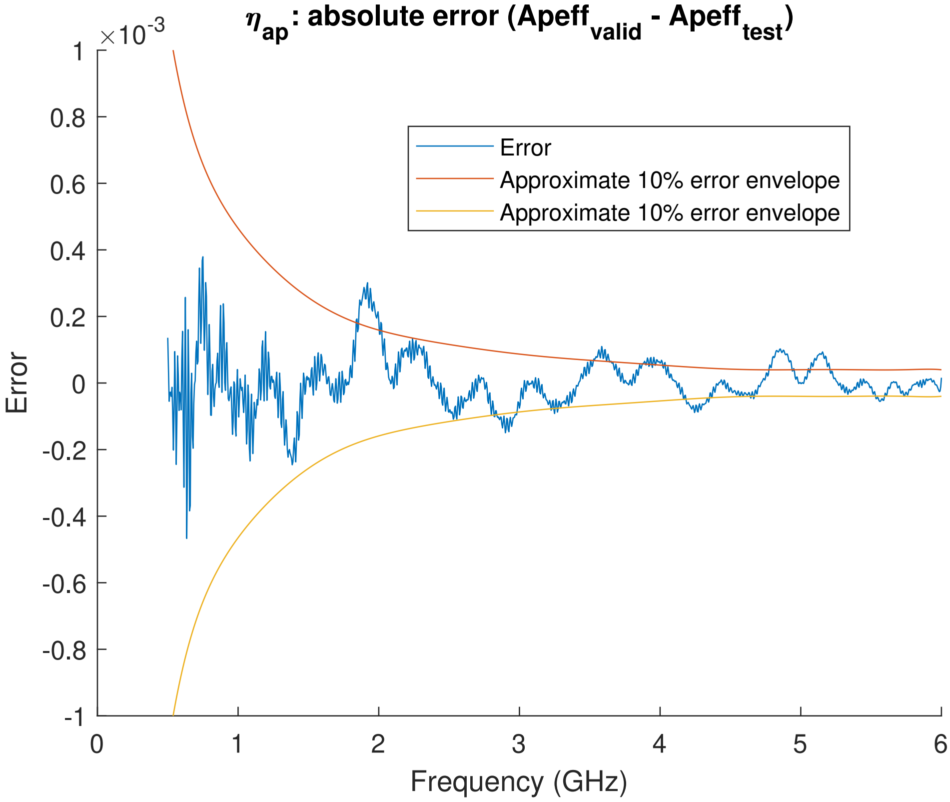

Figure 4.10: Absolute aperture efficiency error $\eta_{ap}[error]$ vs. 10 % of chromatic aberration ripple amplitude in validation set.

The Kriging model requires more samples to obtain an accurate prediction of aperture efficiency due to its equal balance between local and global uncertainty when compared to a polynomial least squares fit, which is more orientated towards function smoothness. As a result, the overall geometric accuracy and broadside beam accuracy increase at similar rates.

The increased number of support samples means there is more geometric data on which the CBFP can perform the SVD, resulting in improved beam prediction accuracy across the band with a factor 2 baseline improvement over the 14 sample test set for both the worst case RMSE of $1.9\,\mathrm{V\,m^{-1}}$ and the mean RMSE of $0.81\,\mathrm{V\,m^{-1}}$.

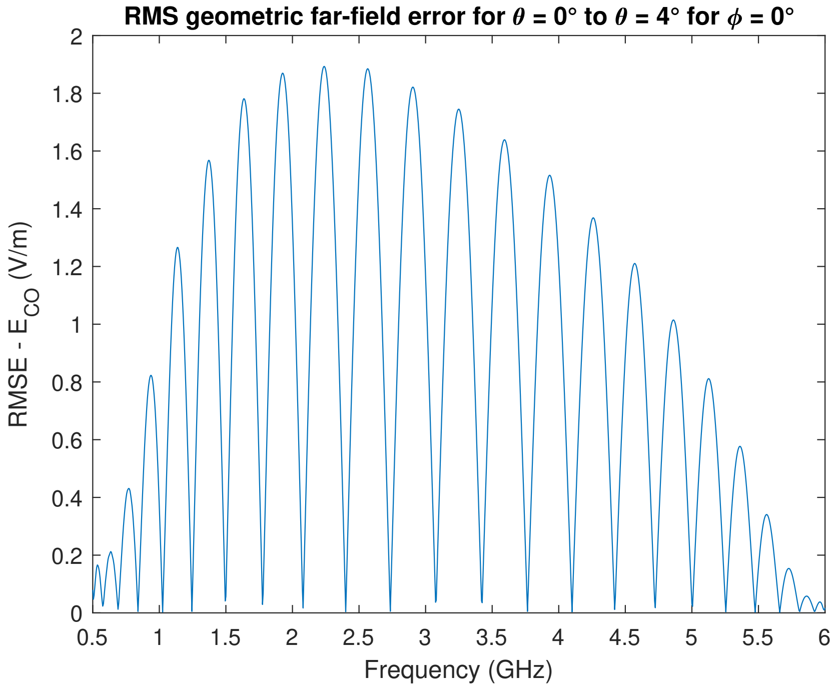

Figure 4.11: RMSE of geometric far-field pattern magnitude for 26 sample simple Kriging CBFP model showing strong correlation to sample density.

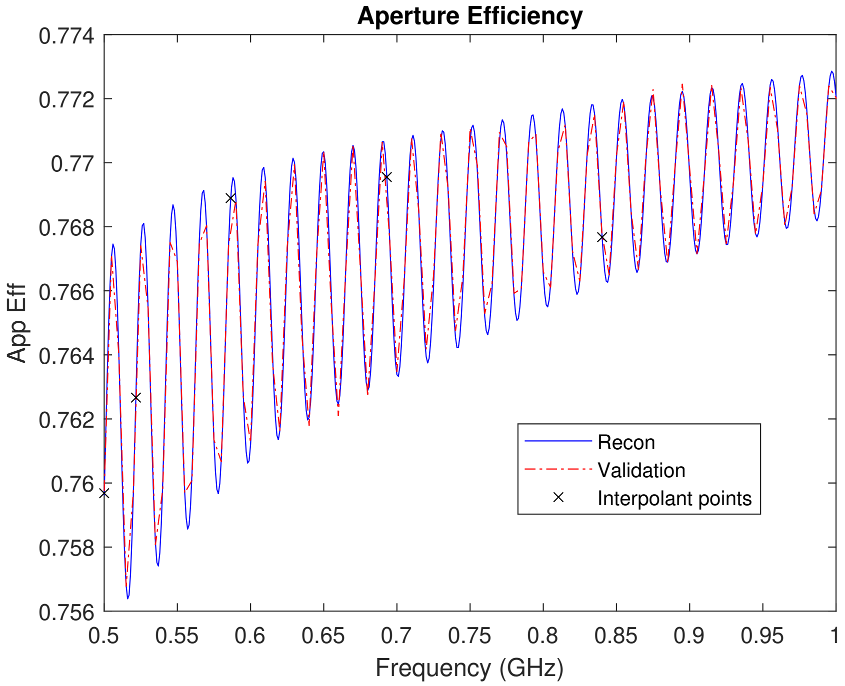

Figure 4.12: Aperture efficiency in the 0.5 GHz to 1 GHz region with higher sample density approximately $\frac{1}{8}^{th}$ of the Nyquist rate with $\eta_{ap}[error]$ of below 8 %.

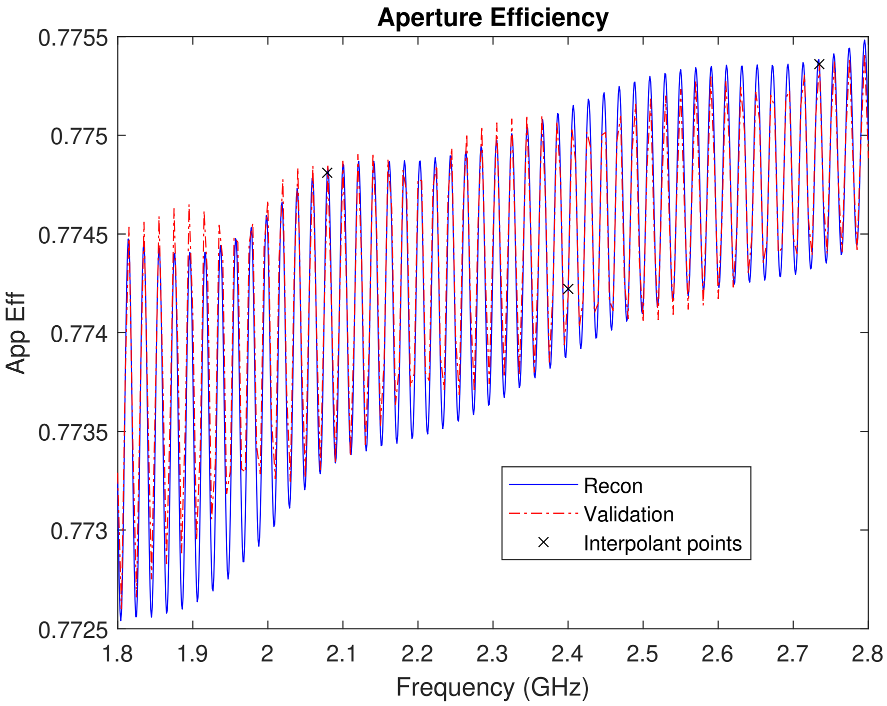

Figure 4.13: Aperture efficiency characterisation with 26 radial sample Kriging model with chromatic aberration ripple period of ≈20 MHz in band with worst case $\eta_{ap}[error]$ of ≈ 15 %.

The sample density holds strong influence over the aperture efficiency error in a particular frequency band, attributed to the local error minimising attempts of the Kriging interpolation for each CBFP coefficient.

The obtained geometric beam patterns had a larger dynamic range of accuracy, due to the increased SVD dimensions allowing for a 24 coefficient CBFP representation of the geometric far-field patterns. This allows for the allocation of more basis functions to capture sidelobes of the beam pattern, which vary faster over the geometric range.

It also results in stronger orthogonality between different frequency dependant geometric features, as more SVD training data allows each obtained singular value to converge closer to a true physical beam feature.

As a result, the predicted beams were accurate until far-out sidelobes, with a dynamic range of 40 dB. The worst and mean case RMSE beam predictions are illustrated in Figures 4.14 and 4.15. This suggests that error in predicted aperture efficiency is no longer tied to the ripple frequency, but rather the accuracy of the slow varying interpolants as postulated.

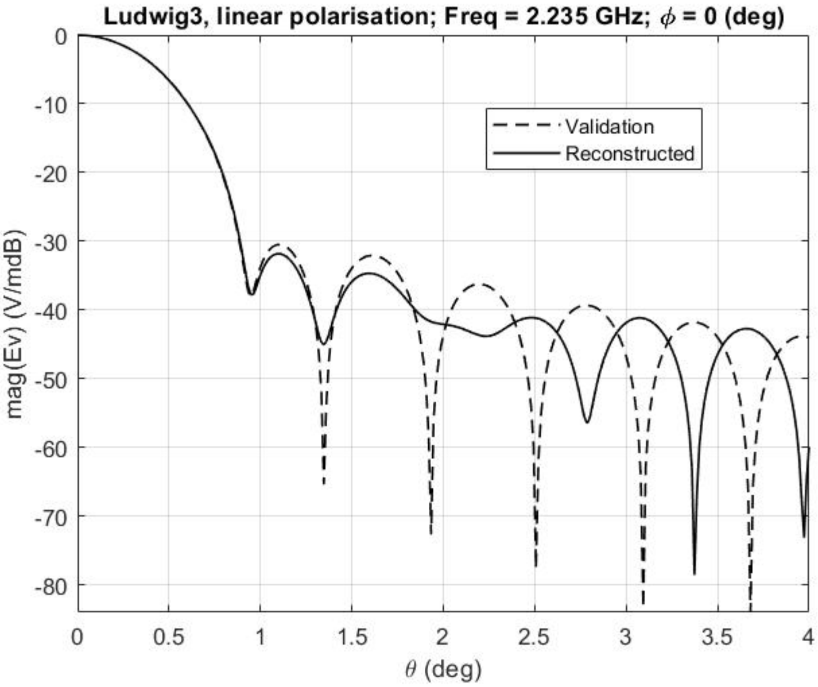

Figure 4.14: Worst case geometric far-field RMSE at 0.86 GHz, generated using 24 basis functions on a 26 radial support sample set.

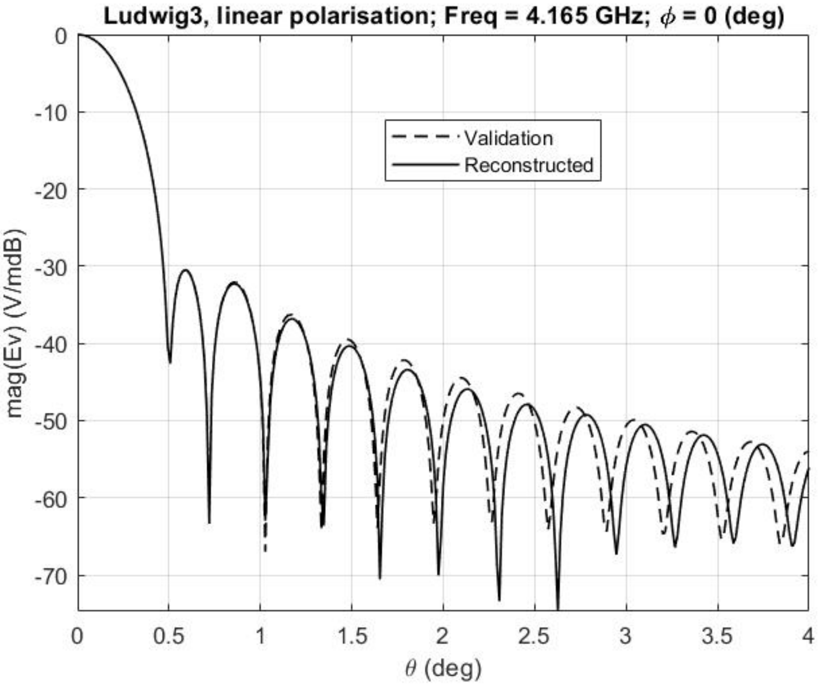

Figure 4.15: Mean geometric far-field RMSE case with 40 dB dynamic range, generated using 24 basis functions on a 26 radial support sample set.

Comparison between the test and validation patterns above illustrates the improved geometric accuracy obtainable with more support samples and basis functions, with even the worst RMSE case capturing the first sidelobe. Accurate geometric beam reconstruction with this pattern range is typically sought after in radio astronomy applications, giving an example of a suitable support sample set for an interpolant which meets interferometry requirements.

To illustrate the case of not enough sample data available for a Kriging model to successfully reduce uncertainty, the aperture efficiency generated using a simple Kriging interpolant without sufficient support samples for calibration is shown below for the 14 radial sample case from 0.5 GHz to 6 GHz:

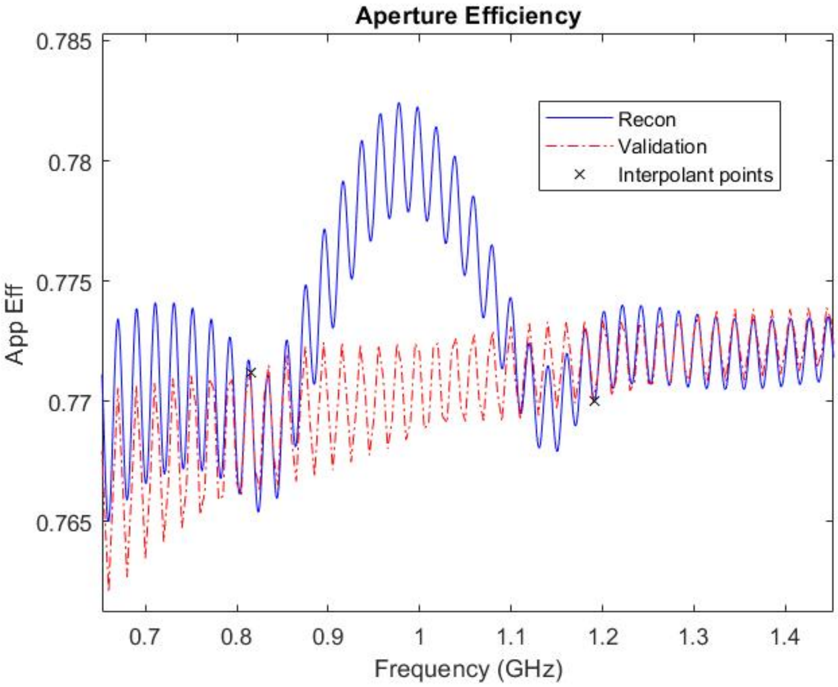

Figure 4.16: Aperture efficiency characterisation from Kriging model showing accurate capture of 20 MHz period ripple despite insufficient sample density for full CBFP convergence

A crucial element in the figure above is the correctly predicted chromatic aberration ripple period in zones where the aperture efficiency is not at the correct level. This confirms the source of the ripple is indeed interference between the main reflector field and components of feed radiation diffracted by the sub-reflector, which is intrinsically captured during superposition of the reconstructed MR and FSR fields. This suggests that capture of the ripple period has been successfully decoupled from the sampling rate.

4.3.3. Comparison between polynomial and Kriging model

To illustrate the differences between the polynomial and Kriging interpolation features, a 21 order polynomial model for the 26 radial sample set was synthesised. Geometric field error for the $\phi = 0°$ plane is again presented using root mean square error between the validation and predicted fields (RMSE), and aperture efficiency error is given in absolute efficiency percentage point difference:

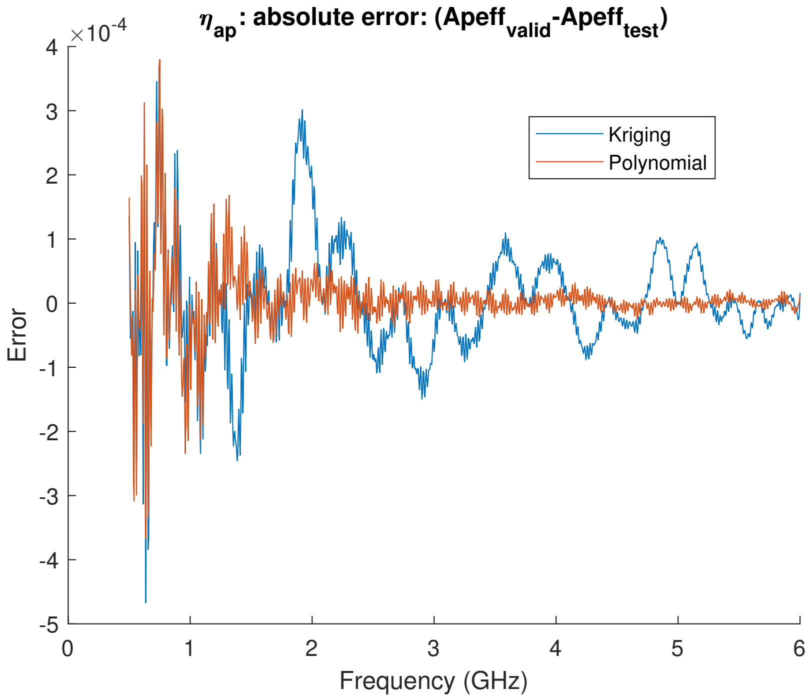

(a) Absolute aperture efficiency error: $\eta_{ap}[error]$

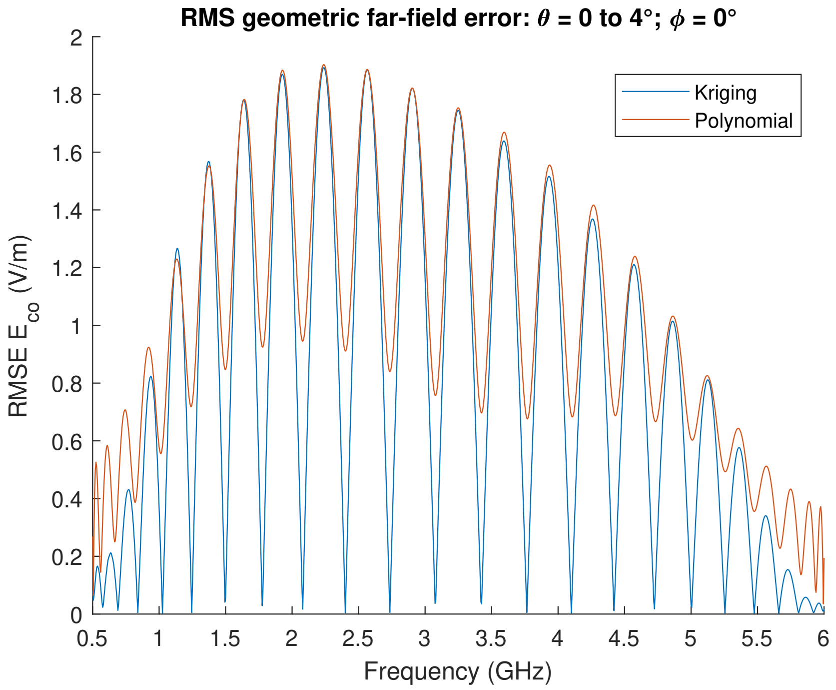

(b) RMS geometric far-field error

Figure 4.17: Error comparison between polynomial and simple Kriging interpolation models for 26 radial support samples.

Results here definitively show that the geometric far-field error is closely tied to the number of interpolant support samples for both interpolation schemes while aperture efficiency error is generally slower varying for the least squares polynomial fit. The error at known samples for the polynomial interpolant is attributed to the global smoothness priority of the polynomial fit when a degree of less than $N-1$ is used to fit N samples.

The degree of the polynomial used in this case had to be reduced to limit over-fitting. Evidence shown here suggests that a interpolant with a global smoothness allows for efficient prediction of aperture efficiency, at the expense of geometric far-field accuracy. Error cases for the polynomial model illustrate the onset of over-fitting in the beam's CBFP expansion:

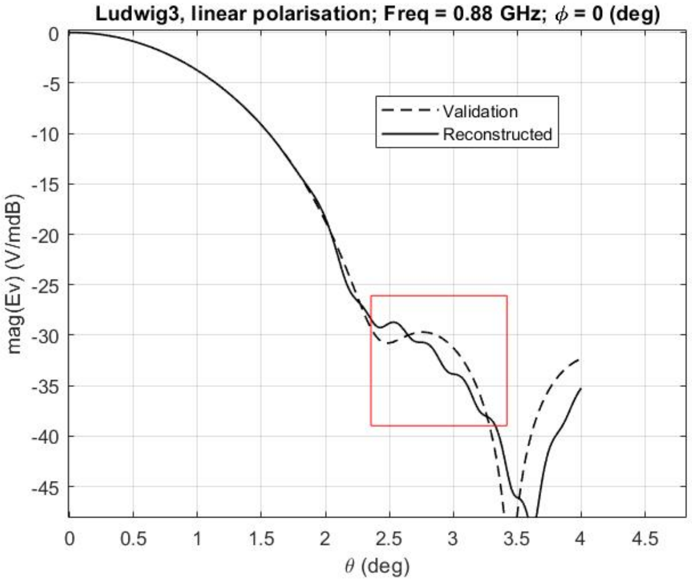

(a) Oscillatory beam due to over-fitting

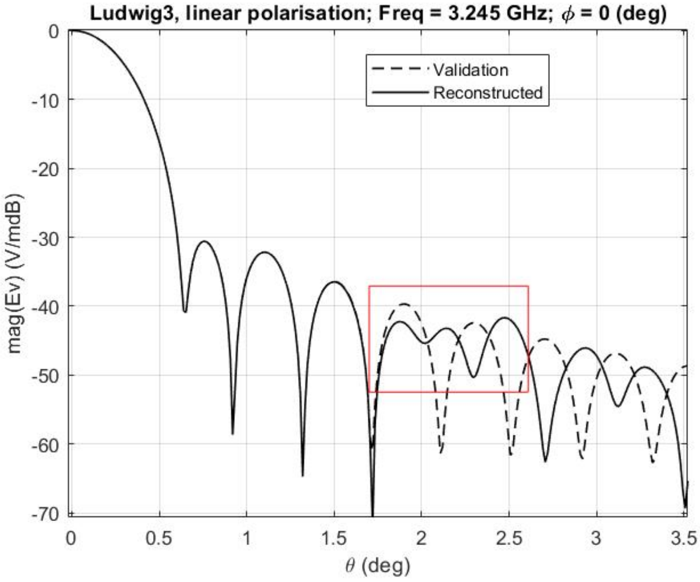

(b) Oscillatory beam due to over-fitting

Figure 4.18: Effect of additional sidelobes and non-physical variation caused by over-fit in the polynomial CBFP interpolants

The rapid variation across θ for the far-field patterns above show the early signs of over-fitting across the basis coefficient sample set. This happens when the least squares method incorrectly assumes a polynomial of a degree too high for the sample fit. A possible contributing factor is the higher order coefficient patterns having rapid oscillations to capture the many sidelobes in the higher frequency beams thus, influencing the polynomial degree used to fit the data. The error is observed as either spurious sidelobes or a ripple across a smooth broad beam lobe which worsens as the degree is increased.

4.3.4. Overall observations

The results conclusively show that variations due to interference of diffracted rays in clear aperture offset geometry are accurately captured by the CBFP superposition method. Furthermore, it is evident that required sample density is linked to solely to the variations of the much slower varying MR and FSR basis coefficients as the ripple frequency is perfectly captured for an effective sample rate of 35 times below the Nyquist threshold.

More samples are typically needed for a Kriging model to capture the aperture efficiency due to the tendency of the model to balance uncertainty evenly across the sample space, however, once converged the increase in CBFP training data is effectively used to improve geometric accuracy able to predict the main beam and first sidelobe of the radiation pattern. Polynomial models allow for an accurate aperture efficiency to be calculated with very few samples, however, they are more susceptible to over-fitting inhibiting broader beam predictions for cases with more than 20 samples.

Throughout the results for both interpolation methods there is a clear indication of vast frequency resolution improvements compared to the direct DR field approach in [22]. The vast improvement in computational efficiency due to tenfold reduction in sample density requirements renders the extra computational expense of projecting of the FSR field to the global co-ordinate system negligible.

4.4. Symmetrical Cassegrain antenna

The CBFP superposition approach will now be applied to an electrically small symmetrical cassegrain antenna in the UHF band (0.3 GHz to 3 GHz) to show it is effective for symmetrical geometry, where blockage contributes to much larger aperture efficiency ripples. Blockage also leads to the formation of harmonic standing wave effects, which are not captured in the PO+PTD modelling shown here. Field error as a function of the number of basis functions used for both interpolated fields is investigated in order to draw robust recommendations regarding sample density and basis set limits.

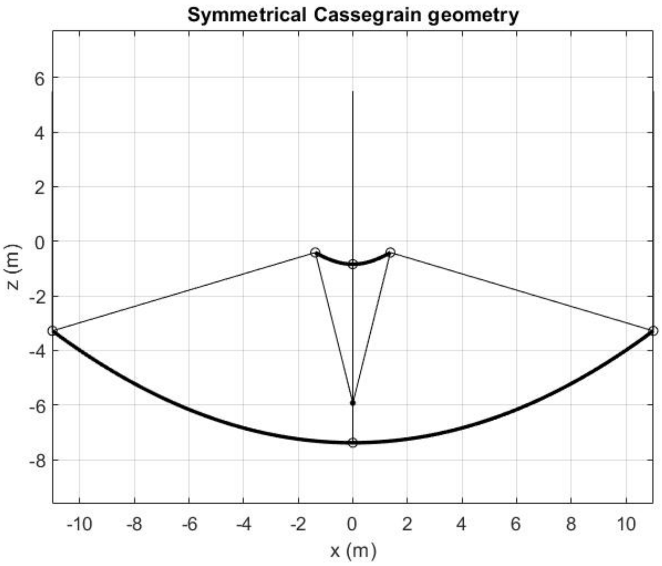

Figure 4.19: Symmetry plane cut of symmetrical Cassegrain antenna test geometry

The antenna features a symmetrical paraboloid main reflector and a hyperboloidal sub-reflector and is a classical example of a Cassegrain antenna for satellite communication [5]. This characterisation varies the electrical size of the main reflector from 22λ to 220λ and the sub-reflector from 2.75λ to 27.5λ. PO+PTD approximations were used to calculate the far-field results with a $-12\,\mathrm{dB}$ Gaussian beam taper for θ_e of 14°, chosen to evaluate the model for a symmetrical case with a large feed antenna.

4.4.1. Polynomial model

9 radial samples provided sufficient coefficient convergence for ripple evaluation with a worst case aperture efficiency error of 24 % on largest low frequency ripple. Interpolation was performed with the method of least squares on 9 MR and 7 FSR basis functions.

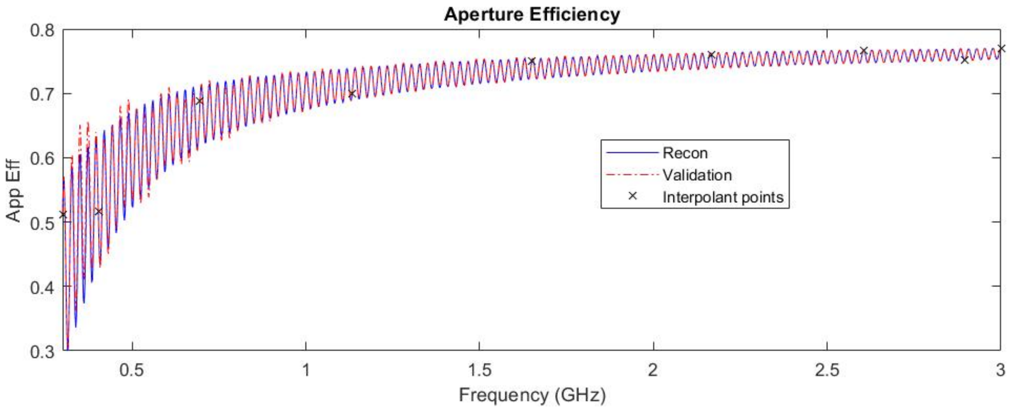

Figure 4.20: Aperture efficiency prediction: 9 sample polynomial model representing $\approx \frac{1}{12}^{th}$ of the Nyquist rate for chromatic aberration ripple period of $\approx 24\,\mathrm{MHz}$.

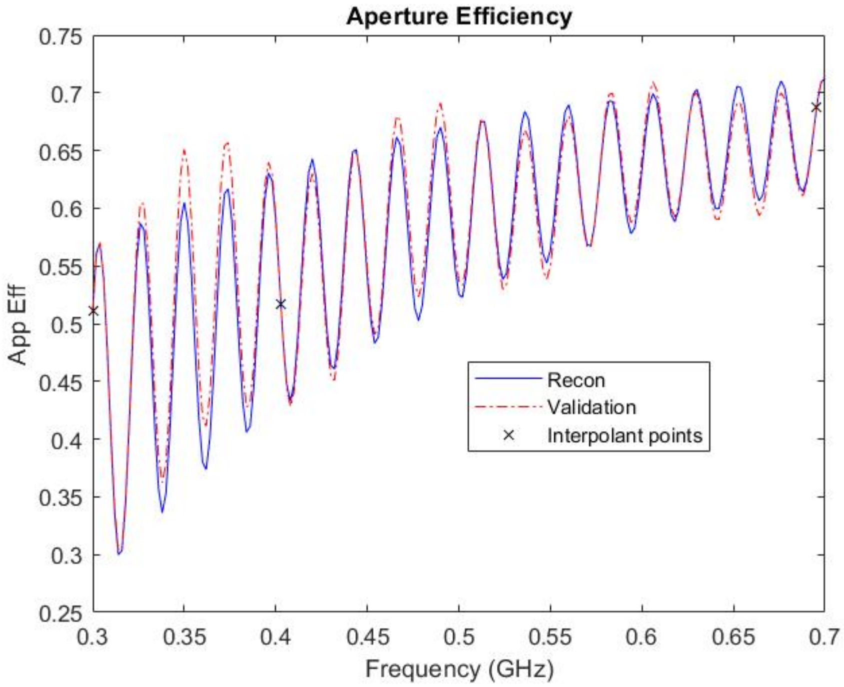

(a) Band with worst case $\eta_{ap}[error]$ of $\approx 24\,\%$

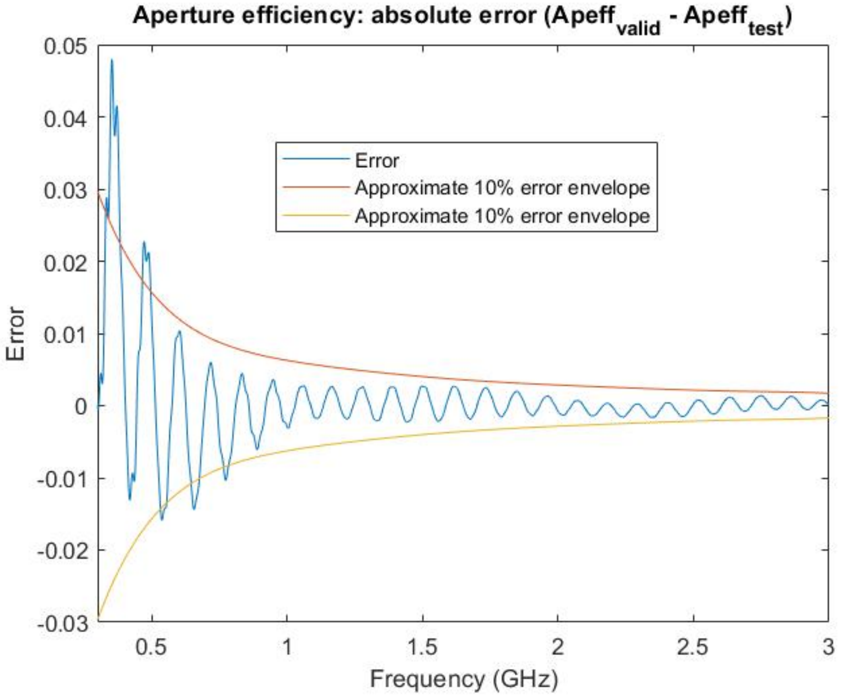

(b) $\eta_{ap}[error]$ vs. $10\,\%$ of chromatic aberration ripple amplitude in validation set.

Figure 4.21: Aperture efficiency predictions with reconstructed $\mathbf{E}_{MR}\&\mathbf{E}_{FSR}$ CBFP interpolants for 9 sample polynomial model.

Pertinent above is that the frequency of the oscillation is perfectly captured across the entire band with only amplitude errors, illustrating again that this method successfully isolates the CBFP into individual slowly varying far-field pattern dimensions across frequency which when added, regenerate the fast ripple. The predicted aperture efficiency error is approximately 10 % of the chromatic aberration amplitude. The small amount of training data for the CBFP expansion limits the θ range of accurate beam predictions. The RMS geometric error and a mean RMSE beam comparison is shown below:

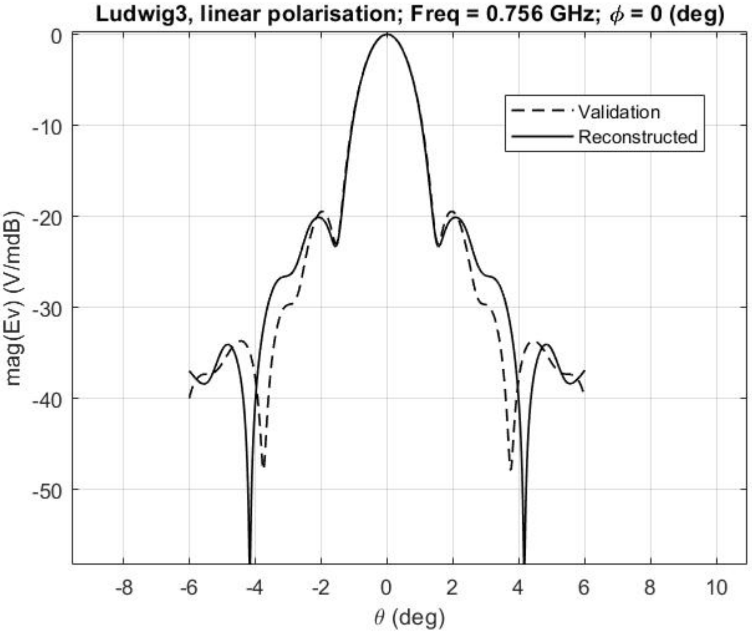

(a) Beam pattern: mean RMSE = $2.65\,\mathrm{V\,m^{-1}}$

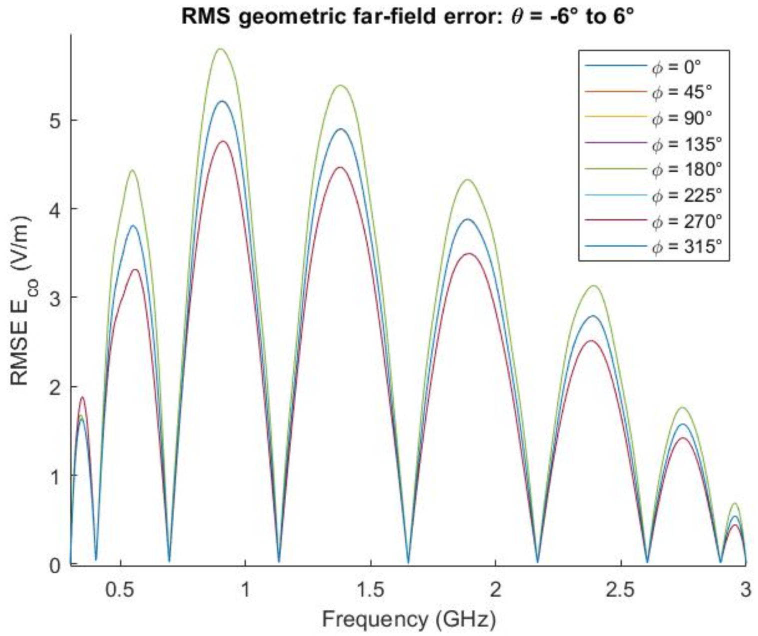

(b) Beam RMSE for principle ϕ cuts

Figure 4.22: Geometric beam predictions with reconstructed $\mathbf{E_{MR}}\&\mathbf{E}_{FSR}$ CBFP interpolants for 9 sample polynomial model.

The predicted and validation beams separate outside the −2° to 2° range, however the dynamic range of the predicted main beam is always captured with an error of below 1 %. The geometric error for a full 360° ϕ range shows clustering at the principle cuts of 0°, 45°

and 90° for each quadrant in the azimuth plane of the antenna, illustrating the method captures all polarisation and field symmetry across ϕ. 9 support samples presents a low risk of over-fitting, making the polynomial least squares fit interpolation model suitable for rapid broadband aperture efficiency analysis. More samples are needed if the geometric beam pattern is of interest. An experiment was conducted to quantify the error connected to the number of basis functions used to represent the far-field component due to the feed and sub-reflector. All 9 possible basis functions were used to represent the MR field:

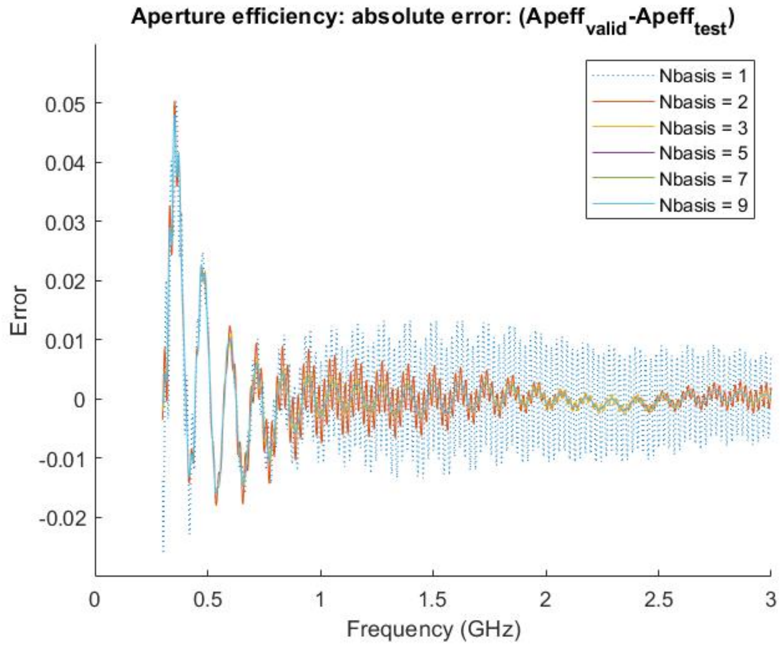

(a) Aperture efficiency prediction error $\eta_{ap}[error]$

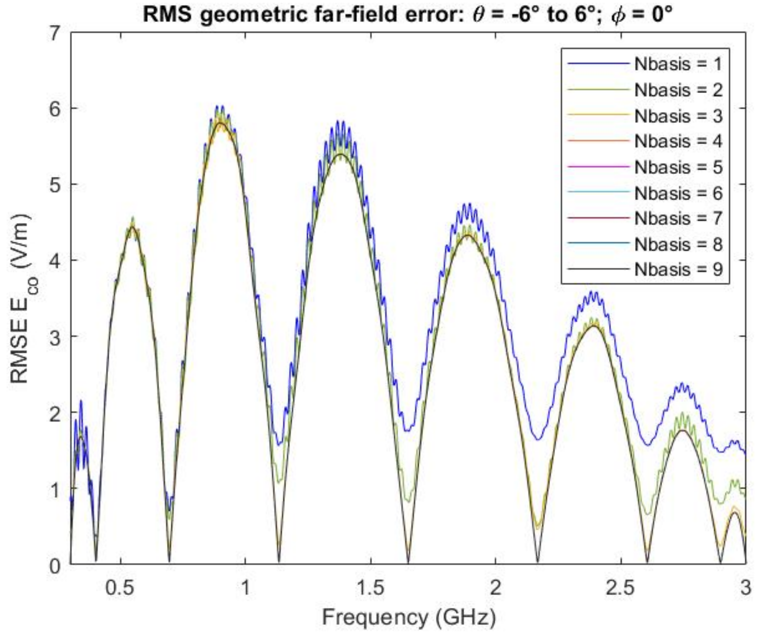

(b) Geometric far-field RMSE

Figure 4.23: Influence of number of basis functions kept after $\mathbf{E}_{FSR}$ SVD on DR far-field prediction accuracy.

These results show that 5 or more basis functions are sufficient to represent the FSR pattern due to its gradual intensity changes, with negligible error improvement when using additional coefficients for this case. At least 7 basis functions are recommended for an unknown antenna to ensure the field is accurately decomposed for cases of larger variation. Inspection of the SVD spectrum, τ of E_{FSR} shown in Figure 4.24, defined as

$$\tau = \frac{SV_{min}}{SV_{max}} \tag{4.7}$$

where SV refers to singular values created during CBFP generation and min and max refer to the most and least significant value respectively, confirms this for the 9 radial sample case with the spectrum value being below 10^{-4} for 6 or more basis functions showing that the significant pattern features in the direct field data have been captured by this point, with the least significant singular value being 10^4 times smaller than the fundamental:

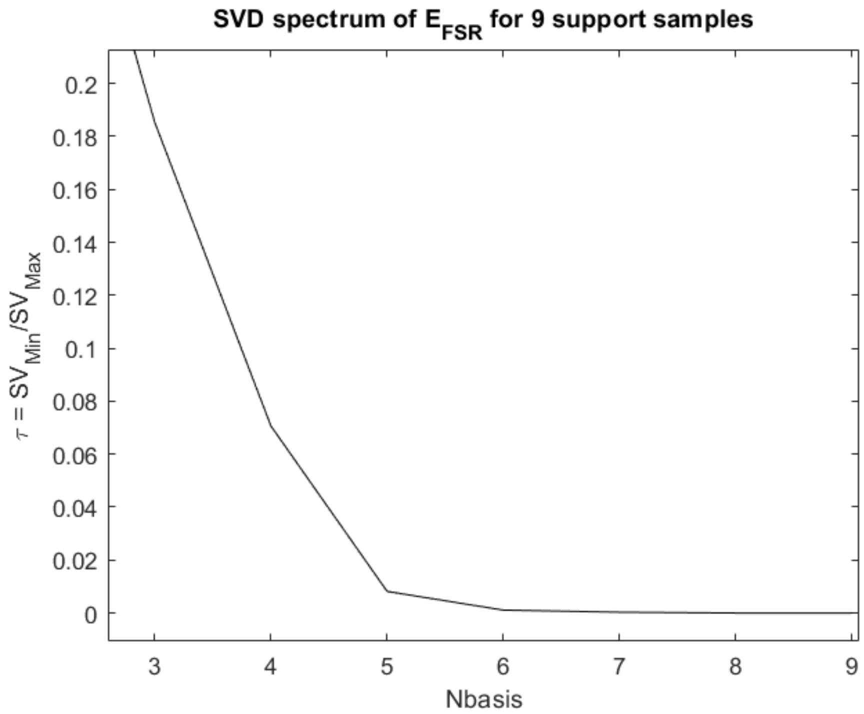

Figure 4.24: SVD spectrum of the CBFP used to model E_{FSR} indicating that 7 basis functions should be sufficient to capture typical Feed and sub-reflector field contributions.

4.4.2. Simple Kriging model

A simple Kriging interpolation model again using the Matérn $(\frac{3}{2})$ covariance function [56] was setup for characterisation. 19 linearly spaced samples at intervals of 150 MHz were used to characterise the model. The VEXPA phase normalisation samples at 323 MHz and 367 MHz corresponding to a 1 MHz grid with $\sigma = 67$ & $\rho = 23$ used for this case were placed at the lower end of the bandwidth to reduce prediction error in that region.

VEXPA samples should be chosen such that they contribute to uncertainty reduction in the interpolant, while not being so large that VEXPA is unable to extract the correct normalisation shifts. (see Figure 3.6) The example above serves as a conservative estimate in this regard.

This dual reflector exhibits an aperture efficiency ripple with an average period of 24 MHz. A phase normalisation shift of 18.95 m and 6.07 m was calculated for $\mathbf{E}_{MR}$ and $\mathbf{E}_{FSR}$ respectively.

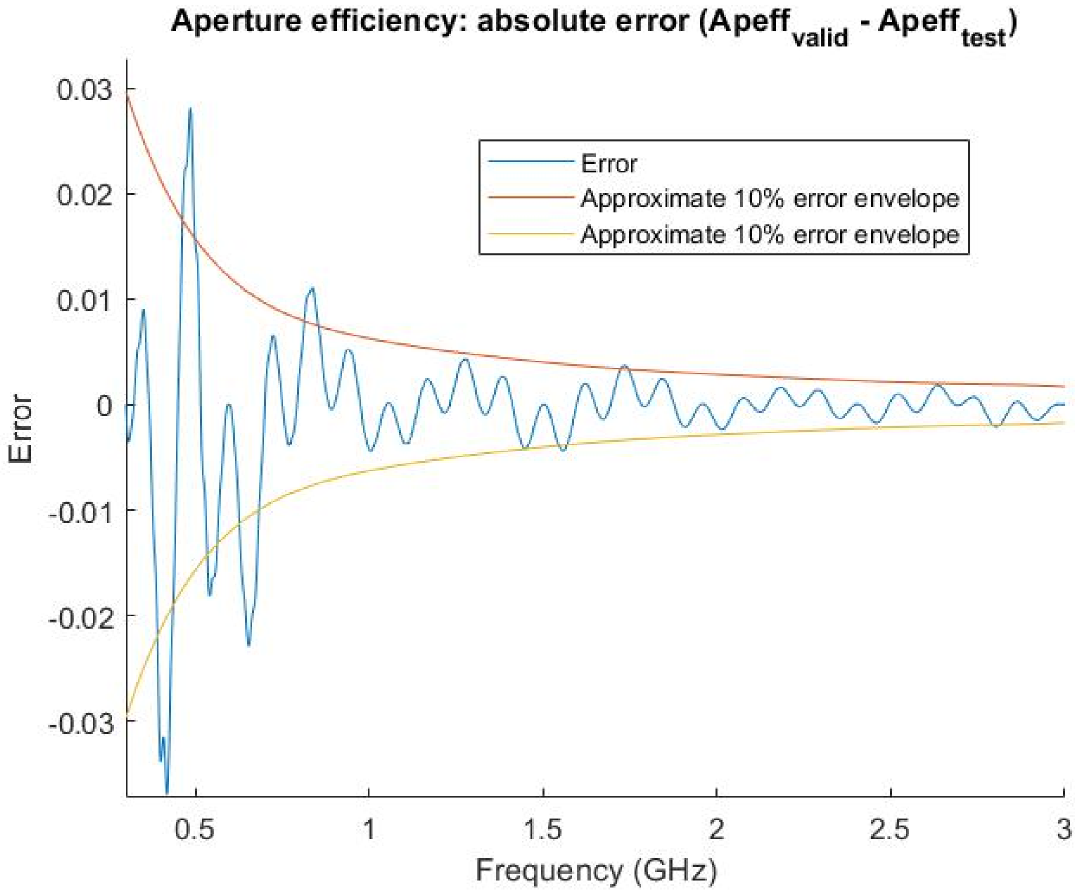

Figure 4.25: Aperture efficiency characterisation with 21 sample Kriging model with chromatic aberration ripple period of approximately 24 MHz in band with worst case $\eta_{ap}[error]$ of $\approx 15\,\%$.

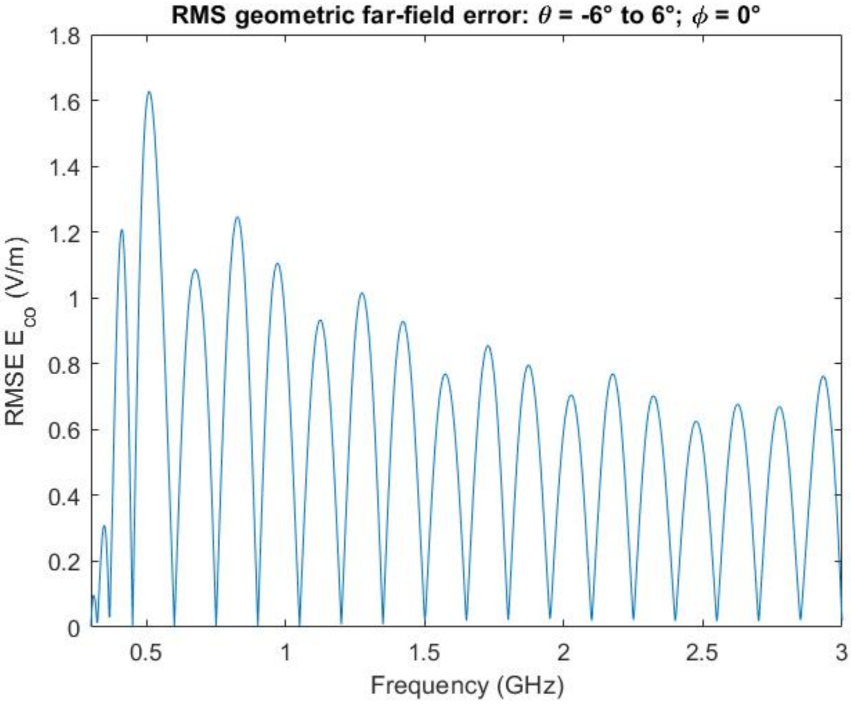

Figure 4.26: Improved Geometric far-field RMSE accuracy with 21 sample Kriging model

All 21 generated basis functions were included in the generation of the main reflector field and 7 basis functions were used to generate the FSR field.

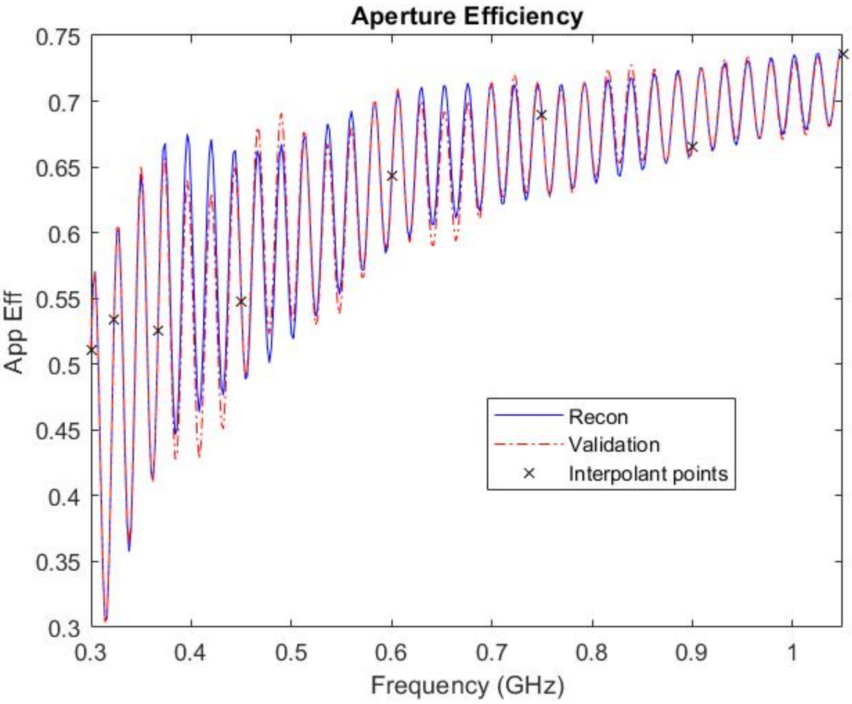

Figure 4.27: Band with maximum aperture efficiency prediction error of $\approx 20\,\%$ on 24 MHz period ripple

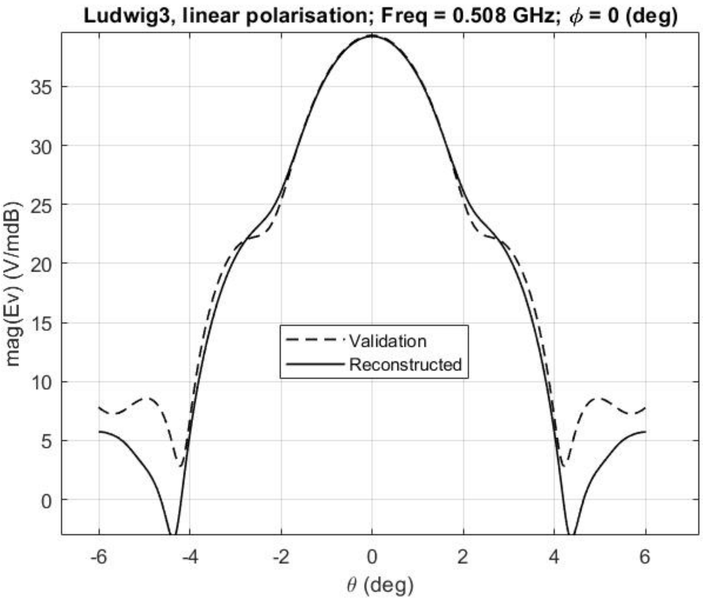

Figure 4.28: Worst RMSE case radiation pattern with accurate geometric beam prediction for $\theta = -2°$ to $2°$.

Geometrically the results were also good with a worst case 30 dB dynamic range of accuracy to 0.1 dB recorded across the band, with a worst case error of approximately 0.1 dB at broadside for the predicted beams around 0.5 GHz.

At least 8 samples per octave bandwidth is recommended to ensure an acceptable far-field accuracy, a robust advantage of the Kriging model is that the user can simply place additional samples in regions with anomalies to improve the reliability of the model at no detriment to the interpolation.

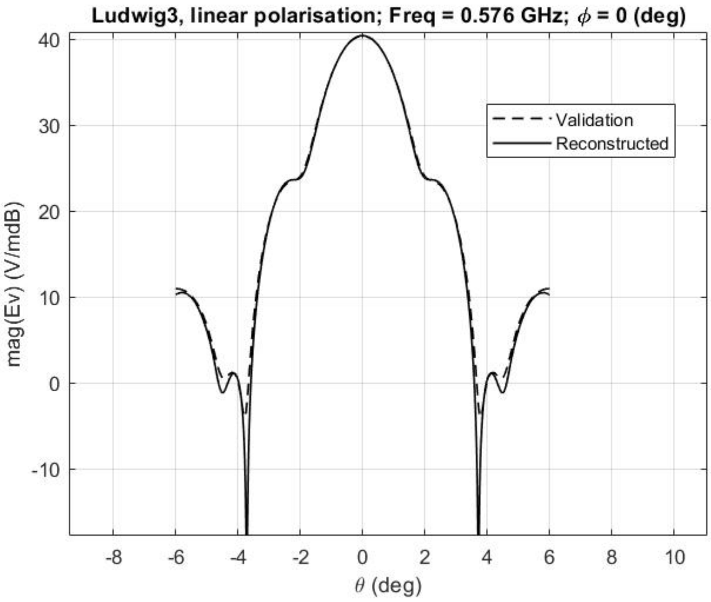

Figure 4.29: Geometric beam reconstruction for mean RMSE error of $\approx 0.58\,\mathrm{V\,m^{-1}}$ with $P_{rad} = \frac{2\pi}{\eta}$ and 40 dB accurate dynamic range.

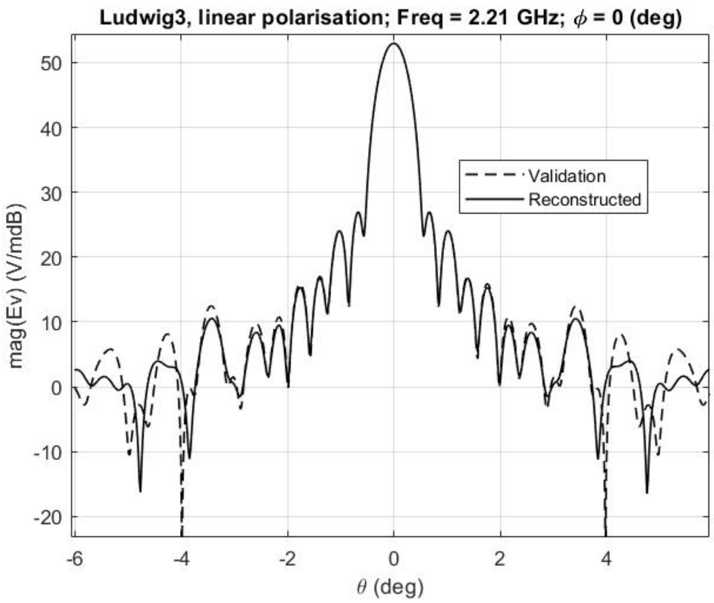

Figure 4.30: Geometric beam reconstruction for mean RMSE error of $\approx 0.58\,\mathrm{V\,m^{-1}}$ with $P_{rad} = \frac{2\pi}{\eta}$ and 40 dB accurate dynamic range.

Using more basis functions increases the geometric range of accuracy in the field predictions, as the SVD has more training data on which to orthogonalise features, as shown above in Figure **??** for beams in the upper and bottom corner of the bandwidth.

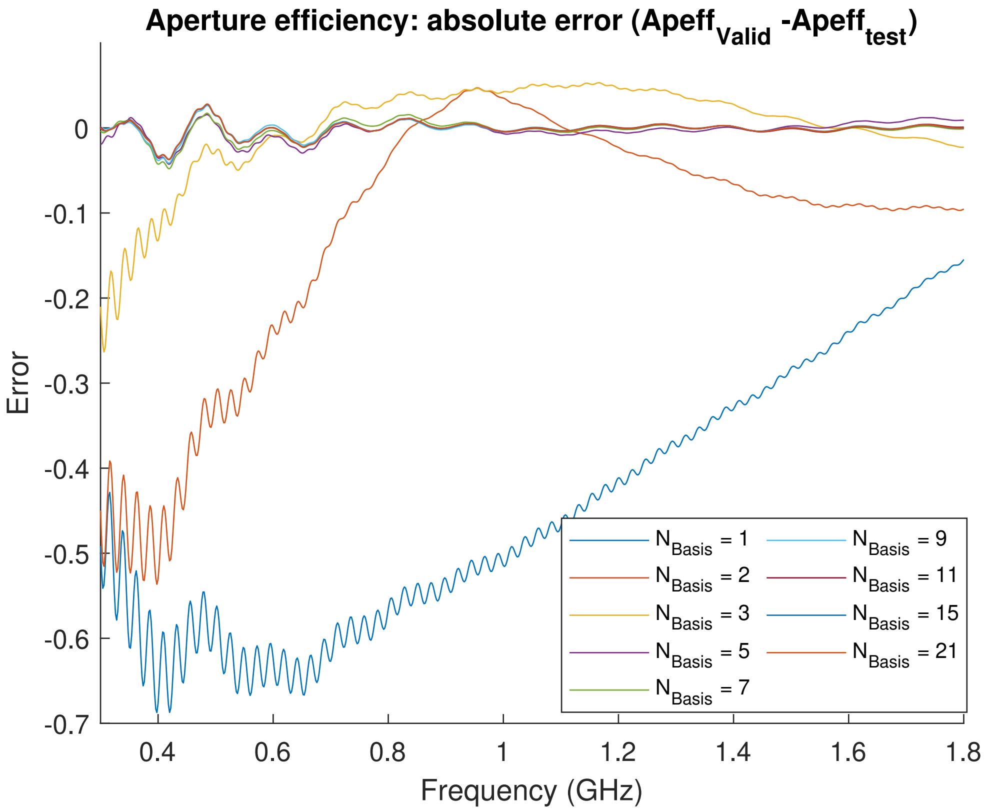

Figure 4.31: Absolute aperture efficiency prediction error attributed to number of basis functions ($\alpha_{1-N}MR$) for 21 sample Kriging model converging after $\approx$ 7 basis functions.

The main reflector is the largest radiating aperture in the system meaning it makes the largest contribution to $\mathbf{E}_{DR}$ intensity across the band. To ascertain how many basis functions available for $\mathbf{E}_{MR}$ samples should be retained during CBFP reconstruction of $\mathbf{E}_{DR}$ to obtain desired accuracy when many frequency samples are available. Aperture efficiency and geometric far-field error for this DR was evaluated while varying the number of $\mathbf{E}_{MR}$ basis functions kept after the SVD was performed on all 21 beam patterns in Figures 4.32 and 4.32.

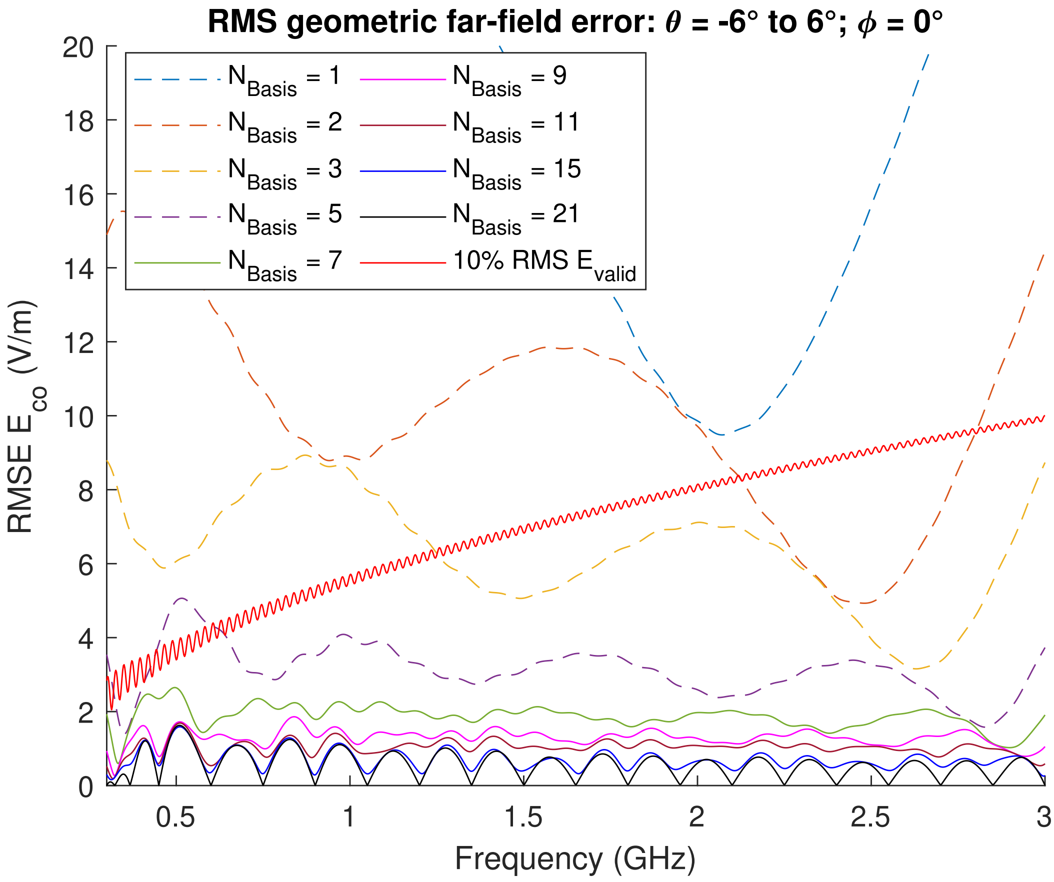

Figure 4.32: Geometric far-field RMSE attributed to number of basis functions ($\alpha_{1-N}MR$) for 21 sample Kriging model vs. 10 % $\mathbf{E}_{DR}$ RMS.

The results above indicate that more than five basis functions are required to model geometric ranges of the beam with error less than 10 % of $\mathbf{E}_{DR}$ RMS intensity. In general for wideband characterisation the main beam and the first sidelobe should be accurate, with some error in the later sidelobes allowed, provided there are no high amplitude spikes. The aperture efficiency error converges to an acceptable level for this case after 15 MR basis functions are used.

It is recommended that at least 15 MR basis functions are kept to model $\mathbf{E}_{MR}$ after the CBFP SVD for test sets with enough available beam data.

4.4.3. Selection criteria for number of significant basis functions

For antenna cases where a high number of samples across frequency are required/or available, higher order coefficients of the basis function may add unecessary storage and processing expense due to the storage of additional coefficients and corresponding numerical basis functions which do not make valuable contributions to accuracy. A robust selection criteria based on the relative level of significant basis coefficients is given below, such that only significant coefficients are included for wideband simulations with large amounts of support data. Consider the coefficients for the 21 support sample case above:

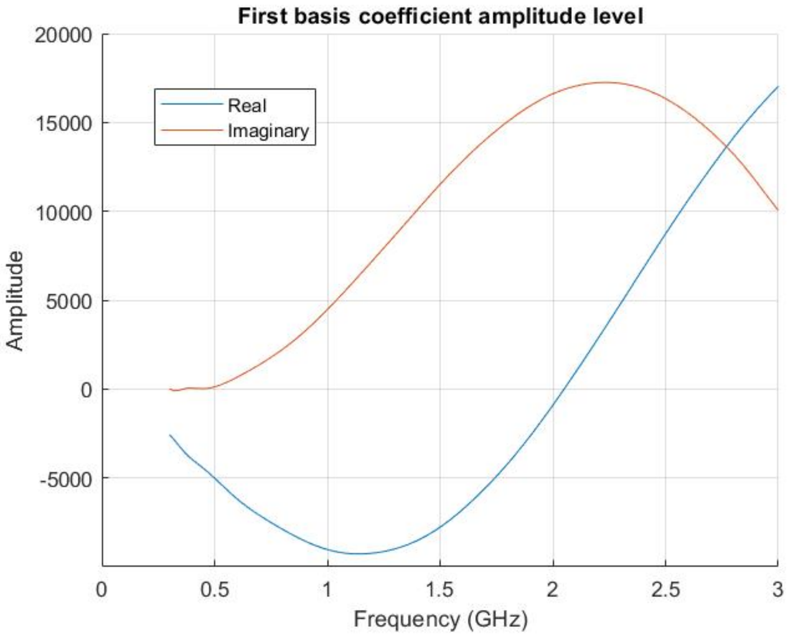

Figure 4.33: Amplitude level of most significant basis function

It is clear in Figure 4.33 that the real and imaginary component of the first coefficient representing the main reflector field have equal maximum amplitudes at approximately 17000 for this antenna.

The maximum amplitude for coefficient 9 of the MR expansion is approximately 200, with common amplitude envelopes for the real and imaginary part of all coefficients visible in Figure 4.34. This gives a 10^2 separation between the maximum of coefficient 1 and 9. The field error obtained for this case suggests that this dynamic range is sufficient for modelling of the aperture efficiency and first lobes of the geometric beam, strongly correlating to the accuracy results shown for the MeerKAT in [22] and [30].

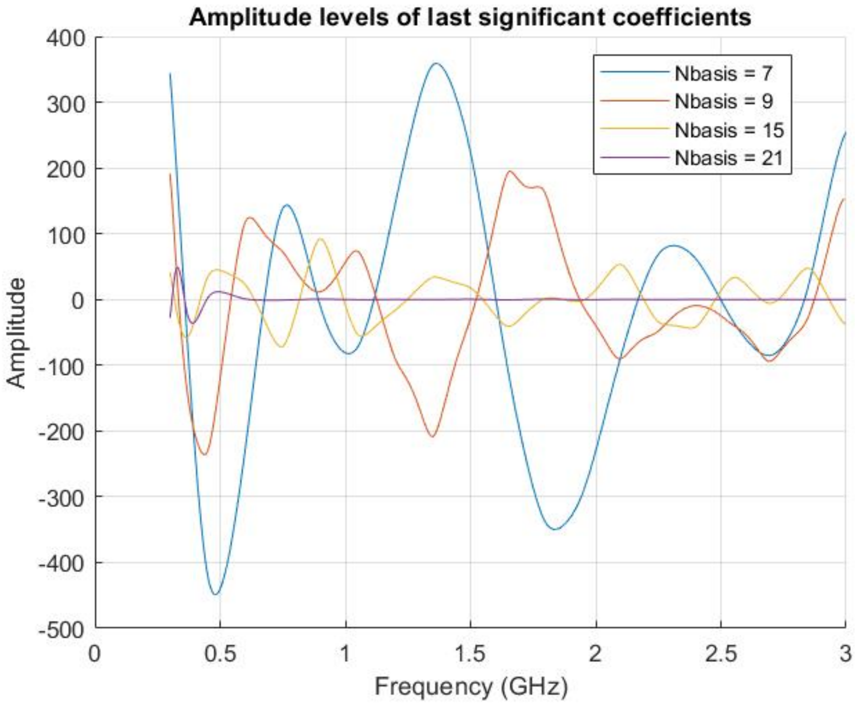

(a) Real coefficient component levels

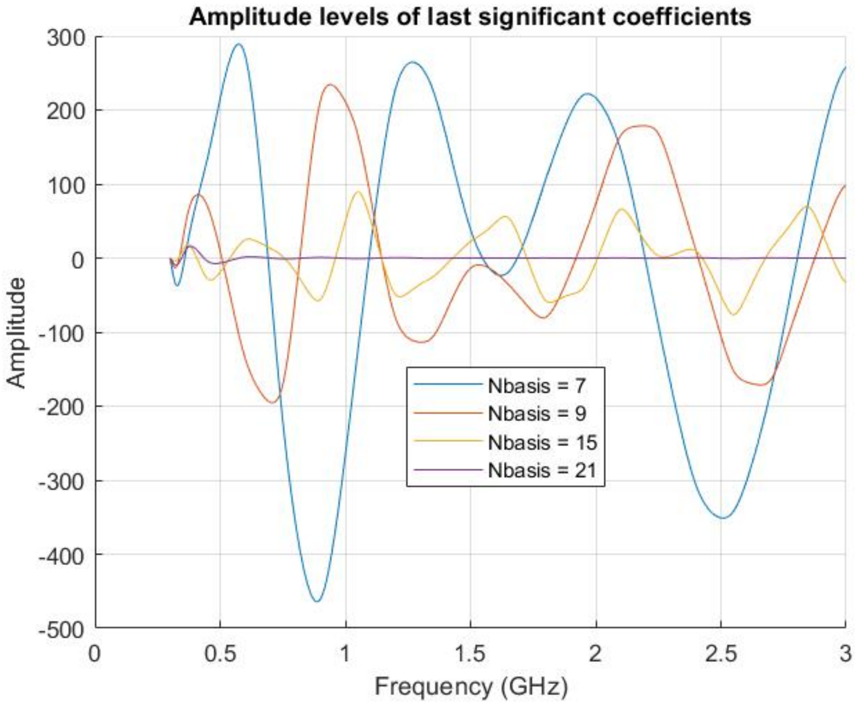

(b) Imaginary coefficient component levels

Figure 4.34: Amplitude level separation for selection of basis function cutoff for large amounts of frequency far-field data

Furthermore, the envelope of coefficient 15 falls beneath 100 for the full band. The envelope of coefficient 21 is predominantly negligible for all regions except for 0.3 GHz to 0.5 GHz and makes a small improvement on accuracy from coefficient 15.

Consider the ratio between the maximum amplitude of α_1 and some higher order coefficient α_x:

$$\frac{|\alpha_1(f_{max})|}{|\alpha_x(f_{max})|} > A_{cutoff}. \tag{4.8}$$

Where f_{max} is the frequency producing maximum amplitude in the coefficient and A_{cutoff} refers to a user specified ratio between the maximum envelope amplitudes. Test data suggests that once the basis levels are below $\frac{1}{100}^{th}$ of the maximum amplitude of α_1, the chromatic aberration ripple should be captured to below 20 % error with an acceptable geometric far-field dynamic range of $\approx$ 30 dB. A robust amplitude recommendation for the selection of significant basis functions is given below:

Table 4.1: Geometric pattern and aperture efficiency accuracy for A_{cutoff} threshold

Cutoff level (A_{cutoff})	Aperture efficiency (%)	Geometric pattern prediction range
100	absolute error below ≈20 %	Approx. main beam
200	absolute error below ≈15 %	Approx. main beam and first side-lobe
500	absolute error below ≈10 %	main beam with side-lobes

Inclusion of basis functions below $\frac{1}{500}^{th}$ of the maximum amplitude of α_1 may simply add computational cost to the interpolation model, without any contribution to accuracy during the reconstruction of $\mathbf{E}_{DR}$. The inequality test of (4.8) is suitable for the FSR coefficients because the basis cutoff is evaluated on relative amplitude levels, ensuring no significant beam contributions are neglected regardless of absolute field intensity or the number of support samples in the data-set.

4.4.4. Observations and interpretation of results

The 9 radial sample polynomial interpolation model was able to characterise the aperture efficiency ripple to below an acceptable ≈15 % error on the ripple amplitude, however, insufficient field data was available for the CBFP expansion to orthogonalise the geometric far-field qualities through application of the SVD to capture all important radiation pattern characteristics.

Applying a simple Kriging model to a larger set of 21 linearly spaced (except for VEXPA samples) provided enough far-field data for the SVD to construct a CBFP able to capture all significant beam characteristics across the bandwidth. Applying the cutoff level $A_{cutoff} = 500$ for accurate aperture efficiency and radiation pattern, corresponds to 19 and 9 significant basis functions for $\mathbf{E}_{MR}$ and $\mathbf{E}_{FSR}$ respectively. This correlates strongly with the intensity contributions of each field evident above as well as the predicted far-field dynamic range accuracy for number of CBFP basis functions in [22].

4.5. ngVLA offset Gregorian antenna

To test and summarise the robust analysis approach for both polynomial and Kriging based models a third test was conducted using the dual reflector geometry of the 18 m single rim supported antenna for the next generation very large array (ngVLA) [60] radio interferometer in New Mexico, USA. The experiment applied the sample density and cutoff criteria from the above sections assuming no prior system knowledge.

The geometry consists of an ellipsoidal sub-reflector with a paraboloidal main reflector. The subtended half angle of 55° was used as the -12 dB taper of Gaussian feed pattern. A test simulation from 0.25 GHz to 2 GHz, varying D_{MR} from 15 to 120λ and D_{SR} from 2.75 to 22 λ, was used to evaluate the interpolation models. VEXPA phase normalisation calculated $r_{norm}a_z$ shifts of 21.5 m and 0.5 m for $\mathbf{E}_{MR}$ & $\mathbf{E}_{FSR}$ respectively.

This antenna exhibits a 14 MHz period chromatic aberration ripple with an amplitude of less than 1 % for frequencies above 450 MHz which can be attributed to the small SR and a feed orientation close to vertical, therefore, an error envelope equal to 20 % of the ripple amplitude was chosen to contextualise the aperture efficiency error.
The geometry under evaluation is illustrated below:

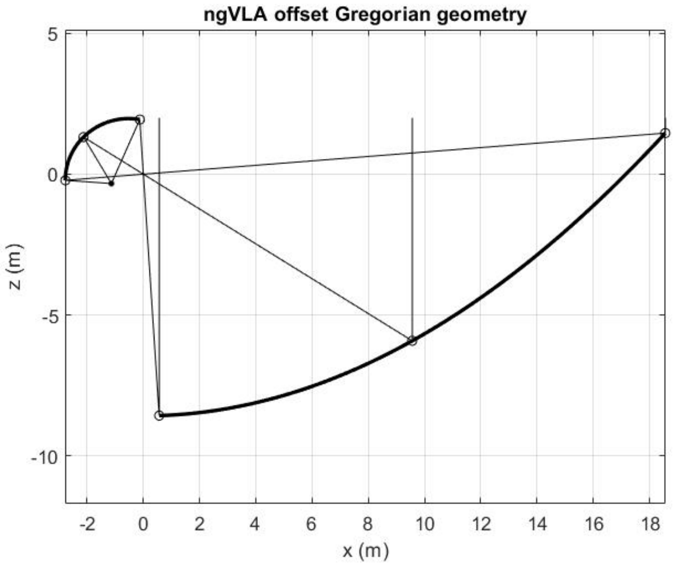

Figure 4.35: Symmetry plane cut of ngVLA offset Gregorian geometry

4.5.1. Polynomial model

Following the recommended sample density of 8 samples per octave bandwidth, 12 radial samples positioned around 0.875 GHz were used to construct the CBFP expansion and polynomial interpolant. The first two radial samples were used for VEXPA analysis.

A_{cutoff} was set to 500 for $\mathbf{E}_{MR}$ & 100 for $\mathbf{E}_{FSR}$ delivering expansions of 11 coefficients for both fields:

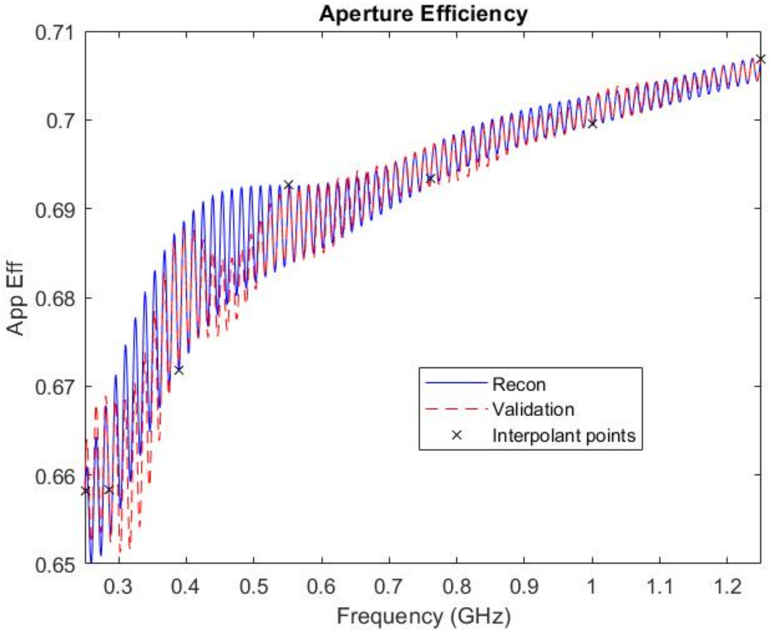

(a) Aperture efficiency: 0.25 GHz to 1.25 GHz

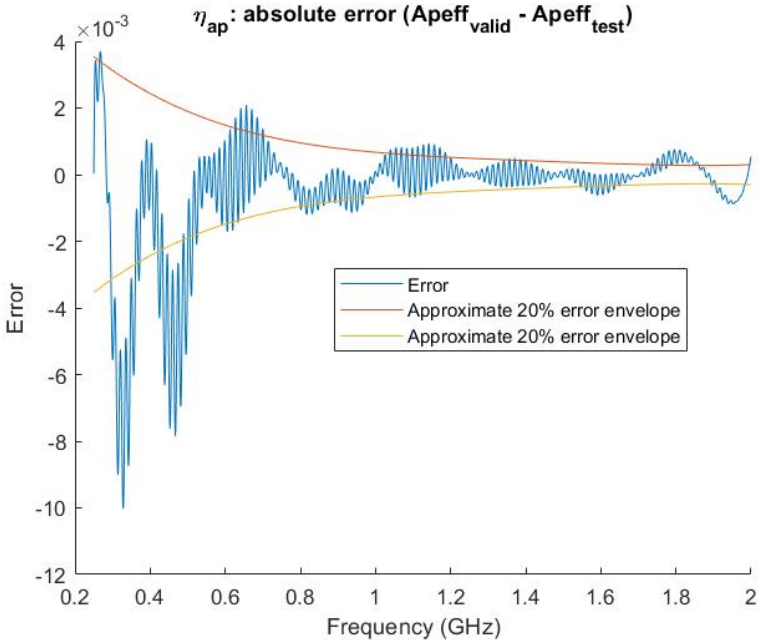

(b) η_{ap} error against 20 % of ripple amplitude

Figure 4.36: Polynomial predicted aperture efficiency comparison and error analysis with ≈14 MHz ripple period

It is evident that this sample density was mostly effective, however, it was not sufficient to capture the dip in efficiency around 450 MHz attributed to a sudden rise in secondary pattern side-lobe level, likely due to unique diffraction on the 4λ SR. This highlights the risk involved with a *single shot* sample distribution approach for model generation which is unable to account for regions of sudden change.

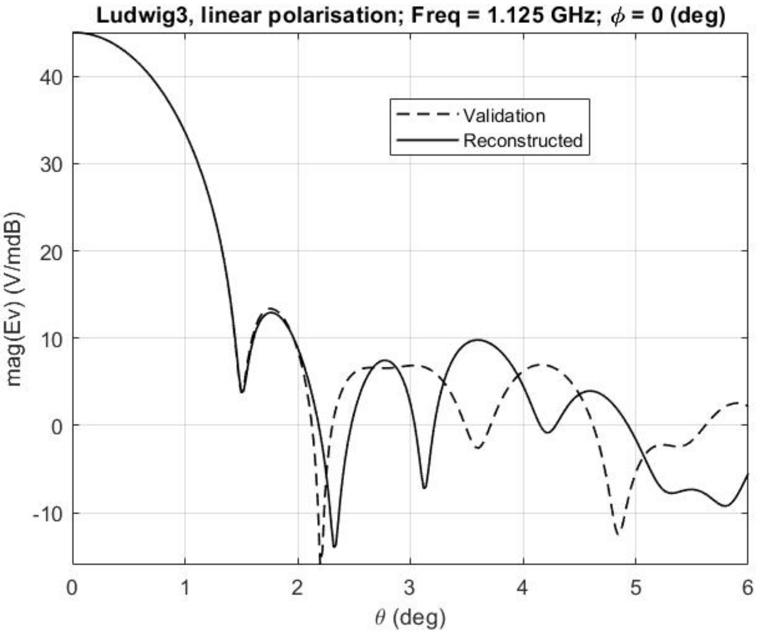

(a) Worst case ε_{RMS} $\approx$2 V m^{-1} beam pattern

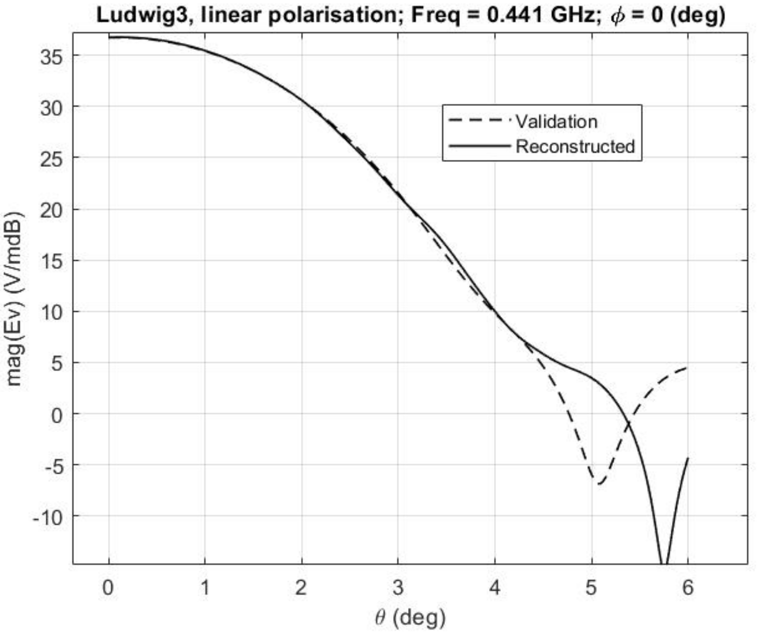

(b) mean case ε_{RMS} $\approx$0.85 V m^{-1}beam pattern

Figure 4.37: Worst and mean RMSE beams for 12 radial sample polynomial model

The worst case scenario pattern show that the model did capture the main beam to an acceptable accuracy with mean RMSE of $\approx 0.85\,\mathrm{V\,m^{-1}}$, the sidelobes however, were missed. The model is still accurate enough to serve as a baseline for the antenna performance and did capture the quickly varying aperture efficiency ripple, but requires more support points to obtain an accuracy sufficient for design comparison.

4.5.2. Simple Kriging model

A linearly spaced sample set with 10 samples per octave was used to build the Kriging model. VEXPA normalisation samples of $\sigma = 157$ & $\rho = 57$ were used, to aid the model by minimising the unknown regions between the first support points, while retaining co-prime spacing. A sample was added at 2 GHz to include the domain boundaries in the interpolation, which affect the accuracy of interpolation considerably [56].

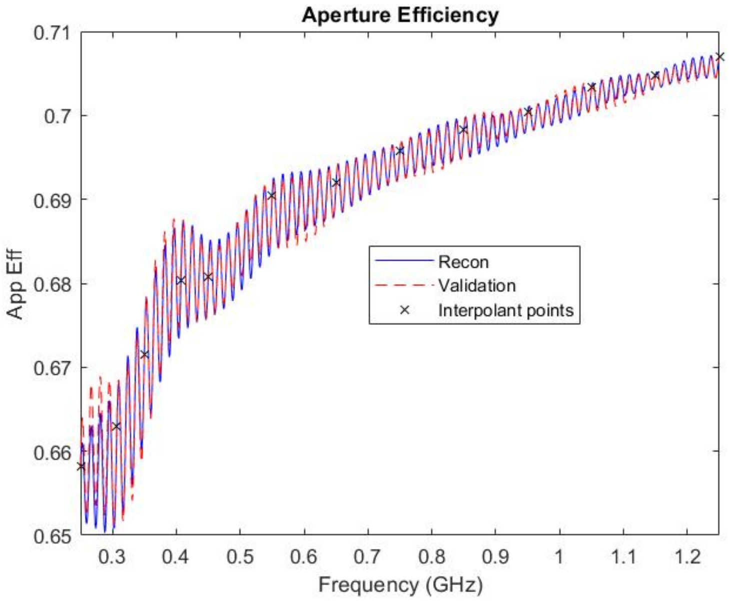

(a) Aperture efficiency: 0.25 GHz to 1.25 GHz

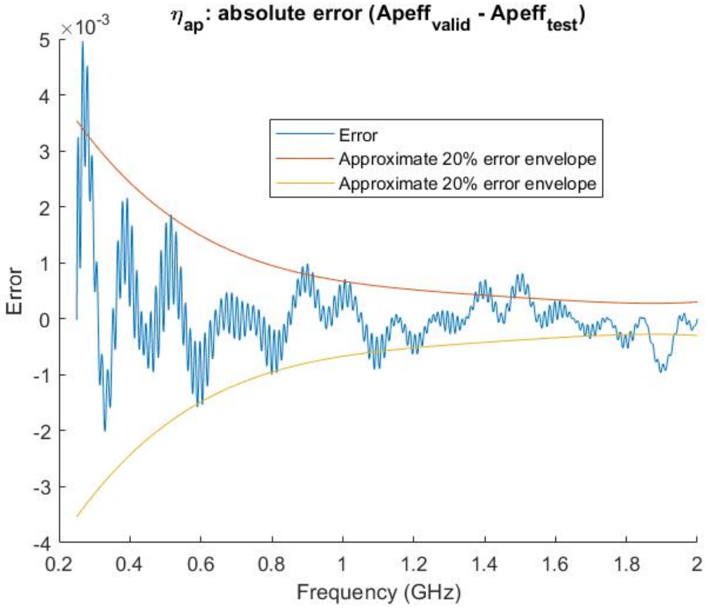

(b) η_{ap} error against 20 % of ripple amplitude

Figure 4.38: Kriging predicted aperture efficiency with 21 support points

A relative basis cutoff level of $A_{cutoff} = 200$ resulted in 18 MR basis functions and 13 FSR basis functions being deemed significant. The predicted aperture efficiency separates from the validation at the upper boundary of the band as a result of badly located samples which both catch the rapid variation at identical cycle positions at the upper frequency boundary. The magnitude patterns for the worst case and mean RMS geometric far-field errors for this model are plotted below:

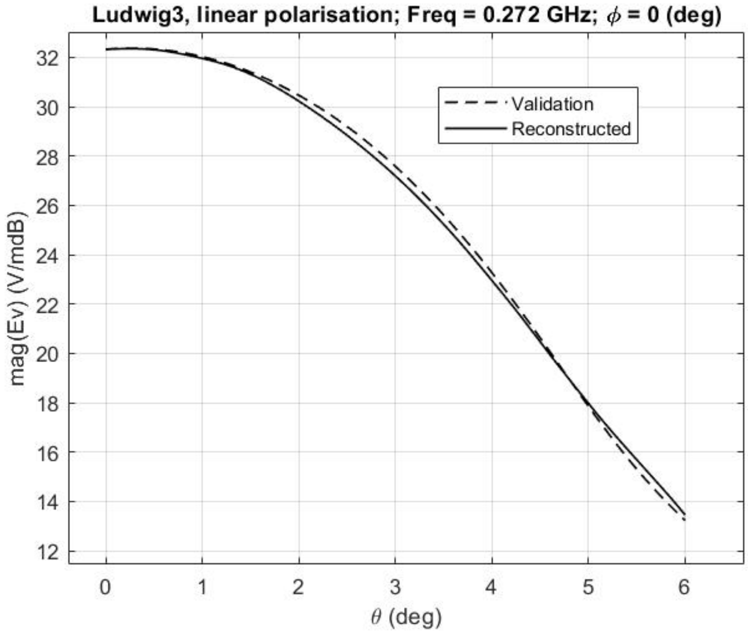

(a) Worst case RMSE beam: $0.9\,\mathrm{V\,m^{-1}}$

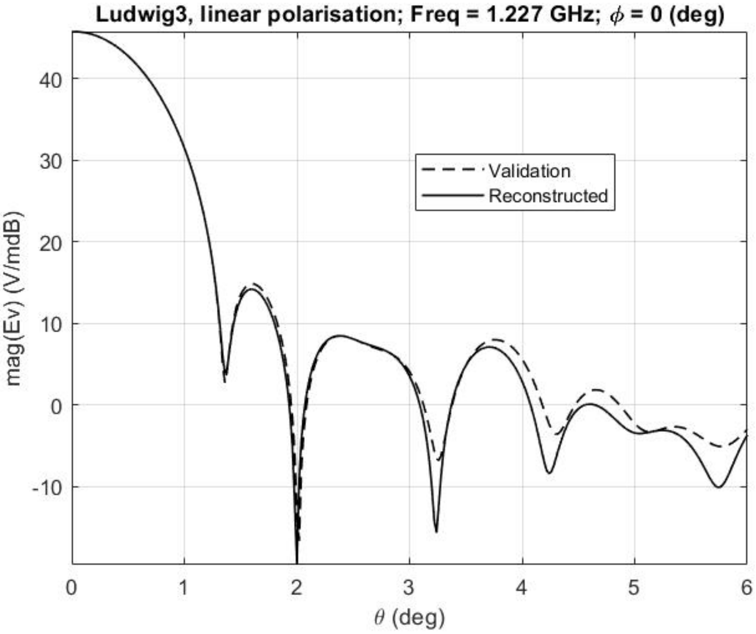

(b) mean case RMSE beam: $0.3\,\mathrm{V\,m^{-1}}$

Figure 4.39: Worst case scenario Kriging generated geometric beam patterns

It is evident here that the 21 sample Kriging model characterisation was successful, and the rapid variations for this geometry were successfully captured.

4.5.3. Comparison of Polynomial and Kriging result

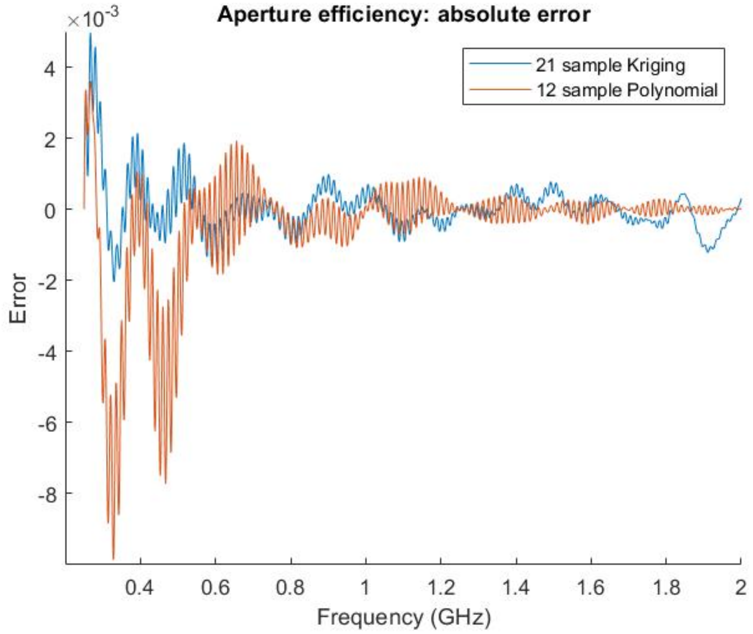

(a) Absolute aperture efficiency error

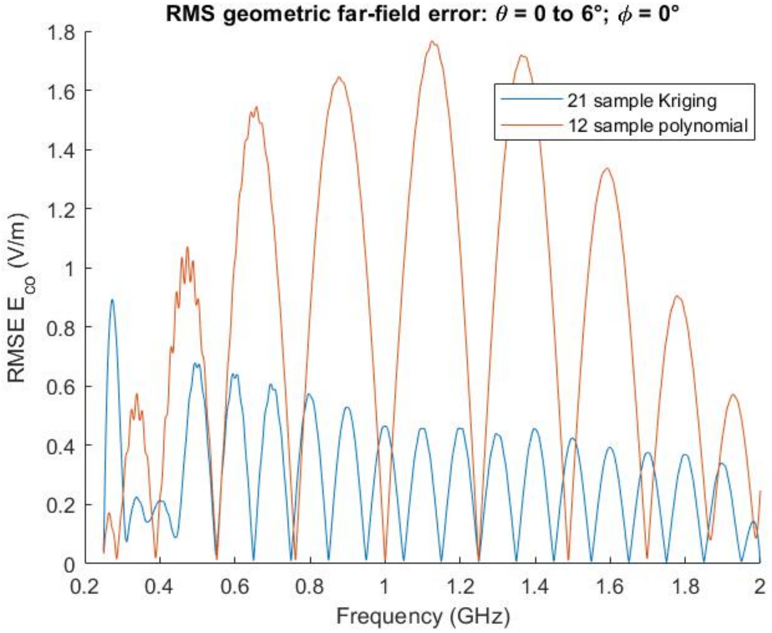

(b) Average geometric E-field error

Figure 4.40: Comparison of absolute aperture efficiency error and geometric far-field RMSE for 21 sample Kriging model and 12 radial sample polynomial model

Analysis here shows that a very rapid aperture efficiency prediction accurate enough to serve as a rough starting point for a dual reflector design is obtainable with very few direct simulations, through polynomial interpolation of a radial set which allows for excellent modelling with smooth functions generated from minimal support points. This approach is, however, not suitable if a fairly large geometric range of the far-field pattern is the simulation goal.

The CBFP expansion typically requires approximately 20 samples to successfully decompose the beam into orthogonal frequency dependant beam features, while a polynomial fit can be used here, there is a risk of over-fitting if the system behaviour is unknown. Fortunately simple Kriging interpolation with a Matérn $(\frac{3}{2})$ covariance function emerges as a more robust approach less encumbered by over-fitting which can utilise the increased support sample data to safely reduce prediction error for both aperture efficiency and far-field radiation patterns.

In general a Kriging-Matérn approach built from linear support samples is recommended, due to its robustness for data-sets providing sufficient data for the singular value decomposition which orientates the CBFP and stress free addition of samples in anomalous regions to improve the interpolant.

4.6. Conclusions

Overall the CBFP superposition method facilitates accurate wideband characterisation, capturing all physically driven dual reflector field interaction effects, for both polynomial and simple Kriging based interpolation models generated with a sample density well below (typically $\approx \frac{1}{8}^{th}$) the Nyquist threshold of the associated chromatic aberration oscillations. Evidence suggests field estimation accuracy has been decoupled from the chormatic aberration ripple period.

While a polynomial fit offers a computationally cheap option for broadband aperture efficiency approximation, its susceptibility to oscillations and divergence for non-radial sample patterns hinder its overall effectiveness, especially for unknown antennas.

A Kriging model mitigates this risk, as its support of irregular sampling distributions would allow the user to continually add samples at will to improve the interpolant and further refine the SVD in the CBFP expansion. Furthermore, the ability of the Kriging behaviour to be tuned using the covariance function and return a measure of model uncertainty make it the more robust and attractive approach when compared to a polynomial least squares fit.

Chapter 5

Adaptive sampling based surrogate CBFP model

This chapter documents the implementation of a Kriging based surrogate model which incorporates an exploratory adaptive sampling scheme in the $\mathbf{E}_{MR}$ design space to generate an accurate interpolation model. The approach eliminates the need for any prior system knowledge or pre-defined sample density, by sequentially evaluating the convergence of the most significant CBFP coefficients across frequency using Frobenius distance, facilitating software driven design of electrically small dual reflectors with minimal user input.

5.1. Overview of adaptive sampling approach

An important characteristic of Kriging based interpolation is the uncertainty prediction it is coupled to. This feature allows for an iterative analytical approach to be used when exploring a design space of interest. This concept is termed *adaptive sampling*, whereby the model re-evaluates the uncertainty in the Kriging covariance matrix to place the next sample at a position where the information gain is maximised, thus, reducing the global surrogate model error as quickly as possible.

An exploratory approach adopts certain criteria, defined using parameters of a *sampling function*, for analysis of the uncertainty matrix such that each subsequent sample is placed far away from previous samples given a certain interpolant distribution. For applications where the entire design space is of interest density based sampling functions orientated towards filling the design space as quickly as possible, such as furthest site Delaunay triangulation, have been shown to be effective in minimising the number of expensive support samples needed to generate accurate predictions at any point in the design space [61].

5.2. Dynamic nature of CBFP coefficients

Typically a sequential design or adaptive sampling approach is applied to a stationary underlying problem, whereby the support points added to the model are valid across multiple iterations. For the CBFP expansion this is not the case, and every time more direct simulation data becomes available, the singular value decomposition will generate a new tiered basis function set, with different envelopes and support values.

As a consequence of this, every time a direct simulation result at a new frequency is added to the CBFP training data-set, a new Kriging model must be generated for each coefficient. This inhibits the efficiency of a complex modelling approach, especially at the start of the iterative process, as sample selection considering multiple CBFP dimensions may be generated from an SVD extracting far-field features which are not properly ordered in terms of true significance for the antenna under analysis, and therefore, contain incorrect information, resulting in pointless computational expenditure.

5.3. Iterative modelling approach

In the context of frequency interpolation of simulated antenna results, the singular value decomposition, the foundation on which characteristic basis functions are generated, is driven by the common features in the far-field patterns across frequency. Henceforth, the fundamental coefficient represents the amplitude of a function capturing the dominating far-field pattern at all frequencies. The later coefficients describe features in the lower parts of the dynamic range, and eventually, specific side-lobe artefacts.

The process of obtaining new support data is far more costly than simple Kriging model generation, therefore, it is important that only coefficients which are true representations of the underlying antenna fields are considered for sample placement. As the CBFP expansion obtains more antenna field data on which to refine the basis functions (by sampling more frequency points), the singular vectors form a basis which spans the far-field subspace of the antenna in the band of interest. It is safe to assume that the fundamental coefficient will be the first to converge as it is defined with the strongest eigenvalue of the data-set, with the later coefficients converging in order thereafter.

A simple and efficient iterative approach, which exploits this hierarchical cascade of information, is to use the two single dimension interpolants of the highest order converged complex coefficient at each step to place the next frequency sample. This ensures that only the most valuable uncertainty model built with true antenna field information is used to calculate the next best sample location, contributing to a sequential reduction of model error across frequency, while not limiting the number of samples attached to a single coefficient. This robust framework allows for intuitive user control over the design process with two parameters:

1. The convergence threshold for individual CBFP coefficients.
2. The number of converged CBFP coefficients required for far-field reconstruction.

Provided these two parameters are tuned to acceptable levels, the extremely low computational cost of generating a single complex Kriging-Matérn interpolant improves the rate of basis function refinement when compared to a fixed predefined sample approach, allowing for accurate far-field reconstruction with fewer support points in the band of interest. There are, of course, a variety of suitable approaches to such a broad problem, however, this simple low computational cost strategy is adopted in the implementation presented here.

5.4. Coefficient convergence tracking

The convergence progress for a specific CBFP coefficient is measured using the Frobenius distance between the complex values of the common support points for two iterations. The real and imaginary distance components are individually evaluated with the same threshold. The magnitude of the coefficients should not be used, as it may result in misleading results due to the removal of negative values, under estimating the true distance. A breakdown of the procedure is shown below.

Consider the currently available CBFP interpolant for a set of $k+1$ support samples, α_n, and the interpolant for the same basis coefficient generated with k support samples, γ_n. n refers to the order of the CBFP coefficient. The Frobenius distance, μ_n, between the common support points of a coefficient for two iterations is defined as:

$$\Re(\mu_n) = \sum \frac{\sum_{p=1}^{k} |\Re(\alpha_p) - \Re(\gamma_p)|}{k} \tag{5.1}$$

$$\Im(\mu_n) = \sum \frac{\sum_{p=1}^{k} |\Im(\alpha_p) - \Im(\gamma_p)|}{k}. \tag{5.2}$$

The inequality applied individually to both the real ($\Re$) and imaginary ($\Im$) part of the coefficient to classify it as converged is:

$$\mu_n < S\frac{C}{100} \quad for \quad \Re \quad \& \quad \Im \tag{5.3}$$

where S represents the distance between the global maximum and minimum of γ_n produced with k frequency samples. C represents a user controlled model parameter which denotes the convergence threshold as a percentage of the maximum deviation in the coefficient support points for the previous set of frequency samples,(k), such that it can be interpreted in a somewhat intuitive way. An illustration summarising the method composed in 5.3 is illustrated in Figure 5.1 for a single CBFP coefficient amplitude:

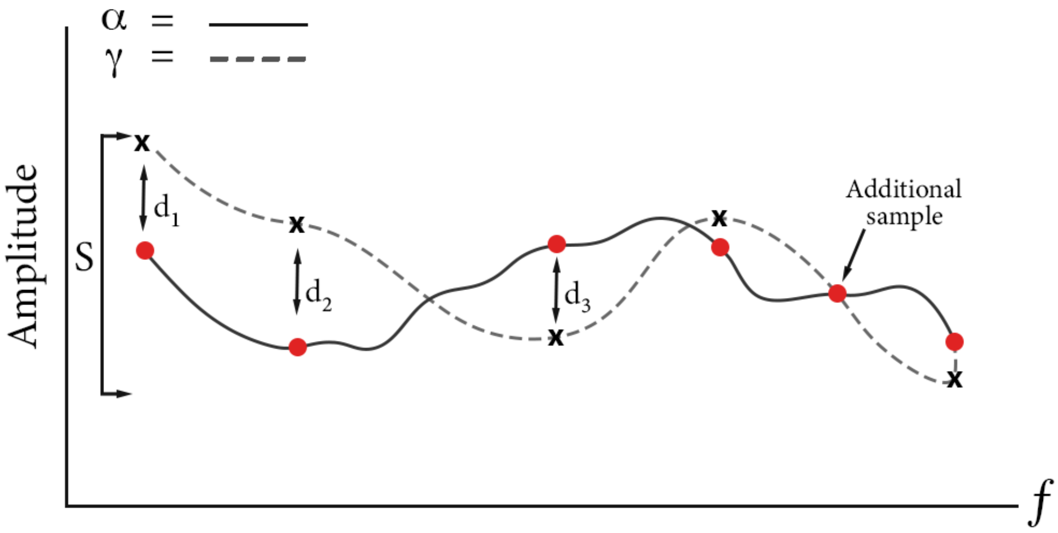

Figure 5.1: Illustration of the convergence measurement for a dynamic CBFP basis coefficient iteration

Again this is not the only suitable method for tracking the convergence progress of coefficients, and was chosen specifically for simple user interpretation and computational simplicity.

5.5. Sequential design implementation

Using the above approach, a fully functional software implementation was developed in MATLAB which independently interfaces with GRASP in batch mode operation for the generation of new support samples at specified frequencies to construct the surrogate model allowing for field data predictions at the desired frequency resolution to be returned to the user [27], [58].

The implementation considers only the CBFP coefficients associated with the mathematically defined $\mathbf{E}_{MR} = \mathbf{E}_{DR} - \mathbf{E}_{FSR}$ field, as the main reflector aperture makes the most significant contribution to the macro-behaviour of the dual reflector across frequency. The model assumes that the coefficients of $\mathbf{E}_{FSR}$ will converge on the same sample set, and not contribute to sample selection in a meaningful way.

5.5.1. User inputs

The program requires the following user inputs:

1. The Bandwidth of interest as f_{max} and f_{min} in GHz.
2. The antenna geometry defined using the geometric parameters presented in either [40] or [39].
3. The Coefficient convergence threshold as a percentage of the maximum deviation in the previous sample set.
4. The number of coefficients to be considered for individual convergence evaluation.
5. The amplitude above which coefficients are deemed significant, A_{cutoff} as defined in equation 4.8.

The User may also specify the VEXPA parameters of the system, however they are set to sensible robust default values of $\sigma = 67$ and $\rho = 23$ with a grid resolution of 1 MHz orientated at the lowest frequency in the bandwidth to reduce simulation cost. These values offer a conservative trade-off between accuracy and cost, ensuring the underlying functions are sufficiently slowly varying for effective phase normalisation with the σ sample far enough away from the base frequency to assist interpolation.

5.5.2. Default initial design

A default initial design frequency sample set is used to fill the design space before adaptive sampling iterations begin:

Table 5.1: Default initial exploratory frequency sample distribution

Frequency position	Description
f_{min}	The lowest frequency in the desired bandwidth (VEXPA base)
$f_{min} + \sigma$	The largest sample used during VEXPA phase normalisation
$\frac{f_{max}+f_{min}}{2}$	The centre frequency of the desired bandwidth
f_{max}	The highest frequency in the desired bandwidth

The user may also specify an initial set of frequency samples. These are chosen as they are the obvious best starting point for design space exploration, and will almost always be chosen by exploratory algorithms [27]. The first Kriging model will evaluate the fundamental coefficient of main reflector CBFP using these 4 samples, and then suggest the next sample placement according to a furthest distance Delaunay triangulation and begin to track convergence starting at α_1 for the first automatically placed sample on top of the initial design set.

5.5.3. Guidelines for convergence criteria

The shape of the slowly varying $\mathbf{E}_{MR}$ basis coefficients is always specific to the antenna geometry under evaluation, and as such it is impossible to guarantee successful convergence for all possible dual reflector configurations, it is, however, possible to define a robust set of guidelines to ensure an accurate global model is established while prioritising either speed or accuracy.

The results presented in the previous chapter lend credibility to the assumption that a typical dual reflector system will probably require less than 25 samples to produce an acceptable interpolation model accuracy over an octave bandwidth, therefore, a default number of 5 converged coefficients with defined with an intuitive Frobenius distance level (FDL) of less than 50 % of the previous iteration maximum deviation is recommended. This ensures a minimum of 13 samples is used to create the Kriging model, which allows for the generation of more than the significant 10 basis functions typically required to capture a dual reflector beam including the first side-lobe as shown in [22].

5.6. Symmetrical Gregorian geometry

Although symmetrical Gregorian geometry is not typically used at frequencies where the geometry is electrically small, it is common in practical systems, and an example is, therefore, included to illustrate that the physics based superposition model is able to capture aperture efficiency diffraction variations caused by direct blockage.

The Model was generated for 1.5 GHz to 3.0 GHz varying the electrical size of the main reflector from 25λ to 50λ and the sub-reflector from 6λ to 12λ. A Gaussian beam pattern with a -10 dB taper across the subtended half angle of 15° was used for illumination [39].

Convergence was defined using 50 % deviation for the first five coefficients and classified the $\mathbf{E}_{MR}$ CBFP set as converged with 13 support samples. A_{cutoff} was set to 500 and 100 for the MR and FSR fields respectively, using all 13 basis functions for $\mathbf{E}_{MR}$ and 7 for $\mathbf{E}_{FSR}$. The convergence progress is documented in Table 5.2.

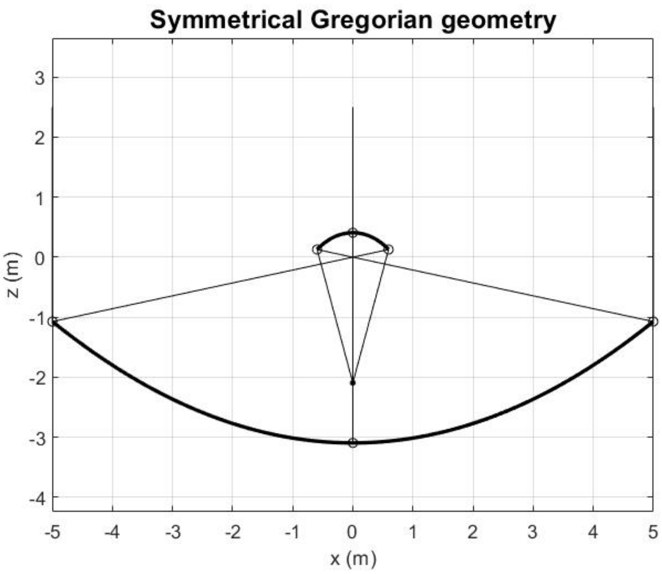

Figure 5.2: Symmetry plane cut of symmetrical Gregorian with $D_{MR} = 10\,\text{m}$ $D_{SR} = 1.2\,\text{m}$ & $\theta_e = 15°$

Table 5.2: CBFP convergence progress against frequency samples for $FDL = 50\,\%$

Number of frequency support samples	Highest order converged coefficient
5	α_1
7	α_2
8	α_3
12	α_4
13	α_5

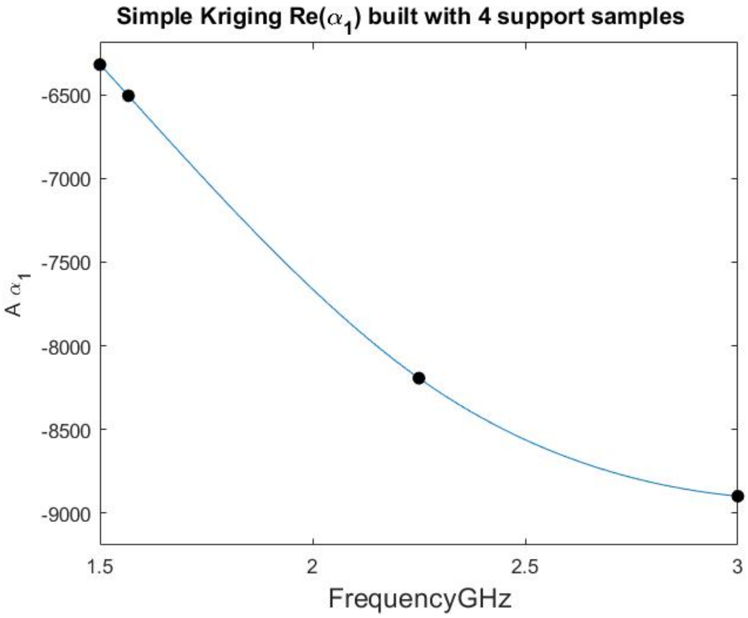

Figure 5.3: Initial 4 sample placement for start of adaptive sample process in the symmetrical Gregorian $\mathbf{E}_{MR}$ design space. A simple Kriging-Matérn $(\frac{3}{2})$ interpolant for α_1 is shown with circles indicating support points.

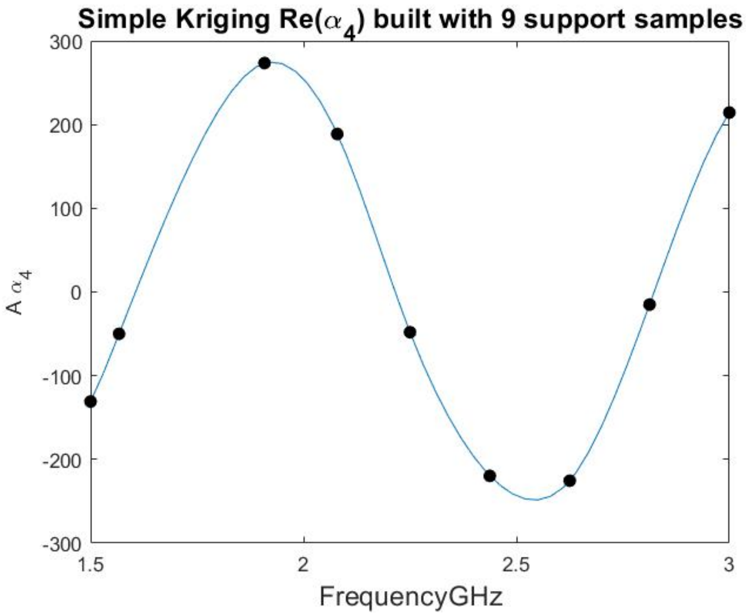

Figure 5.4: Snapshot at 9 samples with α_{1-3} classified as converged, the algorithm now considers CBFP α_4 for the next sample in the $\mathbf{E}_{MR}$ design space.

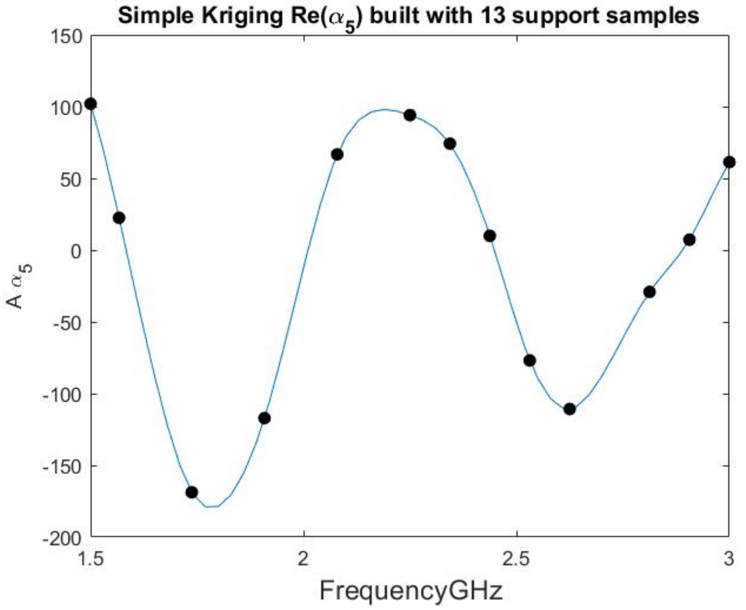

Figure 5.5: Final Adaptive sample placement in the $\mathbf{E}_{MR}$ design space, leading to the convergence of α_5 below set thresholds and the initiation of field prediction.

The dual reflector's chromatic aberration ripple with period of $\approx 40\,\text{MHz}$ was successfully captured with a sample density equivalent to $\approx \frac{1}{5}^{th}$ of the Nyquist rate. The maximum error is approximately 10 % of the ripple amplitude shown in Figure 5.6:

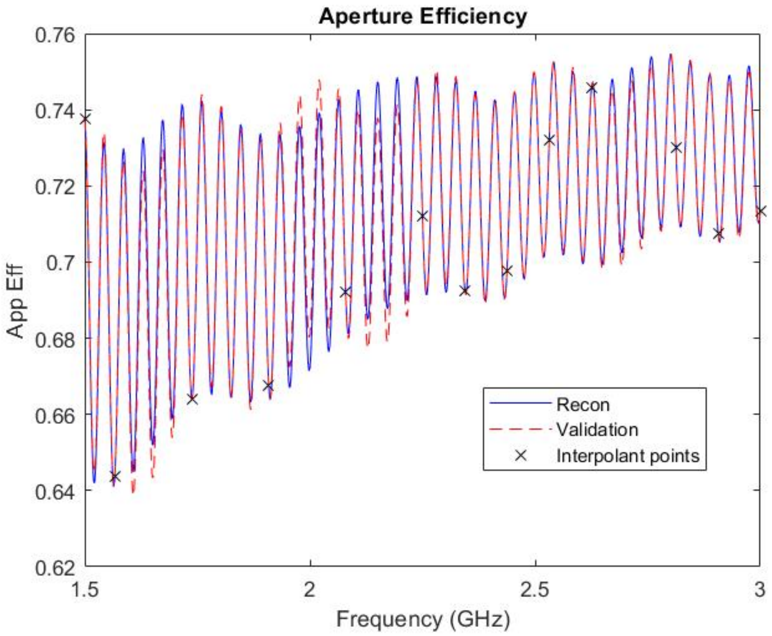

(a) Aperture efficiency prediction: 1.5 GHz to 3 GHz

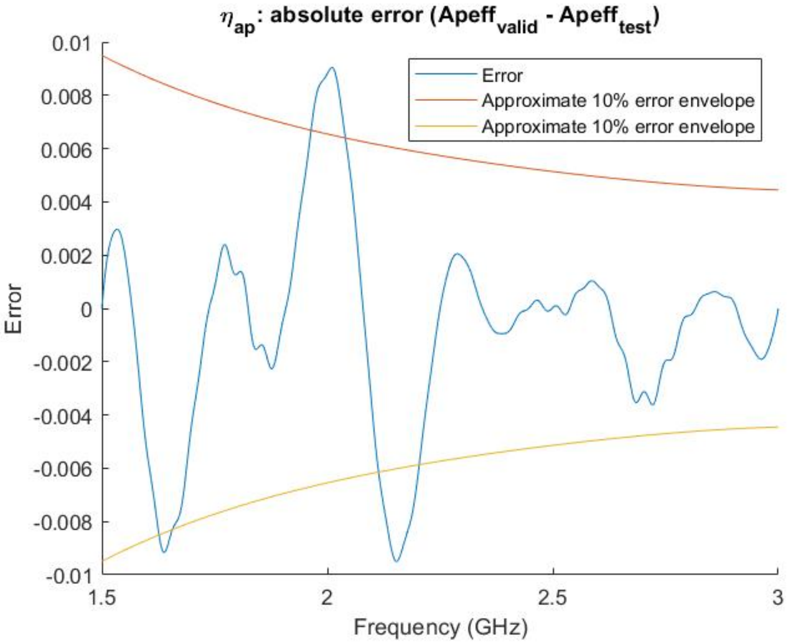

(b) η_{ap} error against 10 % of ripple amplitude

Figure 5.6: Symmetrical Gregorian aperture efficiency prediction with ≈40 MHz chromatic aberration ripple based on adaptive sampling in the $\mathbf{E}_{MR}$ design space according to the convergence of CBFP expansion coefficients α_{1-5}.

Analysis of the ripple reconstruction using CBFP interpolants shows the accuracy is tractable for design analysis. Predictions are based off of simple Kriging-Matérn $(\frac{3}{2})$ interpolation of support samples placed with an exploratory adaptive sampling scheme in the $\mathbf{E}_{MR}$ design space, according to the convergence of CBFP expansion coefficients α_{1-5}. The predicted radiation patterns further confirm this, with RMSE across $\theta = -6^\circ$ to 6° for $\phi = 0^\circ$ below 2 % of the RMS of the validation geometric far-field pattern $\mathbf{E}_{DR}$, with

$N_\theta[f]$ the number of discrete θ samples for frequency f and square brackets to show discrete simulation based data:

$$RMS(\mathbf{E}_{DR}[\theta,\phi,f]) = \sqrt{\frac{1}{N_\theta[f]}\sum_{\theta=\theta_{min}}^{\theta_{max}} |\mathbf{E}_{DR}[\theta,\phi,f]|^2}. \tag{5.4}$$

The main beam and two side-lobes were accurately predicted in the worst case far-field pattern. The geometric prediction accuracy is illustrated in Figure 5.7.

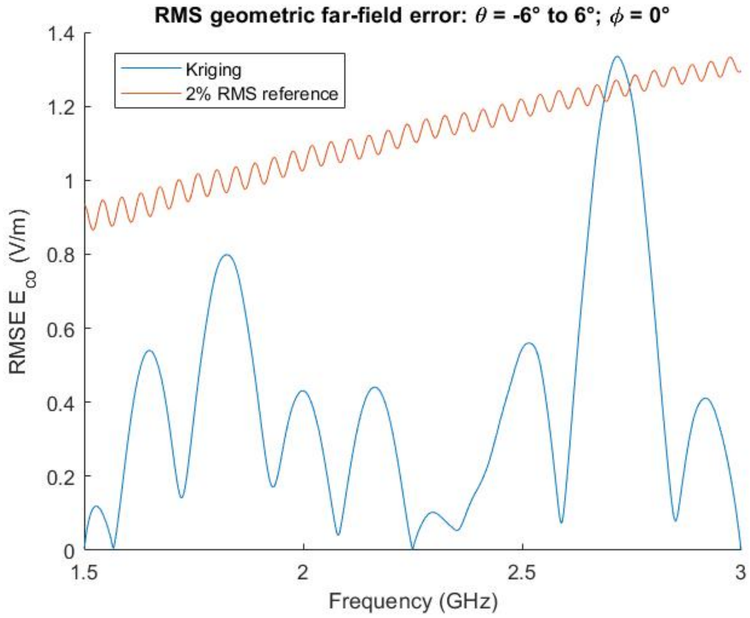

(a) Far-field RMSE against 2 % $\mathbf{E}_{DR}$ validation RMS

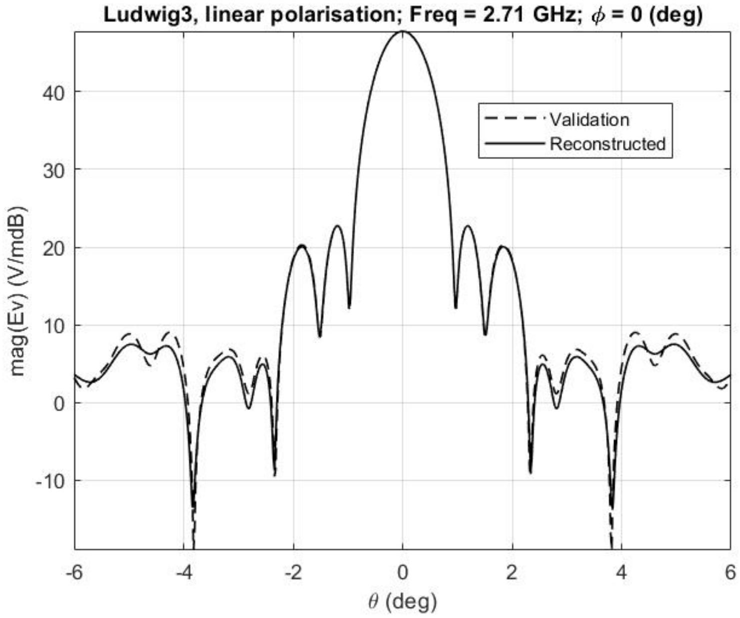

(b) Worst RMSE case beam

Figure 5.7: Symmetrical Gregorian geometric far-field predictions with $P_{rad} = \frac{2\pi}{\eta}$ capturing the main lobe and first sidelobes in all cases

These results provide sufficient evidence that robust sequential convergence methodology followed by the algorithm is suitable for the wide-band characterisation of a symmetrical dual reflector configuration.

5.7. SKAU offset Gregorian antenna

A practical example of a dual reflector used at frequencies where the geometry is electrically small is now used to evaluate the adaptive sampling implementation. The offset Gregorian features a large subtended half angle at the feed, $\theta_e = 55°$, suitable for a cheap and compact horn antenna with a sub-reflector extension to reduce spillover [44].

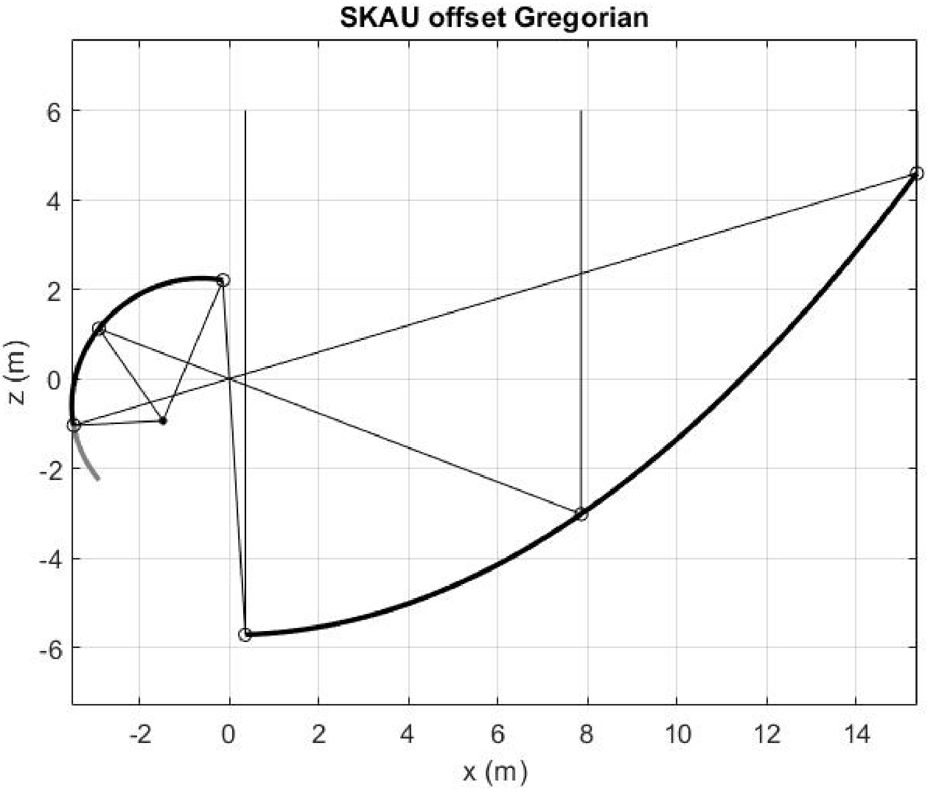

Figure 5.8: Symmetry plane cut of clear aperture SKAU offset Gregorian geometry

The simulation bandwidth was chosen as 0.3 GHz to 2 GHz to cover the SKA mid band for which this dish is designed for as well as some additional range varying the 15 m equivalent D_{MR} from 15 to 100λ and the 4 m D_{SR}, ellipsoidal sub-reflector from 4 to 27λ. Offset configurations exhibit contours over broadside in their radiation pattern as a result of field diffraction on the sub-reflector, which also drives the chromatic aberration ripple.

This *beam squint* results in differing sidelobe levels on either side of the $\theta = 0°$, and increases the complexity of generating an orthogonal CBFP basis through SVD which accurately captures all beam contours. More samples are therefore required to accurately capture asymmetrical side-lobe behaviour in far-field patterns.

Beam contour is of interest in radio interferometry, and in order to account for this, stricter convergence criteria is recommended for the CBFP coefficients in question.

5 basis coefficients, converged to below $FDL = 25\,\%$, was deemed necessary for final model generation on the SKAU geometry. 19 support samples were required to classify the basis set, α_{1-5} for $\mathbf{E}_{MR}$, as converged. The sequential sample placement is shown in Table 5.3 and Figures 5.9, 5.10 and 5.11:

Table 5.3: CBFP convergence progress against frequency samples for $FDL = 25\,\%$

Number of frequency support samples	Highest order converged coefficient
7	α_1
11	α_2
12	α_3
14	α_4
19	α_5

Coefficient 5 took the longest out of the basis set to converge, requiring 5 additional samples. Snapshots of the iterative sample placement according to the exploratory adaptive sampling algorithm are shown below:

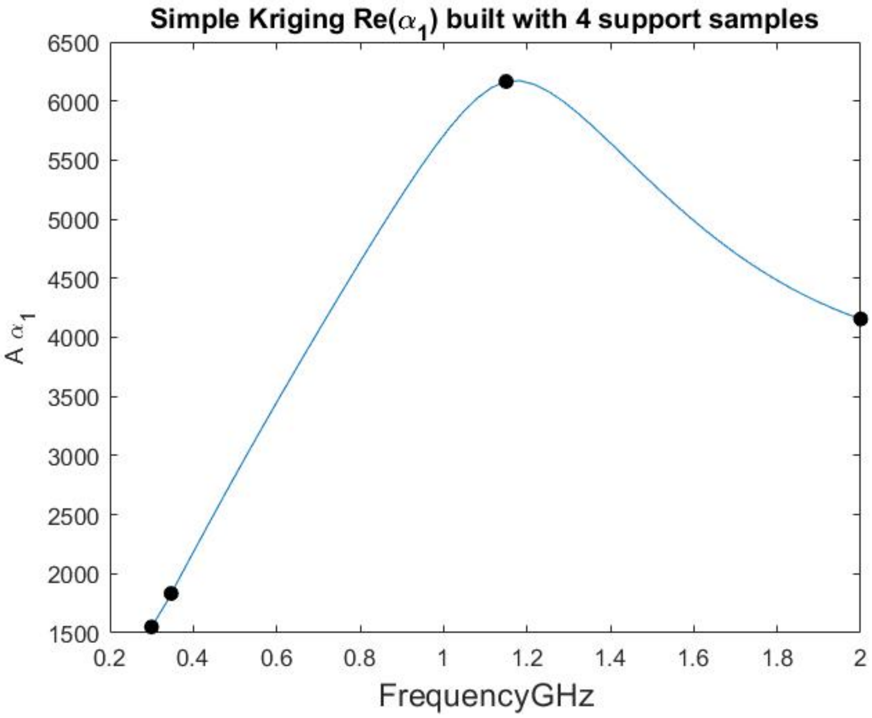

Figure 5.9: Initial 4 sample placement for start of adaptive sample process in the SKAU $\mathbf{E}_{\mathbf{MR}}$ design space. A simple Kriging-Matérn $(\frac{3}{2})$ interpolant for α_1 is shown with circles indicating support points.

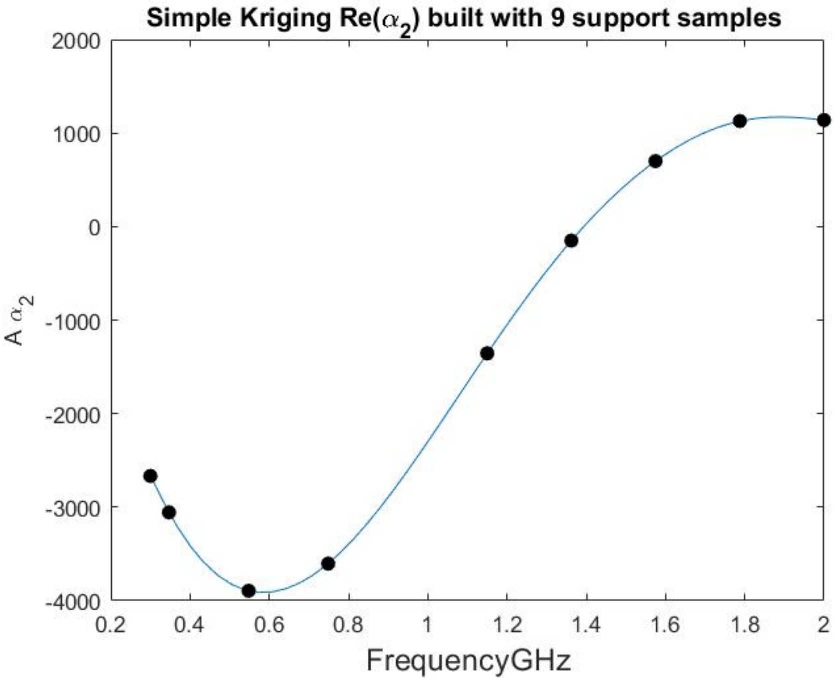

Figure 5.10: Snapshot at 9 samples with α_1 classified as converged, the algorithm now considers CBFP α_2 for the next sample in the SKAU $\mathbf{E}_{MR}$ design space.

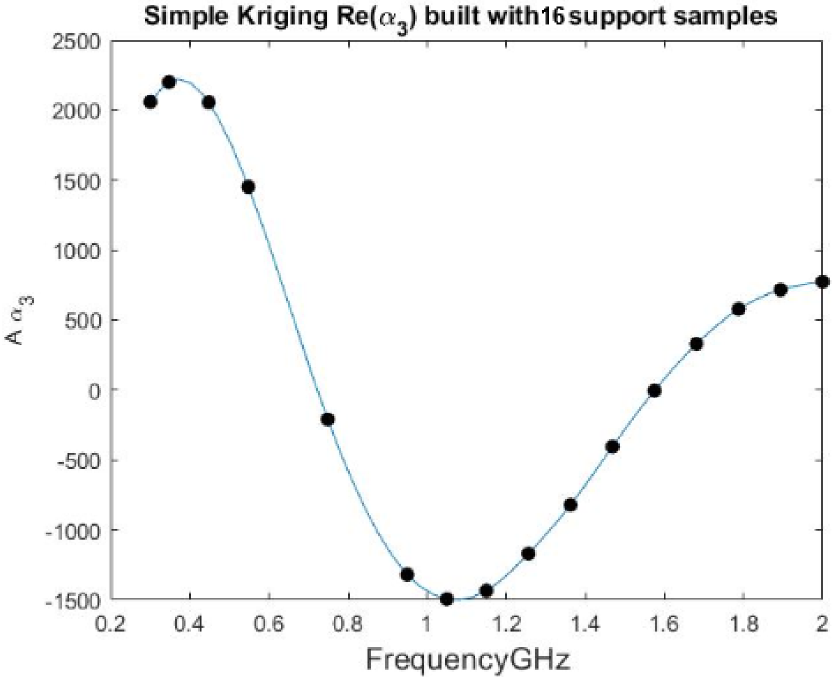

Figure 5.11: Snapshot at 16 samples with α_2 classified as converged, the algorithm now considers CBFP α_3 for the next sample in the SKAU $\mathbf{E}_{MR}$ design space.

The final basis coefficients are fairly slowly varying, and exhibit behaviour which is expected from a phase normalised CBFP set with a Gaussian feed pattern. This indicates that the robust VEXPA setup of $\sigma = 67$ and $\rho = 23$ on a 1 MHz grid was effective in removing any artificial frequency variation produced during software modelling.

Figure 5.12 shows the first 5 basis coefficients obtained once the exploratory algorithm classified them as converged with 19 frequency samples.

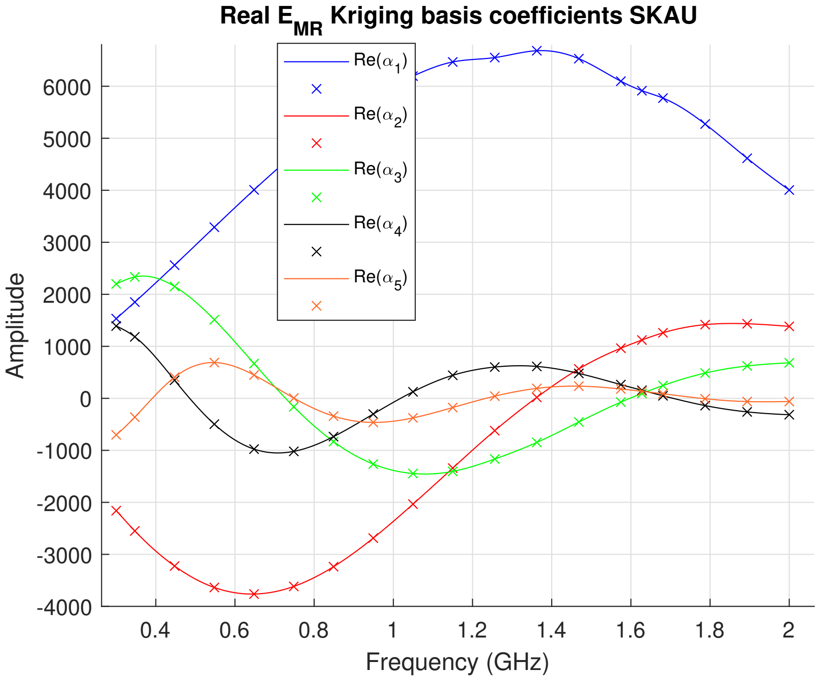

(a) $\Re(\alpha_{1-5})$ 19 support samples

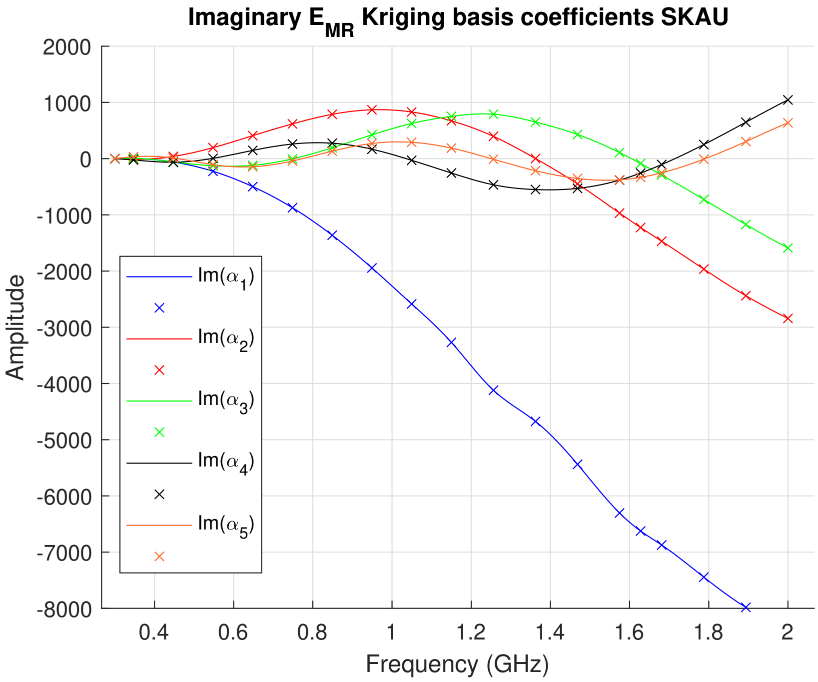

(b) $\Im(\alpha_{1-5})$ 19 support samples

Figure 5.12: Converged $\mathbf{E}_{MR}$ complex basis coefficients (α_{1-5}) with 19 support samples placed through adaptive sampling indicated as crosses.

Figure 5.12 indicates that the SVD has orientated the characteristic basis set such that the significant frequency dependant features of the radiation pattern are captured by the first 5 $\mathbf{E}_{MR}$ CBFP coefficients, with $|\alpha_5|$ being approximately 7 times smaller than $|\alpha_1|$ across the band. The SVD spectrum for $\mathbf{E}_{MR}$ is shown in Figure 5.13 for the 9,12,15,17 and 19 sample case. It indicates that after 10 basis functions are used the benefit of using additional functions begins to diminish, however due to the contoured nature of the equivalent main reflector pattern the SVD value spectrum for the first 18 basis functions is still in the order of 10^{-3}.

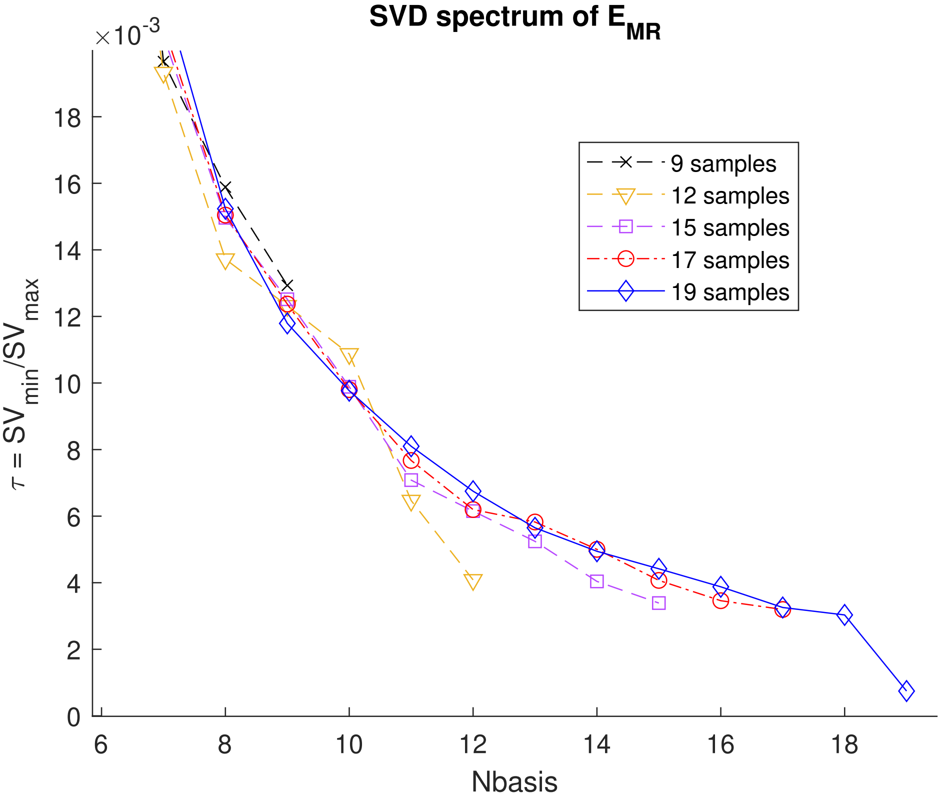

Figure 5.13: SVD spectrum obtained for SKAU $\mathbf{E}_{MR}$ equivalent field for different intermediate sample steps

The reduction in gradient after 12 basis functions are included suggest that the field could be approximated to an acceptable accuracy using 13 or more basis functions.

5.8. Progression of estimation accuracy with adaptive sample placement

In order to visualise the progression of the first 5 CBFP coefficients converging with the addition of adaptive samples the real parts of $\mathbf{E}_{MR} : \alpha_{1-5}$ are shown in Figures 5.14, 5.15 and 5.16 for consecutive samples. This illustrates how placing samples according to CBFP coefficient convergence influences the adaptive sampling process. Red crosses indicate the previous sample set with black crosses representing the current sample set. The coefficients are colour coded according to basis function.

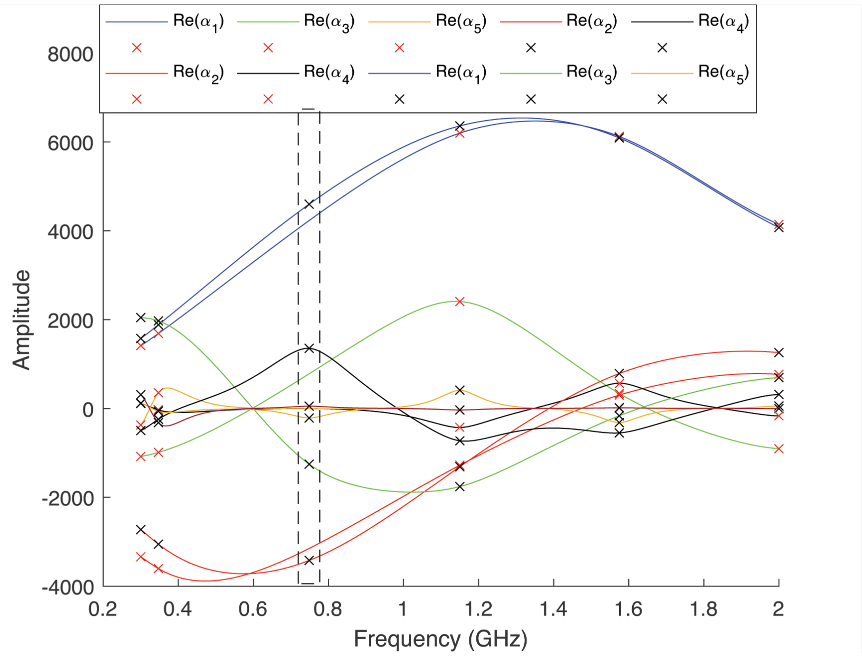

Figure 5.14: Placement of sample 6 according to analysis of α_1 with no coefficients deemed converged

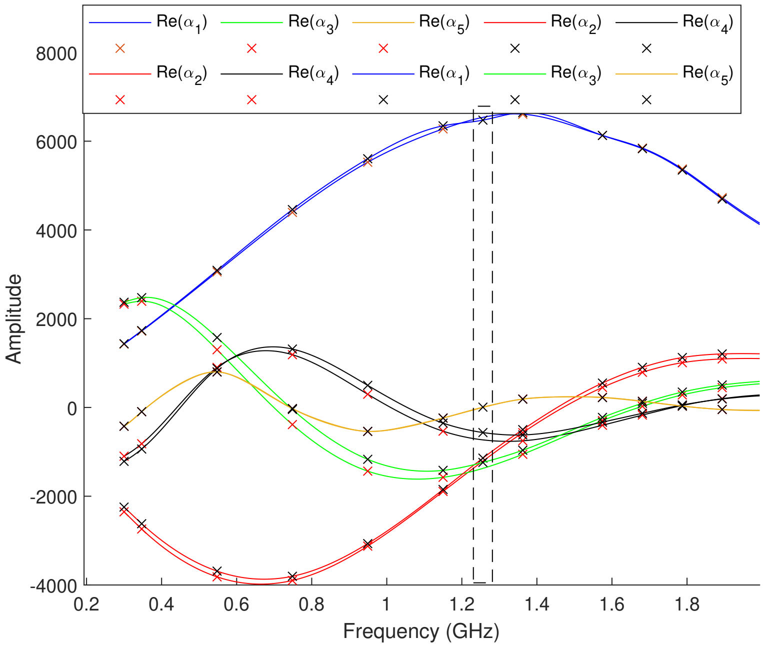

Figure 5.15: Placement of sample 13 according to analysis of α_4 with coefficients α_{1-3} deemed converged

It is clear from Figures 5.15 and 5.16 that once the most significant CBFP coefficients have converged significantly their overall shape does not change with the addition of new samples. This provides empirical evidence supporting the validity of placing frequency samples according to the least significant non-converged coefficient.

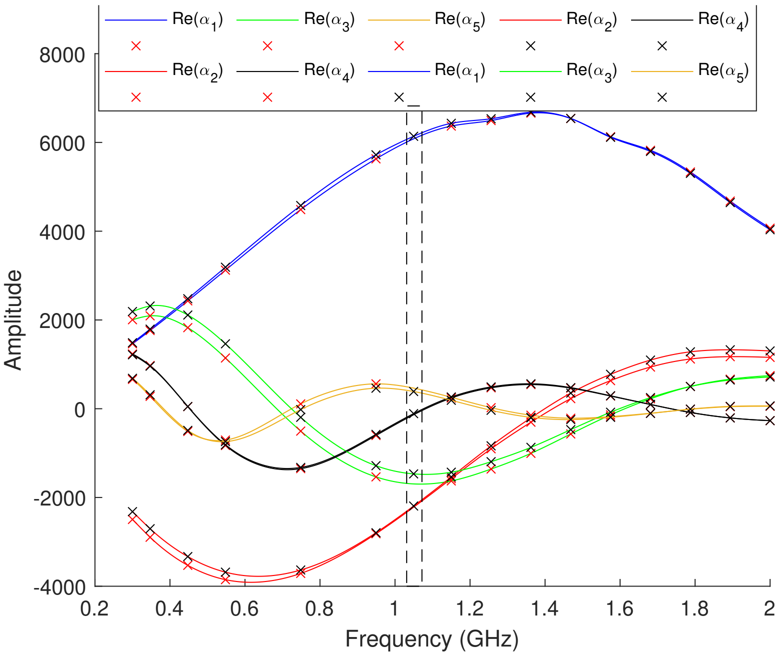

Figure 5.16: Placement of sample 16 according to analysis of α_5 with coefficients α_{1-4} deemed converged

In order to show the effectiveness of the convergence criteria at satisfying desired error limits without wasted computation time, the full DR field was reconstructed using a 13, 15 and 17 sample set. In all cases 7 CBFP basis functions were used to model $\mathbf{E}_{FSR}$ with $\mathbf{E}_{MR}$ modelled with $N_{basis} = N_{samples}$.

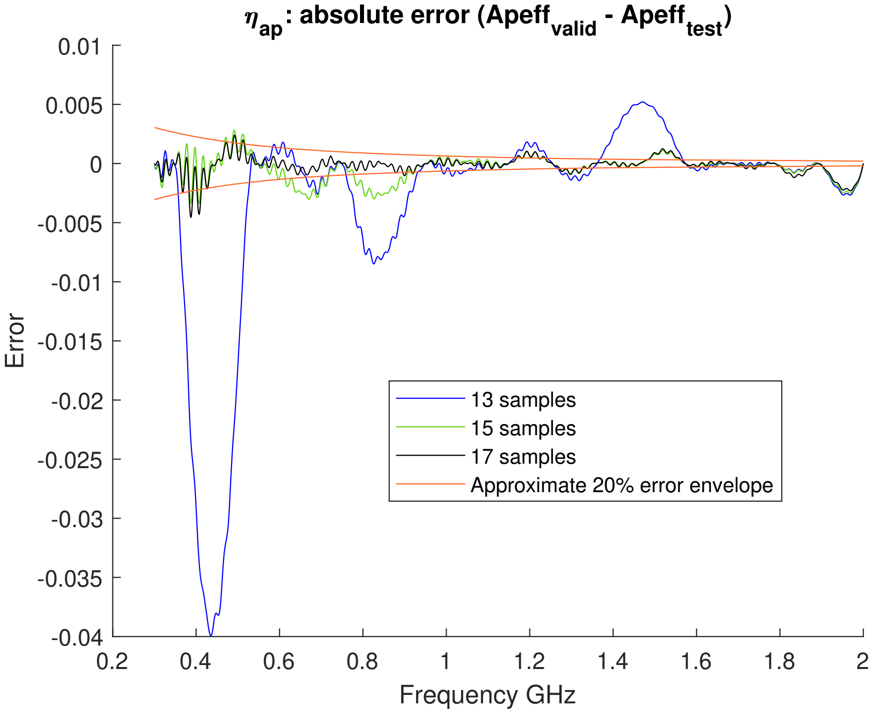

Figure 5.17: Reduction of absolute aperture efficiency error as adaptive sampling places samples in the $\mathbf{E}_{MR}$ design space

Figure 5.17 indicates that a stable aperture efficiency error approximation can be made once 13 samples were placed through application of the exploratory algorithm. The field predicted using 17 samples exhibits approximately a 20 % error on the chromatic aberration ripple amplitude. The results for geometric far-field error are largely the same, with the error decreasing steadily with the adaptive placement of more samples.

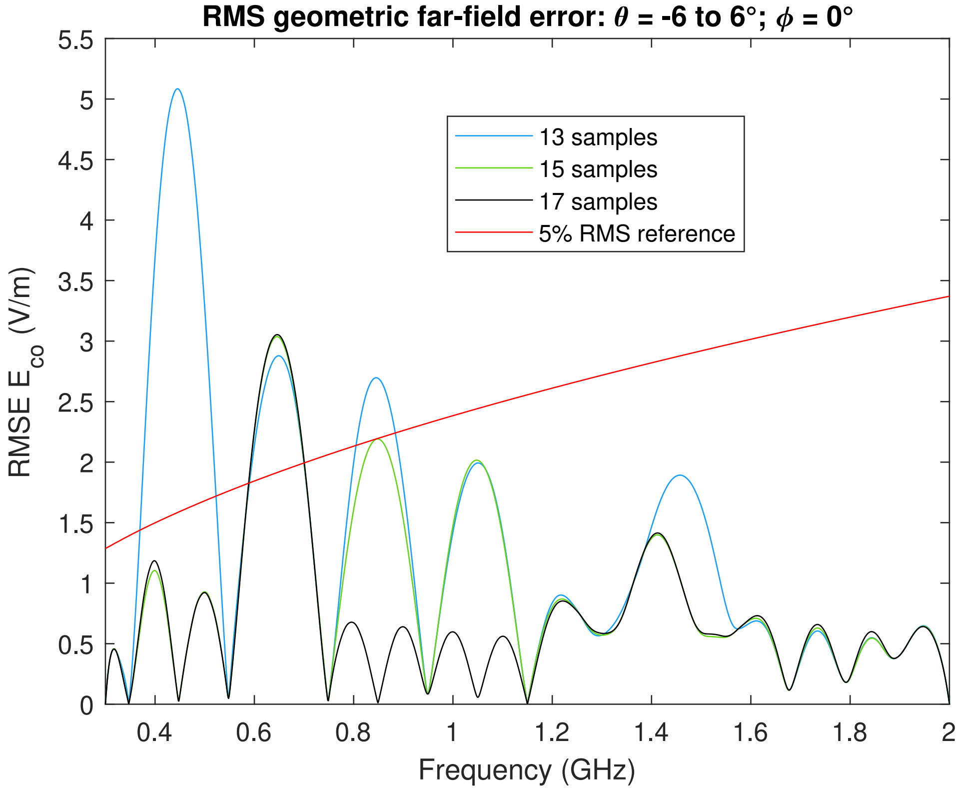

Figure 5.18: Reduction of RMS geometric far-field error as adaptive sampling places samples in the $\mathbf{E}_{MR}$ design space

This suggests the algorithm is filling unknown regions of the design space in a productive manner, decreasing overall field estimation error to desired levels without excessive computation. Furthermore it shows that tracking the convergence of the first 5 basis using an FDL threshold grants the user suitable accuracy vs. cost control over the system. There may be alternate implementations which could achieve superior cost to accuracy results, however, the method above provides a suitably flexible and robust approach for DR design procedures.

The field predictions obtained with the final 19 sample set are given in Figure 5.19 below. Superposition of the $\mathbf{E}_{MR}$ and $\mathbf{E}_{FSR}$ reconstructed with a CBFP expansion 19 and 10 coefficients respectively, as per $A_{cutoff} = 500$ in Equation 4.8 did capture the 19 MHz period chromatic aberration ripple. However, more samples are required in the upper quarter of the bandwidth, as the predicted aperture efficiency exhibits spurious, incorrect behaviour.

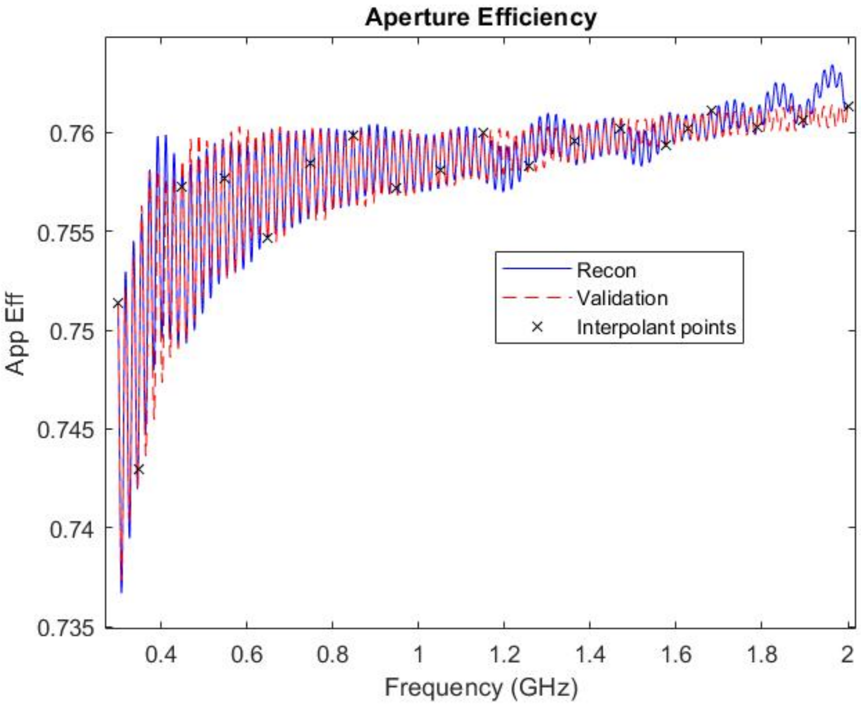

(a) Predicted aperture efficiency 0.3 GHz to 2 GHz

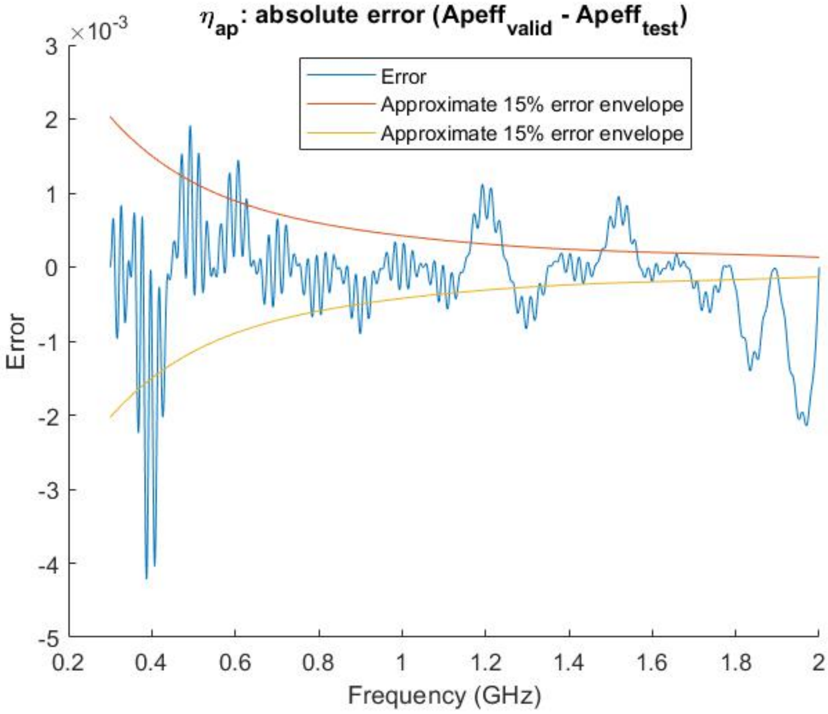

(b) η_{ap} error against 15 % of ripple amplitude

Figure 5.19: SKA adaptive sampling predicted predicted aperture efficiency with ≈19 MHz ripple period

Figure 5.21 shows the far-field patterns for the two worst case errors. The over and undershoot error on the aperture efficiency is a direct result of incorrect side-lobe levels in field predictions at higher frequency, this can be attributed to insufficient training data for the CBFP to accurately model the many contoured sidelobes at higher frequencies, to which aperture efficiency is sensitive.

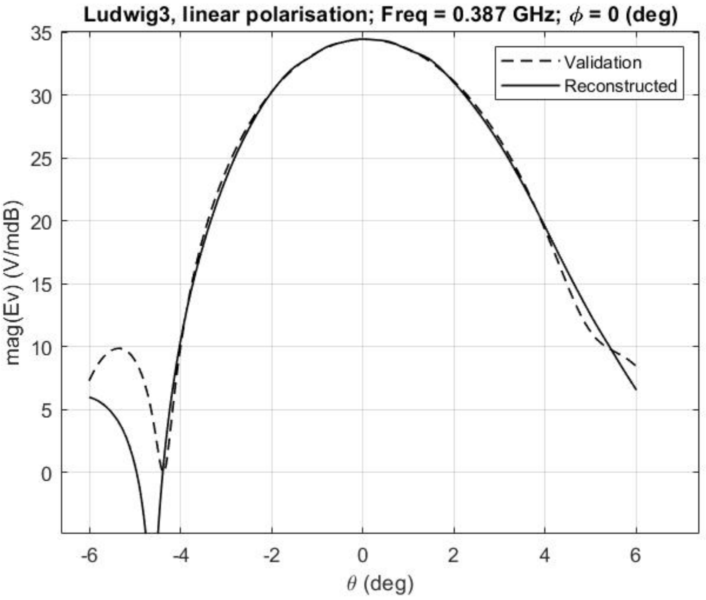

(a) Worst case η_{ap} pattern

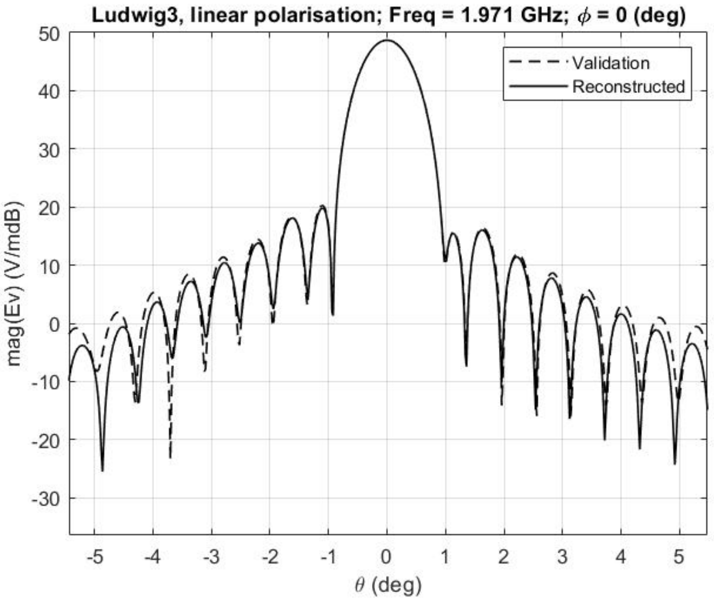

(b) Second worst case η_{ap} pattern

Figure 5.20: SKAU adaptive sample set geometric far-field predictions with $P_{rad} = \frac{2\pi}{\eta}$ with pattern contour leading to slight side-lobe level errors impacting η_{ap}.

The wideband characterisation was successful, with the physics driven basis expansion capturing the contoured radiation patterns with an average geometric far-field RMSE below 2 % RMS of the validation beam intensity. The aperture efficiency was captured to approximately 15 % error on the ripple amplitude.

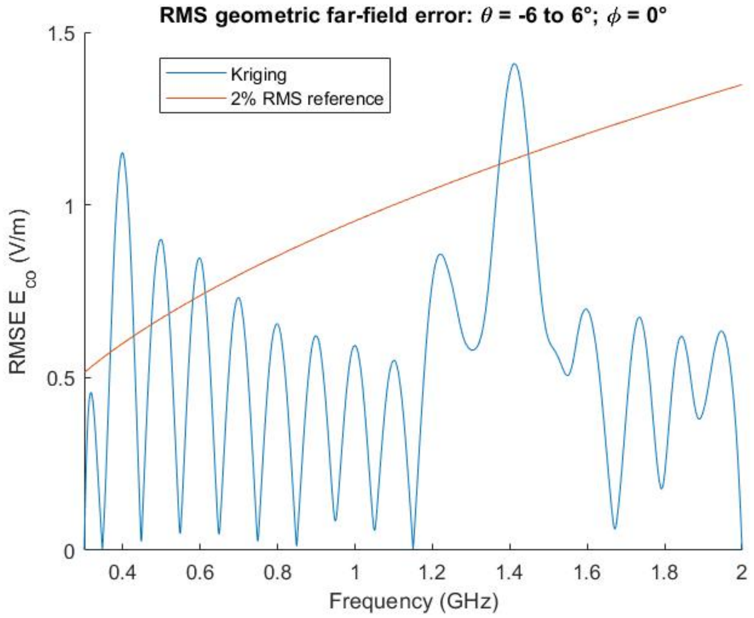

(a) Geometric far-field RMSE vs. 2 % validation $\mathbf{E}_{DR}$ RMS

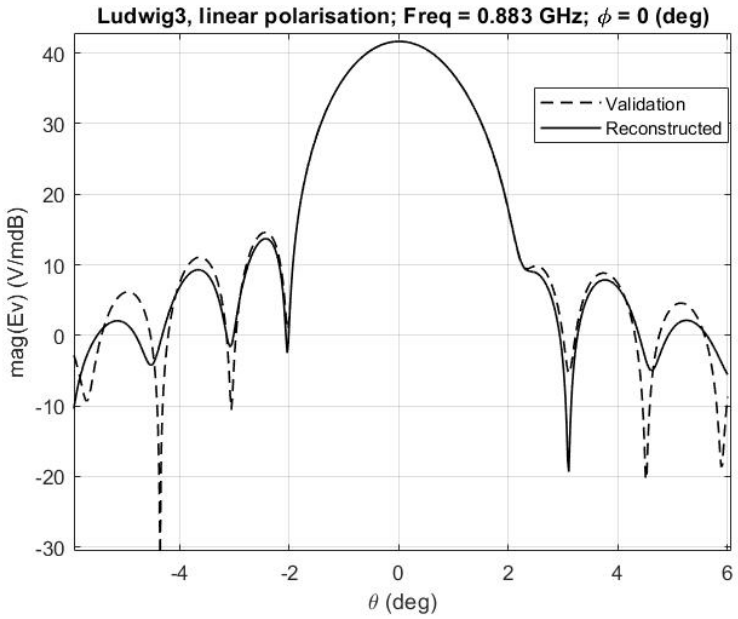

(b) Mean RMSE: $0.54\,\mathrm{V\,m^{-1}}$ contoured beam prediction accuracy

Figure 5.21: Adaptive sampling predicted radiation pattern accuracy with $P_{rad} = \frac{2\pi}{\eta}$.

5.9. Conclusions

Results indicate a significant improvement on other fully simulation based approaches for aperture efficiency characterisation such as in [29], with robust CBFP convergence metrics producing satisfactory results. The implementation allows for reliable ripple modelling without any ray path analysis. Evidence suggests errors in aperture efficiency prediction are tied solely to the accuracy of the far-fields reconstructed using CBFP interpolants, and is in no way related to the periodicity of the chromatic aberration.

Chapter 6

Adaptive sampling model with practical QRFH horn feed pattern

This chapter documents the implementation procedure for the CBFP superposition based surrogate model on a fully practical dual reflector antenna, where the feed pattern is computationally obtained from a physical antenna subject to physics dependant changes across frequency, in order to ascertain its overall validity as a computationally efficient design analysis tool.

6.1. Influence of feed pattern variations on DR performance

The most significant feature of the primary radiation pattern on the directivity performance of a dual reflector is the $-12\,\mathrm{dB}$ beamwidth of the illuminating radiation, as it links directly to the uniformity of $\mathbf{J}_{SR}$ and, therefore, the field incident on the main reflector. The BOR_1 efficiency is also important to quantify the uniformity of the pattern across ϕ, but is secondary to the taper itself.

Stabilisation of an antenna's beam pattern across wide bandwidths is extremely difficult, and pattern variations are unavoidable. This results in a field taper illuminating the sub-reflector which varies across frequency contributing to aperture efficiency variations not modelled by Gaussian pattern approximations.

Most importantly, the macro frequency changes in the dual reflector secondary pattern are typically due to changes of the primary field's phase centre or pattern, particularly when physically compact feeds are used. Rapid changes in the beamwidth or phase centre of the primary pattern lead to sharp changes in aperture efficiency across frequency, and as such, present a challenge from a modelling perspective.

6.2. QRFH aperture controlled Horn antenna

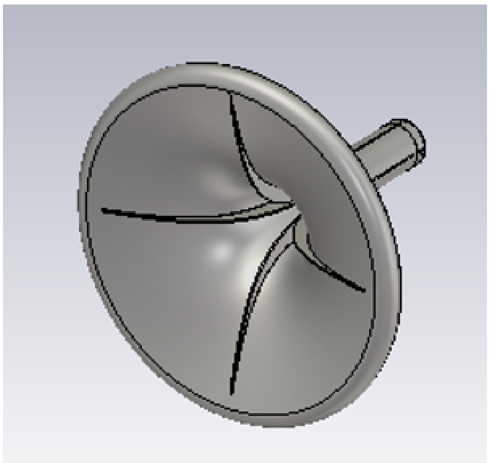

Figure 6.1: 3D CST model of QRFH dual reflector feed horn [3].

The horn presented by Mokhupuki in [3] is a typical example of the type of antenna used in modern compact wideband DR feed systems. Full wave solutions generated via MoM simulations of the antenna in the CST electromagnetic solver were used to illuminate the dual reflector geometries in GRASP. The figure below illustrates the typical feed pattern variations across frequency associated with a well designed feed horn:

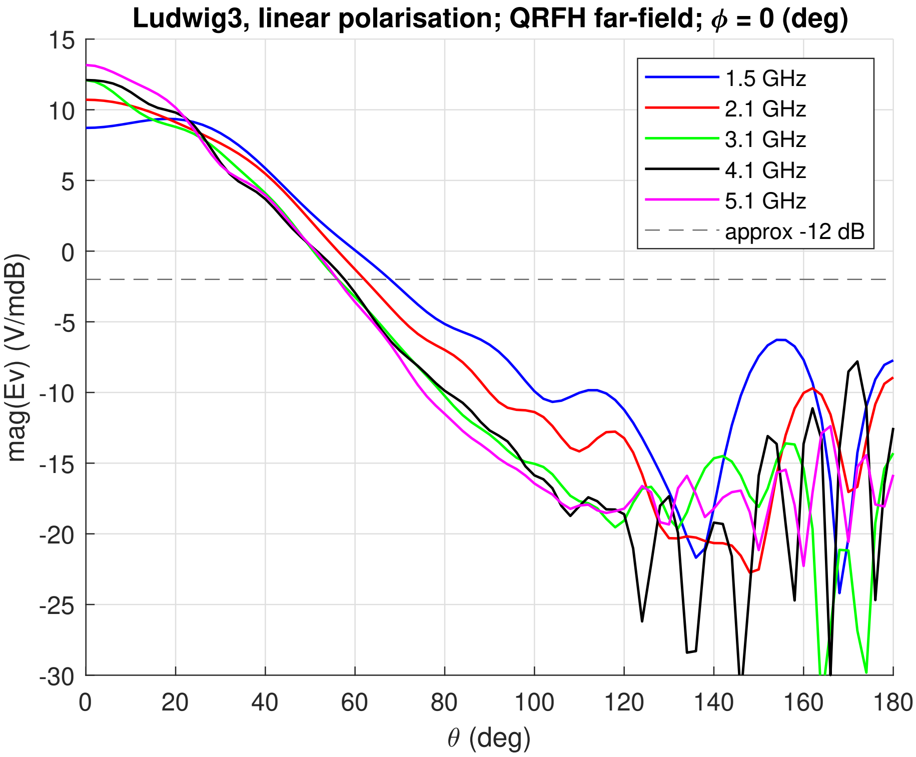

Figure 6.2: Wideband far-field patterns of QRFH feed horn used for dual reflector illumination.

The -12 dB beamwidth sits between 48° and 60° for a band of operation from 1.5 GHz to 5.15 GHz making it more suitable for offset Gregorian reflector geometry which can accommodate larger subtended angles. Wide-band behaviour is of interest here, as this is what contributes to fluctuations in the overall DR secondary fields targeted by this model. This set of feed patterns is sufficiently focused for a fair assessment of the adaptive model when placed in a practical dual reflector setup.

6.3. Importance of correct feed placement

Practical feed antennas are subject to frequency dependant phase centre shifts, and incorrect positioning of its aperture with respect to the focal point of the sub-reflector can lead to spurious field variations and surface current densities at certain frequencies [26].

For the modelling presented here, the phase centre of the QRFH horn was calculated by applying the method presented by Kildal in [25] to the complex field data from CST. The feed was then shifted along its axis to a point minimising deviation of the phase centre, such that the spherical antenna radiation in GRASP was centred as close as possible to the focal point of the sub-reflector for all frequencies. It is stressed to the reader that small changes in the positioning of the feed have dramatic effects on aperture efficiency, and a well positioned primary pattern source is imperative for correct dual reflector performance and modelling.

6.4. VEXPA considerations for practical feeds

The VEXPA approach is dependant on the assumption that the underlying function on which the complex exponential modulation occurs is extremely slow varying.

For a practical feed antenna there may be rapid changes in the feed pattern due to newly propagating modes, these rapid changes affect the stability of the aperture fields of the main and sub-reflector, leading to minor errors in the phase normalisation shift calculation if the values of σ and ρ are too high, creating a need for more computationally expensive samples to capture new artificial phase variations in the secondary pattern.

It is recommended that shifts in frequency which cause more than a 1 dB change in primary pattern directivity are avoided to prevent this, as the secondary dual reflector pattern must be qualitatively constant over the VEXPA analysis bandwidth.

6.5. Computational considerations for practical feed modelling

The implementation for this sequential design process passes single frequency batch mode operation commands for the QRFH horn antenna to CST. Such an ordering of computations can present a severe hindrance to the over-all computational speed of the surrogate model if CST is not instructed to store mesh information from previous instances in batch mode, resulting in regeneration of the mesh upon each instance. Full-wave estimations of the primary pattern typically take longer than the calculation of the dual reflector fields in GRASP (when using PO+PTD).

It is, therefore, recommended that the CST project is setup in the target bandwidth with a mesh suitable for predictions at the highest target frequency and adaptive mesh refinement is switched off. Otherwise the mesh refinement step continuously adds tetrahedrons causing additional computational overhead at each instance increasing computational cost while not improving the accuracy of the field estimation.

Dense field data is typically available for the final software models of such horn feeds, and as such, utilising available data where possible rather than prompting additional costly simulations is a faster and more elegant approach.

For the experiments shown here QRFH field data was calculated using the general purpose frequency domain solver of CST with an adaptive tetrahedral mesh at 5 MHz intervals. The closest value contained in these samples was then used to facilitate the generation of fields at specific frequencies requested by the DR interpolation model.

The model presented here supports generation of new field data at each desired frequency through visual basic batch mode instructions, and if high fidelity data for the feed in question is not available, a single frequency CST simulation approach is preferred.

6.6. Wide-band Offset Gregorian experiment

An offset Gregorian geometry was synthesised using the parameter framework in [40] with a D_{MR} =8 m paraboloid and an extended ellipsoidal sub-reflector with D_{SR} =3.6 m separated by a distance of 1.5 m from the MR aperture, subtending a half angle of θ_e =57° at the SR focal point. The geometry is designed to represent a practical example of a compact dual reflector where chromatic aberration ripple inhibits modelling.

A modelling experiment varying D_{MR} from 40 to 137λ and D_{SR} from 18 to 62λ was conducted to evaluate the prediction error as a function of support points in practical settings. The experiment varied the Frobenius distance criteria for the first 5 $\mathbf{E}_{MR}$ basis coefficients α_{1-5} from 10 % to 50 % to control the number of frequency samples used by the surrogate model across the 1.7 octave bandwidth (1.5 GHz to 5.15 GHz). In all cases $A_{cutoff} = 500$ for both $\mathbf{E}_{MR}$ and $\mathbf{E}_{FSR}$. VEXPA normalisation was done on an 1 MHz grid with $\sigma = 15$ and $\rho = 7$, with the σ sample at 1.515 GHz included for the initial support set.

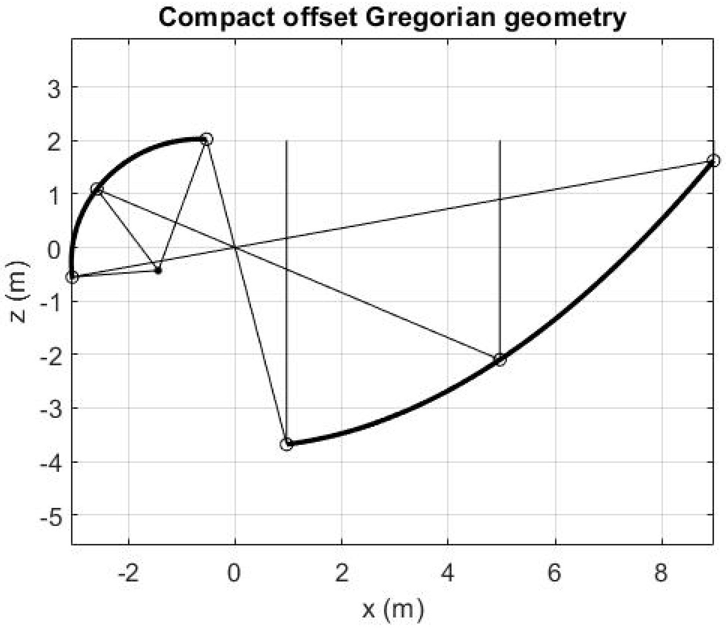

Figure 6.3: Offset Gregorian geometry evaluated from 1.5 GHz to 5.15 GHz

Table 6.1: CBFP convergence criteria and number of selected frequency samples according to FDL for $\mathbf{E}_{MR}$ α_{1-5}.

Frobenius distance threshold (%)	support samples	mean far-field RMSE ($\mathrm{V\,m^{-1}}$) $\theta = -4°$ to $4°$; $\phi = 0°$
10	58	0.13
20	41	0.12
25	30	0.23
30	27	0.31
40	19	0.7
50	17	1.4

It is evident that there is a large increase in error reduction per sample up until a certain number of samples where the improvement begins to waver, as the CBFP expansion aoproaches convergence limits. This is typical in such problems, as at the start any new information is highly valuable to an interpolant, but gradually the information per sample begins to decay. The validation dual reflector field has a mean RMS intensity of 60 $\mathrm{V\,m^{-1}}$

in the $\phi = 0°$ cut, with 2 % of this intensity equal to 1.2 V m^{-1}. With error below this, the main beam and first side-lobe should be accurately predicted. The geometric far-field $RMSE_{\phi=0°}$ across frequency for each support set in Table 6.1 is plotted below.

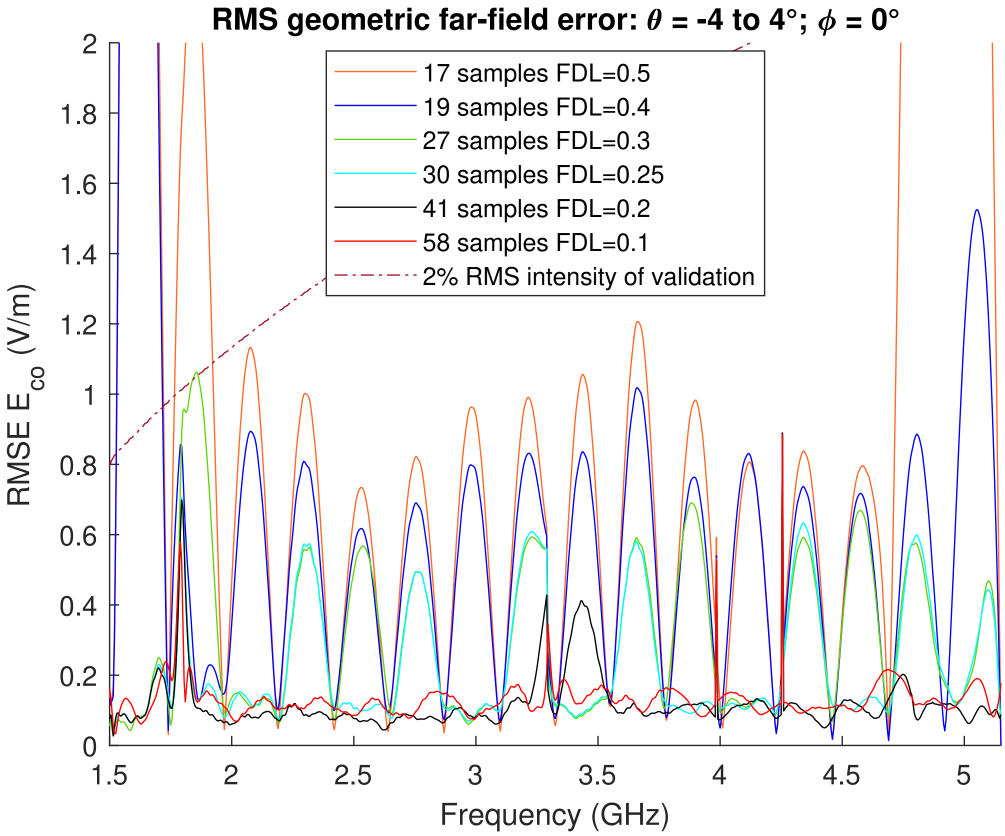

Figure 6.4: Geometric far-field RMSE across θ for increased number of support samples vs. 2 % RMS validation field intensity in the $\phi = 0°$ plane.

The increase in mean geometric error for the 58 sample case can be attributed to the onset of over-fitting inside the CBFP coefficients. The basis cutoff threshold of A_{cutoff} (Equation 4.8) = 500 is effective as a maximum of 18 basis coefficients were used to generate $\mathbf{E}_{MR}$ and 15 for $\mathbf{E}_{FSR}$, for all cases above 19 support samples. At this point it is likely that the SVD has extracted the geometric features to a higher resolution allowing for near perfect beam reconstruction with the first 15 coefficients as shown in [22].

Analysis of the RMSE suggests that the optimal position for a trade-off between accuracy and cost is a convergence threshold in the range of 20 % to 25 % with more than 30 samples in total. This allows for accurate beam prediction up to far-out sidelobes.

The aperture efficiency and beam reconstruction for the highest accuracy 41 sample case represents the upper bound of accuracy obtainable while the density remains significantly below the Nyquist rate of the ≈ 25 MHz period chromatic ripple evident in the far-fields of this dual reflector. A linear density approach at Nyquist rate would require 290 samples.

A comparison between the reconstructed (*recon*) aperture efficiency across frequency and a mean RMSE farfield prediction is illustrated in Figures 6.5 and 6.6. The result perfectly illustrates the need for a method which does not approximate the ripple as an amplitude modulation when using practical primary patterns, as the ripple amplitude changes erratically with frequency as the internal field interactions change.

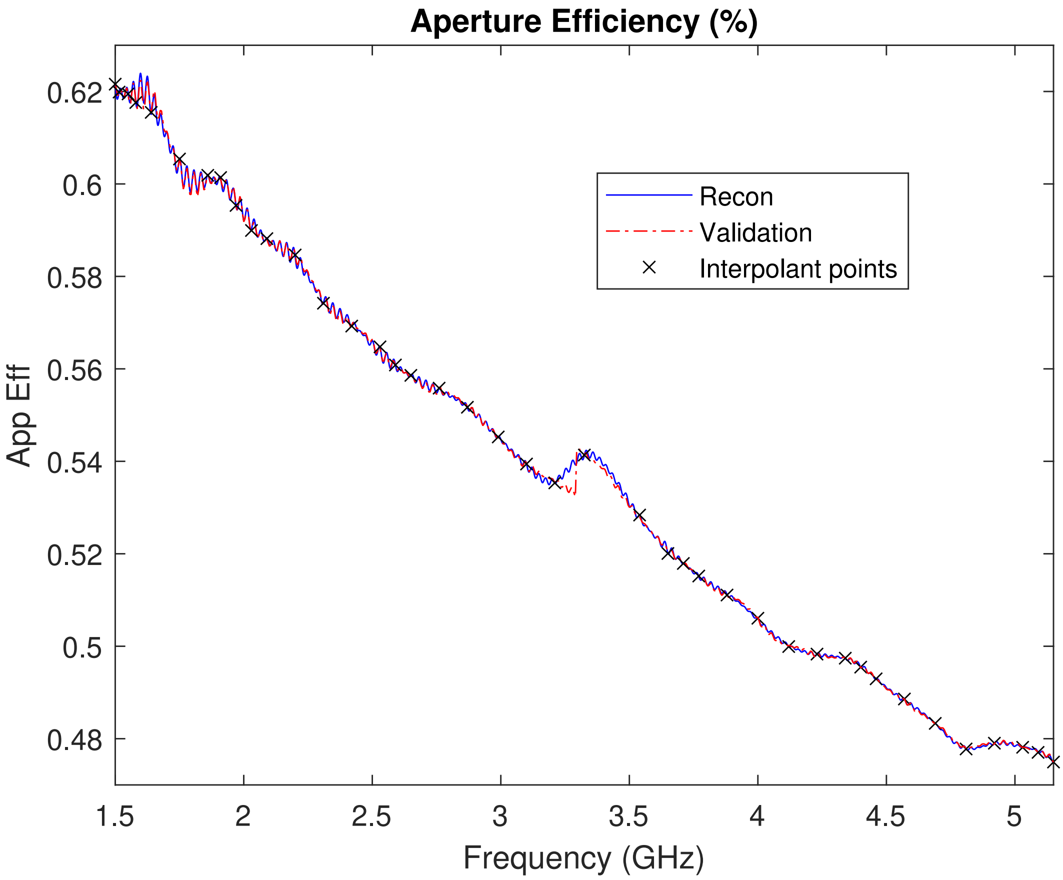

Figure 6.5: Comparison between aperture efficiency reconstructed with superposition of $\mathbf{E}_{MR}$ and $\mathbf{E}_{FSR}$ CBFP Kriging-Matérn $(\frac{3}{2})$ interpolants using 41 adaptive samples and validation set marking accuracy convergence.

The superposition approach captures zones where the diffraction effects are not the primary ripple factor, as well as regions where the ripple is pronounced to the same accuracy. This again contributes to the fact that the required sample density is independent of the ripple period. The beam prediction error below 0.01 dB across the full geometric range for a 41 sample mean RMSE case of $0.12\,\mathrm{V\,m^{-1}}$ is illustrated below in Figure 6.6.

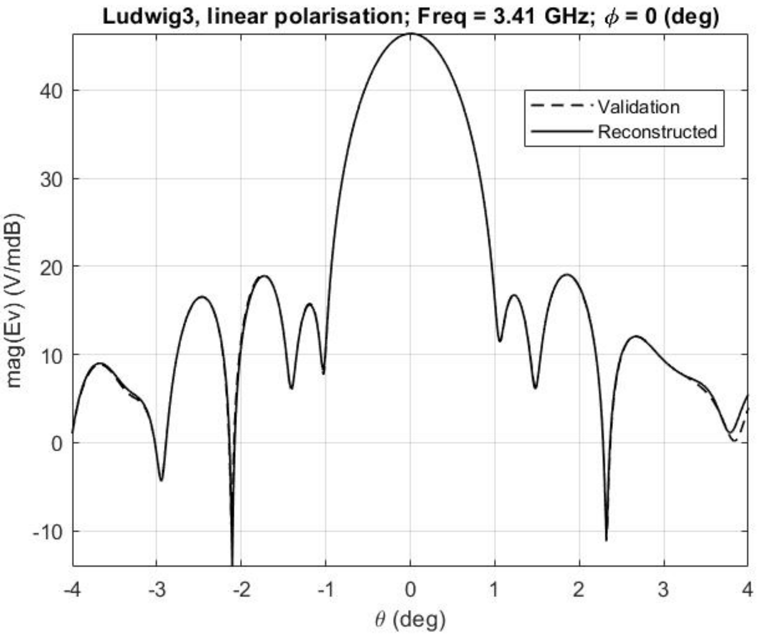

Figure 6.6: Mean RMSE beam for 41 sample case using 18 and 15 basis functions for E_{MR} and E_{FSR} respectively.

6.7. Influence of Primary pattern on secondary pattern

The shape of the primary radiation pattern is typically responsible for the macro changes in dual reflector aperture efficiency across frequency. This is clearly visible in the correlation between the directivity of the feed across frequency and aperture efficiency.

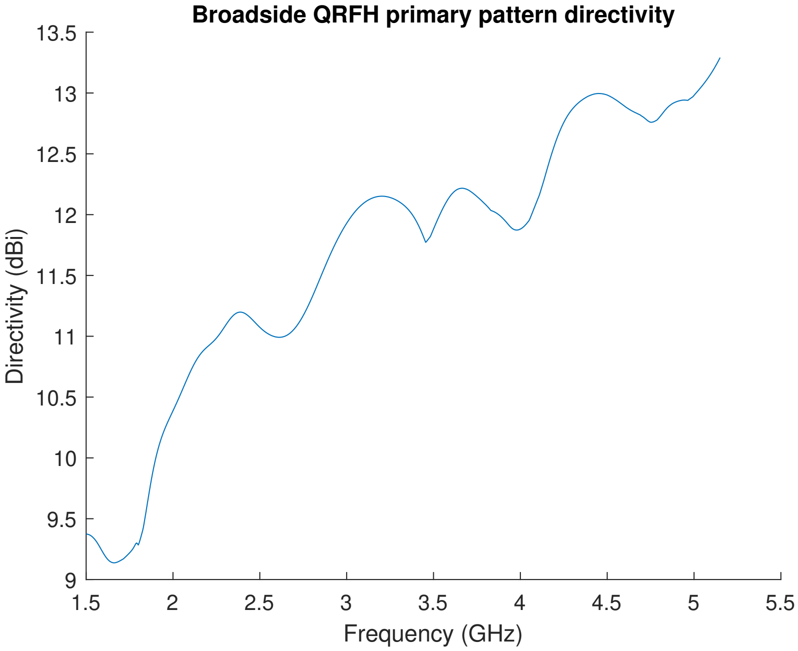

Figure 6.7: Primary pattern directivity obtained with QRFH horn presented in [3] used for illumination of dual reflectors in this chapter.

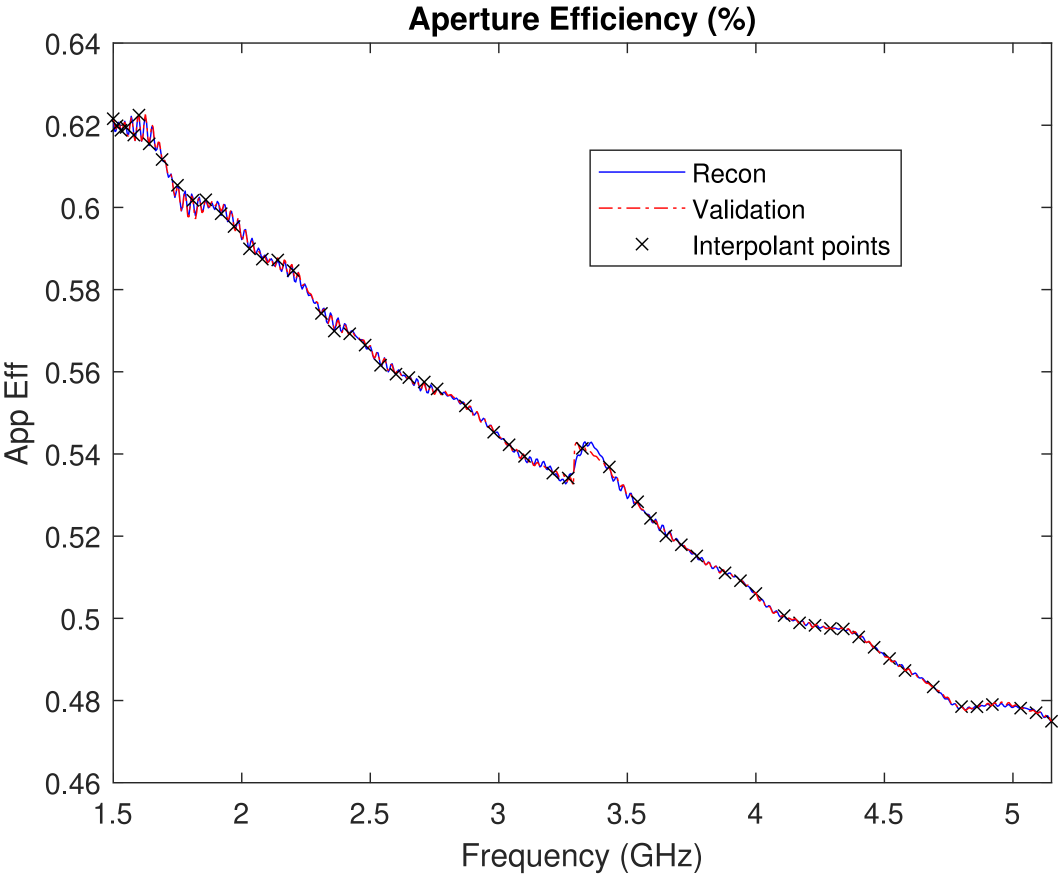

Figure 6.8: Illustration CBFP interpolant model tolerating high non-linearity in primary pattern if sufficiently sampled.

The sharp rise in directivity at 3.35 GHz is attributed to the suppression of a higher order mode by the axial ridges in the horn, and illustrates how sharp changes in the primary pattern are carried through to the aperture efficiency. This can only be captured by a sparse density model if a large number of samples fall in that region as shown in Figure 6.8 for the 58 sample case.

6.8. SKAU offset Gregorian at SKA mid-band

The QRFH horn fields were then scaled by a linear factor of 5 such that they represented primary patterns from 0.3 GHz to 1.03 GHz such the model could be tested in an approximate range of its target SKA mid bandwidth, 0.35 GHz to 1.05 GHz. This is a strong example of an actual dual reflector for radio interferometry, where modelling of the aperture efficiency variations is high priority.

A consequence of this is that feed pattern variations across absolute frequency are artificially sped up, presenting a larger challenge during modelling.

These variations are still valid for practical testing, and simply relate to an identical horn 5 times larger in electrical size with free-space impedance transformed to an impedance other that 50 Ω.

The first 5 basis coefficients were used to classify the model as converged, using a Frobenius distance convergence threshold of 25 %. VEXPA normalisation was performed with $\sigma = 11$ and $\rho = 7$ to account for the compressed feed pattern behaviour. The σ VEXPA sample at 311 MHz was included in the initial support sample design.

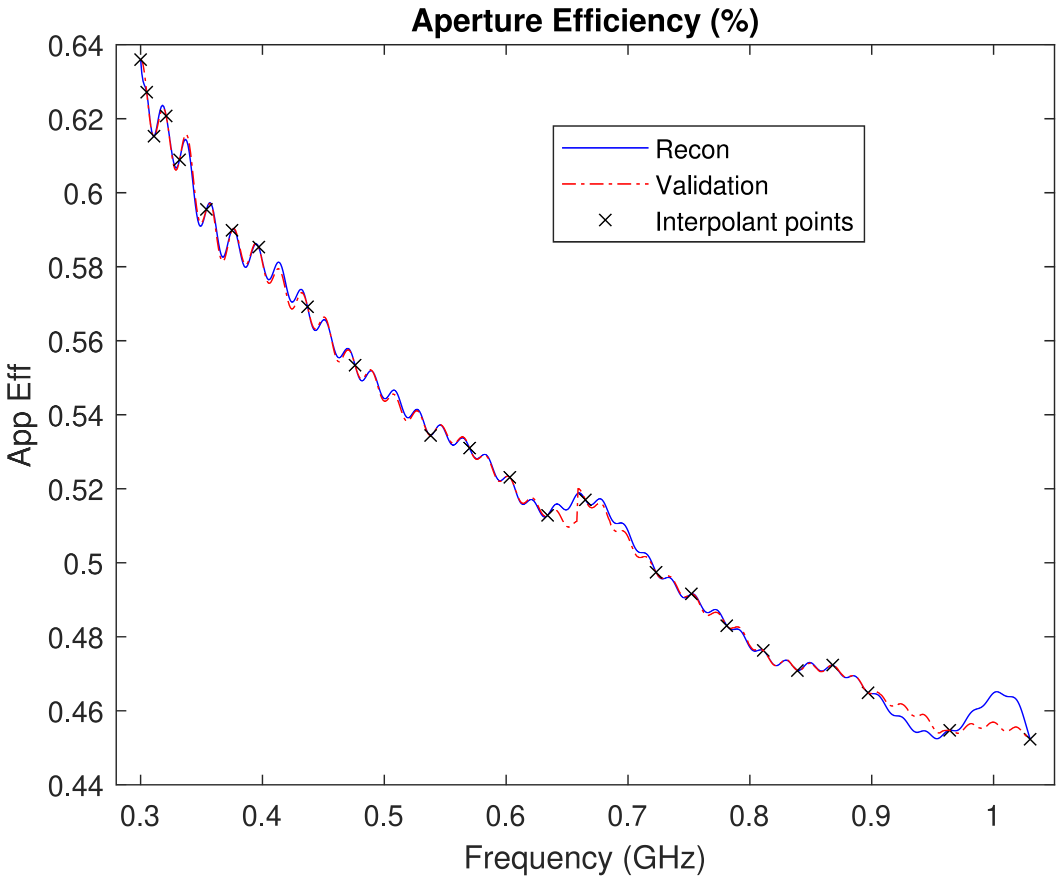

Figure 6.9: Comparison between aperture efficiency reconstructed with superposition of $\mathbf{E}_{MR}$ and $\mathbf{E}_{FSR}$ CBFP Kriging-Matérn ($\frac{3}{2}$) interpolants using 24 adaptive samples and validation set.

The convergence criteria required 24 samples across the bandwidth to classify the $\mathbf{E}_{MR}$ CBFP expansion as converged. $A_{cutoff} = 500$ corresponded to reconstruction using 16 interpolated MR basis functions and 12 interpolated FSR basis functions.

The aperture efficiency prediction is well within acceptable error except around 1 GHz where spurious oscillation due to insufficient sample density is observed. The beam reconstruction for the peak of this spike is shown in Figure 6.10:

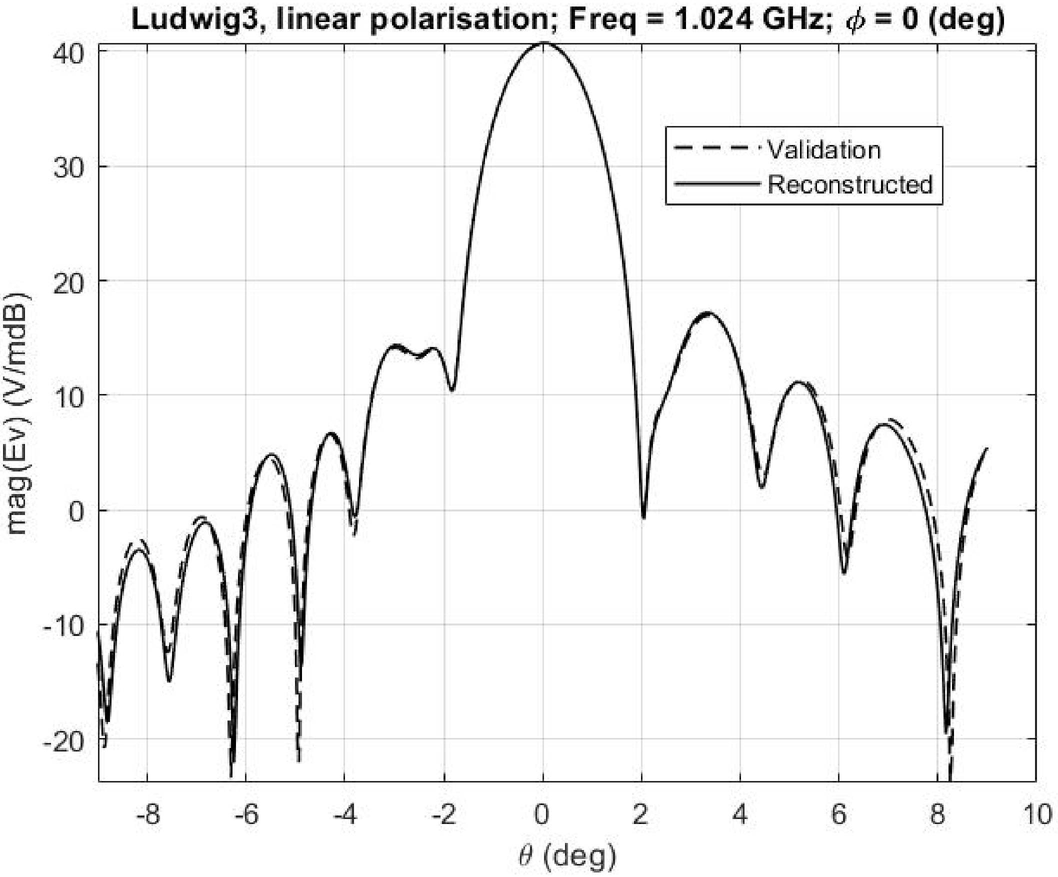

Figure 6.10: Predicted far-field pattern at peak of aperture efficiency spike around 1 GHz showing main beam and first side-lobe remains at acceptable accuracy.

It is clear that the exploratory adaptive sampling algorithm was able to utilise the CBFP superposition method to characterise the aperture efficiency with an absolute worst case error of 1 %.

6.9. Convergence Considerations with non-ideal feed patterns

To evaluate how close the CBFP coefficients obtained with the converged 24 direct sample Kriging model are to those of an ideal orthogonal basis set which perfectly isolates all far-field features of the underlying antenna, the validation field solutions from GRASP were used to generate 16 basis coefficients for $\mathbf{E}_{MR}$. Direct comparisons of coefficients 1,2,3, and 5 are plotted in Figure 6.11:

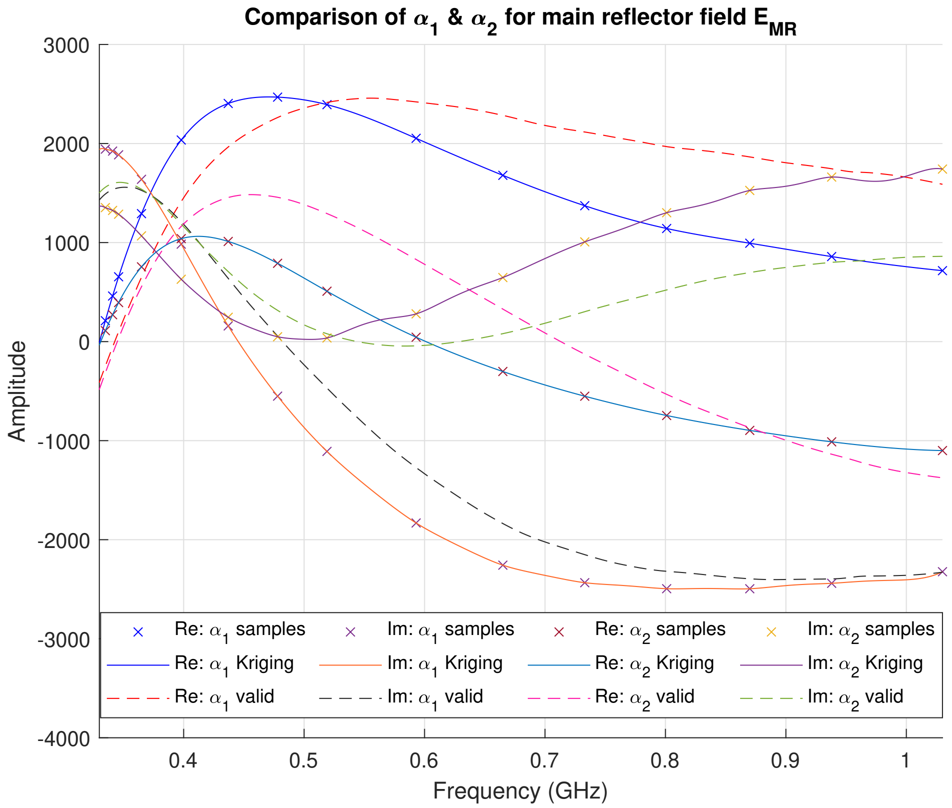

(a) Comparison for CBFP coefficients 1 & 2

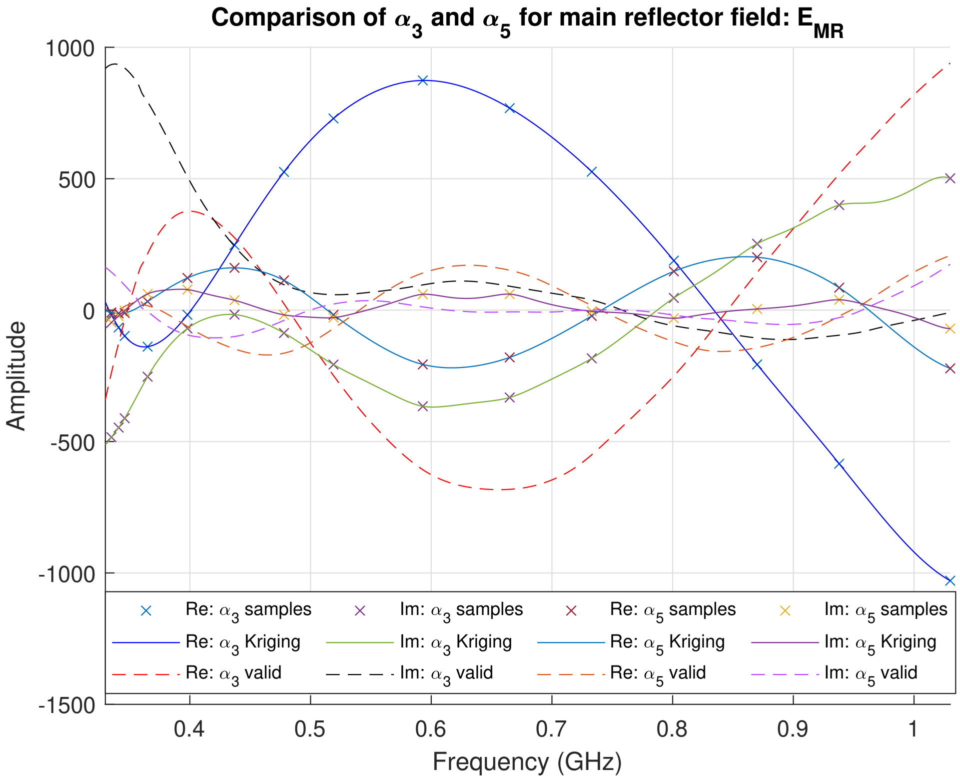

(b) Comparison for CBFP coefficients 3 & 5

Figure 6.11: Comparison between 24 adaptive sample set Kriging-Matérn CBFP interpolant coefficients and validation CBFP coefficients

There is a strong correlation between the first two coefficients across the band, with relatively small changes in the function shape. The later coefficients show more deviation with the amplitudes larger for our model generated using sparser samples.

This is expected as the validation basis functions have an incredibly large amount of training data such that the physical elements are isolated with increased orthogonality. This shows the impressive robustness of the CBFP interpolation method as the fields were reproduced to a high accuracy even with basis functions which are not yet perfectly locked onto individual physical features due to a sparser sample density.

6.10. Conclusions and recommendations

Analysis of the CBFP patterns produced with a practical feed antenna indicate that the variations in the primary pattern directivity have a significant influence on the wideband shape of DR aperture efficiency, with strong correlation at frequency points of inflection.

These variations become the limiting factor for the adaptive sampling algorithm, as it is likely that the variations in the feed pattern are more rapid than those of $\mathbf{E}_{MR}$ and $\mathbf{E}_{FSR}$.

Furthermore, the range of bandwidth used for VEXPA analysis must be decreased to a region with a stable primary pattern to ensure the correct extraction of artificial phase periodic variations.

The simulation data provides strong evidence for the case that the overall model error for far-field prediction is tied to the successful singular value decomposition of the geometric beam behaviour across frequency, with the chromatic aberration ripple, regardless of its frequency, included at minimal additional cost to direct simulations at support frequencies when employing the CBFP superposition approach.

Using the convergence criteria for this implementation, it is recommended that at least the first 5 basis coefficients with a Frobenius distance threshold of 20 % is used to for an accurate main beam and first sidelobe in a contoured pattern.

Furthermore, for octave bandwidths a base set of more than 20 samples should deliver far-field patterns accurate to several sidelobes. Stricter convergence methods improve error to a point, however, improvement saturates at ≈35 samples per octave, above which results may degrade due to over-fitting.

Chapter 7

Conclusion and Recommendations

This thesis illustrates that the CBFP superposition method is a suitable foundation for interpolation based global surrogate models which can facilitate fully software driven wideband analysis of dual reflector secondary far-field patterns. Considering the fields of the main reflector and feed and sub-reflector separately can provide a tenfold improvement in computational efficiency when compared to direct dual reflector far-field interpolation, particularly in geometry where the ripple is extremely quick, by successfully isolating each slowly varying field component contributing to the rapid variations.

A robust exploratory adaptive sampling approach facilitates the placement of expensive direct simulation data to synthesise an accurate global model without any prior knowledge or analysis of the dual reflector geometry under test. The model is only hindered by over-fitting for extremely large data-sets and the possible waste of one expensive simulation during phase normalisation through VEXPA.

Ultimately, surrogate modelling with the CBFP superposition approach was successful, allowing for the rapid chromatic aberration ripple present in dual reflector far-fields to be captured with a sample density independent of its frequency, offering a significant reduction in computational cost compared to direct secondary pattern interpolation.

7.1. Future Research

Future work could involve investigation into other interpolation models and adaptive sampling algorithms to optimise the robust approach shown here. An investigation into beam pattern normalisation using Bessel or other basis functions as in [22] to minimise the number of CBFP coefficients required for accurate generation of $\mathbf{E}_{MR}$ and $\mathbf{E}_{FSR}$ respectively is also of value.

In a broader scope, the physics based field superposition approach could be adopted in the design of a Pareto base multi-objective framework for fully software driven design and optimisation of dual reflector geometry.

Bibliography

[1] A. Stockert, “Photograph of the two cassegrain antennas used at the stockert radio telescope,” free for personal or commercial use. [Online]. Available: https://pixabay.com/de/photos/radioteleskop-astronomie-forschung-5817469/

[2] R.-M. Weideman, “Linear sparse regular array antenna demonstrator,” Master’s thesis, Faculty of Engineering, Stellenbosch University, Stellenbosch, South Africa, March 2021, supervisor: Prof. D. I. L. de Villiers.

[3] F. T. T. Mokhupuki, “Efficient optimisation of wideband reflector feed antennas,” Ph.D. dissertation, Faculty of Electrical Engineering, University of Stellenbosch, Stellenbosch, South Africa, 2021.

[4] R. Graf, *Modern Dictionary of Electronics*, ser. Electronics & Electrical. Elsevier Science, 1999. [Online]. Available: https://books.google.co.za/books?id=uah1PkxWeKYC

[5] R. Johnson, *Antenna Engineering Handbook*, 3rd ed. McGraw Hill Inc., 1993.

[6] C. A. Balanis, *Modern antenna handbook*, 1st ed. Wiley, 2008.

[7] M. A. Cordiner, N. L. J. Cox, C. J. Evans, C. Trundle, K. T. Smith, P. J. Sarre, and K. D. Gordon, “A survey of diffuse interstellar bands in the andromeda galaxy: Optical spectroscopy of m31 ob stars,” *The Astrophysical Journal*, vol. 726, Dec 2010. [Online]. Available: https://iopscience.iop.org/article/10.1088/0004-637X/726/1/39/pdf

[8] V. A. Moss, J. R. Allison, E. M. Sadler, R. Urquhart, R. Soria, J. Callingham, S. J. Curran, A. Musaeva, E. K. Mahony, M. Glowacki, S. A. Farrell, K. W. Bannister, A. P. Chippendale, P. G. Edwards, L. Harvey-Smith, I. Heywood, A. W. Hotan, B. T. Indermuehle, E. Lenc, J. Marvil, D. McConnell, J. E. Reynolds, M. A. Voronkov, R. M. Wark, and M. T. Whiting, “Connecting X-ray absorption and 21 cm neutral hydrogen absorption in obscured radio AGN,” *Monthly Notices of the Royal Astronomical Society*, vol. 471, no. 3, pp. 2952–2973, 07 2017. [Online]. Available: https://doi.org/10.1093/mnras/stx1679

[9] J. Baars, *The Paraboloidal Reflector Antenna in Radio Astronomy and Communication: Theory and Practice*, 01 2007.

[10] R. Lehmensiek and I. P. Theron, "Minimizing the meerkat system noise temperature," in *2014 XXXIth URSI General Assembly and Scientific Symposium (URSI GASS)*, 2014, pp. 1–4.

[11] S. G. K. P. Foldes, "Theoretical and experimental study of wideband paraboloid antenna with central reflector feed," *RCA Review*, vol. 21, pp. 94–116, March 1960.

[12] J. L. Volakis, *Antenna Engineering Handbook*, 4th ed. McGraw-Hill Inc., 2007.

[13] R. Lehmensiek, I. Theron, and D. De Villiers, "Deriving an optimum shaped reflector system for the ska single pixel feeds," 07 2015, pp. 1370–1371.

[14] R. A. Santos, R. A. Penchel, C. S. Arismar, and J. F. Mologni, "High-performance omnidirectional dual-reflector antenna based on a dieletric subrefletor support," in *2015 SBMO/IEEE MTT-S International Microwave and Optoelectronics Conference (IMOC)*, 2015, pp. 1–5.

[15] A. R. Thompson, J. M. Moran, and G. W. Swenson, *Introductory Theory of Interferometry and Synthesis Imaging.* Cham: Springer International Publishing, 2017, pp. 59–88. [Online]. Available: https://doi.org/10.1007/978-3-319-44431-4_2

[16] A. R. Thompson, J. M. Moran, and G. W. Swenson, *Introductory Theory of Interferometry and Synthesis Imaging.* Cham: Springer International Publishing, 2017, ch. 4. [Online]. Available: https://doi.org/10.1007/978-3-319-44431-4_2

[17] D. C. Price, "4 - real-time stream processing in radio astronomy," in *Big Data in Astronomy*, L. Kong, T. Huang, Y. Zhu, and S. Yu, Eds. Elsevier, 2020, pp. 83–112. [Online]. Available: https://www.sciencedirect.com/science/article/pii/B9780128190845000134

[18] J. McKean. (2015) Lecture: An introduction to modern radio interferometers. [Online]. Available: https://www.eso.org/2Fsci/2Fmeetings/2F2015/2Feris2015/2FL3_ModernInterferometers.pdf&usg=AOvVaw0CcRTGOatKYWWm_u2x8dqP

[19] T. Huang, Y. Zhu, and Y. Zheng, "3 - preprocessing pipeline on fpga," in *Big Data in Astronomy*, L. Kong, T. Huang, Y. Zhu, and S. Yu, Eds. Elsevier, 2020, pp. 61–81. [Online]. Available: https://www.sciencedirect.com/science/article/pii/B9780128190845000122

[20] Y. Zhu, H. You, J. Hou, Y. Zheng, T. Huang, and Y. Song, "12 - high-performance computing for astronomical big data," in *Big Data in Astronomy*, L. Kong, T. Huang, Y. Zhu, and S. Yu, Eds. Elsevier, 2020, pp. 305–323. [Online]. Available: https://www.sciencedirect.com/science/article/pii/B978012819084500002X

[21] D. I. L. de Villiers, “Gain ripple in small offset gregorian antennas,” *IEEE Interneation Symposium on Antennas and propagation, VOL. 61, NO. 5*, July 2011.

[22] D. I. L. de Villiers, “Characteristic basis function pattern modeling of wideband reflector antenna beam pattern frequency variations,” 09 2018, pp. 220–223.

[23] D. I. L. de Villiers, “Prediction of aperture efficiency ripple in clear aperture offset gregorian antennas,” *Antennas and Propagation, IEEE Transactions on*, vol. 61, pp. 2457–2465, 05 2013.

[24] D. I. L. de Villiers, R. Lehmensiek, and M. V. Ivashina, “Effects of diffraction and feed pattern variation in shaped offset gregorian reflectors,” *IEICE Trans. Commun.*, vol. 101-B, no. 2, pp. 316–323, 2018. [Online]. Available: https://doi.org/10.1587/transcom.2017ISP0006

[25] P. Kildal, *Foundation of Antennas: A Unified Approach.* Professional Publishing Svc., 2000. [Online]. Available: https://books.google.co.za/books?id=YqrgngEACAAJ

[26] E. Jørgensen, “Ticra tools user’s manual ver 20.1.0,” 01 2021, overview of PO, PTD, MOM, BOR-MOM as applied by the GRASP solver.

[27] D. Gorissen, I. Couckuyt, P. Demeester, T. Dhaene, and K. Crombecq, “A surrogate modeling and adaptive sampling toolbox for computer based design,” *Journal of Machine Learning Research*, vol. 11, pp. 2051–2055, 07 2010.

[28] R. Lehmensiek and P. Meyer, “Creating accurate multivariate rational interpolation models of microwave circuits by using efficient adaptive sampling to minimize the number of computational electromagnetic analyses,” *IEEE Transactions on Microwave Theory and Techniques*, vol. 49, no. 8, pp. 1419–1430, 2001.

[29] J. P. Jacobs and D. I. L. de Villiers, “Gaussian process modeling of aperture efficiency ripple in reflector antennas,” in *2015 Loughborough Antennas Propagation Conference (LAPC)*, 2015, pp. 1–4.

[30] A. Young, R. Maaskant, M. V. Ivashina, D. I. L. de Villiers, and D. B. Davidson, “Accurate beam prediction through characteristic basis function patterns for the meerkat/ska radio telescope antenna,” *IEEE Transactions on Antennas and Propagation*, vol. 61, no. 5, pp. 2466–2473, 2013.

[31] D. Morris, “Chromatism in radio telescopes due to blocking and feed scattering.” *Astron. Astrophys., VOL. 67*, pp. 221–228, September 1978.

[32] IEEE, “Ieee standard for definitions of terms for antennas,” *IEEE Std 145-2013 (Revision of IEEE Std 145-1993)*, pp. 1–50, 2014.

[33] L. Sevgi, "The antenna as a transducer: Simple circuit and electromagnetic models," *IEEE Antennas and Propagation Magazine*, vol. 49, no. 6, pp. 211–218, 2007.

[34] J. D. Kraus and K. R. Carver, *Electromagnetics [by] John D. Kraus [and] Keith R. Carver*, 2nd ed. McGraw-Hill New York, 1973.

[35] R. F. Harrington, *Time-harmonic electromagnetic fields.* Syracuse University: McGRAWHILL BOOK COMPANY, 1961, the classic reference for electromagnetics.

[36] D. I. L. de Villiers and R. Lehmensiek, "Rapid calculation of antenna noise temperature in offset gregorian reflector systems," *IEEE Transactions on Antennas and Propagation*, vol. 63, no. 4, pp. 1564–1571, 2015.

[37] W. Cerfonteyn, "Geometric argument based modelling for noise temperature of dual reflector antennas," active PHD research, University of Stellenbosch, unpublished.

[38] C. Granet, H. Zhang, K. Greene, G. James, A. Forsyth, T. Bird, R. Manchester, M. Sinclair, and P. Sykes, "A dual-band feed system for the parkes radio telescope," in *IEEE Antennas and Propagation Society International Symposium. 2001 Digest. Held in conjunction with: USNC/URSI National Radio Science Meeting (Cat. No.01CH37229)*, vol. 2, 2001, pp. 296–299 vol.2.

[39] C. Granet, "Designing axially symmetric cassegrain or gregorian dual-reflector antennas from combinations of prescribed geometric parameters. 2. minimum blockage condition while taking into account the phase-center of the feed," *IEEE Antennas and Propagation Magazine*, vol. 40, no. 3, pp. 82–89, 1998.

[40] C. Granet, "Designing classical offset cassegrain or gregorian dual-reflector antennas from combinations of prescribed geometric parameters," *IEEE Antennas and Propagation Magazine*, vol. 44, no. 3, pp. 114–123, 2002.

[41] Y. Mizugutch, M. Akagawa, and H. Yokoi, "Offset Dual Reflector Antenna," in *IEEE International Symposium on Antennas and Propagation Digest*, Jan. 1976, pp. 2–5.

[42] P.-S. Kildal, "Synthesis of multireflector antennas by kinematic and dynamic ray tracing," *IEEE Transactions on Antennas and Propagation*, vol. 38, no. 10, pp. 1587–1599, 1990.

[43] D. I. L. de Villiers and R. Lehmensiek, "Offset gregorian reflector shaping for optimum sensitivity," 08 2014, pp. 585–588.

[44] D. I. L. de Villiers, R. Lehmensiek, and M. V. Ivashina, "Low frequency diffraction effects when shaping the offset gregorian reflector system of the ska," in *2016 International Symposium on Antennas and Propagation (ISAP)*, 2016, pp. 802–803.

[45] Y. Rahmat-Samii and J. Mumford, “Reflector diffraction synthesis using global coefficients optimization techniques,” in *Digest on Antennas and Propagation Society International Symposium*, 1989, pp. 1166–1169 vol.3.

[46] A. Rudge and N. Adatia, “Offset-parabolic-reflector antennas: A review,” *Proceedings of the IEEE*, vol. 66, no. 12, pp. 1592–1618, 1978.

[47] M. Abbas-Azimi, F. Mazlumi, and F. Behnia, “Design of broadband constant-beamwidth conical corrugated-horn antennas [antenna designer’s notebook],” *IEEE Antennas and Propagation Magazine*, vol. 51, no. 5, pp. 109–114, 2009.

[48] T. S. Bird, “Investigation of crosspolarisation in offset cassegrain antennas,” *Electronics Letters*, vol. 17, no. 17, pp. 585–586, 1981.

[49] V. Galindo, “Synthesis of dual reflector antennas,” Air Force Office of Scientific Research, July 1964.

[50] J. B. Keller, “Geometrical theory of diffraction∗,” *J. Opt. Soc. Am.*, vol. 52, no. 2, pp. 116–130, Feb 1962. [Online]. Available: http://www.osapublishing.org/abstract.cfm?URI=josa-52-2-116

[51] F. A. Molinet, “Modern high frequency techniques for rcs computation: A comparative analysis,” *Invited Papers for Societe MOTHESIM*, vol. RN 186, 92357, 1991.

[52] R. Paknys, *Physical Theory of Diffraction*, 09 2016, pp. 317–334.

[53] V. Philippov, N. Kirpichnikova, and A. Kirpichnikova, “Effects of diffraction of a creeping wave from a line of jump of curvature,” in *International Seminar. Day on Diffraction. Proceedings (IEEE Cat. No.99EX367)*, 1999, pp. 87–96.

[54] E. Jørgensen and P. Meincke, “Design tool for high-performance rotationally symmetric reflector antennas,” in *2012 International Symposium on Antennas and Propagation (ISAP)*, 2012, pp. 1381–1384.

[55] E. Jørgensen and P. Meincke, “Design tool for high-performance rotationally symmetric reflector antennas,” in *2012 International Symposium on Antennas and Propagation (ISAP)*, 2012, pp. 1381–1384.

[56] I. Couckuyt, T. Dhaene, and P. Demeester, “oodace toolbox: A flexible object-oriented kriging implementation,” *Journal of Machine Learning Research*, vol. 15, no. 91, pp. 3183–3186, 2014. [Online]. Available: http://jmlr.org/papers/v15/couckuyt14a.html

[57] G. Matheron, “Principles of geostatistics,” *Economic Geology*, vol. 58, no. 8, pp. 1246–1266, 12 1963. [Online]. Available: https://doi.org/10.2113/gsecongeo.58.8.1246

[58] A. J. Booker, J. E. Dennis, P. D. Frank, D. B. Serafini, V. Torczon, and M. W. Trosset, “A rigorous framework for optimization of expensive functions by surrogates,” *Structural Optimization*, vol. 17, no. 1, p. 1–13, Nov 1999.

[59] M. Briani, A. Cuyt, F. Knaepkens, and W.-s. Lee, “Vexpa: Validated exponential analysis through regular sub-sampling,” *Signal Processing*, vol. 177, Dec 2020. [Online]. Available: http://dx.doi.org/10.1016/j.sigpro.2020.107722

[60] R. Lehmensiek and D. I. L. de Villiers, “An optimal 18-meter shaped offset gregorian reflector for the ngvla radio telescope,” *IEEE Transactions on Antennas and Propagation*, vol. PP, pp. 1–1, 06 2021.

[61] J. van der Herten, I. Couckuyt, D. Deschrijver, and T. Dhaene, “Adaptive classification under computational budget constraints using sequential data gathering,” *Advances in Engineering Software*, vol. 99, pp. 137–146, 09 2016.

Appendix A

Mathematics, Diagrams and Additional Results

A.1. Additional Mathematics

A.1.1. Maxwell's equations

For clarity, a full description of Maxwell's equations in time harmonic differential phasor form is given below in the notation style of this paper.
We begin with Faraday's law applied to a PEC surface:

$$\nabla \times \boldsymbol{E} = -j\omega\mu\boldsymbol{H} - \boldsymbol{M_s} \tag{A.1}$$

where μ is the magnetic permeability of the medium (free-space $\mu = \mu_0$).
Ampere's law is given as:

$$\nabla \times \boldsymbol{H} = \boldsymbol{J}_s + j\omega\varepsilon\boldsymbol{E} + \boldsymbol{J_i} \tag{A.2}$$

with ε the electric permittivity $\boldsymbol{E}$ & $\boldsymbol{H}$ represent the vector form of the electric and magnetic field strength respectively. $\boldsymbol{J}_s$ & $\boldsymbol{J}_i$ represent the conduction electric current and impressed electric current density respectively. $\boldsymbol{M}_i$ is the impressed magnetic current density, a physically non-observable mathematical abstraction current to balance the equations.
Gauss's law states:

$$\begin{aligned} \nabla \cdot \varepsilon\boldsymbol{E} &= \rho_v \\ \nabla \cdot \mu\boldsymbol{H} &= \rho_m \end{aligned} \tag{A.3}$$

ρ_v is the electric charge density and ρ_m is a purely abstract entity for analytical purposes.
Continuity is defined as the condition:

$$\nabla \cdot (\boldsymbol{J}_c + \boldsymbol{J}_c) = -j\omega\rho_v \tag{A.4}$$

For incident Fields on a PEC reflector the following boundary value conditions apply:

$$\text{PEC surface boundary} \begin{cases} \hat{\boldsymbol{n}} \times \boldsymbol{E} = 0 \\ \hat{\boldsymbol{n}} \times \boldsymbol{H} = \boldsymbol{J}_s \\ \hat{\boldsymbol{n}} \cdot \varepsilon \boldsymbol{E} = \rho_{\mathrm{es}} \\ \hat{\boldsymbol{n}} \cdot \mu \boldsymbol{H} = 0 \\ E_{PEC} = 0 \\ H_{PEC} = 0 \end{cases} \tag{A.5}$$

A.1.2. Other electromagnetic relations

The duality equations used to solve dual field problems:

$$\begin{array}{ll} \nabla \times \mathbf{E}_A = -j\omega\mu\mathbf{H}_A & \nabla \times \mathbf{H}_F = j\omega\epsilon\mathbf{E}_F \\ \nabla \times \mathbf{H}_A = \mathbf{J} + j\omega\epsilon\mathbf{E}_A & -\nabla \times \mathbf{E}_F = \mathbf{M} + j\omega\mu\mathbf{H}_F \\ \nabla^2\mathbf{A} + \beta^2\mathbf{A} = -\mu\mathbf{J} & \nabla^2\mathbf{F} + \beta^2\mathbf{F} = -\epsilon\mathbf{M} \\ \mathbf{A} = \frac{\mu}{4\pi}\iiint_V \mathbf{J}\frac{e^{-j\beta R}}{R}dv' & \mathbf{F} = \frac{\epsilon}{4\pi}\iiint_V \mathbf{M}\frac{e^{-j\beta R}}{R}dv' \\ \mathbf{H}_A = \frac{1}{\mu}\nabla \times \mathbf{A} & \mathbf{E}_F = -\frac{1}{\epsilon}\nabla \times \mathbf{F} \\ \mathbf{E}_A = -j\omega\mathbf{A} - j\frac{1}{\omega\mu\epsilon}\nabla(\nabla \cdot \mathbf{A}) & \mathbf{H}_F = -j\omega\mathbf{F} - j\frac{1}{\omega\mu\epsilon}\nabla(\nabla \cdot \mathbf{F}) \end{array} \tag{A.6}$$

$\omega = 2\pi f$ where f is frequency in Hertz. $\mathbf{A}$ is the magnetic vector potential and $\mathbf{F}$ is the electric vector potential, mathematical abstractions used during the calculation of radiated fields from surface current densities as in chapter 2. $\beta = \frac{2\pi}{\lambda}$ is the propagation constant. The theorem of reciprocity is given as:

$$\iiint_V (\mathbf{E}_1 \cdot \mathbf{J}_2 - \mathbf{H}_1 \cdot \mathbf{M}_2)\, dv = \iiint_V (\mathbf{E}_2 \cdot \mathbf{J}_1 - \mathbf{H}_2 \cdot \mathbf{M}_1)\, dv \tag{A.7}$$

And relates the field coupling of the magnetic and electric fields in region one, produced from the surface currents in that region, to the surface currents in region two, which in turn create the EM fields in region two and visa versa. A highly valuable theorem in the context of designing antennas, such that surface currents induced by excitation will be identical if a field of the same strength is received by the antenna.

A.1.3. Huygen's principle and equivalent

The Huygen's equivalent refers to a point source comprised of an infinitesimally small magnetic and electric dipole current. The far-field of this useful equivalent antenna source is given as:

$$\mathbf{E}(r,\theta,\phi) = E_0\frac{e^{-jkr}}{r}(1+\cos\theta)(\cos\phi\hat{\boldsymbol{\theta}} - \sin\phi\hat{\boldsymbol{\phi}}) \tag{A.8}$$

A.1.4. Prony form

Prony's problem or *Prony* form refers to the work by Gaspard Riche de Prony and has many useful applications in electrical in engineering and signal processing as it relates to regular sampling of an underlying function which exhibits oscillatory behaviour and allows for the complex exponential base terms which build the an underlying function $f(t)$ to be retrieved using eigenvalues [59].

$$\begin{aligned}\hat{f}(t) &= \sum_{i=1}^{M} A_i \exp(\sigma_i t) \cos(\omega_i t + \phi_i) \\ &= \sum_{i=1}^{M} \frac{1}{2} A_i \left(\exp(j\phi_i)\exp(\lambda_i^+ t) + \exp(-j\phi_i)\exp(\lambda_i^- t)\right)\end{aligned} \tag{A.9}$$

with λ_i representing the eigenvalues of the function. σ_i are the damping components and ϕ_i are the phase components. A_i are the amplitude components with j the imaginary unit $(j^2 = -1)$.

A.2. Additional Results

A.2.1. Increased zoom perspective results for SKA and synthesised offset configuration in chapter 6.

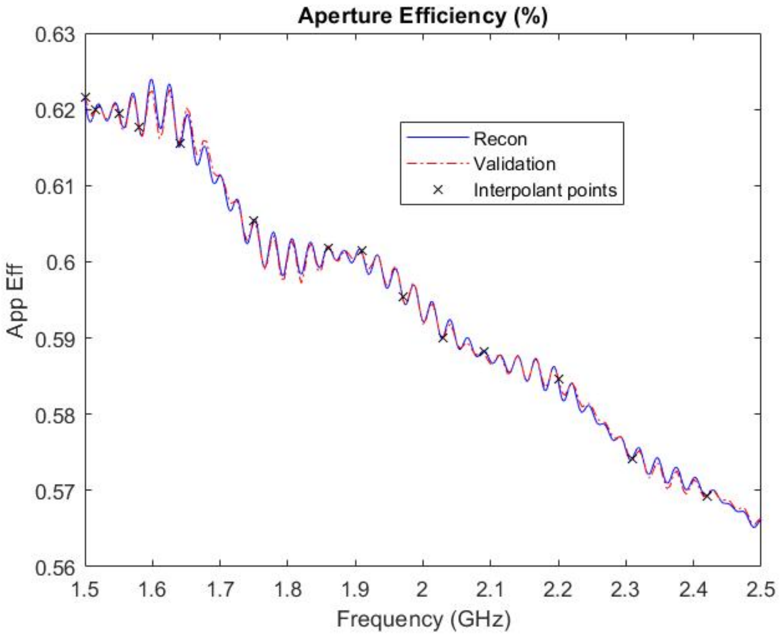

Figure A.1: Zoomed comparison of aperture efficiency reconstructed with superposition of $\mathbf{E}_{MR}$ and $\mathbf{E}_{FSR}$ CBFP Kriging-Matérn $(\frac{3}{2})$ interpolants using 41 adaptive samples.

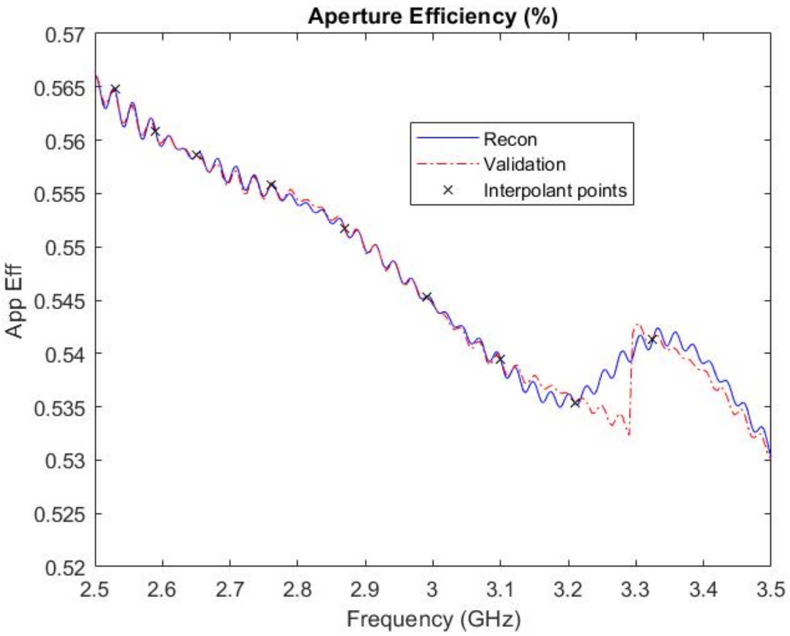

Figure A.2: Zoomed comparison of aperture efficiency reconstructed with superposition of $\mathbf{E}_{MR}$ and $\mathbf{E}_{FSR}$ CBFP Kriging-Matérn $(\frac{3}{2})$ interpolants using 41 adaptive samples.

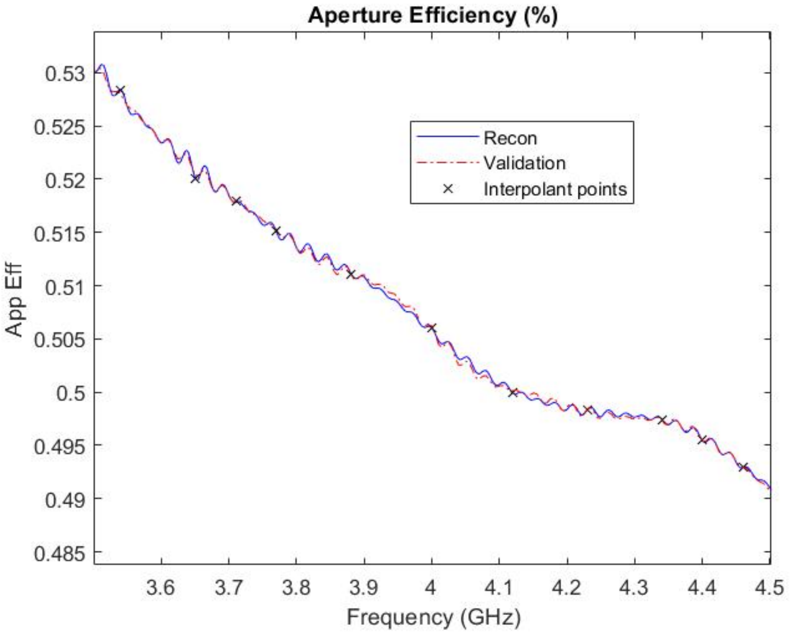

Figure A.3: Zoomed comparison of aperture efficiency reconstructed with superposition of $\mathbf{E}_{MR}$ and $\mathbf{E}_{FSR}$ CBFP Kriging-Matérn $(\frac{3}{2})$ interpolants using 41 adaptive samples.

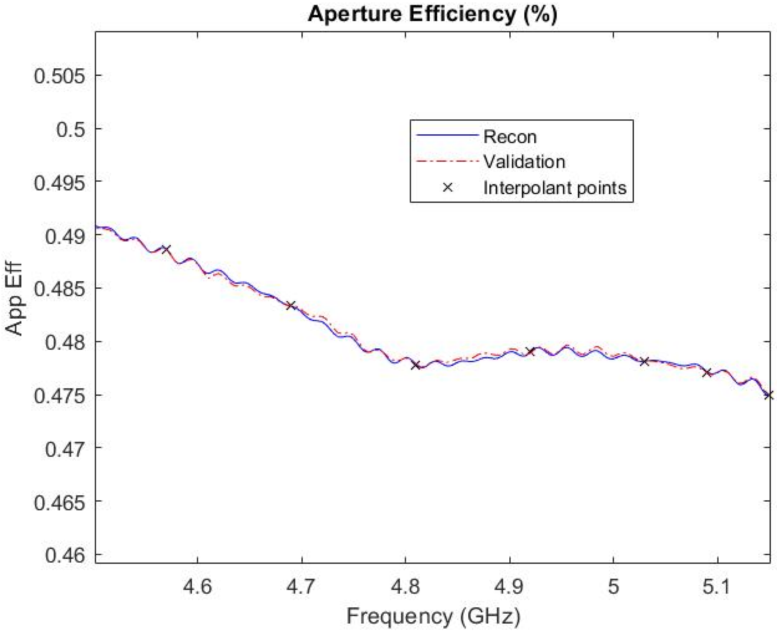

Figure A.4: Zoomed comparison of aperture efficiency reconstructed with superposition of $\mathbf{E}_{MR}$ and $\mathbf{E}_{FSR}$ CBFP Kriging-Matérn $(\frac{3}{2})$ interpolants using 41 adaptive samples.

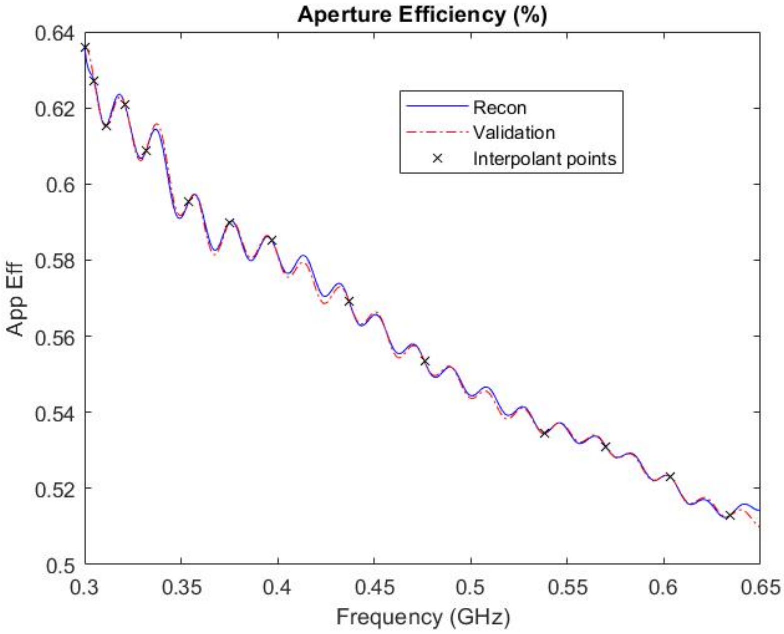

Figure A.5: Zoomed comparison of aperture efficiency reconstructed with superposition of $\mathbf{E}_{MR}$ and $\mathbf{E}_{FSR}$ CBFP Kriging-Matérn $(\frac{3}{2})$ interpolants using 24 adaptive samples.

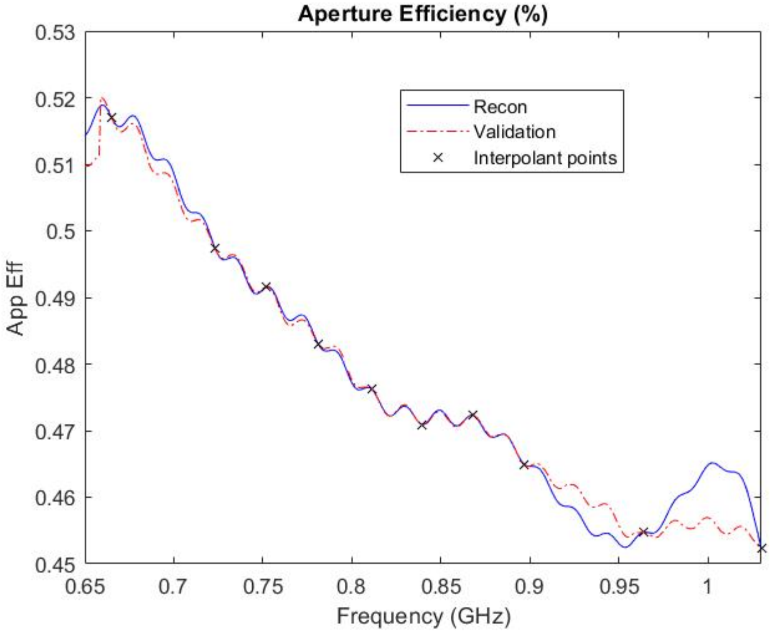

Figure A.6: Zoomed comparison of aperture efficiency reconstructed with superposition of $\mathbf{E}_{MR}$ and $\mathbf{E}_{FSR}$ CBFP Kriging-Matérn $(\frac{3}{2})$ interpolants using 24 adaptive samples.

A.2.2. Additional comparisons according to number of support samples for synthesised DR

Additional comparisons between aperture efficiency reconstructions from simple Kriging-Matérn $(\frac{3}{2})$ CBFP interpolants and validation sets from GRASP for the dual reflector geometry illustrated in Figure: 6.3.

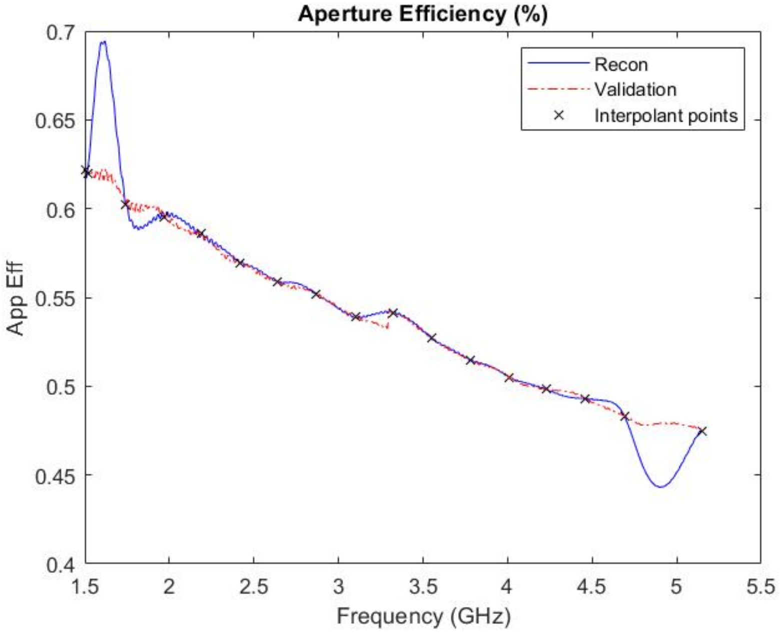

Figure A.7: Comparison between aperture efficiency reconstructed with superposition of $\mathbf{E}_{MR}$ and $\mathbf{E}_{FSR}$ CBFP Kriging-Matérn $(\frac{3}{2})$ interpolants using 17 adaptive samples with divergence at boundaries.

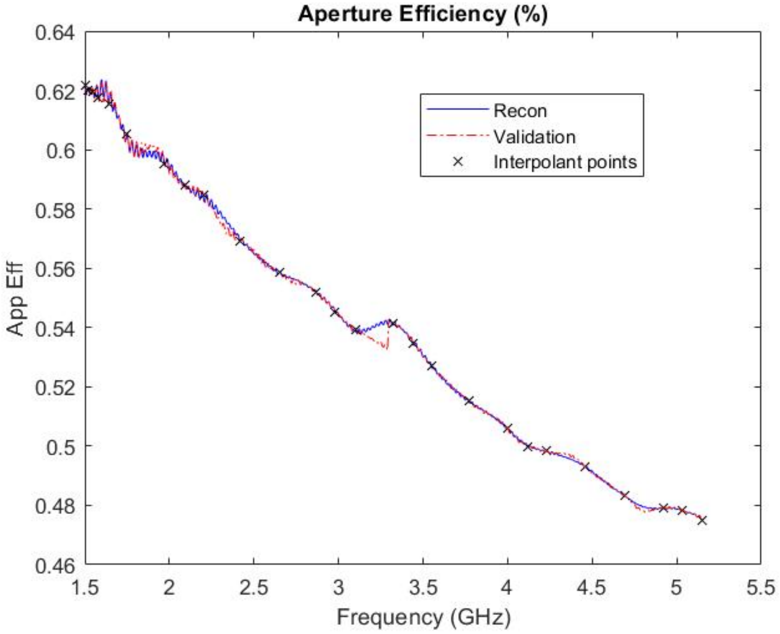

Figure A.8: Comparison between aperture efficiency reconstructed with superposition of $\mathbf{E}_{MR}$ and $\mathbf{E}_{FSR}$ CBFP Kriging-Matérn $(\frac{3}{2})$ interpolants using 27 adaptive samples.

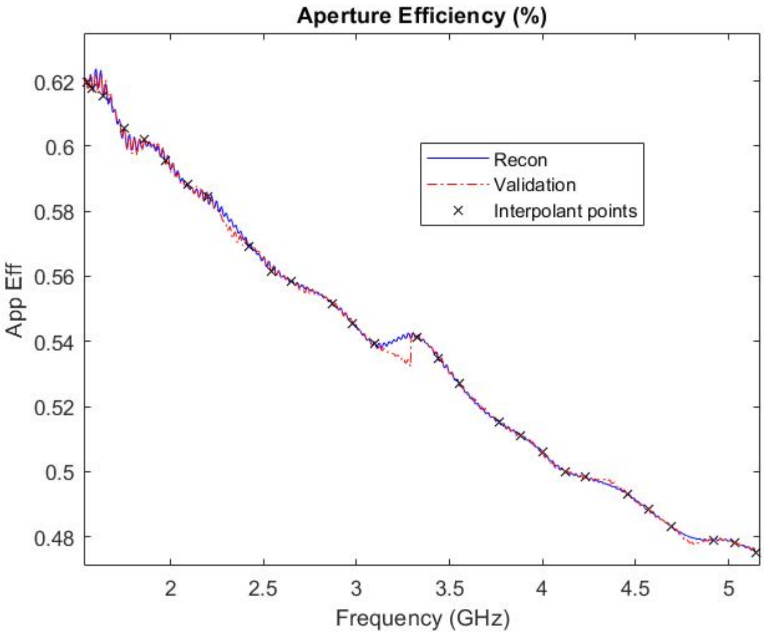

Figure A.9: Comparison between aperture efficiency reconstructed with superposition of $\mathbf{E}_{MR}$ and $\mathbf{E}_{FSR}$ CBFP Kriging-Matérn ($\frac{3}{2}$) interpolants using 30 adaptive samples.

A.2.3. Impact of incorrect feed positioning and or unstable primary patterns shown on SKAU offset Gregorian

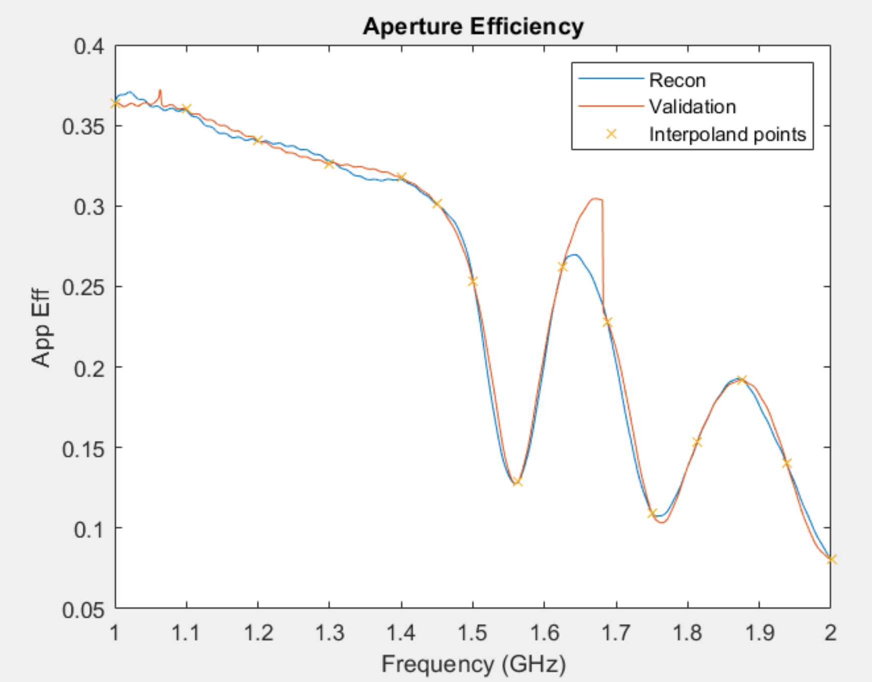

Figure A.10: Catastrophic aperture efficiency obtained with incorrect feed modelling, here the phase center was on average 0.15 m away from the sub-reflector focal point. The model was still able to interpolate, however, the result is pointless.

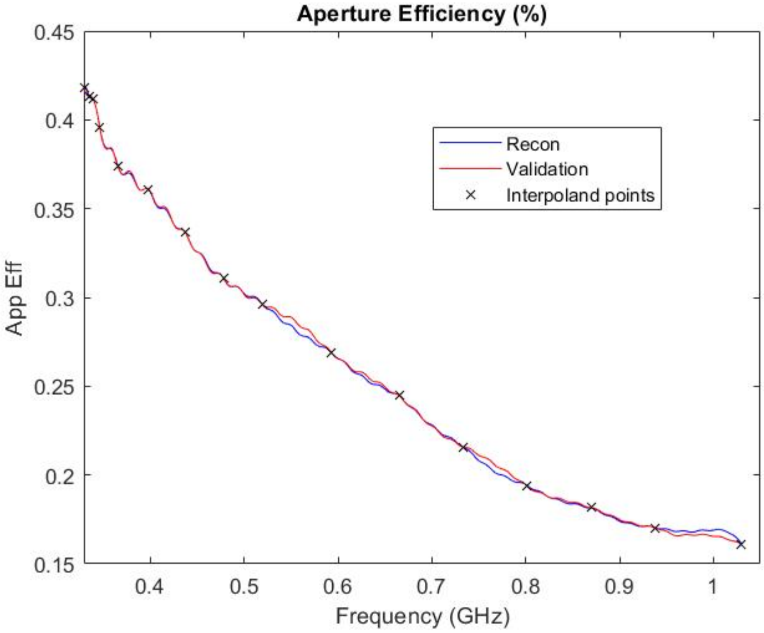

Figure A.11: Impact of higher order modes propagating in feed horn causing extremely rapid variations in secondary pattern aperture efficiency. For these situations exploitative adaptive sampling is needed, however, this should only be applicable for a *broken* feed antenna.

A.2.4. User Interface Script

```
%> @file "SUMOScript"
%> @author Jacques Wolmarans
%> @version FINAL - original FEED files - full convergence good result.
%> @date $2021/06/24$
%> @date Copyright 2021
%> Contact : 19918836@sun.ac.za / jacqueswolmarans@gmail.com
%> SOFTWARE PACKAGES REQUIRED:
%>SUMO toolbox - University of Antwerp
%>DACE toolbox - University of Antwerp
%>MEMACS & MEMACSpvt from University of Stellenbosch
%> UPDATED FOR CST/MOM FEED PATTERNS
% ======================================================================
%> User Instructions: For sequential Dual Reflector Interpolation using CBFP
%> 1) Setup GRASP TCI directory and SUMO directories & files
%> 2) Load Dual reflector Design - Ideal Gaussian feeds used as default
%> 3) First set the Frequency bounds and Farfield CUT file parameters
%> 4) Setup VEXPA grid spacing: default grid resolution must be changed
%   using angle spacing variable. Large shifts > 50 for sigma may cause
%   ambiguous shift results. [SEVERE PROBLEM] visible modulation present.
%
%> 5) set the number of Coefficients to be evaluated individually for
%   convergence and their criteriaas a percentage.
%> 6) Set whether to do a full coefficient sequential design run - ensure
%   relevent XML files are updated and correlate
%> 7) Run the script in Matlab command window
%>
%> Take note of cut names prefixcut.cut and prefixFSRcut.cut
% ======================================================================
%USER PARAMETER SETTINGS:
```

```
%clear all;
close all;
%Set the simulationPath directories:
Prefix = 'Sumotest'; %ensure this is correct in corresponding TCI file !
MATLAB_Path = 'C:\Users\19918836\Documents\MATLAB'; %location of your matlab directory with CBFP objects etc.
simpath = 'C:\Users\19918836\Documents\MATLAB\MengJW19918836\QRFHJacquesODR\JODRSUMO\working';
%GRASP simulation directory with tci files
CSTpath = 'C:\Program Files (x86)\CST Studio Suite 2021\CST DESIGN ENVIRONMENT.exe';
%this should be the path of a project with the feed model you wish to
%simulate, we change the frequency of the monitors as we go.
CSTProjectPath = 'C:\Users\19918836\Documents\QRFH\QRFHdev_SingleFreq.cst'
%file here then call the file as in GRASP call
%this should be a cst project file using frequency domain solver with the
%mesh already calculated at the highest frequency in the band of interest.
%such that our script simply adds a new farfield monitor at the frequency
%in question and exports that field in grasp format
%Feed_cut = 'MATLABtwogset.cut'; %PLACE This file inside working folder - prevents search issues
num_feed_Phicuts = 72;
%below are relative to MATLAB path
SUMOdatasetPath = 'MengJW19918836\QRFHJacquesODR\VexpaCoeffs.txt' ; %text file for coeffs
%- ensure this matches the corresponding SUMO .xml files
SUMOsingleCoeffPath = 'MengJW19918836\QRFHJacquesODR\SingleCoConfig.xml';
%Set the Antenna to Simulate:
TestAntenna = DualReflector.ODRparSize(8,1.0,3.6,9.6,1.5,1,0.026,1,0.2);
%load the test gemoetry here using the Dual Reflector class
%frequency ranges of Simulation - must match corresponding sim.xml file
Lowend = 1500; %lowest freq of interest in MHz
highend = 5150; %highest freq of interest in MHz
%Cut file parameters: Geometric range of the far field simulation in GRASP
ThetaMin = -4; %deg
ThetaMax = 4; %deg
numTheta = 601;
PhiMin = 0;%deg
PhiMax = 180;%deg
numPhi = 37;
%feedtaperdegrees = -12.0;%deg
TORname = 'SumoTest.tor'; %must have .tor ! else batch error will occur !
DRtoTorPath = [simpath,'\',TORname];
%setup VEXPA frequencies: Default grid resolution: 1MHz
%sufficient unless antenna is very large >50m Dm
sigma = 15; % distance in virtual Grid Frequency steps - basically as big as we can go
rho = 11; %chosen to be larger such that CBFP expansion is not too naive over frequency for the antenna
VexpaFreq = zeros(3,1);
VexpaFreq(1) = Lowend;
VexpaFreq(2) = Lowend+rho;
VexpaFreq(3) = Lowend+sigma;
%initial Design frequencies
freqLow = Lowend;
freqHigh = highend;
B = freqHigh-freqLow;
Center = (freqHigh+freqLow)/2.0;
%Finally define the convergence threshold and number of coefficients for
%individual evaluation - adjust SUMO files for combined call accordingly.
numcoeffs = 6;
COeffConvergenceThreshold = 25; %Convergence as a percentage of the max previous coefficient deviation [Frobenius distance]
CoeffNoiseFloor = 500;
%can also be an array of [numcoeffs]
% ======================================================================
% END OF USER CONSTANTS
```

```
%write CST config and execute field monitors
CSTfreqGHZ = [freqLow,1515,Center,freqHigh];
%CSTfreqGHZ = [freqLow,Center,freqHigh];
CSTfreqGHZ = CSTfreqGHZ./1e3;
%callfunchere
%make sure file is in matlabPath
%VEXPA CODE:
FFVexpaMR = [FarField(),FarField(),FarField()];
FFVexpaFSR = [FarField(),FarField(),FarField()];
%arrays for VEXPA normalisation. this next section can be for looped
%we first need to get the farfields for all initial frequency monitors from
%CST/MOM solver )
WriteMonitortoBas(CSTfreqGHZ,"functionwritten.bas"); %this is such that all of the necessary monitors are pre-calculated.
!"C:\Program Files (x86)\CST Studio Suite 2021\CST DESIGN ENVIRONMENT.exe" -m
C:\Users\19918836\Documents\MATLAB\functionwritten.bas
%the line above initiates the batch call for CST which will export farfield
%patterns to the desired working directory.
%code to find default CST export cut file format name:
%f=1.2 [1]
cutprefix = 'CSTGraspFeed_FFapprox_on_(farfield (f=';
cutsuffix = ') [1]_L3-CoCx).cut'; %ensure correct polarisation!
%NB> configure the output path and ensure FDsolvr is setup with a valid
%mesh prior to call. else the code will run with short circuits and break!
for n = (1:1:3)
%run MOM on feed - create farfield object and export to .cut - This should
%work?
%set/update TOR with new frequency and relevent tabulated feed.
cutname = [cutprefix,convertStringsToChars(string(VexpaFreq(n)/1e3)),cutsuffix]; %takenoteofscaling

TestAntenna.exportDRTabFeedwithFSRcutToTOR(DRtoTorPath,VexpaFreq(n)/1e3,Prefix,
ThetaMin,ThetaMax,numTheta
,PhiMin,PhiMax,numPhi,cutname,72);
%TestAntenna.exportDualReflectorToTOR(DRtoTorPath,VexpaFreq(n
)/1e3,Prefix,ThetaMin,ThetaMax,numTheta,PhiMin,PhiMax,numPhi,feedtaperdegrees);
%now run GRASP sim at this frequency
[FFtotal,FFFSR] = AutoGraspDR(simpath,TORname,Prefix,VexpaFreq(1)/1e3,numPhi);%note freq in GHz
%Populate this VEXPA frequency in array:
FFVexpaFSR(n) = FFFSR;
MRtemp = FFtotal - FFFSR;
FFVexpaMR(n) = MRtemp; %frequency should be set already
end

%VEXPA: Ensure the main beam of the primary electric field is passed :)
VEXPAS1 = [FFVexpaMR(1).E2(301,1),FFVexpaMR(3).E2(301,1)];
VEXPAS2 = FFVexpaMR(2).E2(301,1); %be careful, make sure it's broadside of the field patterns !
fsamp = 1;
%sigma = 47; % distance in virtual Grid Frequency steps
%rho = 23; %chosen to be larger such that CBFP expansion is not too naive over frequency for the antenna
%co - prime needed for harmonic extraction below nyquist
M_sigma = 2; %sigma samples
M_rho = 1; %Rho samples
subsnaps = 1; % Number of snapshots chosen from total snapshots for R-MUSIC to use - always 1
Nt = 1; %number of snapshots Fsamp irrelevant
MinPts1 = Nt; % Number of snapshots in cluster for bt_s
MinPts2 = Nt; % Number of snapshots in cluster for bt_r
%we need to select the various frequency indices from the field set to send
%into VEXPA

% Scaled signal
```

```
si_1 = transpose(VEXPAS1);
% Shifted signal
si_2 = transpose(VEXPAS2);
%VEXPA - Provided by Rina Weidemann
bt_s = NaN(1,Nt);
bt_r = NaN(1,Nt);
for k = 1:Nt
    indexes = randperm(Nt,subsnaps);
    bt_s = MatrixP(si_1,1);
    V = vandermonde(bt_s(k),max(M_sigma,M_rho));
    alpha = V\si_1(:,indexes);
    bt_r(k) = mean(V(1:M_rho)\si_2(:,indexes)./alpha);
end
idx = clustering(bt_s.', bt_r.', round(MinPts1), round(MinPts2));
bt = De_aliasing(mean(bt_s(idx)), sigma, mean(bt_r(idx)), rho);
x_returned = 1/(abs(imag(log(bt)))./(2*pi)./(1/fsamp)) ;
%argument of Greens function - this must be converted to shift in meters
angleSpacing = 1e6; %virtual VEXPA grid spacing for ripple frequency extraction
%linear function of frequency

fprintf('Returned x: %f \n', x_returned);
%Convert to shift in meters using Green's function
c0 = 299792458;
Vexpa_Shift = c0/(x_returned*angleSpacing);
fprintf('Required Shift: %f \n', Vexpa_Shift);
%now we run the same code again for Secondary field.
VEXPAS1 = [FFVexpaFSR(1).E2(301,1),FFVexpaFSR(3).E2(301,1)];
VEXPAS2 = FFVexpaFSR(2).E2(301,1); %be careful, make sure it's broadside of the field patterns !
% Scaled signal
si_1 = transpose(VEXPAS1);
% Shifted signal
si_2 = transpose(VEXPAS2);
%VEXPA - Provided by Rina Weidemann
bt_s = NaN(1,Nt);
bt_r = NaN(1,Nt);
for k = 1:Nt
    indexes = randperm(Nt,subsnaps);
    [~, bt_s(k)] = rootMUSIC(si_1(:,indexes),1);
    %bt_s = MatrixP(si_1,1); - % 1 dimensional alternative returns
    %effectively the same result
    V = vandermonde(bt_s(k),max(M_sigma,M_rho));
    alpha = V\si_1(:,indexes);
    bt_r(k) = mean(V(1:M_rho)\si_2(:,indexes)./alpha);
end
idx = clustering(bt_s.', bt_r.', round(MinPts1), round(MinPts2));
bt = De_aliasing(mean(bt_s(idx)), sigma, mean(bt_r(idx)), rho);
x_returned = 1/(abs(imag(log(bt)))./(2*pi)./(1/fsamp)) ;
%argument of Greens function - this must be converted to shift in meters
angleSpacing = 1e6; %virtual VEXPA grid spacing for ripple frequency extraction
fprintf('Returned x: : Feed & Sub-reflector) %f \n', x_returned);
%Convert to shift in meters using Green's function
c0 = 299792458;
Vexpa_Shift_FeedSR = c0/(x_returned*angleSpacing);
fprintf('Required Shift: %f \n', Vexpa_Shift_FeedSR);

%END OF VEXPA CODE
%Generate phase normalised patterns:
patternMR = CBFP(FFVexpaMR);
MRcoeffs = patternMR.farField2Coeffs(FFVexpaMR);
```

```
patternFSR = CBFP(FFVexpaFSR);
FSRcoeffs = patternFSR.farField2Coeffs(FFVexpaFSR);
%Initiate Initial Design: Min,Max,Halfway.
lowGHz = CSTfreqGHZ(1)
%lowGHz = 0.33;
highGHz = CSTfreqGHZ(2:end); %adjust samples if more wanted prior to first SUMO call
%start the interp field lists
FFMRinterp = FFVexpaMR(1,1);
frequencies = VexpaFreq(1);
frequenciesGHZ = frequencies./1e3;
FFFSRinterp = FFVexpaFSR;
%initially sorted:
FFMRinterpsorted = FFMRinterp(1,1).shift([0,0,Vexpa_Shift]); %the sorted field from the previous iteration - now unsorted
FFFSRinterpsorted = FFFSRinterp(1,1).shift([0,0,Vexpa_Shift_FeedSR]);

%highfreqloop:
for n = 1:1:numel(highGHz)
    %note these can simply be appended !
nextfreqGHz = highGHz(1,n);
%farfield arrays:
cutname = [cutprefix,convertStringsToChars(string(nextfreqGHz)),cutsuffix];
TestAntenna.exportDRTabFeedwithFSRcutToTOR(DRtoTorPath,nextfr
eqGHz,Prefix,ThetaMin,ThetaMax,numTheta,PhiMin,PhiMax,numPhi,cutname,72);
[FFtotal,FFFSR] = AutoGraspDR(simpath,TORname,Prefix,nextfreqGHz,numPhi);%note freq in GHz
MRtemp = FFtotal - FFFSR;
MRtemp = MRtemp.shift([0,0,Vexpa_Shift]);
FFFSR = FFFSR.shift([0,0,Vexpa_Shift_FeedSR]); %always shift before appending !
frequenciesGHZ = [frequenciesGHZ,nextfreqGHz];
FFMRinterpsorted = [FFMRinterpsorted,MRtemp];
FFFSRinterpsorted = [FFFSRinterpsorted,FFFSR];
end

% now catfreq and generate initialise CBFP for SUMO loops to begin

FFFSRcatinterp = FFFSRinterpsorted.catFreq();
FFFSRcatinterp = FFFSRcatinterp.setFreq(frequenciesGHZ,'GHz');
FFMRcatinterp = FFMRinterpsorted.catFreq();
FFMRcatinterp = FFMRcatinterp.setFreq(frequenciesGHZ,'GHz');
patternMR = CBFP(FFMRcatinterp); %we use these first two basis coefficients to converge
MRcoeffs = patternMR.farField2Coeffs(FFMRcatinterp);
%now lets package it into the dataset for initial design txt file and send to SUMO:
%Write these Initial Samples samples to the file for SUMO to understand
fileID = fopen(SUMOdatasetPath, 'w');
for n = 1:1:numel(frequenciesGHZ)
fprintf(fileID,'%f %f %f',frequenciesGHZ(1,n),real(MRcoeffs{1,1}(1,n)),imag(MRcoeffs{1,1}(1,n)));
fprintf(fileID,'\n');
end
fclose(fileID);
%make first call to start SUMO loops
go(SUMOsingleCoeffPath) %call with user defined initial dataset
%get the next frequency
nextfreqGHz = getGlobalx();
%Activate sequential Loop:
%now we have to rewrite the bas file to poll frequencies for CST.

for x = 1:1:numcoeffs
    patternMR = CBFP(FFMRcatinterp);
    MRcoeffs = patternMR.farField2Coeffs(FFMRcatinterp);
    convergedflag = 0;
```

```
    convprogress = [];
    disp("New Coefficient Loop starting now:")
    while (convergedflag == 0)
        nextfreqGHz = getGlobalx()
        nextfreqMHz = nextfreqGHz*1e3;
        if(mod(nextfreqMHz, 5) ~= 0)
        nextfreqGHz = round(nextfreqGHz,2)
        end %round to nearest 10MHz - if not a multiple of 5
        prevMRcoeffs = MRcoeffs;
        FFMRinterp = FFMRinterpsorted; %the sorted field from the previous iteration - now unsorted
        FFFSRinterp = FFFSRinterpsorted;
        %farfield arrays:
%        WriteMonitortoBas(nextfreqGHz,"functionwritten.bas")
        %!"C:\Program Files (x86)\CST Studio Suite 2021\CST DESIGN ENVIRONMENT.exe" -m
        C:\Users\19918836\Documents\MATLAB\functionwritten.bas
        cutname = [cutprefix,convertStringsToChars(string(nextfreqGHz)),cutsuffix];
        TestAntenna.exportDRTabFeedwithFSRcutToTOR(DRtoTorPath
        ,nextfreqGHz,Prefix,ThetaMin,ThetaMax,numTheta,PhiMin,PhiMax,numPhi,cutname,72);
        [FFtotal,FFFSR] = AutoGraspDR(simpath,TORname,Prefix,nextfreqGHz,numPhi);%note freq in GHz
        MRtemp = FFtotal - FFFSR;
        MRtemp = MRtemp.shift([0,0,Vexpa_Shift]);
        FFFSR = FFFSR.shift([0,0,Vexpa_Shift_FeedSR]); %always shift before appending !
        %append fields and generate CBFP patterns for SUMO/interpolation
        %Sort fields in order of frequency
        frequenciesGHZ = [frequenciesGHZ,nextfreqGHz];
        frequenciesGHZ = sort(frequenciesGHZ);
        %populate the new MR field array using a for loop with simple check on freq
        FFMRinterpsorted = FFMRinterp(1,1);
        FFFSRinterpsorted = FFFSRinterp(1,1);
        Originalfreqindex = 0;
        %we know the first frequency will always be the lowest frequency in the band
        %loop till we append our new frequency
        for n = 2:1:numel(frequenciesGHZ)
            if frequenciesGHZ(1,n) == MRtemp.freq
                FFMRinterpsorted = [FFMRinterpsorted,MRtemp]
                FFFSRinterpsorted = [FFFSRinterpsorted,FFFSR];
                endoforiginalFREQ = n-1;
                n = n+1;
                break;
            else
                FFMRinterpsorted = [FFMRinterpsorted,FFMRinterp(1,n)]
                FFFSRinterpsorted = [FFFSRinterpsorted,FFFSRinterp(1,n)]
            end
        end
        %fill the rest of the array up now offsetting the loop counter
        %NOTE: when using CATFREQ it is a good idea to re-specify the frequency for
        %safety betwen MHz and GHz
        while(n<=numel(frequenciesGHZ))
            Originalfreqindex = n-1;
            FFMRinterpsorted = [FFMRinterpsorted,FFMRinterp(1,Originalfreqindex)];
            FFFSRinterpsorted = [FFFSRinterpsorted,FFFSRinterp(1,Originalfreqindex)];
            n = n+1;
        end
        %catantenate frequencies:
        FFMRcatinterp = FFMRinterpsorted.catFreq();
        FFMRcatinterp = FFMRcatinterp.setFreq(frequenciesGHZ,'GHz');
        %Generate CBFP coeffs:
        patternMR = CBFP(FFMRcatinterp);
        %patternMR = CBFP(FFMRcatinterp); %we use these first two basis coefficients to converge
```

```
        MRcoeffs = patternMR.farField2Coeffs(FFMRcatinterp);
        %now we check if they have converged - if not we execute again.
        %assemble this and previous pattern into comparable doubles. lets try
        %This coefficient only:
        prevcomplexco = [];
        currentcomplexco =[];

        for n = 1:1:endoforiginalFREQ
            prevcomplexco(1,n) = prevMRcoeffs{1,1}(x,n);
            currentcomplexco(1,n) = MRcoeffs{1,1}(x,n);
        end
        adjustedIndex = endoforiginalFREQ+1; %skip the new frequency but append the rest for subtraction
        for n = adjustedIndex:1:numel(frequenciesGHZ)
            prevcomplexco(1,n) = prevMRcoeffs{1,1}(x,n-1);
            currentcomplexco(1,n) = MRcoeffs{1,1}(x,n);
        end
        %now calculate Convergence:
        difference = currentcomplexco-prevcomplexco; %should be square of same dimensions
        %let us use the frobenius distance on the entire matrix against max:
        Peak = max(currentcomplexco);
        %Peak = max(prevcomplexco)-min(prevcomplexco); %largest deviation in previous coeff
        sim = sqrt(sum((difference).^2,2));
        CurrentConv = abs(sim)/abs(Peak);
        convprogress = [convprogress,CurrentConv]
        if(CurrentConv<=(COeffConvergenceThreshold/100))
            convergedflag = 1;
            figure()
            plot(convprogress),title("Convergence Progress"),xlabel("Iteration"),ylabel("Fractional Frobenius Convergence")
            disp('CONVERGED COEFFICIENT !')
        end
        %then run threshold check here. also I want to run some different
        %algorithms. let's set that up now.
        %now we need to do some logic - maybe ask dirk for guidance

        %now lets package it into the dataset for initial design txt file and send to SUMO:
        fileID = fopen(SUMOdatasetPath, 'w');
        for n = 1:1:numel(frequenciesGHZ)
            fprintf(fileID,'%f %f %f',frequenciesGHZ(1,n),real(MRcoeffs{1,1}(x,n)),imag(MRcoeffs{1,1}(x,n)));
            fprintf(fileID,'\n');
        end
        fclose(fileID);

        if numel(frequenciesGHZ)>65%Safety to Prevent Infinite loops - may be an issue for extreme wideband sims
            convergedflag = 1;
            break;
        end%failsafe as it should converge by then
        %run SUMO -> read in next frequency from samples.txt -> check convergence

        go(SUMOsingleCoeffPath)
    end
    disp("Coefficient: ")
    disp(x)
    disp(" Complete")
end
disp("All individual coefficient convergence loops complete.")
%COMBINED COEFFICIENt SEQUENTIAL DESIGN LOOP

%RECONSTRUCTION OF ANTENNA FIELDS
Freq = [1.5,1.505,1.507,1.510,1.511,(1.515:0.005:5.15)];
```

```
%%%%%%%####DEBUG LINES
%FFMRcatinterp = FFMRcatinterp.shift([0,0,Vexpa_Shift]);%shift back to original position
%FFFSRcatinterp = FFFSRcatinterp.shift([0,0,Vexpa_Shift_FeedSR]);
%%%%%%#####VEXPADEBUGLINES
FFMRcatinterp= FFMRinterpsorted.catFreq();
FFMRcatinterp = FFMRcatinterp.setFreq(frequenciesGHZ,’GHz’);
FFFSRcatinterp = FFFSRinterpsorted.catFreq();
FFFSRcatinterp = FFFSRcatinterp.setFreq(frequenciesGHZ,’GHz’);
BASIS = DetermineBasisA(FFMRcatinterp,CoeffNoiseFloor);
FFMRint = CBFPFieldexpanderDACE(FFMRcatinterp,frequenciesGHZ,Freq,BASIS,’true’);
figure()
FFsec = CBFPFieldexpanderDACE(FFFSRcatinterp,frequenciesGHZ,Freq,15,’true’); %3 sufficient, you can add more using BASIS
FFMRint = FFMRint.setFreq(Freq,’GHz’);
FFsec = FFsec.setFreq(Freq,’GHz’);

FFMRint = FFMRint.shift([0,0,-Vexpa_Shift]);%shift back to original position !
FFsec = FFsec.shift([0,0,-Vexpa_Shift_FeedSR]);
FFrecon = FFMRint+FFsec; %reconstrct the field using our basis expanded fields at the original point
%PLOT RELEVANT DATA - AND POSSIBLE VALIDATION SET
%END OF SCRIPT
```

A.2.5. Conic sections commonly used in dual reflector antennas

This is a very brief summary of the appendix A-7 in [26] and it is advised to refer there for more detailed mathematics.

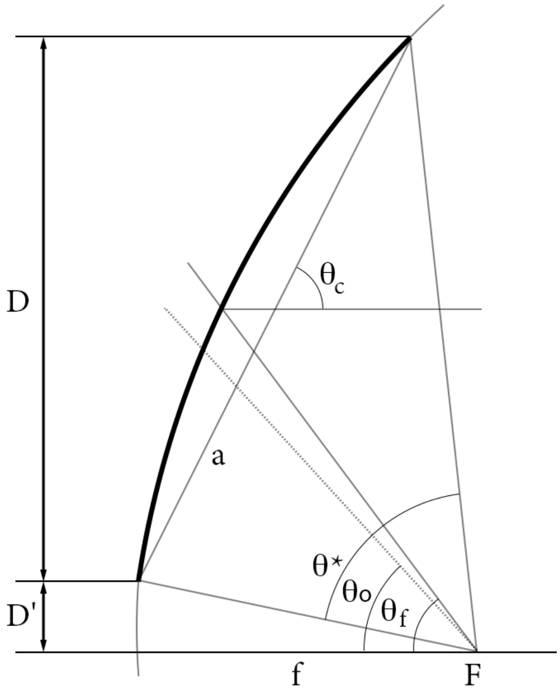

Figure A.12: Offset paraboloid geometry with focal point F, focal length f and offset angle u defined in cartesian co-ordinates.

A general paraboloid surface has the following relations:

$$\begin{aligned} \rho^2 &= x^2 + y^2 \\ \rho^2 &= 4fz \\ r &= \frac{2f}{1+\cos 2u} \\ &= f + z \\ &= \frac{f}{\cos^2 u} \\ \rho &= r\sin 2u \\ &= 2f\tan u \\ z &= f\tan^2 u \\ u &= \arctan\left\{\frac{\rho}{2f}\right\} \end{aligned} \tag{A.10}$$

For the offset case as shown in Figure A.12 the necessary feed axis,θ_f going through F is found as:

$$\theta_f = 2\arctan\left\{\frac{D' + \frac{D}{2}}{2f}\right\} \tag{A.11}$$

The effective aperture at high frequencies is in the plane defined using θ_c as:

$$\theta_c = \arctan\left\{\frac{2f}{D' + \frac{D}{2}}\right\} \tag{A.12}$$

D and D' expressed by f, θ_0 and θ^* become

$$D = \frac{4f\sin\theta^*}{\cos\theta_0 + \cos\theta^*}$$

and

$$D' = 2f\tan\left(\frac{\theta_0 - \theta^*}{2}\right)$$

These are the standard derivations followed for the synthesis of a classical main reflector for an offset Gregorian antenna.

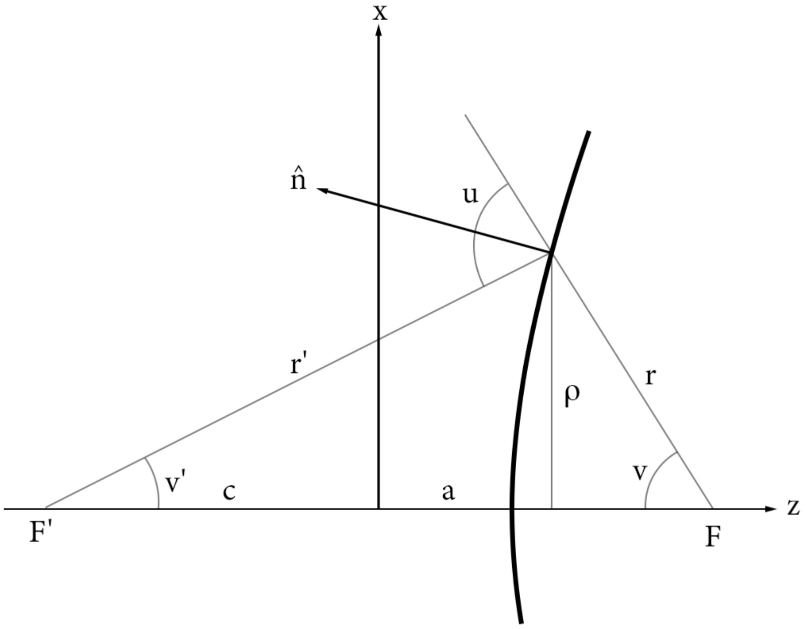

Figure A.13: Hyperboloid and typical geometric parameters

Hyperboloids have the following relations, please refer to [26] A-7 for detail.

$$\rho^2 = x^2 + y^2$$
$$\frac{z^2}{a^2} - \frac{\rho^2}{b^2} = 1$$

where

$$b^2 = c^2 - a^2$$

The eccentricity is

$$e = \frac{c}{a}$$

and

$$r = \frac{a\left(e^2 - 1\right)}{e\cos v + 1}$$
$$r' = \frac{a\left(e^2 - 1\right)}{e\cos v' - 1}$$
$$\rho = r\sin v = r'\sin v'$$
$$e = \frac{\sin\frac{v+v'}{2}}{\sin\frac{v-v'}{2}}$$
$$(e+1)\tan\frac{v'}{2} = (e-1)\tan\frac{v}{2}$$
$$2u = v + v'$$

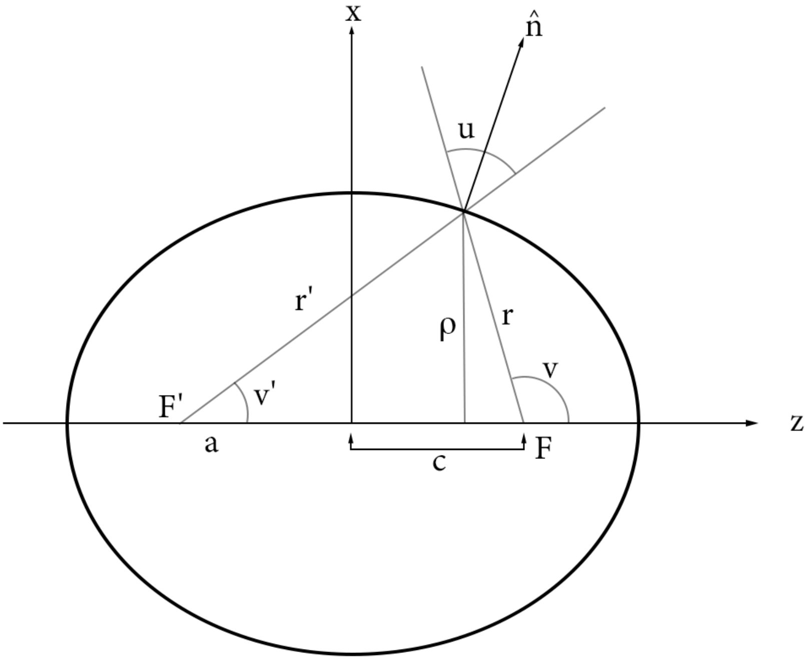

Figure A.14: rotationally symmetric ellipsoid as shown above with major axis = $2a$ and focal distance $2c$.

The ellipsoid has the following relations:

$$\rho^2 = x^2 + y^2$$
$$\frac{z^2}{a^2} + \frac{\rho^2}{b^2} = 1$$

where

$$b^2 = a^2 - c^2$$

The eccentricity is

$$e = \frac{c}{a}$$

and

$$r = \frac{a\left(1 - e^2\right)}{1 + e\cos v}$$
$$r' = \frac{a\left(1 - e^2\right)}{1 - e\cos v'}$$
$$\rho = r\sin v = r'\sin v'$$
$$e = \frac{\sin\frac{v-v'}{2}}{\sin\frac{v+v'}{2}}$$
$$2u = v - v'$$
$$(1+e)\tan\frac{v'}{2} = (1-e)\tan\frac{v}{2}$$